



## KEPLERATES: FROM ELECTRONIC STRUCTURE TO DYNAMIC PROPERTIES.

María Dolores Melgar Freire

Dipòsit Legal: T 258-2016

**ADVERTIMENT.** L'accés als continguts d'aquesta tesi doctoral i la seva utilització ha de respectar els drets de la persona autora. Pot ser utilitzada per a consulta o estudi personal, així com en activitats o materials d'investigació i docència en els termes establerts a l'art. 32 del Text Refós de la Llei de Propietat Intel·lectual (RDL 1/1996). Per altres utilitzacions es requereix l'autorització prèvia i expressa de la persona autora. En qualsevol cas, en la utilització dels seus continguts caldrà indicar de forma clara el nom i cognoms de la persona autora i el títol de la tesi doctoral. No s'autoritza la seva reproducció o altres formes d'explotació efectuades amb finalitats de lucre ni la seva comunicació pública des d'un lloc aliè al servei TDX. Tampoc s'autoritza la presentació del seu contingut en una finestra o marc aliè a TDX (framing). Aquesta reserva de drets afecta tant als continguts de la tesi com als seus resums i índexs.

**ADVERTENCIA.** El acceso a los contenidos de esta tesis doctoral y su utilización debe respetar los derechos de la persona autora. Puede ser utilizada para consulta o estudio personal, así como en actividades o materiales de investigación y docencia en los términos establecidos en el art. 32 del Texto Refundido de la Ley de Propiedad Intelectual (RDL 1/1996). Para otros usos se requiere la autorización previa y expresa de la persona autora. En cualquier caso, en la utilización de sus contenidos se deberá indicar de forma clara el nombre y apellidos de la persona autora y el título de la tesis doctoral. No se autoriza su reproducción u otras formas de explotación efectuadas con fines lucrativos ni su comunicación pública desde un sitio ajeno al servicio TDR. Tampoco se autoriza la presentación de su contenido en una ventana o marco ajeno a TDR (framing). Esta reserva de derechos afecta tanto al contenido de la tesis como a sus resúmenes e índices.

**WARNING.** Access to the contents of this doctoral thesis and its use must respect the rights of the author. It can be used for reference or private study, as well as research and learning activities or materials in the terms established by the 32nd article of the Spanish Consolidated Copyright Act (RDL 1/1996). Express and previous authorization of the author is required for any other uses. In any case, when using its content, full name of the author and title of the thesis must be clearly indicated. Reproduction or other forms of for profit use or public communication from outside TDX service is not allowed. Presentation of its content in a window or frame external to TDX (framing) is not authorized either. These rights affect both the content of the thesis and its abstracts and indexes.

UNIVERSITAT ROVIRA I VIRGILI

KEPLERATES: FROM ELECTRONIC STRUCTURE TO DYNAMIC PROPERTIES.

María Dolores Melgar Freire

Dipòsit Legal: T 258-2016

UNIVERSITAT ROVIRA I VIRGILI

KEPLERATES: FROM ELECTRONIC STRUCTURE TO DYNAMIC PROPERTIES.

María Dolores Melgar Freire

Dipòsit Legal: T 258-2016

María Dolores Melgar Freire

# Keplerates: from Electronic Structure to Dynamic Properties

**Ph. D. Thesis**

Supervised by Dr. Josep Bonet Ávalos and Dr. Carles Bo Jané



Tarragona

2015



UNIVERSITAT ROVIRA I VIRGILI

KEPLERATES: FROM ELECTRONIC STRUCTURE TO DYNAMIC PROPERTIES.

María Dolores Melgar Freire

Dipòsit Legal: T 258-2016



UNIVERSITAT  
ROVIRA I VIRGILI

**Departament d'Enginyeria  
Química**

Campus Sescelades  
Av. Països Catalans, 26  
43007 Tarragona  
Tel. 977 55 96 03

Dr. Josep Bonet i Ávalos, professor del Departament d'Enginyeria Química de la Universitat Rovira i Virgili i Dr. Carles Bo professor de l'Institut Català d'Investigació Química,

FEM CONSTAR que el treball amb títol "*Keplerates: from Electronic Structure to Dynamic Properties*", que presenta la Sra. María Dolores Melgar Freire per l'obtenció del títol de Doctora en Enginyeria Química, s'ha dut a terme sota la nostra direcció i en el Departament d'Enginyeria Química de la Universidad Rovira i Virgili i l'Institut Català de d'Investigació Química, i que compleix els requisits per poder optar a la Menció Europea.

Tarragona, 9 de Octubre de 2015

Els directors de la tesi doctoral

Dr. Josep Bonet i Ávalos

Dr. Carles Bo i Jané

UNIVERSITAT ROVIRA I VIRGILI

KEPLERATES: FROM ELECTRONIC STRUCTURE TO DYNAMIC PROPERTIES.

María Dolores Melgar Freire

Dipòsit Legal: T 258-2016

## Acknowledgements

Por fin, después de más de tres años, ha llegado el momento de escribir estas líneas. Llegar hasta aquí habría sido imposible sin el apoyo de muchas personas que, por ello, se merecen mi más profundo agradecimiento.

Quisiera agradecer en primer lugar a mis padres y a mis hermanos, porque estoy convencida de que el entorno en el que he crecido ha sido clave para llegar a este punto. También a las nuevas incorporaciones de la familia (Eloy, María y Sandra) y a los más pequeños (Martín, Iván, Jimena y Roi), porque su llegada ha marcado un antes y un después en casa.

Por otro lado, mis directores de tesis, Carles y Josep, merecen una mención especial. No tengo palabras para expresar lo que habéis supuesto en mi vida. Gracias por la confianza puesta en mí y por toda la paciencia que habéis mostrado. Durante todo este tiempo me he sentido muy afortunada de teneros como jefes. He ganado muchísimo profesionalmente, pero también a nivel personal.

A la URV y el ICIQ les agradezco el apoyo económico y los recursos a los que he tenido acceso. También quiero agradecer al COST-PoCheMoN por haber financiado mis estancias en el extranjero, de las cuales me llevo muy buenas experiencias.

I would like to thank Lee Cronin and his group (specially Laia and Harris) for their hospitality and for giving me the opportunity to learn from a such good team.

Je voulais remercier le group de Solides Moléculaires de l'Institut Lavoisier de Versailles, spécialement Emmanuel Cadot et Sébastien Floquet, pour les collaborations scientifiques et pour leur amabilité pendant le deux mois à Versailles. Je voulais aussi remercier Mhamad, William, Nancy et Irene (ma chère colocataire), pour le soutien et la patience au labo, mais aussi dehors.

Quiero agradecer a las verdaderas autoridades del grupo de teóricos del ICIQ, a Núria Vendrell y Martín Gumbau, porque nos hacen la vida más fácil y sin ellos todo se vendría abajo. Tampoco me quiero olvidar al resto de la gente que forma o ha formado parte de esta oficina a la que llamamos laboratorio: Adiran

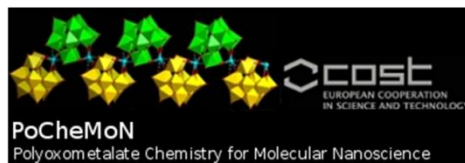
De Aguirre, Lluís Artús, María Besora, Marçal Capdevila, Damien Cornu, Víctor Fernández, Ignacio Funes, Rodrigo García, Charles Goehry, Franziska Hegner, Michael Higham, Jesús Jover, Rositha Kuniyil, Oier Lakuntza, Qiang Li, Abel Locati, Núria López, Feliu Maseras, Anna Mateo, Ángel Luís Mudarra, Elena de Orbe, Cristina Pubill, Marcos Rellán, Guillem Revilla, Xavi Sanz, Crisa Vargas y Laia Vilella. A Neyvis le agradezco haber facilitado tanto mi integración al llegar y todos los momentos que hemos compartido. Gracias a Max por los grandes descubrimientos en series que han hecho más ameno el camino. Gracias a Luca, por los múltiples consejos y lo mucho aprendido. Muchísimas gracias a Miquel, que siempre ha sacado un rato para resolverme algún problema. Millones de gracias para el resto de miembros del grupo: a Fernando, que tantísimo me ayudó desde el primer momento (qué bueno es trabajar con alguien que siempre está sonriendo); a Joan, porque no pude tener mejor herencia del Man, por estos últimos meses, por las labores de diseñador gráfico, por estar siempre dispuesto a escucharme y echarme una mano; a Nuno, por el importante papel que ha tenido en esta Tesis y por estar siempre dispuesto a enseñarme; y, por último, Stefano, que nos salvó la vida en Fulda (*eine Wasser ohne Gas, bitte*) y que es, sin duda, uno de los mejores fichajes de los últimos tiempos.

Fuera del mundo teórico, no puedo olvidarme de Jordi, por ejercer de Rey Mago y por las noches de Champions; de Carol y Raúl, por nuestras teorías de conspiración; de Antonio, por su hospitalidad; de Nelson y Sanela y, en general, a todos los que han hecho que estos años fuera de casa hayan valido la pena.

Y desde casa, hay personas que a pesar de estar lejos, han estado muy cerca durante todo este proceso: Shere, que es mi pilar fundamental y de la que aprendo cada día a ser mejor persona; Helena y Ana, que aguantan todas mis quejas y aún así me soportan. A Nuria y Martín: gracias por todo lo vivido durante los años compostelanos, sabéis de sobra que sin vosotros el camino habría sido mucho más duro.

Y finalmente, debo agradecerle a Ximo, a mi compañero, el haber recorrido este camino a mi lado, apoyándome siempre: por tener palabras de ánimo cuando DL\_POLY me hace la vida imposible, por darme fuerza en los momentos más bajos, por la paciencia mientras estábamos lejos y, en definitiva, por hacerme feliz. Gracias, porque esta Tesis, meu ben, también es mérito tuyo.

## Funding Agencies



UNIVERSITAT ROVIRA I VIRGILI

KEPLERATES: FROM ELECTRONIC STRUCTURE TO DYNAMIC PROPERTIES.

María Dolores Melgar Freire

Dipòsit Legal: T 258-2016

## List of Publications

### Related with this Thesis

**"Hydrophobic Effect as a Driving Force for Host-Guest Chemistry of a Multi-Receptor Keplerate-Type Capsule"**, Nancy Watfa, Dolores Melgar, Mohamed Haouas, Francis Taulelle, Akram Hijazi, Daoud Naoufal, Josep Bonet Ávalos, Sébastien Floquet, Carles Bo, Emmanuel Cadot, *Journal of American Chemical Society*, **2015**, 137, 5845-5851.

**"Direct Observation of the Formation Pathway of Mo<sub>132</sub> Keplerates"**, Subharanjan Biswas, Dolores Melgar, Amitava Srimany, Antonio Rodríguez-Forteza, Thalappil Pradeep, Carles Bo, Josep M. Poblet, Soumyajit Roy, *manuscript in revision*.

**"Analysis of Plugging Effect with Different Cations in Mo<sub>132</sub> Keplerate"**, Dolores Melgar, Carles Bo, Josep Bonet Ávalos, *manuscript in preparation*.

**"Electronic Structure of Keplerates: New Mixed Mo-W Based Capsule"**, Dolores Melgar, Mhamad Aly Moussawi, Sébastien Floquet, Emmanuel Cadot, Carles Bo, *manuscript in preparation*.

**"Interaction Between the Mo<sub>132</sub> Capsule and its Internal Ligands"**, Dolores Melgar, Josep Bonet Ávalos, Carles Bo, *submitted*.

### Not Related with this Thesis

**"Polyoxometalate as Cryptate for Apolar Ions : Synthesis, Structure and 1H DOSY NMR Study"**, Dolores Melgar, Nancy Watfa, Nuno Bandeira, Sébastien Floquet, Mohamed Haouas, Carles Bo and Emmanuel Cadot, *manuscript in preparation*.



UNIVERSITAT ROVIRA I VIRGILI

KEPLERATES: FROM ELECTRONIC STRUCTURE TO DYNAMIC PROPERTIES.

María Dolores Melgar Freire

Dipòsit Legal: T 258-2016

*"The diversity of the phenomena of nature is so great, and the treasures hidden in the skies so rich, precisely in order that the human mind shall never be lacking in fresh nourishment"*

**– Johannes Kepler**

*A Martín, Iván, Jimena y Roi*

UNIVERSITAT ROVIRA I VIRGILI

KEPLERATES: FROM ELECTRONIC STRUCTURE TO DYNAMIC PROPERTIES.

María Dolores Melgar Freire

Dipòsit Legal: T 258-2016

# Contents

---

<b>Abstract .....</b>	<b>1</b>
<b>Chapter 1: General Introduction.....</b>	<b>5</b>
1.1 - Introduction .....	7
1.2 - Polyoxometalates.....	11
1.3 - Keplerates .....	14
1.4 - Objectives.....	20
<b>Chapter 2: Theoretical Background .....</b>	<b>23</b>
2.1- Computational methods .....	25
2.2 - Quantum Mechanics: Density Functional Theory.....	26
2.2.1 - Quantum Mechanics Fundamentals .....	26
2.2.2 - Density Functional Theory .....	28
2.2.2.1) Local Density Approximation .....	30
2.2.2.2) Generalised Gradients Approximation .....	32
2.2.2.3) Hybrid Functionals .....	34
2.2.2.4) Meta-GGA .....	34
2.2.2.5) Hyper-GGA .....	35
2.2.2.6) Basis Functions Set.....	35
2.2.2.7) DFT Studies on POMs.....	36
2.3 - Classical Mechanics: Molecular Dynamics.....	37
2.3.1 - Classical Mechanics Fundamentals.....	37
2.3.1.1) Classical and Statistical Mechanics .....	37
b) Canonical Ensemble (NVT).....	39
c) Isothermal-Isobaric Ensemble (NPT).....	40
d) Grand Canonical Ensemble ( $\mu$ VT).....	41

2.3.1.2 - Classical Molecular Dynamics.....	42
a) Force Field .....	44
a.1) Short-ranged forces: the Lennard-Jones model .....	45
a.2) Long-ranged Forces: the Ewald Summation Technique .....	50
a.3) Point Charges Distribution.....	52
b) Integration of the Equations of Motion .....	59
c) Implementation of the Constant Temperature and Pressure Constraints.....	65
c.1) Constant Temperature: Nosé-Hoover Thermostat.....	65
c.2) Constant Pressure: The Andersen Barostat.....	69
2.3.2 - Classical Molecular Dynamics Simulations with POMs .....	71
<b>Chapter 3: Electronic Structure of Keplerates .....</b>	<b>75</b>
3.1 - Introduction.....	77
3.1.1 - Goals .....	78
3.2 - Computational Details.....	79
3.3 - Results .....	79
3.3.1 - Effects of the DFT functional and the COSMO model .....	79
3.3.2 - Electronic Structure of Well-Known Keplerate Systems .....	84
3.3.3 - Not Empty Capsules: Presence of Ligands and Coordination Water Molecules .....	92
3.3.4 - Predictions.....	95
3.3 - Conclusions.....	104
<b>Chapter 4: Interaction between the Mo<sub>132</sub> Capsule and its Internal Ligands.....</b>	<b>105</b>
4.1 - Introduction.....	107
4.2 - Computational Details.....	109
4.3 - Results .....	111
4.3.1 - [(H <sub>8</sub> Mo <sup>VI</sup> <sub>6</sub> O <sub>21</sub> ) <sub>2</sub> (Mo <sup>V</sup> <sub>2</sub> O <sub>4</sub> )] <sup>6+</sup> Model .....	111
4.3.2 - [(Mo <sup>VI</sup> <sub>6</sub> O <sub>21</sub> ) <sub>2</sub> (Mo <sup>V</sup> <sub>2</sub> O <sub>4</sub> )] <sup>10-</sup> Model .....	114

4.3.3 - $[(\text{Mo}^{\text{VI}}_6\text{O}_{21})_{12}(\text{Mo}^{\text{V}}_2\text{O}_4)_{30}]^{12-}$ Capsule .....	116
4.4 - Conclusions .....	119
<b>Chapter 5: Formation Pathway of <math>\text{Mo}_{132}</math> .....</b>	<b>121</b>
5.1 - Introduction .....	123
5.1.1 - Summary of Roy's group experimental results .....	126
5.1.2 - Summary of Poblet's group CP-MD results .....	130
5.1.3 - Goals .....	131
5.2 - Computational Details .....	131
5.3 - Results .....	132
5.3.1 - Theoretical Raman Spectra .....	132
5.3.2 - Condensation Process .....	140
5.4 - Conclusions .....	144
<b>Chapter 6: Ionic Behaviour of <math>\text{Mo}_{132}</math> in Aqueous Solution .....</b>	<b>147</b>
6.1 - Introduction .....	149
6.1.1 - Summary of the State of the Art .....	150
6.1.2 - New Model for the $\text{Mo}_{132}$ Keplerate in Aqueous Solution .....	156
6.1.1 - Goals .....	157
6.2 - Computational Details .....	158
6.3 - Results .....	159
6.3.1 - Comparison Between the Primitive and the New model .....	159
6.3.2 - Analysis of the behaviour of different counter-cations .....	164
6.3.3 - Temperature Effects .....	173
6.4 - Conclusions .....	186
<b>Chapter 7: Hydrophobicity as Driving Force of the Plugging Process of the <math>\text{Mo}_{132}</math> Pores .....</b>	<b>189</b>
7.1 - Introduction .....	191
7.1.1 - Summary of Cadot's group experimental results .....	192
7.1.2 - Goals .....	196

7.2 - Computational Details.....	196
7.2.1 - Density Functional Theory (DFT) .....	196
7.2.2 - Classical Molecular Dynamics (MD) .....	197
7.3 - Results .....	199
7.4 - Conclusions.....	206
<b>Chapter 8: Conclusions .....</b>	<b>209</b>
<b>References.....</b>	<b>213</b>

# Abstract

---

Polyoxometalates (POMs) are a wide family of anionic inorganic clusters with very interesting properties and applications. POMs are composed of a variable number of metal-oxygen units. The metal centres are usually transition metal atoms in their highest oxidation state ( $\text{Mo}^{\text{VI}}$ ,  $\text{W}^{\text{VI}}$ ,  $\text{V}^{\text{V}}$ , etc.). Such transition metal atoms can be coordinated in different ways, which give rise to a huge variety of geometrical structures with an increasing number of metal centres: from the smallest Lindqvist anions, with six metal centres, to the Giant Polyoxometalates, with hundreds of atoms and a nanometric size. Among those called Giant POMs, a family of icosahedral symmetric molecules, the so-called Keplerates, is unique. Keplerates are composed of two main type of building blocks, namely, pentagonal and linker units, resulting on a quasi-spherical capsule with a fullerene-like structure and 20 hexagonal pores. The most representative example of Keplerates is the  $\text{Mo}_{132}$  capsule, in which this Thesis is focused. Several bidentate ligands have been reported to be coordinated to the linker units, thus modifying the capsule properties such as the charge and the hydrophobic/hydrophilic character of the inner surface. The present Thesis has as main objective the application of modern computational methods to the study of different properties of Keplerates. Both electronic structure properties in one hand, and aqueous solution dynamic properties in the other hand, have been analysed.

First chapter aims at introducing POMs in terms of general properties and structures, and particularly, the Keplerate family, highlighting their relevance in Chemistry because of their interesting applications. Moreover, Chapter 1 also includes the general objectives of this Thesis. Specific objectives are included too at the beginning of each chapter. Second chapter describes the theoretical background on which this Thesis relies. Firstly, the basic concepts of Density Functional Theory (DFT) are summarised. Then follows a description of the main characteristics of classical Molecular Dynamics (MD) methods. Moreover, this chapter also includes details about the calculation of parameters required to perform MD simulations of Keplerates in aqueous solution. The optimal electron density of the  $\text{Mo}_{132}$  molecule obtained by means of DFT was used to



assign point charges to atomic positions in order to carry out Molecular Dynamics in the presence of different types of cationic species. Charge is not an observable from a quantum mechanics point of view, so different models for charge assignment were tested in order to choose the one that better reproduces experimental observations.

Chapter 3 presents a systematic study of the Keplerate family, regarding its electronic structure. Besides the  $\text{Mo}_{132}$  capsule, several variants on its composition have also been analysed, as some molybdenum atoms can be substituted by tungsten atoms ( $\text{W}_{72}\text{Mo}_{60}$ ), and some oxygen sites can be also occupied by sulphur atoms ( $(\mu\text{-O})$  or  $(\mu\text{-S})$  systems). Such composition variations have been studied in terms of their electronic structure and, particularly, regarding their HOMO-LUMO gaps. The presence of different internal ligands and coordination water molecules has also been considered. Indeed, Chapter 4 is focused on the interaction of the  $\text{Mo}_{132}$  macro-ion and its 30 inner ligands. Different bidentate species have considered as decoration of the inner surface of the  $\text{Mo}_{132}$  cavity. This analysis has been carried out using different models for the  $\text{Mo}_{132}$  cluster. Moreover, decomposition of the bonding energy between the ligands and the capsule has been achieved using a fragment analysis approach. The relevance of the different energetic contribution (steric, orbital interaction and solvation) for each case has been highlighted.

Chapter 5 collects the results of regarding the  $\text{Mo}_{132}$  formation mechanism, basically centred in Raman spectra calculations. This chapter presents our contribution to a collaboration with the Quantum Chemistry group of the University Rovira i Virgili (Tarragona, Spain) and the Eco-Friendly Applied Materials Laboratory of the Indian Institute of Science Education and Research (Kolkata, India). Theoretical results have been compared with experimental Raman analysis in order to shed some light on how the building blocks assemble to generate a quasi-spherical capsule as  $\text{Mo}_{132}$ .

Chapter 6 collects a series of analysis on the interaction in aqueous solution of the  $\text{Mo}_{132}$  cluster with water molecules and a set of cationic species by means of classical Molecular Dynamics. In addition, the effect of temperature on such interactions has also been studied. Chapter 7 is also related to the interaction between the  $\text{Mo}_{132}$  Keplerate and organic cations in aqueous solution, but in

this case we focused on the effect that the hydrophobic character of the cations could have on such interactions. This chapter collects our contribution to collaboration with the group of Molecular Solids of the Institute Lavoisier (University of Versailles-Saint Quentin, France). Our Molecular Dynamics results have been compared with experimental observations, resulting in a very good agreement.

Finally, Chapter 8 aims at summarizing the main conclusions of this Thesis since the specific conclusions are included at the end of each chapter.

UNIVERSITAT ROVIRA I VIRGILI

KEPLERATES: FROM ELECTRONIC STRUCTURE TO DYNAMIC PROPERTIES.

María Dolores Melgar Freire

Dipòsit Legal: T 258-2016

# Chapter 1: General Introduction

---

UNIVERSITAT ROVIRA I VIRGILI

KEPLERATES: FROM ELECTRONIC STRUCTURE TO DYNAMIC PROPERTIES.

María Dolores Melgar Freire

Dipòsit Legal: T 258-2016

## 1.1 - Introduction

In the last century, the capacity and potential of computers have increased significantly. The Turing Machine<sup>1</sup> proposed by Alan Turing in 1936 laid the foundations of modern programmable computers. In the 20th century, the computational power has exponentially increased from computers with few processors to the actual supercomputers with hundreds of processors. Such availability on computing power allows an enormous presence in scientific fields such as Physics and Chemistry, as seen nowadays. Computer simulations are thus *in silico* experiments that reproduce physico-chemical properties of the systems as the real experiments are able to measure. The accuracy of these predictions of reality relies on the capacity of the models to provide sufficiently quantitative results. Therefore, such theoretical experiments are widely used to complement experimental observations, but their most genuine interest is to provide estimates of physico-chemical properties under conditions that are hard to achieve experimentally.

There is a huge variety of computational methods, depending on the size of the system but also on the time-scale of the phenomenon of interest, whether equilibrium conditions or dynamic properties are pursued. In this Thesis quantum and classical computational approaches are combined in order to study structural and dynamic properties of polyoxometalates: the well-known Keplerate family.

Polyoxometalates (POMs) are anionic inorganic metal oxide clusters composed of  $MO_n$  units. M atoms are referred to as *addenda* atoms, while the O stands for oxygen atoms, and n represents the coordination state of the M atom. Addenda atoms are usually transition metal atoms in their highest oxidation state, namely  $Mo^{VI}$ ,  $W^{VI}$ ,  $V^V$ , etc. *Isopolyoxoanions* are POMs in which only M and O elements are present. When other elements are also introduced, the so-called *heteroatoms*, POMs are referred to as *heteropolyoxoanions*.

The type of coordination in the  $MO_n$  units depends on various factors: charge, ionic radii, and ability to form metal-oxygen (or other ligands) bond. POMs present four main types of coordination modes for the  $MO_n$  units (Figure 1.1):

the tetrahedral  $MO_4$ , the square pyramid  $MO_5$ , the octahedral  $MO_6$  and the pentagonal dipyramid  $MO_7$ . The  $n=4$  and  $n=7$  forms are the less common coordination modes, while the most frequent basic unit found in POMs is the octahedral  $MO_6$ . The Lindqvist anion is an example of POM with only  $MO_6$  units. Usually, different types of coordination for the metal atoms are present in POM molecules. The combination of different coordination modes, together with the use of different metal species, give rise to a huge variety of POM structures with many different and interesting properties: from the smallest Lindqvist and Anderson anions (Figure 1.2), with only 6 metal centres, to the largest members of the family, the so-called Giant POMs, with hundreds of atoms (Figure 1.3). Among the Giant POMs, Keplerates are a family of nanocapsules with icosahedral symmetry. They are composed of two main types of building blocks, namely, pentagons and linkers, which result on buckyball-like structure with a hollow centre and with 20 hexagonal pores homogeneously distributed. The size of both, the pores and the cavity, depends on whether one has monomers or dimers as linkers (Figure 1.4). Particularly, this Thesis is addressed to the computational study of the particular case of Keplerates with dimeric linkers, such as the  $Mo_{132}$ .

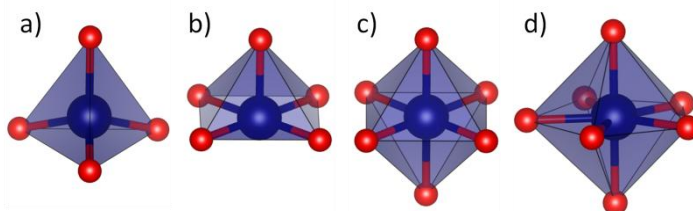


**Figure 1.1:** Examples of  $MO_n$  units. Blue polyhedra highlight the unit geometrical shape and red balls stand for oxygen atoms. **a)**  $MO_4$  **b)**  $MO_5$  **c)**  $MO_6$  **d)**  $MO_7$

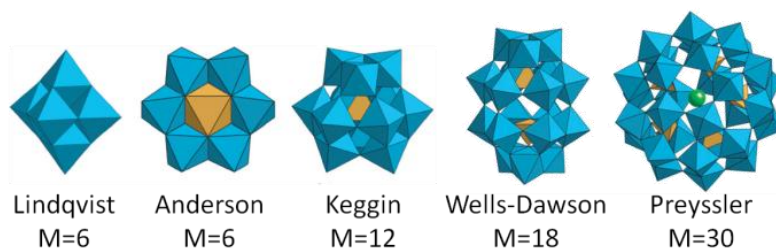


**Figure 1.2:** Examples of the smallest members of the POM family.  $M$  is the number of metal centres.  $MO_6$  units are represented by blue polyhedra, while heteroatoms are represented by orange polyhedra. This figure was published in Chemical Society Reviews in 2012.<sup>2</sup>

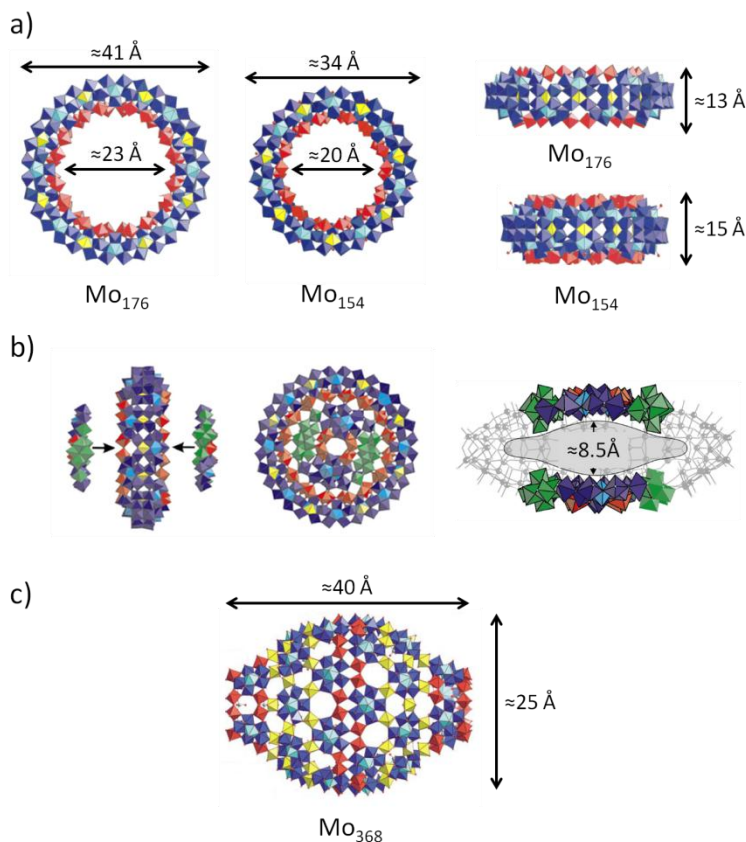


**Figure 1.3:** Examples of Giant POMs: **a)** Front and side view of polyhedra representation of the  $\text{Mo}_{176}$  and  $\text{Mo}_{154}$  clusters. **b)** Polyhedra representation of the formation of the  $\text{Mo}_{258}$  cluster from the  $\text{Mo}_{176}$  wheel (left), highlighting the size of its inner cavity (right). **c)** Polyhedra representation of  $\text{Mo}_{368}$ . The colour code for a, b and c goes as follows: yellow polyhedra for the Mo monomers, red for the dimers, blue for the pentagons with the central unit highlighted on light blue, and green polyhedra for the equivalent unit of  $\text{Mo}_{36}$ . These schemes are reproductions from publications on *Angewandte Chemie International Edition*<sup>3</sup>, *Nature*<sup>4</sup>, and *Angewandte Chemie*<sup>5</sup> for a, b, and c respectively.

The name  $\text{Mo}_{132}$  refers to the  $[\{\text{Mo}^{\text{VI}}(\text{Mo}^{\text{VI}}_5\text{O}_{21})\}_{12}\{\text{Mo}^{\text{V}}_2\text{O}_4(\text{L}^{\text{n-}})\}_{30}]^{(12+30)\text{n-}}$  molecule. Synthesised for the first time by Müller in 1998,<sup>6</sup> this molecule is composed of 12 pentagonal units  $\{\text{Mo}^{\text{VI}}(\text{Mo}^{\text{VI}}_5\text{O}_{21})\}$ , and 30 dimeric linkers  $\{\text{Mo}^{\text{V}}_2\text{O}_4\}$  (blue and red polyhedra in Figure 1.4 left, respectively). There is a variety of bidentate ligands (L) that can be coordinated to the linker units. The presence of such internal ligands changes the total charge of the system, but also modifies properties of the cavity, such as its size and the hydrophobic/hydrophilic character of the inner surface, among others. The relevance of the  $\text{Mo}_{132}$  nanocapsule has increased in recent years due to its



particular characteristics. The  $\text{Mo}_{132}$  pores size allows the exchange with the external environment of small cations<sup>7</sup> but also of larger anions,<sup>8</sup> allowing a certain look on the  $\text{Mo}_{132}$  nanocapsule as an artificial cell.<sup>9</sup> Moreover,  $\text{Mo}_{132}$  has been used as a nanoreactor for catalytic applications.<sup>10</sup> Different projects on catalytic mechanisms related to the  $\text{Mo}_{132}$  activity have been theoretically carried out using the Density Functional Theory (DFT).<sup>11</sup> Furthermore, the analysis of the behaviour of water encapsulated in  $\text{Mo}_{132}$  has also been carried out.<sup>12</sup> Confined water molecules in  $\text{Mo}_{132}$  form concentric layer structures, whose dynamics have been analysed by means of classical Molecular Dynamics (MD) simulations, achieving accurate results when compared with experiments. Recently,  $\text{Mo}_{132}$  has also been used in biological applications, as the inhibition of peptides aggregation related with Alzheimer's disease.<sup>13</sup> More applications are expected to see the light in the near future.

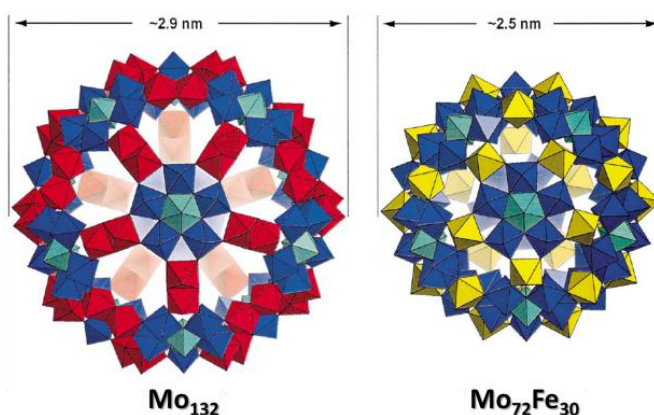


**Figure 1.4:** Polyhedra representation of two types of Keplerales with dimers ( $\text{Mo}_{132}$ ) and with monomers ( $\text{Mo}_{72}\text{Fe}_{30}$ ) as linkers. The building blocks have been represented with different colours: blue for the pentagonal units (with the central metal site in light blue) and red and yellow for the  $\text{Mo}_{132}$  and  $\text{Mo}_{72}\text{Fe}_{30}$  linkers. This figure is a reproduction from Coordination Chemistry Reviews.<sup>14</sup>

From a methodological point of view, DFT calculations and classical MD simulations are the main computational methods used throughout this Thesis. DFT stems from the quantum nature of the system and provides its electronic properties. DFT has been widely applied on the field of Computational Chemistry in order to study the structure and reactivity of an overwhelming variety of systems. Particularly, DFT has demonstrate a high accuracy regarding the POM properties.<sup>15</sup> Nevertheless, long time, many-body properties, such as diffusion or interactions with solvent, which involve a large number of atoms,

cannot be studied from first principles because of the unaffordable computational cost. This is the case for liquid properties, in which, usually, quantum effects are not expected to play a key role and thus a classical approach is suitable. In this context, classical Molecular Dynamic simulations have been demonstrated to be a very efficient tool because these permit the study of liquid properties under a very wide range of conditions, including those that are hard to obtain experimentally. The use of MD techniques to the study of POMs in solution is also widely extended nowadays. For instance, the properties of confined water inside  $\text{Mo}_{132}$  cavities have been analysed.<sup>12</sup> Sometimes, both DFT and MD methods are complementary used in subsequent steps in order to solve a given problem,<sup>16</sup> from which scarce or inexistent microscopic data exists. This is the overall approach followed in this Thesis, in which information obtained by means of DFT is later used to perform MD simulations in order to shed some light on the behaviour of  $\text{Mo}_{132}$  in aqueous solution.

## 1.2 - Polyoxometalates

Polyoxometalates (POMs) stand for a unique and ever growing family of inorganic anionic molecules with highly symmetric architectures composed of a variable number of metal centres connected through a network of bridging and terminal oxygen atoms, hydroxo and/or peroxy ligands. To date, the majority of known POMs contain Mo, W, V, Nb, and Ta or mixtures of these as framework elements,<sup>17</sup> though new compounds with actinide elements (U, Th, Np) have been recently discovered,<sup>18</sup> and only few examples of late transition metals POMs, containing Pd<sup>19</sup> and Au<sup>19b, 20</sup>, have been reported. POMs present an overwhelming amount of diversity in their structures and shapes since nearly all of the elements of the periodic table can be incorporated into a POM framework by the inclusion of coordination addenda and/or molecular grafting, thus enabling a chemical tuning of their properties and their functionalization towards hybrid organic/inorganic molecular systems,<sup>21</sup> or extended systems such as those known as polyoxometalate metal-organic frameworks (POMOFs).<sup>22</sup> These features make POMs highly versatile systems that display a broad range of outstanding properties, which span from applications in

sensing<sup>23</sup> and magnetic resonance imaging;<sup>24</sup> and from energy storage systems<sup>25</sup> to dye-sensitised solar cells<sup>26</sup> and to spintronics.<sup>27</sup>

The high oxidation states of the metal centres, Lewis acidity and anionic charges also renders POMs as prime candidates for catalytic uses be it in the synthesis of fine chemicals or in large scale industrial applications.<sup>28</sup> Since small molybdate oxo clusters are also present in living organisms,<sup>29</sup> it is not surprising that some POMs are biocompatible, with applications in medicine.<sup>30</sup> Indeed some of them display anti-viral,<sup>31</sup> anti-tumoral<sup>32</sup> and anti-diabetic<sup>33</sup> properties and are active against peptide aggregation<sup>13</sup> (associated with Alzheimer's disease). Therefore, POM based materials occupy a prominent position in the way to meet the demands of our society regarding green technologies, optimal use of resources, health, environment, energy, and information technologies, among others.

The biggest advantage of POMs chemistry is their simplicity, since synthetic reactions are often performed in open-air aqueous solution under careful control of the pH, ionic strength, and selection of counter-ions and templating ions. Polyoxo-tungstates, -molybdates, and -vanadates are synthesised in acidic aqueous solution, whereas polyoxo-niobates, -tantalates and polyperoxouranates are synthesised in a basic aqueous media. Starting from the corresponding mononuclear salts, slow and controlled pH variations can push the hydrolysis and condensation processes further, which result in cluster formation. Experimentalists refer to concepts such as "dynamic libraries" of interconverting building blocks<sup>34</sup> to explain the formation of these complex structures - analogous to synthons in organic chemistry. The molecular details of the processes that give rise to the assembly of very large clusters are still shrouded in obscurity, although the use of ESI-MS techniques recently enabled to enlighten some issues.<sup>35</sup> On the other hand, ab-initio molecular dynamics simulations can provide atomistic details of the fundamental steps of the growth processes of the smallest clusters.<sup>36</sup> Unfortunately, due to the huge computational cost, this type of studies is still scarce.

Theoretical and computational methods have been successfully applied to study the structure, electronic properties, spectroscopy and reactivity of POM clusters. The progress achieved during the past decade has been spectacular, although some big challenges remain. From a computational point of view,

carrying out calculations and simulations on this sort of systems at a well-defined pH is not a trivial task, nor is it clear how to define this pH unless simulations taking into account a fairly large number of water molecules are performed.<sup>37</sup> A new approach to overcome this big issue is the development of parameters to carry out molecular dynamics simulations using reactive force fields, as it has been applied to polyoxoniobates.<sup>38</sup>

In a broader scope, dealing with ionic salts in water using computational methods is now a hot topic that is attracting great interest.<sup>39</sup> Atomic and molecular level ion-pairing and acid-base behaviour in aqueous systems control important phenomena in both synthetic and natural systems. These include self-assembly and precipitation of ionic solids, electron-transfer reactions, separation chemistries, and growth of complex and novel forms of materials and lattices. In the geosphere, these processes include mineral growth and dissolution, surface adsorption and desorption, colloid formation and contaminant transport, and coupled chemical-electrochemical reactions. In living systems, charge-transport is also intimately tied with the behaviour of metal cations and oxo-anions. Furthermore, synthetic materials expected to function in our oxygen and water rich environment are guaranteed to be stable if synthesised in similar environments. Water is the universal solvent of choice for industrial syntheses. But the behaviour of aqueous systems is complex, dynamic, and often unpredictable. This arises in part from the fact that the solvent ( $\text{H}_2\text{O}$ ) plays the role of metal ligand, in the form of  $\text{O}^{2-}$  or  $\text{OH}^-$ , and multiple chemical equilibria take place simultaneously. For a more deliberate approach aiming at obtaining functional materials from water, there is a pressing need to understand the many factors that drive self-assembly. Group V/VI polyoxometalates, as outlined above, provide a unique opportunity to understand ion-pairing and associated aqueous phenomena.

## 1.3 - Keplerates

During the last decade, POM chemistry enabled growing impressive new giant molecular metal oxide nanostructures. In some cases, the shape of the POM framework is such that it forms inner cavities, which are usually filled with other molecular species. These two characteristics are found in the unique family of compounds known as Keplerates, which are spherical capsules that can assemble either 102 or 132 metal atoms (Figure 1.4).<sup>14, 34, 40</sup> The first and most relevant member of this family is known as Mo<sub>132</sub> (Figure 1.4, left; Figure 1.5) and it was discovered by Müller and co-workers in 1998.<sup>6</sup> With general formula  $[(\text{Mo}^{\text{VI}}(\text{Mo}^{\text{VI}})_5\text{O}_{21}(\text{H}_2\text{O})_6)_{12}(\text{Mo}^{\text{V}}_2(\mu\text{-O})_2\text{O}_2(\text{L}^{n-}))_{30}]^{(12+n)-}$ , where  $\text{L}^{n-}$  is a bridging anionic ligand, the sphere is highly negatively charged, holding a charge of -42 for monovalent anions ( $\text{L}^-$ ) and -72 for divalent anionic ligands ( $\text{L}^{2-}$ ). This sort of capsule thus is built from twelve pentagonal Mo(Mo)<sub>5</sub>O<sub>21</sub> units, which are placed at the vertices of an icosahedron and contain Mo<sup>VI</sup> atoms. These units are connected by (Mo<sub>2</sub>(μ-O)<sub>2</sub>O<sub>2</sub>(L<sup>n-</sup>)) dimers or linkers, holding Mo<sup>V</sup> atoms thus thirty of these units are needed to complete the spherical capsule. This building blocks combination is highlighted on Figure 1.5. In a simplified notation, we will address this species as Mo<sub>72</sub>Mo<sub>60</sub>, or Mo<sub>132</sub> for short. As we will see below, Keplerates family incorporates nowadays both Mo and W as elements constituting the pentagonal units, although Mo, Fe, V, and Cr atoms can be incorporated as linkers. Moreover, the L anionic ligands can be carboxylate type ligands, but also sulphate and other bridging groups. The size and the charge of the capsule, and also the size and chemical nature of the inner cavity can thus be fine tuned by chemical modification.

Since the initial synthesis of Mo<sub>132</sub>, Müller and coworkers noticed that other combinations of pentagons and linkers could be possible, and readily discovered Mo<sub>72</sub>Fe<sub>30</sub> (Figure 1.4, right),<sup>41</sup> a Keplerate with Mo(Mo)<sub>5</sub> pentagonal units and Fe<sup>III</sup> as linkers. The concept of building blocks was firstly used in a paper of the same group, where they reported a related Mo<sub>75</sub>V<sub>20</sub> capsule.<sup>42</sup> The Mo<sub>102</sub> Keplerate was Synthesised next,<sup>43</sup> which is formally the Mo<sub>72</sub>Mo<sub>30</sub> Keplerate, by incorporating MoO<sup>3-</sup> groups as linkers. Using the same strategy, the Mo<sub>72</sub>V<sub>30</sub> containing V<sup>IV</sup>O units as linkers<sup>44</sup> and the Mo<sub>72</sub>Cr<sub>30</sub> with Cr<sup>III</sup> linkers<sup>45</sup> were synthesised in recent years. The next advance was the ability to generate pentagonal units with W atoms, i.e., W(W)<sub>5</sub> building blocks, that were

assembled using both dimeric and monoatomic linkers. Thus, the  $W_{72}Mo_{60}$ <sup>46</sup> and  $W_{72}Fe_{30}$ <sup>47</sup> were described.

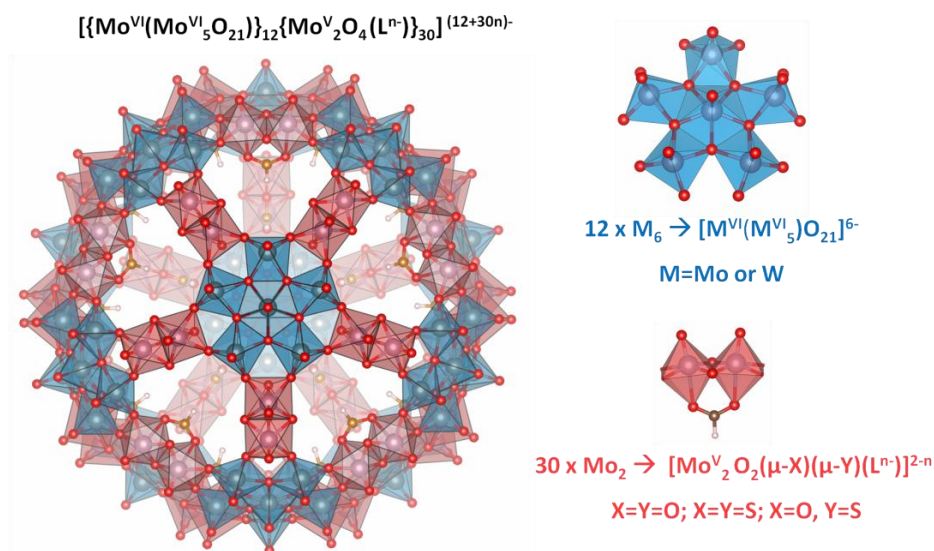


**Figure 1.5:** Polyhedral representation of the  $Mo_{132}$  geometry (left) with formate groups acting as ligands, in which the two main types of building blocks have been highlighted: blue for the pentagonal units and red for the linkers. In addition, some composition variants in the pentagons and in the linkers that give rise to other  $Mo_{132}$ -like systems have been indicated together with the two main types of building blocks (right).

Further chemical synthesis enabled changing the  $Mo^V_2(\mu-O)_2O_2$  linkers by sulphur bridged  $Mo^V_2(\mu-S)_2O_2$  units, so the equivalent  $W_{72}Mo_{60}(\mu-S)$ <sup>41</sup> and  $Mo_{132}(\mu-S)$ <sup>42</sup> Keplerates were obtained (Figure 1.5, right). It is worth mentioning that in this last case reported by the group of Molecular Solids of the Institute Lavoisier (University of Versailles-Saint Quentin, France) led by Cadot, a cubic cluster was obtained under slightly different experimental conditions, in which triangular six member units were formed instead of pentagons. A further step towards chemical tuning of Keplerates' properties consisted of using a mixed oxo-sulfur linker, such as  $Mo^V_2(\mu-O)(\mu-S)O_2$  which was introduced in a  $W_{72}Mo_{60}$  cluster.<sup>43</sup> Note that the full tungsten analog  $W_{132}$  remains elusive till now, as well as mixed W/Mo pentagonal units. Our group reported the first electronic structure study using DFT based methods on  $Mo_{132}$  and  $W_{72}Mo_{60}$  systems.<sup>44</sup> This Thesis aims at exploring the electronic structure of the whole Keplerate family and predict the stability of not yet reported systems.

The concept of dynamic library of fragments, i.e., pentagons and linkers, which condense and self-assemble to obtain the most symmetrical structure has been demonstrated by the facts just exposed above, but also by some studies addressing this issue specifically. Thus, Roy detected in 2007 Mo<sub>116</sub> species which are incomplete Mo<sub>132</sub> capsules.<sup>45</sup> Moreover,<sup>46</sup> Schäffer proved that deliberate addition of linkers in a dynamic library resulted in the ready assembly of the Mo<sub>132</sub> capsule. However, the mechanism of formation is not known in detail. Understanding how the reaction conditions affect the nature of the building blocks and the assembly processes is thus of capital importance. This issue has been addressed in this Thesis in collaboration with Roy's experimental group.

The structure of Mo<sub>132</sub> capsules displays twenty pores homogeneously distributed in the sphere surface and forms therefore an open cavity where a large quantity of water molecules, cations or other species can be confined in. Note that the cavity is large enough to encapsulate a Keggin anion [XM<sub>12</sub>O<sub>40</sub>], as that found for instance in PMo<sub>12</sub>@Mo<sub>72</sub>Fe<sub>30</sub>.<sup>47</sup> Indeed, the fact that the capsules are not empty was precisely realised from the very beginning. Actually, after characterizing the structure Mo<sub>132</sub> framework, the X-ray structure of encapsulated water molecules was unravelled in the form of water clusters structured in layers.<sup>48</sup> It took four years to synthesise suitable crystals that enabled full X-ray characterization of those encapsulated water molecules. In the case of mixed sulphate/hypophosphite ligands, a perfectly structured (H<sub>2</sub>O)<sub>100</sub> cluster was revealed.<sup>49</sup> In other cases, the presence of counter-cations, such as NH<sub>4</sub><sup>+</sup>, inside the capsule affected both the number of encapsulated water molecules and their structure.<sup>50</sup> More recently, the presence of butyrate groups as ligands enabled the characterization of a (H<sub>2</sub>O)<sub>20</sub> cluster in W<sub>72</sub>Mo<sub>60</sub> capsules,<sup>51</sup> which emphasizes the importance of hydrophobic effects in water clustering. For Mo<sub>72</sub>Fe<sub>30</sub>, Mo<sub>72</sub>Cr<sub>30</sub> and Mo<sub>72</sub>V<sub>30</sub> Faraone and co-workers carried out quasielastic neutron scattering experimental studies that revealed different behaviour of the encapsulated water.<sup>52</sup> Our group, in collaboration with Müller (University of Bielefeld, Germany), have largely contributed to understand the effect that confinement in Mo<sub>132</sub> nanocapsules induces in the structure and dynamic behaviour of encapsulated water molecules, and reproduced those effects by means of molecular dynamics simulations (Figure 1.6).<sup>12</sup> All classical Molecular Dynamics simulations carried out until now were conducted considering the pores of the capsules closed. Thus, a goal of this Thesis is to



advance in this direction by considering the pores open thus enabling exchange between encapsulated and bulk water molecules.

Keplerate capsules holding large pores allow water, cations, anions and small molecules to pass through. These properties can be exploited in different manners.<sup>53</sup> For instance, inside/outside cation exchange has been proved by NMR experiments for  $\text{Li}^+$ <sup>9, 54</sup> and  $\text{Al}^{3+}$ .<sup>55</sup> These results brought the idea that these capsules could be used as models of ion-channels in membranes, and this was explored firstly by using coarse-grained simulations.<sup>56</sup> Indeed, the experiments were performed a posteriori and showed that, in a competing experiment with  $\text{Li}^+$ ,  $\text{Na}^+$  and  $\text{K}^+$  cations, the higher selectivity was for the smallest cation.<sup>7c</sup> Larger cations, such as guanidinium and tetra-methyl amonium ( $\text{TMA}$  or  $\text{NMe}_4^+$ ) cannot pass through the pores, but can remain coordinated to external face of the pores. A detailed analysis of such interactions has been carried in this Thesis in collaboration with the group of Molecular Solids of the Institute Lavoisier (University of Versailles-Saint Quentin, France).<sup>57</sup>

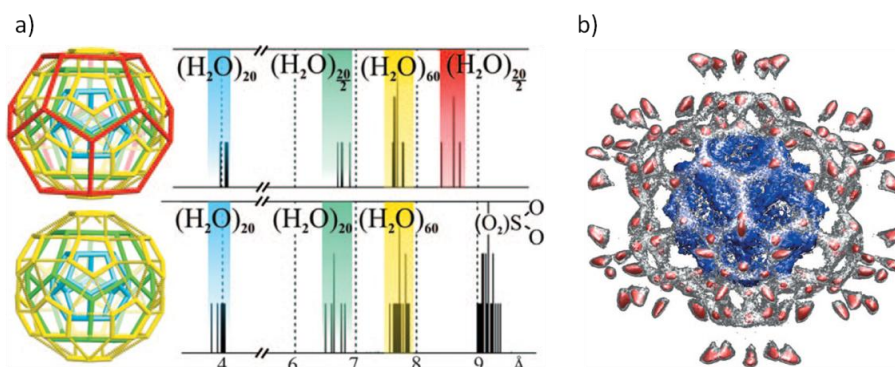


**Figure 1.6:** **a)** Schematic representation of the layered water structure with its corresponding distance histogram of water oxygen atoms to the centre of the  $\text{Mo}_{132}$  cavity for formate (top) and sulphate ligands (bottom). **b)** Spatial distribution function of water molecules encapsulated inside the  $\text{Mo}_{132}$  Keplerate with sulphate ligands. Red colour represents the second and third layer, together with the coordination waters. Grey colour corresponds to the exchange between the second and third layer. Blue colour stands for the inner shell. Both figures have been reproduced from the publication of Mitra et al.<sup>12a</sup>

The ligands  $L$  in the linker ( $\text{Mo}^{\text{V}}_2(\mu\text{-O})_2\text{O}_2(L^n)$ ) units are generally bidentate anions (formate, sulphate, phosphates, carboxylates, ...). According to the synthetic methodology, it is possible to exchange them after the capsule is



formed. Indeed, it has been demonstrated that the exchange rate through the pores depends on the size of the carboxylate substituent,<sup>8b</sup> and that internal capsule sites can exchange with each other, in addition with the exchange with the outside.<sup>58</sup> More recently, it was shown that the hydrophobic environment generated by propionate ligands allow encapsulation of 1-hexanol,<sup>59</sup> and that when longer carbon chains are introduced, as in n-Pr-CO<sub>2</sub><sup>-</sup> carboxylates, they self-assemble step-wise inside the capsule.<sup>8a</sup> To the best of our knowledge, the most recent advance in encapsulating new species has been reported by Floquet, Cadot and coworkers who achieved encapsulating di-carboxylate species.<sup>60</sup>

The ability to control the inside/outside exchange of molecular species within this type of capsules suggested the possibility of their use as nanoreactors. As a matter of fact, some outstanding catalytic processes occurring in the presence of this type of capsules have already been accomplished. In a pioneering work in 2009, Izarova et al. reported the catalytic activity of Mo<sub>72</sub>Fe<sub>30</sub> in the selective oxidation of sulfides.<sup>61</sup> Many polyoxometalates are active catalysts in oxidation reactions, so this reactivity is not surprising. However, the authors did not demonstrate whether the reaction occurred inside or outside the capsule. The same year, the same Mo<sub>72</sub>Fe<sub>30</sub> Keplerate was used to fabricate electrocatalytic electrodes by hybrid thin film deposition.<sup>62</sup> In 2012, the first real application of Mo<sub>132</sub> as a nanoreactor was described, namely the hydrolysis of methyl tert-butyl ether. In a close collaboration with Weinstock's group, the computational studies carried out in our group enabled proposing a reaction mechanism and suggested the existence of unexpected reaction intermediates, which were detected experimentally as well.<sup>63</sup> Mo<sub>132</sub> nanoreactor has shown to be capable of modifying the regioselectivity of the Huisgen reaction,<sup>10b</sup> and very remarkably, to uptake CO<sub>2</sub> and transform it to carbonate.<sup>10a</sup> Both transformations are being studied computationally in our group. For CO<sub>2</sub> reactivity, they provided evidences that the CO<sub>2</sub> hydration reaction is accelerated by the capsule because of the role played by Mo<sup>VI</sup> and Mo<sup>V</sup> centres.<sup>11a</sup> Related to CO<sub>2</sub> uptake, Garai et al. recently reported the transformation of SO<sub>2</sub> gas into SO<sub>3</sub><sup>2-</sup> ligands.<sup>64</sup>

Other examples of the catalytic activity of Keplerates all fall in the category of oxidation reactions, which probably occur outside the capsule. It is worth mentioning that  $H_2O_2$  is used as oxidant in all the cases but one. The latter is the case reported by Rezaeifard et al.<sup>65</sup> who claim alkenes epoxidation using  $Mo_{132}$  and  $O_2$ . The number of examples is growing:  $Mo_{132}$  has been found active in the synthesis of 1,2,4,5-tetrasubstituted imidazoles,<sup>66</sup> in the oxidation of sulfides,<sup>67</sup> in the oxidation of pyridine to N-oxides,<sup>68</sup> in the synthesis of 1,8-dioxo-octahydroxanthenes and 1,8-dioxodecahydroacridines,<sup>69</sup> and in the condensation of 1,2-diamines with 1,2-dicarbonyls.<sup>70</sup> Moreover, heterometallic Keplerates  $M_{72}M'_{30}$  ( $M=Mo, W$ ;  $M'=Fe, V, Cr$ ) also have shown catalytic activity in the oxidation of alcohols<sup>71</sup> and sulfides<sup>72</sup> and in the epoxidation of alkenes.<sup>73</sup>

Other interesting properties have been found in Keplerates, like, for instance, the magnetism displayed by those systems containing  $Fe$ <sup>74</sup> and  $V$ .<sup>75</sup> In another order of spatial and temporal scales, it has been largely demonstrated that Keplerates in aqueous solution self-assemble in spherical hollow aggregates called blackberries, which were discovered by Liu in 2002.<sup>76</sup> It is particularly relevant the self-recognition observed during the assembly process for mixtures of  $Mo_{72}Fe_{30}$  and  $Mo_{72}Cr_{30}$ . Indeed, only blackberries of the pure components were detected. Thus, this is a unique example of highly selective assembly despite the similarity of the components.<sup>77</sup>

Finally, Keplerates are being explored as agents in surfactants,<sup>78</sup> in ionic-liquids<sup>79</sup> and liquid crystals,<sup>80</sup> as stabilizing agents for synthesising gold nanoparticles,<sup>81</sup> and they also display interesting electric conductivity<sup>82</sup> and non-linear optics properties.<sup>83</sup> Last but not least, it has been found that  $Mo_{132}$  is able to inhibit peptides aggregation related with Alzheimer's disease.<sup>13</sup>

In the following years we expect that this family of compounds will provide new and exciting discoveries in the field of nanoscience and nanotechnology, with applications in catalysis, membranes and energy.

## 1.4 - Objectives

This Thesis aims at studying properties of Keplerates, mainly of the  $\text{Mo}_{132}$  system. Regarding the methodology, this Thesis can be divided into two main parts. Firstly, we have used Density Functional Theory (DFT) methods in order to characterize the electronic structure of the Keplerate family. Despite the large number of atoms in Keplerates, its high symmetry makes possible to treat them in a routine way at the DFT level. Therefore, DFT allows us to compute an optimised electron density for each system. In the case of  $\text{Mo}_{132}$ , we went a step further and used DFT information to calculate the input parameters required to perform classical Molecular Dynamics (MD) simulations on the  $\text{Mo}_{132}$  capsules in aqueous solution. The analysis of such Classical MD simulations is addressed in the second part of this Thesis.

In the following, we summarise the specific objectives of each chapter. Further details can be found at the beginning of each chapter.

### **Chapter 3: "Electronic Structure of Keplerates"**

- Analysis of the effects on the electronic structure of already known Keplerates when some variations in the capsule components take place (W/Mo ratio, S and/or O bridging sites at the linkers, different bidentate ligands and the inclusion of coordination water molecules in the DFT calculations).
- Theoretical prediction of the stability in terms of electronic structure (HOMO-LUMO gap) of some Keplerate systems that have not been reported in the literature at the moment:  $\text{W}_{132}$ ,  $\text{W}_{12}\text{Mo}_{120}$  and the fully oxidised  $\text{Mo}_{132}$ .

### **Chapter 4: "Interaction Between the $\text{Mo}_{132}$ Capsule and its Internal Ligands"**

- Study of the effect of the presence of inner ligands in the electronic structure of the  $\text{Mo}_{132}$  capsule
- Bonding energy decomposition analysis of  $\text{Mo}_{132}$  and the corresponding ligands, considering the following energy contributions: Pauli repulsion, electrostatic interaction, orbital interaction and solvation energy.

- Proposal of models, considering part of or the whole  $\text{Mo}_{132}$  system to perform the mentioned energy decomposition.

#### **Chapter 5: "Formation Pathway of $\text{Mo}_{132}$ "**

- Modelling the  $\text{Mo}_{132}$  Raman spectra evolution, inspired by the experimental observations. Such modelling ranges from the starting  $[\text{Mo}_7\text{O}_{24}]^{6-}$  molybdate to combinations of the main building blocks of the  $\text{Mo}_{132}$  cluster.
- Evaluation of condensation energies at the DFT level involving pentagonal and dimeric units with different degrees of protonation.

#### **Chapter 6: "Ionic Behaviour of $\text{Mo}_{132}$ in Aqueous Solution"**

- Application of the parameters obtained by means of DFT to perform Classical Molecular Dynamics Simulations for the  $\text{Mo}_{132}$ : comparison between main results obtained with the previous (closed capsule with no external solvent) and current model (open capsule with external solvent)
- Description from a theoretical point of view of the distribution of cations around or inside the capsule for a set of cationic species.
- Effects of the temperature on the distribution of water molecules and cationic groups.

#### **Chapter 7: "Hydrophobicity as Driving Force of the Plugging Process of the $\text{Mo}_{132}$ Pores"**

- Understanding the nature of the interactions between the Keplerate ion and a set of cationic species (ammonium, guanidinium and tetramethyl ammonium cations) by means of Molecular Dynamics simulations.
- Estimation of the binding energy of the capsule and the cationic guests through DFT calculations.
- Analysis of the self-diffusion coefficient of the cationic species using their mean squared displacement (MSD), calculated from Molecular Dynamics trajectories.

- Developing of a post-treatment code to distinguish between the different dynamic regimes of the cationic species, inspired by their radial distribution function.

## Chapter 2: Theoretical Background

---



"The Nobel Prize in Chemistry 2013 - Press Release". Nobelprize.org. Nobel Media AB 2014. Web. 28 Sep 2015. <[http://www.nobelprize.org/nobel\\_prizes/chemistry/laureates/2013/press.html](http://www.nobelprize.org/nobel_prizes/chemistry/laureates/2013/press.html)>

UNIVERSITAT ROVIRA I VIRGILI

KEPLERATES: FROM ELECTRONIC STRUCTURE TO DYNAMIC PROPERTIES.

María Dolores Melgar Freire

Dipòsit Legal: T 258-2016

## 2.1- Computational methods

Nowadays, computational methods are very powerful tools to deepen the knowledge of a huge variety of systems. One of the most important features to take into account when choosing a computational method for the study of a particular phenomenon is the balance between the level of accuracy required and the computational cost. The computational cost is evaluated in terms of CPU time and memory requirements. It depends not only on the level of accuracy of the model, but also on the size and time scales of the given phenomenon. Both factors are intimately related (Figure 2.1). The level of accuracy depends on the type of studies that are to be performed. If the properties to be analysed depend on the quantum behaviour of the system, first principles methods are required. If the phenomenon to study is not influenced by the electronic behaviour of the system and it depends rather on the interatomic interactions, other methods as Molecular Dynamics can be used. QM/MM methods are an intermediate hybrid approach between the quantum and molecular mechanics levels, where part of the system is treated from a quantum point of view, while the rest is analysed from a classical perspective. If rather than interatomic interactions the interest is focused on intermolecular interactions (or even interactions between building blocks of the system), coarse-grained approximations can be applied. Finally, at the macroscopic level, Finite Element Analysis can be performed on continuous fields of the relevant properties like mass, momentum or energy.

This Thesis is addressed to the study of Keplerates, with regards to their electronic structure and their behaviour in aqueous solution. With this purpose different computational methods are applied. For the study of the electronic structure, a quantum mechanics approach, namely Density Functional Theory, is used. In order to study the behaviour in solution, classical Molecular Dynamics simulations have been performed. Both methods are introduced in the following sections.



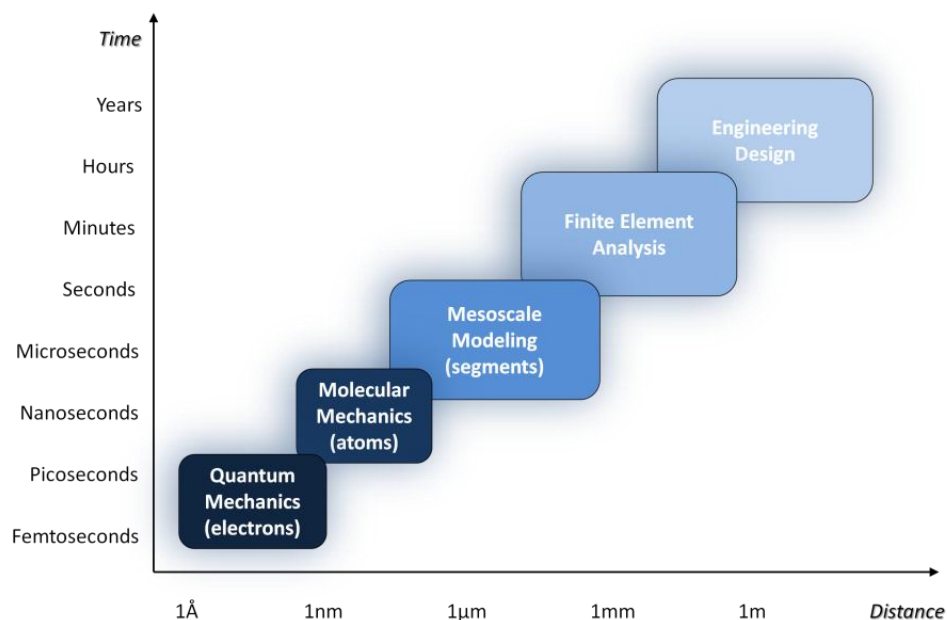


**Figure 2.1:** Schematic representation of different computational methods in terms of their time and size scales.

## 2.2 - Quantum Mechanics: Density Functional Theory

### 2.2.1 - Quantum Mechanics Fundamentals

Quantum Mechanics (QM) pursues the mathematical description of the behaviour of any physical system. This approach arises on the first half of the 20th century, at almost the same time as the Theory of Relativity of Einstein. QM can be constructed from six postulates.<sup>84</sup>

- I. The state of a QM particle is completely specified by its wavefunction  $\Psi(\vec{r}, t)$ . The square modulus of a particle's wavefunction is the probability of finding that particle on a differentiate volume located at  $\vec{r}$  at time  $t$ . The wavefunction is single-valued, continuous and finite.

Moreover, the wavefunction must verify the normalization condition expressed in Equation 2.1.

$$\int_{-\infty}^{+\infty} |\Psi(\vec{r}, t)|^2 d\tau = 1 \quad (2.1)$$

- II. Every observable ( $A$ ) in Classical Mechanics corresponds to a linear Hermitian operator in Quantum Mechanics ( $\hat{A}$ ).
- III. When an observable  $A$  is measured, the only values that can be observed are the eigenvalues ( $a$ ). These eigenvalues satisfy the eigenvalue equation (Equation 2.2).

$$\hat{A}\Psi = a\Psi \quad (2.2)$$

When a system is in an eigenstate, any measurement of the observable  $A$  will give  $a$  as a result. If the system is not in an eigenstate, the state can be expanded in the complete set of eigenvectors of  $\hat{A}$  (Equation 2.3). Then, the measurement can result in any value of  $a_i$  as a result, with a probability of  $|c_i|^2$ .

$$\begin{aligned} \hat{A}\Psi_i &= a_i\Psi_i \\ \Psi &= \sum_{i=1}^n c_i\Psi_i \end{aligned} \quad (2.3)$$

Once the measurement is performed, the wavefunction collapses into the corresponding eigenstate  $\Psi_i$ . Therefore, the measurement affects the state of the system.

- IV. The average value of  $A$  is shown in Equation 2.4.

$$\langle A \rangle = \int_{-\infty}^{+\infty} \Psi^* A\Psi d\tau \quad (2.4)$$

- V. The time evolution of a wavefunction is described by the time-dependent Schrödinger equation (Equation 2.5).

$$\hat{H}\Psi(\vec{r}, t) = i\hbar \frac{\partial\Psi}{\partial t} \quad (2.5)$$

- VI. A wavefunction must be antisymmetric with respect to the exchange of all coordinates of one fermion with those of another, including the electronic spin.

Equation 2.5 represents the time-dependent Schrödinger equation. It must be introduced as a postulate of QM, but the time-independent version (Equation 2.6) can be derived from the classical wave equation and the de Broglie relation. Effectively, introducing the eigenfunctions and eigenvalues of H results in Equation 2.6.

$$\hat{H}\Psi(\vec{r}) = E\Psi(\vec{r}) \quad (2.6)$$

Considering a given eigenstate, the relation between the time-dependent and time-independent Schrödinger equations is shown in Equation 2.7.

$$\Psi(\vec{r}, t) = \Psi(\vec{r}) \cdot \exp(-iEt / \hbar) \quad (2.7)$$

From Equation 2.7 two main consequences are derived: both the probability  $|\Psi(\vec{r}, t)|^2$  and the expectation value of A for any time-independent operator applied on an energy eigenfunction is also time-independent.

## 2.2.2 - Density Functional Theory

The six postulates introduced in the previous section make the wavefunction the central mathematical object of QM. However,  $\Psi$  cannot be directly observed. Furthermore, the time-independent wavefunction for a system with N particles will depend on the coordinates (spatial and spin coordinates) of the N particles. In contrast, the corresponding electron density ( $\rho$ ), which is, in addition, indeed physically observable, depends on only 3 spatial variables, independently on the number of particles. The electron density is the probability of finding one of the N electrons within an element of space ( $\vec{r}$ ) with arbitrary spin ( $s_i$ ), considering the other electrons with arbitrary positions and spin ( $\vec{r}_i, s_i$ ) (Equation 2.8). Therefore, it is easier to work with the electron density instead of the wavefunction for polyelectronic systems. This idea is the basis of the Density Functional Theory (DFT).

$$\rho(\vec{r}) = N \int \dots \int \Psi^*(\vec{r}, s_1, \dots, \vec{r}_N, s_N) \Psi(\vec{r}, s_1, \dots, \vec{r}_N, s_N) ds_1 d\vec{r}_2 ds_2 \dots d\vec{r}_N ds_N \quad (2.8)$$

Besides the electron density treatment, there are some theorems and approximations that contribute to build up the DFT, which are introduced in the following paragraphs.

Hohenberg and Kohn published in 1964 a discussion about the ground state of an interacting electron gas in an external potential.<sup>85</sup> This treatment led to the so-called Hohenberg-Kohn Theorems. The first theorem establishes that there is a one-to-one relationship between the electron density and the external potential ( $v$ ), which means that the external potential is a unique functional of the electron density. As for each external potential there is a solution of the Schrödinger equation, therefore, the ground state electron density can be used to determine the energy of the system and other properties. The second Hohenberg-Kohn theorem states that the ground state electron density is the only one that minimises the energy functional. This can be understood as an extension of the variational principle to DFT. Equation 2.9 shows the system's energy ( $E$ ) as a functional of the electron density.  $F$  is the universal functional that includes the kinetic energy and the interaction between the  $N$  electrons of the system.  $F$  is not known exactly because of the particularities of the interaction between electrons, so further approximations are needed in order to remove such indetermination.

$$E[\rho] = F[\rho] + \int d\vec{r} \rho(\vec{r})v(\vec{r}) \quad (2.9)$$

The Kohn-Sham approach<sup>86</sup> solves the problem of the unknown universal functional  $F$  by means of an effective potential, which includes the effects of the electronic interaction. Such approach reduces the problem to a situation where the electrons are not interacting in this effective potential ( $v_s$ ).

A Slater determinant is a solution for the wavefunction of a multi-fermionic system, as it fulfils the Pauli Exclusion Principle. For the Kohn-Sham system, the system's wavefunction should be a single Slater determinant constructed from the Kohn-Sham orbitals ( $\phi$ ). Kohn-Sham orbitals verify Equation 2.10 and are related to the electron density, as Equation 2.11 shows.

$$\left( -\frac{\hbar}{2m} \nabla^2 + v_s(\vec{r}) \right) \phi_i(\vec{r}) = \varepsilon_i \phi_i(\vec{r}) \quad (2.10)$$

$$\rho(\vec{r}) = \sum_{i=1}^N |\phi_i(\vec{r})| \quad (2.11)$$

The Kohn-Sham universal functional  $F$  is presented in Equation 2.12. The first term represents the classical coulombic electron-electron interaction. The second term ( $T_s$ ) is the kinetic energy of the system with non interacting electrons. The last term in Equation 2.12 ( $E_{xc}$ ) is the exchange-correlation energy of the interacting system, which includes the difference between the exact and non-interacting kinetic energies and the non-classical contribution to the electron-electron interaction. This  $E_{xc}$  term is the part of the universal potential  $F$  that remains unknown. Therefore, in the Kohn-Sham approach the problem of the unknown universal potential  $F$  has been reduced to the unknown exchange-correlation term. Thus, approximations for  $E_{xc}$  term must be done. Perdew introduced the Jacob's Ladder scheme (Figure 2.2).<sup>87</sup> The Ladder starts at the Hartree level, where no correlation energy is considered. Then, different terms are taken into account (electron density and/or its gradient, non-interacting kinetic energy density, exact exchange energy, unoccupied orbitals, etc.) until one arrives to the so-called *Heaven of Chemical Accuracy*, in which errors in bonding energies are less than  $1\text{kcal}\cdot\text{mol}^{-1}$ . Some of the approaches schematised on Figure 2.2 are described on the following paragraphs.

$$F[\rho] = \frac{1}{2} \iint \frac{\rho(\vec{r})\rho(\vec{r}')}{|\vec{r} - \vec{r}'|} d\vec{r}d\vec{r}' + T_s[\rho] + E_{xc}[\rho] \quad (2.12)$$

### 2.2.2.1) Local Density Approximation

The Local Density Approximation (LDA) builds the expression for the exchange-correlation energy as an analogy with a homogeneous electron gas, as the Kohn-Sham model. Such electron gas is composed of electrons in presence of positive background charges, making the system electrically neutral. In this hypothetical system, both the number of electrons and the volume approaches infinity, while  $\rho = N/V$  is finite. If the real system has a  $\rho$  that is slowly varying, the  $E_{xc}$  at each point can be assumed to be the same as for the homogeneous electron gas with the same  $\rho$  (Equation 2.13).

In Equation 2.13,  $\epsilon_{XC}$  represents the exchange-correlation energy per particle of the homogeneous electron gas.  $\epsilon_{XC}$  is a spin averaged density. In the Local Spin Density Approximation (LSDA), the energy density of the polarised homogeneous electron gas is used.<sup>88</sup>

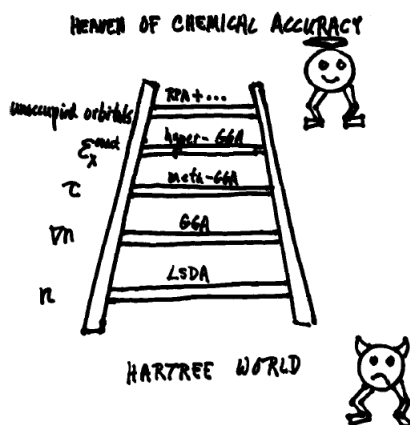


**Figure 1.2:** Representation of Jacob's Ladder introduced by Perdew, reproduced from ref. [94].  $n$  represents the electron density,  $\tau$  is the non-interacting kinetic energy density and  $\epsilon_x$  the exact exchange energy density.

$$E_{XC}^{LDA}[\rho(\vec{r})] = \int \rho(\vec{r}) \epsilon_{XC}^{LDA}(\rho) d\vec{r} \quad (2.13)$$

In the context of LDA,  $E_{XC}$  is divided into two terms: the exchange and correlation energies. For the exchange energy, the analytic expression from the homogeneous electron gas is shown in Equation 2.14.

$$E_X^{LDA}[\rho(\vec{r})] = -\frac{3}{4} \left( \frac{3}{\pi} \right)^{1/3} \int \rho(\vec{r})^{4/3} d\vec{r} \quad (2.14)$$

However, for the correlation part, there is no analytical expression, even though very good results can be achieved by means of Monte Carlo simulations.<sup>89</sup> Such stochastic approach leads to several approximations for the correlation energy, for instance: VWN (Vosko-Wilk-Nusair),<sup>88</sup> PZ81 (Perdew-Zunger),<sup>90</sup> CP (Cole-Perdew)<sup>91</sup> and PW92 (Perdew-Wang).<sup>92</sup>

The simplicity of LDA makes the model not suitable for some studies, as those involving Van der Waals interactions or excited states. Furthermore, it usually underestimates atomic ground state energies and overestimates binding energies. Also, it unduly favours high spin state structures. Nevertheless, it has been traditionally used in Computational Chemistry for years because, even though its weak points, the errors in the exchange and correlation energy densities tend to cancel and it works better as the size of the system increases.

### 2.2.2.2) Generalised Gradients Approximation

In order to improve LDA, the non-homogeneity of the electron density should be taken into account. With that purpose, the Generalised Gradients Approximation (GGA) includes in the exchange-correlation energy the dependence, not only on the electron density, but also on its gradient (Equation 2.15).

$$E_{XC}^{GGA}[\rho(\vec{r})] = \int \rho(\vec{r}) \varepsilon_{XC}^{GGA}[\rho(\vec{r}), \nabla \rho(\vec{r})] d\vec{r} \quad (2.15)$$

When  $\rho$  is uniform ( $\nabla \rho = 0$ ) the GGA energy density must approach the expression for  $\varepsilon_{XC}^{LDA}$ . In contrast with LDA, there is no simple universal form for the energy density. Thus, each GGA functional has its own formulation for  $\varepsilon_{XC}^{GGA}$ . Some of the most widespread are BP86 (Becke-Perdew),<sup>93</sup> PW91 (Perdew-Wang),<sup>93c, 94</sup> PBE (Perdew-Burke-Ernzerhof)<sup>95</sup> and BLYP (Becke-Lee-Yang-Parr).<sup>93a, 96</sup>

Throughout this Thesis, the main functional used is BP86. It is the result of the combination of the exchange functional proposed by Becke<sup>93a</sup> (Equations 2.16) and the correlation functional from Perdew (Equations 2.17).<sup>93b, c</sup> Both are parametric approaches, in order to reproduce the exchange and correlation energies of noble gases. In the expression for the Becke exchange functional (Equations 2.16),  $\beta$  is the empirical parameter and  $\sigma$  represents the up/down electron spin. The expression for the Perdew correlation functional is shown in Equation 16.  $\varepsilon_c$  is the correlation energy per particle of the uniform electron gas from the parameterization of the Ceperley-Alder results.<sup>89-90</sup>  $\tilde{f}$  is the cutoff parameter, chosen to fit the exact correlation energy of the Neon atom ( $\tilde{f} = 0.11$ ).<sup>97</sup>  $C$  represents the beyond-RPA (Random Phase Approximation) gradient coefficient for the correlation energy<sup>98</sup> and it has been parameterised

by Rasolt and Geldart.<sup>99</sup>  $r_s$  is the parameter used to characterise the bulk density. Furthermore, in Equations 2.17 there are other numerical parameters, as  $\alpha=0.023266$ ,  $\beta=7.389 \cdot 10^{-6}$ ,  $\gamma=8.723$  and  $\delta=0.472$ .

$$E_X^{B88} = E_X^{LDA} - \beta \sum_{\sigma} \rho_{\sigma}^{4/3} \frac{x_{\sigma}^2}{(1 + 6\beta x_{\sigma} \sinh^{-1} x_{\sigma})} d^3 \vec{r} \quad (2.16)$$

$$x_{\sigma} = \frac{|\nabla \rho_{\sigma}|}{\rho_{\sigma}^{4/3}}$$

$$E_C^{P86}[\rho] = \int d^3 r \varepsilon_C(\rho) + \int d^3 r w^{-1} e^{-\Phi} C(\rho) \frac{|\nabla \rho|^2}{\rho^{4/3}}$$

$$\Phi = 1.745 \tilde{f} \frac{C(\infty) |\nabla \rho|}{C(\rho) \rho^{7/6}}$$

$$C(\rho) = 0.001667 + \frac{0.002568 + \alpha r_s + \beta r_s^2}{1 + \gamma r_s + \delta r_s^2 + 10^4 \beta r_s^3} \quad (2.17)$$

$$r_s = \sqrt[3]{\frac{4\pi}{3} \rho}$$

$$w = 2^{1/3} \sqrt{\left(\frac{1+\zeta}{2}\right)^{5/3} + \left(\frac{1-\zeta}{2}\right)^{5/3}}$$

$$\zeta = \frac{\rho_{\uparrow} - \rho_{\downarrow}}{\rho}$$

The greatest improvement over LDA functionals is related to the bonding energies overestimation, leading to structures whose geometries are closer to the X-ray results. Furthermore, it improves transition state barriers. Nevertheless, GGA gives not so accurate results for systems where weak interactions play an important role. This limitation is the reason why the use of GGA is more extended in organometallic compounds.



### 2.2.2.3) Hybrid Functionals

In Jacob's Ladder (Figure 2.2) the Hartree level has been introduced as the level where no correlation energy is taken into account. On the Hartree-Fock model, which is based on the numerical solution of the time-independent Schrödinger equation with the Born-Oppenheimer approximation, the exchange contribution is completely considered, but the correlation contribution is neglected. The exchange energy is usually larger than the correlation energy. Therefore, the exchange contribution is the largest source of error in LDA and GGA functionals. Hybrid functionals consider a partial incorporation of the Hartree-Fock exact exchange energy. For instance, O3LYP takes into account a percentage of the exact exchange energy of 12%;<sup>100</sup> B3LYP, a 20%;<sup>101</sup> X3LYP, a 21.8%;<sup>102</sup> mPW1K, a 25%;<sup>103</sup> mPW1PW, a 42.8%;<sup>104</sup> BHandH, a 50%;<sup>101b</sup> and KMLYP, a 55.7%.<sup>105</sup> It is worth highlighting the importance of the B3LYP functional because of its wide use on the study of different properties.<sup>101a, 106</sup> The B3LYP exchange-correlation energy is represented on Equation 2.18.

$$E_{XC}^{B3LYP} = E_X^{LDA} + a_0(E_X^{HF} + E_X^{LDA}) + a_X(E_X^{GGA} + E_X^{LDA}) + E_C^{LDA} + a_C(E_C^{GGA} + E_C^{LDA}) \quad (2.18)$$

The numerical parameters on Equation 2.18 are  $a_0=0.20$ ,  $a_X=0.72$  and  $a_C=0.81$ . This parameters are inspired by the B3PW91 functional.<sup>107</sup>  $E_X^{GGA}$  is the exchange energy from the Becke88 functional.<sup>93a</sup>  $E_C^{GGA}$  is the correlation energy from the Lee, Yang and Parr approach.<sup>96</sup> Finally,  $E_C^{LDA}$  stands for the correlation energy used on the VWN functional.<sup>88</sup>

### 2.2.2.4) Meta-GGA

Meta-GGA functionals go a step further GGA. They include not only the electron density and its gradient, but also the non interaction kinetic energy density (Equation 2.19).

$$\tau = \frac{1}{2} \sum_i^{occupied} |\nabla \phi_i(\vec{r})|^2 \quad (2.19)$$

Some examples of this type of functionals are TPSS,<sup>108</sup> M06-L,<sup>109</sup> tHCTH,<sup>110</sup> and VSXC.<sup>111</sup>

### 2.2.2.5) Hyper-GGA

Hyper-GGA functionals is an example of the fully non-local rungs of the Jacob's Ladder (Figure 2.2). They take into account the exact exchange energy density (or other property from which the exact exchange energy can be calculated). A representative example of this type of functionals are the proposal of Odashima and Capelle<sup>112</sup> or the alternative approach suggested by Perdew.<sup>113</sup>

### 2.2.2.6) Basis Functions Set

Furthermore the choice of the exchange-correlation energy functional, the accuracy of any quantum calculation depends also on the basis set choice.

In the context of Computational Chemistry, the concept of orbital is associated to the wavefunction for a single electron.<sup>114</sup> Molecular orbitals are, thus, the wavefunctions of the electrons belonging to a given molecule. These wavefunctions can be formulated in terms of a spatial ( $\varphi_i(\vec{r})$ ) and a spin contribution ( $\alpha(s)$  or  $\beta(s)$ , which are orthonormal functions representing the different spin configurations).<sup>115</sup> The product of both spatial and spin functions generates a spin-orbital. The spatial function of the spin-orbital can be expanded as a linear combination of basis functions, the so-called basis set. There are two main categories of basis set: the Slater-type Orbitals (STO)<sup>116</sup> and the Gaussian-type Orbitals (GTO).<sup>117</sup>

Throughout this Thesis, the Amsterdam Density Functional (ADF) program<sup>118</sup> has been chosen to perform different studies at the DFT level. The ADF package uses STO.<sup>119</sup> The STO are centred at the nucleus and their typical structure is shown in Equation 2.20, where  $Y_{lm}$  are spherical harmonics and  $\alpha$  is the parameter that controls the long-range decay of the STO function.

$$\varphi(\vec{r}) = Y_{lm}(\Omega)r^n e^{-\alpha r} \quad (2.20)$$

In contrast to GTO, STO have the required cusp profile at the nucleus and the appropriate long-range decay. Such characteristics allow the achievement of high quality basis set with relatively small number of functions. In contrast, GTO will need approximately a factor of 3 more functions for the same level of quality.

The ADF package has a large number of basis set for all elements, from the simplest single- $\zeta$  to more sophisticated examples, as the doubly polarised triple- $\zeta$ . Furthermore, very diffuse functions for hyperpolarizability calculations can be implemented. In the case of Keplerates, as several transition metal atoms must be considered, we have used a single polarised triple- $\zeta$  basis set (TZP). The "triple" label means that 3 basis functions were used for each atomic orbital. Furthermore, the polarization effect is achieved by mixing a basis function with angular momentum  $l$  with a basis function with angular momentum  $l+1$ . For instance, an  $s$  orbital should be mixed with a  $p$  orbital, a  $p$  orbital with a  $d$  orbital and so on. Such mixing procedure allows the polarization basis functions to reproduce the change on the electronic density of an atom in the presence of other neighbouring species.

### **2.2.2.7) DFT Studies on POMs**

DFT has been used since the early 90's for the study of different POM properties, achieving very accurate results. The most widely used functionals are GGA. Nevertheless, there are some examples on the literature about the application of other approaches.<sup>120</sup> For instance, in our group, theoretical studies have been performed using LDA functionals to carry out a semi-qualitative analysis of the electronic structure of Keplerates.<sup>44</sup>

Among the GGA functionals applied in the study of POMs, BP86 functional is the most relevant. Nevertheless the use of other GGA approaches,<sup>121</sup> BP86 has been extended to a variety of POM systems. The study of POM from a DFT point of view has been highly productive in the last years. Particularly, the BP86 functional has been applied to study different POM features, as magnetic properties,<sup>122</sup> basic character of external oxygens sites,<sup>123</sup> relative stability of isomers,<sup>124</sup> or electronic spectrum characteristics.<sup>125</sup> Furthermore, characterization of dimerizations<sup>126</sup> and cation encapsulation processes<sup>16b</sup> using a BP86 functional have also been published.

Regarding the  $\text{Mo}_{132}$  Keplerate, BP86 has also been applied. For instance, Kopilevich et al. studied  $\text{Mo}_{132}$  as a nanoreactor for catalytic applications to the fully reversible cleavage and formation of methyl tert-butyl ether, both from a theoretical and a experimental point of view.<sup>11b</sup> The controlled removal of acetate ligands makes possible to achieve active sites for catalytic

transformation of the organic guest. It is worth noting that in this work, the Keplerate capsule has been modelled by means of a fragment of the capsule, namely, two pentagons and a linker.

More sophisticated functionals than GGA have been employed on the study of POMs, but their use is less extended. For example, B3LYP has been used to study the electronic structure<sup>127</sup> and catalytic properties<sup>128</sup> of different POMs. Furthermore, more elaborated approximations as Meta-GGA are also applied in POM science,<sup>129</sup> but its use has not been very extended.

## 2.3 - Classical Mechanics: Molecular Dynamics

### 2.3.1 - Classical Mechanics Fundamentals

#### 2.3.1.1) Classical and Statistical Mechanics

Classical Molecular Dynamics simulations (MD) aim at calculating the classical motion of a molecular system at different phases. Classical Mechanics and Statistical Mechanics can be considered as the main pillars of MD.

In the same way as Quantum Mechanics focuses on the solution of the Schrödinger equation, the main objective of Classical Mechanics is to solve Newton's equation of motion (Equations 2.21 and 2.22). In Equation 2.21,  $\vec{v}$  represents the velocity,  $\vec{r}$  the position and  $\vec{p}$  the momenta of a particle. Equation 2.22, known as the Newton's second law ( $\vec{F} = m\vec{a}$ , in which  $\vec{a} = d\vec{v}/dt$  is the acceleration), is, in this case, formulated for a multiparticle system, where  $\vec{F}_E$  is the resultant external force and  $\vec{F}_{ij}$  is the force on particle  $i$  caused by particle  $j$ .

$$\vec{v} = \frac{d\vec{r}}{dt} = \frac{\vec{p}}{m} \quad (2.21)$$

$$\frac{d\vec{p}_i}{dt} = \vec{F}_E + \sum_{i \neq j} \vec{F}_{ij} \quad (2.22)$$

While Thermodynamics allows the calculation of properties of macroscopic systems without linking them to the underlying microscopic properties, the role of Statistical Mechanics is to connect the microscopic and macroscopic world. The macroscopic properties of the system can be computed from the configuration of the particles of the system, resulting in an average value with its corresponding fluctuations. To describe a macrostate, macroscopically measurable independent parameters are specified. Such parameters are macroscopic properties describing a particular situation for the system studied. Some examples of these parameters are the total energy, the volume, the number of particles, the chemical potential, the pressure, etc. For example, a macrostate characterised by  $(N, V, E)$  means that the system is prepared so that it contains  $N$  particles in a volume  $V$ , with a total energy  $E$ . This corresponds to a system enclosed in rigid impermeable and adiabatic walls. The parameters chosen for the macrostate definition determine the statistical ensemble. The most relevant ensembles will be introduced on the following paragraphs.

A microstate represents a particular configuration of the  $N$  particles of the system that is compatible with the given macrostate. There are several configurations that will lead to the same macrostate. For instance, different spatial distribution of the particles in the system could result on the same total energy. A microstate is then characterised by the position and momenta of the  $N$  particles of the system  $\Gamma \equiv (\vec{r}^N, \vec{p}^N)$ , leading to a  $6N$  dimensional space known as phase space.

A statistical ensemble is a collection of systems each of them being in a microstate compatible with the actual macrostate. In other words, an ensemble is defined by the properties that thermodynamically define the macrostate. There are several possibilities for the choice of those properties. The most common ensembles are described on the following paragraphs. Each ensemble has its own partition function  $(Q)$ , which is the function that contains all the thermodynamic information of the system and from which the related properties can be derived. For each kind of boundaries of the system, there is an appropriate thermodynamic potential, which can be directly related to the partition function. By means of thermodynamic relations (for instance, the

Maxwell's relations), other thermodynamic potentials can be calculated. The general definition of the partition function is the sum of the Boltzmann factor over all the compatible microstates, as it is shown in Equation 2.23, in which  $k_B=1.3806504 \cdot 10^{-23}$  J/K is the Boltzmann constant and  $g_i$  is the degeneracy of a given state of energy  $E_i$ .

$$Q = \sum_i g_i \exp\left(\frac{-E_i}{k_B T}\right) \quad (2.23)$$

### a) Microcanonical Ensemble (NVE)

The microcanonical ensemble is defined by the system's number of particles, volume, and energy. Its partition function is shown in Equation 2.24, where  $H$  represents the Hamiltonian. The sum over  $\Gamma$  takes into account the indistinguishability of particles through the Gibbs factor  $1/N!$  in the classical (non quantum) way. The  $1/h^{3N}$  factor arises from the zero entropy for the ideal gas.<sup>130</sup>

$$Q_{NVE} = \sum_{\Gamma} \delta(H(\Gamma) - E) = \frac{1}{N!} \frac{1}{h^{3N}} \int d\vec{r} d\vec{p} \delta(H(\Gamma) - E) \quad (2.24)$$

In this case, the appropriate thermodynamic potential is the negative entropy (Equation 2.25).

$$-\frac{S}{k_B} = -\ln Q_{NVE} \quad (2.25)$$

### b) Canonical Ensemble (NVT)

The canonical ensemble is described by the system's number of particles, volume, and temperature. Equation 2.26 is the expression for its partition function. The appropriate thermodynamic potential in this case is the Helmholtz free energy  $F$  (Equation 2.27).

$$Q_{NVT} = \frac{1}{N!} \frac{1}{h^{3N}} \int d\vec{r} d\vec{p} \exp(H(\Gamma) / k_B T) \quad (2.26)$$

$$\frac{F}{k_B T} = -\ln Q_{NVT} \quad (2.27)$$

As the energy of a NVT system is not a constant, all the values of the energy are, in principle, allowed with non-zero fluctuations. Nevertheless, the energy is conserved and, therefore, the energy fluctuations are due to the heat reservoir connected with our system. The Hamiltonian of each microstate can be divided into the kinetic and potential energy contributions. Hence, the partition function can be also divided into such terms. The first integral in Equation 2.28 is related to the partition function for the ideal gas  $Q_{NVT}^{id}$  (Equation 2.29) and the second integral stands for the excess or configuration partition function  $Q_{NVT}^{ex}$  (Equation 2.30).  $\Lambda$  is the de Broglie thermal wavelength and  $Z_{NVT}$  the so-called configuration integral. As  $Q_{NVT}$  can be divided into an ideal gas term and a configuration contribution, from Equation 2.27, all the properties derived from the Helmholtz free energy can, therefore, be written as a sum of an ideal gas and a configuration part.

$$Q_{NVT} = \frac{1}{N!} \frac{1}{h^{3N}} \int d\vec{p} (-K/k_B T) \int d\vec{r} (-V/k_B T) \quad (2.28)$$

$$Q_{NVT}^{id} = \frac{V^N}{N! \Lambda^{3N}} \quad (2.29)$$

$$\Lambda = \frac{h}{\sqrt{2\pi m k_B T}}$$

$$Q_{NVT}^{ex} = V^{-N} \int d\vec{r} \exp\left(\frac{-V(\vec{r})}{k_B T}\right) = V^{-N} Z_{NVT} \quad (2.30)$$

### c) Isothermal-Isobaric Ensemble (NPT)

In this case, the number of particles, the pressure, and the temperature are the properties that are constant over all the microstates. Equations 2.31 show the expression for the NPT partition function.

$$Q_{NPT} = \sum_{\Gamma} \sum_V \exp(-(H + PV)/k_B T) = \sum_V \exp(-PV/k_B T) Q_{NVT} =$$

$$= \frac{1}{N!} \frac{1}{h^{3N}} \frac{1}{V_0} \int dV \int d\vec{r} d\vec{p} (-H + PV)/k_B T \quad (2.31)$$

$$Z_{NPT} = \int dV \exp(-PV/k_B T) \int d\vec{r} \exp(-V(\vec{r})/k_B T)$$

The appropriate thermodynamic potential is the Gibbs free energy  $G$  (Equation 2.31).

$$\frac{G}{k_B T} = -\ln Q_{NPT} \quad (2.32)$$

#### d) Grand Canonical Ensemble ( $\mu VT$ )

The grand canonical ensemble represents a collection of microstates that have the same chemical potential ( $\mu$ ), volume, and temperature. Equation 2.33 and 2.34 are the partition function and the characteristic thermodynamic functional respectively.

$$\begin{aligned} Q_{\mu VT} &= \sum_{\Gamma} \sum_N \exp(-(H - \mu N)/k_B T) = \sum_N \exp(\mu N/k_B T) Q_{NVT} = \\ &= \sum_N \frac{1}{N!} \frac{1}{h^{3N}} \exp(\mu N/k_B T) \int dr dp \exp(-H/k_B T) \end{aligned} \quad (2.33)$$

$$-\frac{PV}{k_B T} = -\ln Q_{\mu VT} \quad (2.34)$$

In this Thesis, almost all the simulations performed are at the isothermal-isobaric ensemble (NPT), because the real experiments carried out in the laboratory are usually at constant pressure and temperature. The NPT ensemble is achieved simulating a system coupled to a heat reservoir, which makes the temperature constant. Also, the pressure is held constant by changing the volume (see following sections for further details on the used thermostat and barostat algorithms). NPT simulations allow the study of systems at the vicinity of a first-order transition, because for a time long enough, the system is free to transform into the state with lowest energy, while NVT ensemble will keep the average density constant and, thus, it may frustrate the transition due to the high energy of the interface that needs to develop.



### 2.3.1.2 - Classical Molecular Dynamics

There are two main types of statistical computational methods: Monte Carlo methods (MC) and Molecular Dynamics methods (MD). Both approaches allow solving numerically problems that cannot be solved analytically (for instance, the interaction between more than two bodies). Also, statistical methods allow the prediction of some properties of the system before the experimental studies are performed. Therefore, statistical computational methods complement the experiments that need to be carried out in very difficult conditions (for example, in the so-called "no man's land" of the water phase diagram).

MC methods were introduced at the mid-20th century by Metropolis et al. looking for a deeper understanding of the diffusion of neutrons in a fissionable material.<sup>131</sup> The MC approach has been spread to other systems with many coupled degrees of freedom, as fluids or disordered materials. Nowadays, MC is being applied to almost any problem with a probabilistic interpretation as, for example, in the domain of mathematical finances. The main idea of MC methods consists on generating a markovian trajectory in the phase space in a chosen statistical ensemble. With that purpose, an initial configuration is established and then successive configurations are generated. These new configurations are rejected or accepted depending on a given probabilistic criterion. Usually, such criterion is the ratio between Boltzmann factors of the old and new configuration. Therefore, a new phase space configuration is accepted when the transition between the old and the new configuration is favourable in terms of probability. Thus, MC methods are considered as stochastic methods. Some properties can be calculated as averages over the accepted configurations. MC methods take advantage of the Ergodic Hypothesis<sup>132</sup> calculating the system's properties as ensemble averages. As MC trajectories are on the phase state, the dynamics of the system is not the real dynamics, which means that dynamic properties, as transport properties, cannot be straightforwardly computed from MC methods. This is not the case for MD simulations: MD simulations start from an initial configuration  $(\vec{r}^N, \vec{p}^N)$  and, by means of the classical Newton's equation of motion (which requires the knowledge of the forces between particles), the dynamics of the system is computed. Then, when the simulation time is long enough, the equilibrium is reached, and average properties can be calculated. In contrast with MC

methods, in MD simulations any observable property of the system is obtained computing a time average over the trajectory.

In this Thesis, MD methods are employed to study the behaviour of the  $\text{Mo}_{132}$  Keplerate in aqueous solution. The first simulation of a liquid was carried out in 1953 using a MC approach.<sup>133</sup> In 1958, the first MD experiment was carried out by Alder and Wainright<sup>134</sup> in an assembly of hard spheres. In 1960, the first MD simulation of a real material was performed by Gibson et al.<sup>135</sup> Gibson and co-workers focused on the radiation damage in crystalline Cu. Finally, in 1964 the first MD simulation of a liquid (Ar) was published by Rahman.<sup>136</sup> More recently, MD methods have already been applied to the study of confined water inside  $\text{Mo}_{132}$  cavities.<sup>12</sup> The following paragraphs are aimed at introducing some basic concepts on the context of classical MD programs.

The main goal of MD programs is to produce long-time trajectories from initial conditions of the positions and momenta of the particles of the system, to make possible the calculation of equilibrium properties as time averages. To achieve such purpose, information about the interacting forces between atoms is required. So, the first step of a MD program consists on reading the input parameters, which include information about the characteristics of the system and its initial configuration and also of the kind of simulation to be performed (ensemble, macrostate conditions, etc.). Interaction between atoms and/or molecules must be outlined as an input too through the use of a suitable force field. Thermodynamic conditions and the corresponding statistic ensemble must be also established, as well as the size and shape of the simulation box (and periodic boundary conditions, if applicable). Also, the algorithm to integrate the equations of motion and its related details must be specified.

The initial configuration consists on the  $(\vec{r}^N, \vec{p}^N)$  values of all the atom or atom-like units, whose number, type, and molecules they form must be also specified. All the simulations presented in this Thesis were performed starting from an initial configuration generated with the Packmol package<sup>137</sup>, which leads to a starting configuration in such a way that repulsive short-range forces will not disrupt the simulation. The packing strategy employed avoids atoms laying too close and overlapping, which could lead to a undesired initial configuration.<sup>138</sup>

Once all the input parameters are read, the second step consists on computing the forces between particles and, then, integrating the equations of motion. These two steps are repeated on a loop structure until the equilibrium is reached and the trajectories are long enough to have a good sampling for the calculation of averaged properties, which is the final step of a MD simulation.

### **a) Force Field**

Periodic Boundary Conditions (PBC) make possible to simulate an infinite system from a single simulation box. Nevertheless, if the number of particles approaches infinity, the evaluation of the interaction between particles becomes complicated. Forces between atoms and/or molecules are usually conservative. Therefore, such forces can be derived from the corresponding potentials.

In classical MD simulations, the electronic levels of freedom are not considered explicitly, as they are in *Ab Initio* MD. Due to its quantum nature, the electronic properties are not compatible with the time scale of Classical MD theory. In a classical MD simulation, the nuclei are classical particles moving in an effective potential surface, which is called force field. The force field is built as a collection of 2-body potential functions that describe the interactions between atoms and/or molecules. Such potential functions are parameterised from quantum mechanics or empirically. Furthermore, those interactions can be classified into intramolecular or bonded interactions and intermolecular or non-bonded interactions.

Intramolecular interactions are described by means of stretching, bending and torsion potentials. Also, sometimes coupling of degrees of freedom is considered. In all the simulations presented throughout this Thesis, all the molecules were treated as rigid bodies (see next section *Integration of the Equations of Motion*). So, no intramolecular potentials are needed to describe the dynamics of such rigid molecules: only intermolecular potentials must be defined.

Intermolecular forces can be divided in two main groups: short-ranged and long-ranged forces. Most of the intermolecular potentials have an  $r^{-\alpha}$  dependence. When  $\alpha > 3$ , potentials are considered short-ranged functions. When  $\alpha \geq 3$ , potentials are treated as long-ranged interactions.

### a.1) Short-ranged forces: the Lennard-Jones model

For short-ranged forces, the Lennard-Jones (LJ) model is applied. When two atoms are at an intermediate distance, their charge densities are redistributed causing fluctuating instantaneous dipoles, which lead to an attractive interaction between atoms. Such attractive potential is proportional to  $r^{-6}$ . When the distance between atoms is shorter, the overlap of their wavefunctions will cause a repulsive interaction because of the Pauli Exclusion Principle. Such repulsive potential is proportional to  $e^{-r}$ , but, in order to reduce the computational cost, it is usually parameterised as  $r^{-12}$  because of the quadratic relation with the attractive counterpart. The final expression for the LJ potential ( $U_{LJ}$ ) is shown in Equation 2.35, in which  $r_{ij}$  stands for the distance between particles  $i$  and  $j$ . One of the most interesting improvements with respect to, for instance, the hard spheres model is that, in the LJ model, atoms with high energy are able to penetrate the hard core of other atoms.  $\epsilon_{ij}$  is the depth of the well and  $\sigma_{ij}$  is related with the equilibrium distance (at which  $U_{LJ}(2^{1/6}\sigma_{ij})=0$ ) as it is shown in Figure 2.3. Both parameters  $\epsilon$  and  $\sigma$  can be fitted to experimental results and a wide range of pure substances are already characterised on the literature.<sup>139</sup> Nevertheless, in most cases it is more interesting to consider different kind of atoms in the same simulation box. Thus, parameters for pure substances are combined to calculate the corresponding parameters  $\epsilon_{ij}$  and  $\sigma_{ij}$  for such mixtures and describing, then, the interaction between different kinds of atoms.

$$U_{LJ}(r_{ij}) = 4\epsilon_{ij} \left( \left( \frac{\sigma_{ij}}{r_{ij}} \right)^{12} - \left( \frac{\sigma_{ij}}{r_{ij}} \right)^6 \right) \quad (2.35)$$

$$\begin{aligned} \sigma_{ij} &= \frac{\sigma_{ii} + \sigma_{jj}}{2} \\ \epsilon_{ij} &= \sqrt{\epsilon_{ii}\epsilon_{jj}} \end{aligned} \quad (2.36)$$

There are multiple choices regarding the combination of pure-substances LJ parameters ( $\sigma_{ij}$ ,  $\epsilon_{ij}$ ): different mixing rules have been reported in the literature, for instance, by Fender and Halsey,<sup>140</sup> Kong<sup>141</sup>, Waldman and Hangler<sup>142</sup> and Sikora.<sup>143</sup> Nevertheless, one of the most widely used approach are the Lorentz-Berthelot combining rules (Equation 2.36).<sup>144</sup>

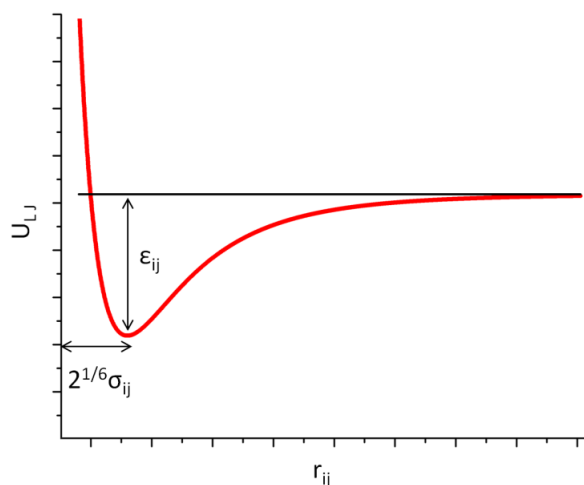


**Figure 2.3:** Lennard-Jones potential ( $U_{LJ}(r_{ij})$ ) as a function of the distance  $r_{ij}$  between a particle  $i$  and a particle  $j$ . The depth of the well  $\epsilon_{ij}$  and the equilibrium distance (related with  $\sigma_{ij}$ ) have been highlighted.

As short range interactions have an  $r^{-\alpha}$  dependence, with  $\alpha > 3$ , a cut-off distance ( $r_c$ ) must be introduced. For a given particle, the most important contribution to the short-ranged potential ( $U_{short}$ ) comes from its closest neighbours ( $r_{ij} < r_c$ ). The cut-off approach consists in splitting the LJ potential into two terms (Equation 2.37): the truncated potential ( $U_c$ ), which is the contribution from the closest neighbours and the contribution from no-closest neighbours ( $U_{r>r_c}$ ). In the simulations presented throughout Thesis, the cut-off distance is set to 16 Å.

$$U_{short} = \sum_{i < j} U_c(r_{ij}) + U_{r > r_c} \quad (2.37)$$

In the case of a LJ potential, the correction to include the contribution of no-closest neighbours ( $U_{r > r_c}^{LJ}$ ) can be expressed in terms of the LJ Lorentz-Berthelot parameters as it is shown in Equation 2.38, in which  $N_{i,j}$  is the number of atoms of type  $i$  or  $j$ .

$$U_{r>r_c}^{LJ} = \frac{8\pi N_i N_j}{V} \sum_{i=1}^{N_i} \sum_{j=1}^{N_j} \frac{\epsilon_{ij} \sigma_{ij}^6}{3} \left( \frac{\sigma_{ij}^6}{3r_c^6 - 1} \right) \quad (2.38)$$

Besides the LJ parameters, the LJ force centres at which such parameters are applied must be indicated in order to reproduce intermolecular interactions. There are two main approaches for establishing LJ force centres: all-atoms (AA)<sup>145</sup> and united-atoms models (UA).<sup>146</sup> In AA description, each atom is a LJ force centre with its corresponding LJ parameters. Nevertheless, to reduce computational cost, in some cases (for instance, hydrocarbon chains), UA models are applied, considering the hydrogen influence through the LJ parameters of the corresponding carbon atom. In this Thesis, this approach was used to describe the dynamics of the methyl groups from the acetate internal ligands of the Mo<sub>132</sub> Keplerate. The CH<sub>3</sub> rotation around the carbon atom has characteristic times much lower than our time step. Thus, a simplification can be performed considering the whole methyl group as a single unit.

In all the simulations performed throughout this Thesis, LJ parameters for the ligands and countercations were extracted from the Optimised Potentials for Liquid Simulations force field (OPLS) developed by Jorgensen et al.<sup>145</sup> Unfortunately, the OPLS force field does not include parameters for most of the transition metals. Thus, an alternative approach must be implemented for the POM atoms. Our choice consists on using LJ parameters for molybdenum and oxygen atoms extracted from previous work carried out in our group.<sup>12b, c, 16c, 147</sup> In those projects, the behaviour of different POMs in aqueous solution was simulated, achieving quite accurate results comparing to experimental data.

In the case of water, there are multiple choices for the LJ parameters because several models have been developed, since water is one of the most interesting and widely investigated liquids. The main causes of the relevance of water in different scientific fields are its abundance and its anomalous behaviour compared with other liquids. Water is the most abundant liquid on Earth and it has a very important role in biological processes. Furthermore, water has a characteristic structure that produces important consequences on its liquid behaviour. Water molecules present a permanent dipole moment that produces the so-called hydrogen bond interaction.<sup>148</sup> Such hydrogen bond network gives water a cohesive nature, which is the main cause of water anomalies. Water anomalies refers to properties of water that differ from the

behaviour of most of liquids.<sup>149</sup> For instance, water presents a high boiling, melting and critical temperature compared with other liquids with similar density. Moreover, bulk water has a large heat capacity and dielectric constant, as well as a high surface tension. At low temperatures, water presents a density maximum around 4°C and also some anomalies related to the isothermal compressibility.<sup>150</sup> Particularly, the structure of water below 0°C gives rise to the concept of amorphous ice (in which Low/High Density ice microdomains are found).<sup>151</sup> At even lower temperatures, some supercooled water properties, such as the heat capacity and the compressibility, diverge when approaching T=228 K. This feature is one of the critical points in the experimental study of the liquid behaviour of supercooled water because at T=235 K bulk water crystallises. The temperature range from T=120 K to T=235 K is known as the *no man's land*, in which experiments on liquid water cannot be performed.<sup>152</sup> Such limitation in experimental studies makes simulations of water even more important. Hence, a huge variety of water models have been developed to satisfy the specific requirements of the different phenomena to study.

The explicit solvent models for water available in the literature are representations of the H<sub>2</sub>O molecule with some variations in the values of the LJ parameters, atomic point charges and geometry, depending on the range of conditions and the properties to be reproduced. Furthermore, water models present different number of atomic sites. For instance, the SSD (Soft Sticky Dipole) model<sup>153</sup> is a single point representation, where only one site is used and characterised by means of a point dipole and a LJ core. More sophisticated models are built as 3-sites representations. The SPC (Simple Point Charge) model<sup>154</sup> is an empirical parameterization composed of three point charges and one LJ centre at the oxygen atom. Usually, in the SPC model, water molecules are considered as a rigid, but there is also a flexible variant.<sup>155</sup> The SPC/E model is, as well, an extension of the original SPC, in which the charge of the oxygen atom has been alternatively parameterised.<sup>155b</sup> Among the 3-site models, some of them are built in order to reproduce polarisable water molecules, as the PPC (Polarisable Point Charge) model.<sup>156</sup> In the PPC model, the effect of an electric field has been included by means of the three point charges and the position of the negative charge. More complex models have been reported using an increasing number of atomic sites. For instance, GCPM (Gaussian Charge Polarisable Model)<sup>157</sup> uses 4 atomic sites and in the six-site model<sup>158</sup> a tetrahedral geometry has been considered.

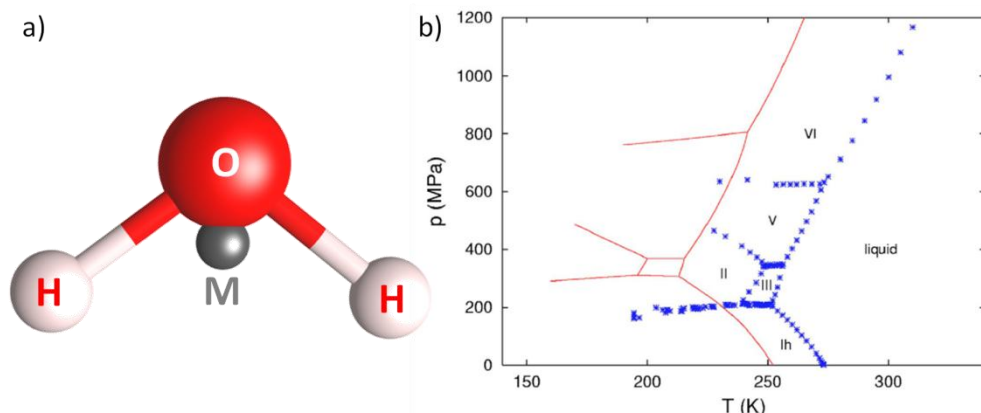


**Figure 2.4:** a) Schematic representation of the molecular geometry for the TIP4P/2005 water model. The O atom has been represented in red, H atoms in white and grey is reserved for the dummy atom M. b) Phase diagram the water model TIP4P/2005 (red line) compared with the experimental results (blue stars). The phase diagram has been reproduced from ref. [169].

Among the different models for water, there is a family of parameterizations with a special relevance due to its versatility and potential applications: the so-called Transferable Intermolecular Potentials (TIP). The TIP group includes models with an increasing number of atomic sites. Some examples of this family are the TIP3P,<sup>159</sup> TIP4P,<sup>160</sup> TIP5P<sup>161</sup> and their corresponding variations. Particularly, throughout this Thesis, water has been represented by means of the TIP4P/2005 model.<sup>162</sup> TIP4P/2005 consists of a rigid planar model with four atomic sites. Besides the sites corresponding to H and O atoms, an extra position has been included to represent a charge displacement of the oxygen atom. Therefore, TIP4P/2005 presents three point charges (at H and M positions) and a LJ centre located at the oxygen atom (see Figure 2.4a for further details). The TIP4P/2005 model has been chosen for this Thesis project for its accurate description of bulk water at a wide range of conditions. A good example of such accurate description is the resulting TIP4P/2005 phase diagram. Figure 2.4b shows how, using the TIP4P/2005 representation, the phase diagram of water has been accurately reproduced by Abascal and Vega. It is worth noting that the obtained phase diagram is shifted around 20 K to low temperatures with respect to the experimental diagram.



### a.2) Long-ranged Forces: the Ewald Summation Technique

The problem of long-ranged forces is usually reduced to the treatment of Coulombic interactions between atoms with assigned point charges. When Periodic Boundary Conditions (PBC) are applied, long-ranged interactions can imply atoms belonging to different cell replicas. Thus, in such situation the Ewald summation technique must be applied.<sup>163</sup>

Considering  $N$  charges  $q_i$  with positions  $\vec{r}_i$  in a cubic volume  $V=L^3$ , the electrostatic energy of the system ( $U_{elec}$ ) is represented in Equation 2.39, where  $\phi_i(r_i)$  is electrostatic potential (Equation 2.40). Such potential is caused not only by the charges belonging to the main cell, but also to the replicas resulting from the PBC. This is the reason why the sum in Equation 2.40 is also in  $\vec{n}$ , which is the vector indicating the cell replica. It is worth noting that when  $\vec{n} = 0$ , the contribution from  $j=i$  must be excluded from the summation, in order to avoid including the interaction of a given atom with itself. Equation 2.39 is only conditionally convergent, which means that the summation in  $i$  converges depending on the order in which the sum is performed. Hence, the Ewald summation technique is introduced in order to avoid such mathematical issue.

$$U_{elec} = \frac{1}{2} \sum_{i=1}^N q_i \phi(\vec{r}_i) \quad (2.39)$$

$$\phi(\vec{r}_i) = \sum_{\vec{n}} \sum_{j=1}^N \frac{q_j}{|\vec{r}_{ij} + \vec{n}L|} \quad (2.40)$$

The Ewald summation technique considers that each point charge is surrounded by a screening charge distribution ( $\rho_s$ ) with the same total charge and opposite sign. Then, a compensating charge distribution ( $\rho_c$ ) must be included at  $\vec{r}_i$ , with total charge  $q_i$ . Both, screening and compensating charge distribution are Gaussian distributions of width  $1/\sqrt{2}\alpha$  (Equation 2.41).

$$\rho_{c,s} = \pm q_i \left( \frac{\alpha^2}{\pi} \right)^{3/2} \exp(-\alpha^2 r^2) \quad (2.41)$$

From Equations 2.39-41, it is possible to propose a set of converging sums for the point charges and the corresponding screening and compensating charge distribution. For the point charges and the screening distribution, the sum is performed in the real space. In contrast, for the compensating charge distribution, the sum is performed in the Fourier space.

Equation 2.42 summarises the electrostatic energy resulting from the Ewald summation technique. The first term stands for the contribution of the compensating charge distribution. The second term represents the contribution of the point charges and their corresponding screening charge distribution. Finally, the negative terms are related to the interaction between the point charges and its own compensating charge distribution and the undesired intramolecular interactions ( $N^*$ ). The error function (erf) and its complementary function (erfc) are defined in Equation 2.43.<sup>164</sup>

$$U_{elec} = \frac{1}{2\epsilon_0 V} \sum_{\vec{k} \neq 0} \sum_{j=1}^N \frac{q_i q_j}{k^2} \exp(-i\vec{k}(\vec{r}_i - \vec{r}_j)) \exp\left(-\frac{k^2}{4\alpha^2}\right) + \frac{1}{8\pi\epsilon_0} \sum_{m \neq j}^{N-N^*} \frac{q_m q_j}{r_{mj}} \operatorname{erfc}(\alpha r_{mj}) - \frac{1}{4\pi\epsilon_0} \left( \frac{\alpha}{\sqrt{\pi}} \sum_{i=1}^N q_i^2 + \sum_{molec} \sum_{l < m}^{N^*} \frac{q_l q_m}{r_{lm}} \operatorname{erf}(\alpha r_{lm}) \right) \quad (2.42)$$

$$\operatorname{erf}(x) = \frac{2}{\sqrt{\pi}} \int_0^x e^{-t^2} dt \quad (2.43)$$

$$\operatorname{erfc}(x) = 1 - \operatorname{erf}(x) = \frac{2}{\sqrt{\pi}} \int_x^\infty e^{-t^2} dt$$

For practical requirements, the first term on Equation 2.42 must be restricted to a set of lattice vectors  $\vec{k}$ , so  $k_{x,y,z} \in [-k_{x,y,z}^{max}, k_{x,y,z}^{max}]$ . Thus, finally, the parameters regarding the Ewald summation technique that must be fixed to perform a MD simulation are  $\alpha$  and  $|k_{x,y,z}^{max}|$ .  $\alpha$  depends on the size of the system. For small values of  $\alpha$ , the second term in Equation 2.42 will converge quickly, but for large values of  $\alpha$  the first term will converge faster. So  $\alpha$  must be chosen in order to improve the time to compute both sums.<sup>165</sup> For the simulations carried out throughout this Thesis,  $\alpha$  and  $|k_{x,y,z}^{max}|$  are set to 0.21 and 6, respectively.

### a.3) Point Charges Distribution

The Ewald summation technique (and any other approach to compute electrostatic interactions in MD simulations) requires the assignment of point charges to atomic positions. Unfortunately, atomic charge is not an observable from a QM point of view.<sup>166</sup> So, point charges cannot be derived directly and in a unique way from the wavefunction of the system. Nevertheless, there are multiple approaches to assign point charges: from empirical parameters (Charge Equilibration method or  $Q_{\text{eq}}$ <sup>167</sup>), fitting electrostatic potential (Charges from Electrostatic Potentials using a Grid-based method or ChelpG<sup>168</sup>), from the atomic polar tensors (Generalised Atomic Polar Tensor or GAP charges<sup>169</sup>), from molecular orbitals (Mulliken<sup>170</sup> and Weinhold-Reed Natural Population Analysis (NPA)<sup>171</sup>), and, finally, from the integration of the electronic density on atomic domains (Hirshfeld,<sup>172</sup> Bader<sup>173</sup> and Voronoi Density Displacement (VDD)<sup>174</sup> approaches).

$Q_{\text{eq}}$  method assigns point charges to atomic positions of a given molecular geometry from experimental atomic properties. The basis of this method is to express the atomic energy ( $E_A$ ) as a Taylor series of the charge (Equation 2.44). The coefficients of the Taylor series are related to empirical atomic parameters such as the ionization potential (IP) and the electron affinity (EA), which are related to the electronegativity ( $\chi_A^0$ ) and to the idempotential or self-Coulomb integral ( $J_{AA}^0$ ), as it is shown in Equations 2.45. The atomic energy is finally expressed as Equation 2.46.  $Q_{\text{eq}}$  equations are summarised as the matrix Equation 2.47.

$$E_A(Q) = E_A(0) + Q_A \left( \frac{\partial E}{\partial Q} \right)_{A0} + \frac{1}{2} Q_A^2 \left( \frac{\partial^2 E}{\partial Q^2} \right)_{A0} + \dots \quad (2.44)$$

$$\left( \frac{\partial E}{\partial Q} \right)_{A0} = \frac{1}{2} (\text{IP} + \text{EA}) = \chi_A^0 \quad (2.45)$$

$$\left( \frac{\partial^2 E}{\partial Q^2} \right)_{A0} = \text{IP} + \text{EA} = J_{AA}^0$$

$$E_A(Q) = E_{A0} + \chi_A^0 Q_A + \frac{1}{2} J_{AA}^0 Q_A^2 \quad (2.46)$$

$$\begin{aligned}
 \mathbf{CD} &= -\mathbf{D} \\
 D_1 &= -Q_{tot} \\
 D_i (i > 1) &= \chi_i^0 - \chi_1^0 \\
 C_{1i} &= Q_i \\
 C_{ij} (i > 1) &= J_{ij} - J_{1j}
 \end{aligned}
 \tag{2.47}$$

$Q_{eq}$  approach was used in previous work performed in our group regarding the structures formed by the water molecules encapsulated within the  $Mo_{132}$  capsule<sup>12b, c</sup>, giving accurate results when compared with X-ray experiments.

Besides empirical parameterizations, another interesting group of methods are those based on the integration of the electron density. When a bond is formed, the partial charge of an atom is the amount of electron density lost to or gained from the other atom involved in the bond. To compute the change on the electron density, a spatial partitioning must be defined, to allow the integration of the electron density in atomic domains. Different partitions will lead to different numerical values for the atomic charges (Table 2.1).

Bader methodology takes advantage from the topology of the electron density, namely, its critical points, to define atomic domains, in which the electron density is integrated. Bader charges are calculated by subtracting such integral value to the nuclear charge (Equation 2.48). The first step consists on identify the critical points of the electron density. The points at which the charge density is a minimum along the bond direction but a maximum in regarding the directions normal to the bond define the atomic regions, which are zero-flux surfaces by construction.

$$Q_A^{Bader} = Z_A - \int_{\text{atomic regions}} \rho(\vec{r}) d\vec{r}
 \tag{2.48}$$

In contrast with Bader approach, the VDD method uses a pure geometric partitioning of the space. For a given atom, its Voronoi cell<sup>175</sup> is the region of the space that is closer to that nucleus than to another one. Hence, a Voronoi cell for a particular atom is bound by the bond midplanes perpendicular to all axes between the given nuclei and its neighbours, like a Wigner-Seitz cell in a crystal structure. Once the spatial partitioning is defined, the deformation density can be calculated, in order to evaluate the flow of charge into/out of

the Voronoi cells. By construction, the VDD method is independent on the choice of basis set and also on the choice of the origin of the molecular geometry. Furthermore, the VDD method does not depend on atomic properties as the electronegativity or Van der Waals radii, which have a certain degree of arbitrariness. The VDD method, like the Hirshfeld method, uses a fictitious promolecule, whose electron density is the superposition of atomic densities. The deformation density ( $\rho_{\text{def}}$ ) is defined as the difference between molecular and promolecular density. Equation 2.49 represents the VDD charge for a given atom A, where  $\omega_A^{\text{Voronoi}}$  corresponds the weight function, which is 1 inside the Voronoi cell and 0 outside. The sum of the atomic VDD charges adds up the total charge and gives us information about the flow of charge caused by the bonding. Positive values of  $Q_A^{\text{VDD}}$  correspond to loss of electrons in the Voronoi cell, while negative values will suggest a gain of electron density.

$$Q_A^{\text{VDD}} = - \int_{\text{Voronoi cell}} (\rho_{\text{molecule}}(\vec{r}) - \rho_{\text{promolecule}}(\vec{r})) d\vec{r} = - \int \omega_A^{\text{Voronoi}} \rho_{\text{def}}(\vec{r}) d\vec{r} \quad (2.49)$$

Different point charges distributions generate different numerical charge values. Therefore, a bad choice of the point charges could lead to unphysical results, as point charges are the source of one of the most important interactions on the defined force field. Table 2.1 collects some examples of the numerical charge values obtained with the point charges distributions described on the previous paragraphs for some of the atoms belonging to the  $\text{Mo}_{132}$  macro-ion.

**Table 2.1:** Examples of numerical values for the point charges assigned to some relevant atomic positions using different approaches ( $Q_{\text{eq}}$ , Bader, and VDD point charges distribution).  $\text{Mo}_{\text{central}}$  stands for the central atom of the pentagonal unit, while  $\text{Mo}_{\text{penta}}$  represents the remaining metal centres in such building block.  $\text{Mo}_{\text{linker}}$  are the metal centres of the linkers.  $\text{O}_{\text{term}}$  corresponds to the terminal oxygen atoms and  $\text{O}_{\text{bridge}}$  to those occupying bridging positions in the linkers.

Atom	$Q_{\text{eq}}$ (e)	Bader (e)	VDD (e)
$\text{Mo}_{\text{central}}$	0.9747	2.5807	0.8860
$\text{Mo}_{\text{penta}}$	0.8845	2.6188	0.8430
$\text{Mo}_{\text{linker}}$	0.8654	2.4074	0.7140
$\text{O}_{\text{term}}$ (linker)	-0.5512	-0.8607	-0.3940
$\text{O}_{\text{term}}$ (pentagon)	-0.5880	-0.8542	-0.3840
$\text{O}_{\text{bridge}}$	-0.3162	-0.9799	-0.4210
$\text{O}_{\text{penta}}$	-0.2908	-1.0684	-0.3350

Due to the several possibilities available for the point charges distribution, a choice must be made, in order to complete the description of the force field. In our case, we performed a series of MD simulations for the  $\text{Mo}_{132}$  ion in solution with guanidinium counter-cations, using different point charges approaches. This system was chosen as reference because of its experimental characterization in terms of the layered water structures formed inside the cavity due to the confinement.<sup>12a</sup> Then, the different approaches for the point charges distribution described on the previous paragraphs ( $Q_{\text{eq}}$ , Bader and VDD methods) were applied to assign point charges to the POM atoms, in order to compare our theoretical results with the experimental ones and make a decision about which method better represents our system.  $Q_{\text{eq}}$  approach was chosen because, despite its semiempirical character, it was already used in previous work performed by our research groups to characterise by means of MD the layered structures of water inside  $\text{Mo}_{132}$  cavity, achieving quite accurate results (Figure 2.5).<sup>12</sup> Bader and VDD methods were chosen in order to take advantage from the electron density calculations carried out at the quantum level as part of this Thesis. The computational details for these quantum calculations correspond to the standard DFT level (ADF2012 / ZORA / BP86 / TZP / COSMO).

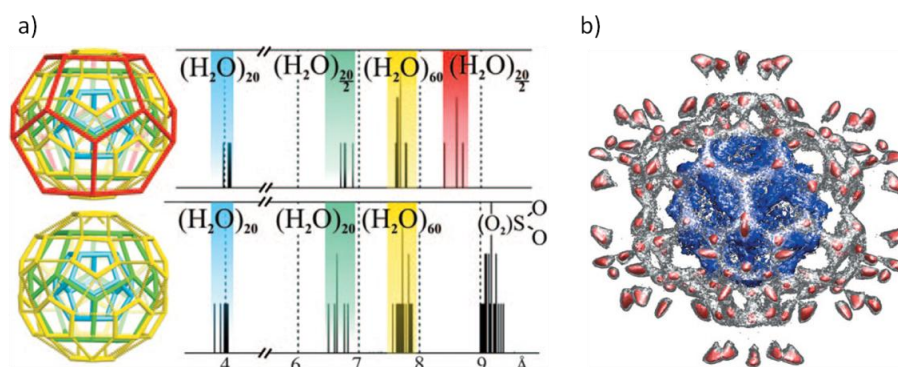


**Figure 2.5:** **a)** Schematic representation of the layered water structure with its corresponding distance histogram of water oxygen atoms to the centre of the  $\text{Mo}_{132}$  cavity for formate (top) and sulphate ligands (bottom). **b)** Spatial distribution function of water molecules encapsulated inside the  $\text{Mo}_{132}$  Keplerate with sulphate ligands. Red colour represents the second and third layer, together with the coordination waters. Grey colour corresponds to the exchange between the second and third layer. Blue colour is reserved for the inner shell. Both figures have been reproduced from the publication of Mitra et al.<sup>12a</sup>

$Q_{eq}$ , Bader and VDD simulations were performed with the DL\_POLY Classic 1.9 package<sup>176</sup>. PBC were applied to a cubic simulation box of initial dimensions of  $7 \times 7 \times 7$  nm<sup>3</sup>, containing one Mo<sub>132</sub> anion with 30 fixed formate ligands, 42 guanidinium cations and 11000 TIP4P/2005 water molecules. All the molecules in this system were treated as rigid objects to reduce the computational cost. Besides the point charge parameters for the Keplerate, the force field must be completed for the cations and ligands by means of the OPLS-AA parameterization. The LJ parameters for the POM were the same used on previous studies performed for the Mo<sub>132</sub> capsule<sup>12</sup> and other polyoxometalates systems.<sup>147, 177</sup> Crossed interactions between unlike atoms have been calculated from Lorentz-Berthelot combining rules.<sup>144</sup> Coulombic interactions are calculated through the Ewald summation technique, with  $\alpha=0.21$  and a maximum of six wave vectors in each direction. Trajectories were computed by means of the Verlet leapfrog algorithm with a time step of 1 fs and a cut-off of 16 Å. The simulations were carried out in the NPT ensemble. Ambient conditions (T=298 K; p=1 atm) were achieved through the Nosé-Hoover thermostat and Andersen barostat, with relaxation times of 0.02 ps and 0.1 ps, respectively. Further details for the integration algorithms, thermostat and barostat are given in following sections. Initial configurations were generated with the Packmol software<sup>137</sup> and equilibrated for 1 ns. Then, the production run was extended 4 ns. Snapshots of the simulations were stored each 1000 time steps. Those snapshots were used to compute radial distribution functions of the different atom types involved on the MD simulation. With that purpose, the simulation box was divided into concentric shells of width of 0.035 Å with their origin at the centre of the Mo<sub>132</sub> capsule.

Classical MD simulations using  $Q_{eq}$ , VDD and Bader methods are compared on Figure 2.6 by means of the radial distribution function of the oxygen atoms of water (Figure 2.6a) and of the carbon atoms of the guanidinium cations (Figure 2.6b). All three models present common features. For instance, the radial distribution function profiles for the water molecules encapsulated inside the Mo<sub>132</sub> cavity show a structured arrangement, resulting on concentric shells of water molecules. Such effect is a consequence of the confinement. Mo<sub>132</sub> pentagonal building blocks are composed of Mo<sup>VI</sup> metal centres. X-ray results show pentagonal structures composed of a pentagonal dipyramid MoO<sub>7</sub> surrounded by 6 MoO<sub>6</sub> octahedra.<sup>12a</sup> To achieve such structure, 72 water molecules must complete the coordination of the pentagon metal centres.

Therefore, the capsule acts as a template for the coordination water molecules: the pentagonal motifs constrain the arrangement of the water molecules closer to the cavity wall. Such imposed arrangement is spread but distorted as approaching the centre of the capsule, giving rise to the particular layered structure of the encapsulated water molecules (Figure 2.5). The layered arrangement of encapsulated water has been previously studied in our group by means of Classical MD simulations, achieving a very good agreement with the experimental X-ray results.<sup>12</sup> For example, Mitra et al. compared the effect that the ligand size will have on the arrangement of the water layers inside the  $\text{Mo}_{132}$  cavity. The authors have shown that the size of the ligands strongly affects the available space on the cavity, altering the layered structure of water. For instance, when formate groups are acting as internal ligands, in addition to the 72 coordination water molecules, the inner 100 molecules cluster is composed of four layers: the innermost  $\{\text{H}_2\text{O}\}_{20}$  dodecahedron, a partially occupied  $\{\text{H}_2\text{O}\}_{20/2}$  dodecahedron, a  $\{\text{H}_2\text{O}\}_{60}$  distorted rhombicosidodecahedron and another partially occupied  $\{\text{H}_2\text{O}\}_{20/2}$  dodecahedron. Further details on this kind of water layered structures are described in Chapter 6.

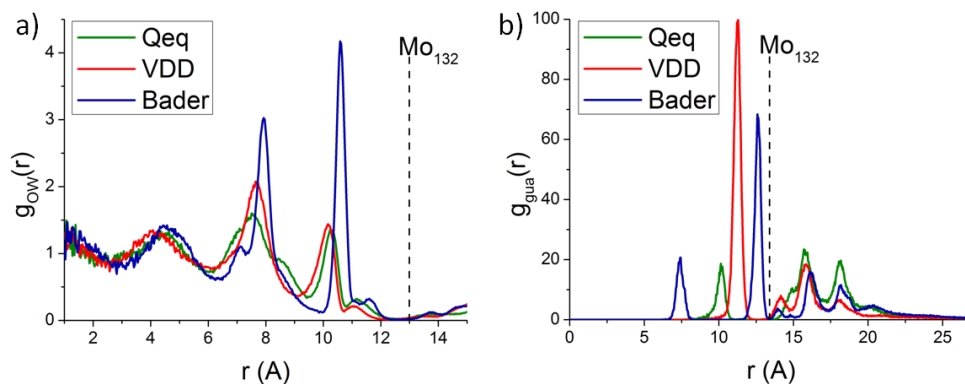


**Figure 2.6:** Radial distribution functions for: **a)** the oxygen atom of water ( $g_{ow}$ ) and **b)** the carbon atom of guanidinium cations ( $g_{gua}$ ). Three different models for the point charges assignments have been used:  $Q_{eq}$  (green line), VDD (red line) and Bader (blue line) methods. The black dashed line represents the polyoxometalate scaffold.

All the previous studies related to the  $\text{Mo}_{132}$  capsule and the analysis of the structural properties of the water molecules encapsulated were performed using the  $Q_{eq}$  method and the molecular geometry extracted from X-ray results. Furthermore, the capsule was treated as a closed system 20 guanidinium



cations fixed plugging the pores and no external solvent considered. In contrast, the simulations presented throughout this Thesis consider the capsule in aqueous solution in the presence of countercations initially randomly distributed along the simulation box. Additionally, the molecular geometry was extracted from DFT calculations instead from X-ray results. Despite these differences, all three charge models compared in Figure 2.6a reproduce the layered structure of water molecules inside. Obviously, changes in the charge distribution and on the capsule's description cause some differences on the distribution of the water molecules. However, all three models have radial distribution patterns with the same number of peaks approximately at the same position. Nevertheless, the integration of the radial distribution function leads to a different number of water molecules inside the capsule. The Bader method results in more than 200 water molecules encapsulated, while  $Q_{eq}$  and VDD simulations lead to 167 and 162 water molecules inside the cavity respectively. The latter results are in better agreement with the experimental observations (172 water molecules encapsulated: a 100 molecules cluster and 72 coordination water molecules). Such result indicates that, regarding the water molecules distribution,  $Q_{eq}$  and VDD method seem to be better descriptors of the  $Mo_{132}$  capsule in solution.

As far as the counter-cation distribution is concerned, different profiles are observed for the three point charges models in Figure 2.6b. The cation distribution will be the final criterion to decide which charge choice better describes our system in the desired conditions. X-ray results show that the guanidinium countercations are located at the pores, at 12.3 Å from the centre of the capsule. Using the Bader methodology, the radial distribution function for the guanidinium cations shows two peaks inside the cavity: around 7.5 Å and 12.5 Å from the centre of the capsule. The integration of those peaks corresponds to 10 guanidinium cations. The  $Q_{eq}$  radial distribution only presents a peak at 10 Å inside the capsule, corresponding to only 2 guanidinium cations. Finally, in the case of the VDD method, only one peak is observed between the centre of the capsule and the positions of the Mo atoms, placed around 11.25 Å. This peak represents 11 guanidinium cations placed at the pores.

Summing up, the Bader method overestimates the amount of water molecules encapsulated and also allows cations to penetrate inside the cavity. These two features lead us to discard Bader methodology as a suitable point charges distribution choice to describe the interaction between the Mo<sub>132</sub> anion and guanidinium cations. When Q<sub>eq</sub> or VDD methods are applied, the number of water molecules encapsulated inside the Keplerate is 167 and 162 respectively. These numbers are in better agreement with experimental results than the Bader methodology. Regarding the counter-cation distribution, Q<sub>eq</sub> method leads to a radial distribution peak at 10 Å corresponding to two guanidinium cations. In contrast, the application of the VDD methodology causes a peak in the radial distribution function at 11.25 Å, which corresponds to 11 counter-cations. Therefore, VDD point charges distribution produces results that are in better agreement with the cation distribution observed experimentally (at 12.3 Å from the centre of the capsule). Thus, VDD method is the one chosen to perform the classical MD simulations presented throughout this Thesis.

### ***b) Integration of the Equations of Motion***

Once the force field is defined, the Newton's equations of motion can be integrated to generate a classical trajectory for all the particles of the system. The procedure will be different depending on the nature of the interaction and bonds between atoms. For instance, the characteristic time and quantum nature of stretching and bending displacements make classical MD inappropriate to characterize such movements. A good approach to solve the chemical bond description is to introduce constraints during the integration of the equation of motion to some distances and angles. This can be done by means of the Lagrangian multiplier method, which will introduce a constraining force in the Newton's equation of motion. The most widely used algorithm to perform this kind of constraints is the shake algorithm, introduced by Berendsen et al.<sup>178</sup> Nevertheless, the constraint method is recommended for systems with a small number of constraints compared with the number of particles. When the number of constraints increases, the shake algorithm will strongly increase the computational cost. Then, for systems with a larger number of constraints than atoms, the rigid body approximation becomes more practical than the constraint method. In this Thesis, all the MD simulations were performed under the rigid body approximation: each molecule is considered as a rigid unit that interact with other rigid units keeping its

characteristic geometry. The rigid body approach allows saving computational time without losing critical information, because we are interested in properties of the system that are not expected to be affected by the particular details of the vibrational motion or the flexibility of the many bonds present in our molecules.

As we are considering all the molecules as rigid bodies, for a given unit the integration of the equations of motion can be divided on the translational motion of the centre of mass and the rotation of the given unit around its centre of mass.

For the integration of the equations of translational motion, the simplest and widely used method is the Verlet algorithm.<sup>130, 163a</sup> The starting point is to consider the position of a particle at a time step ( $\Delta t$ ) after and before an instant  $t$  and express it as a Taylor series of time (Equations 2.50 and 2.51, respectively).

$$\vec{r}(t + \Delta t) = \vec{r}(t) + \vec{v}(t)\Delta t + \frac{\vec{a}(t)}{2}(\Delta t)^2 + \frac{1}{6} \frac{d^3\vec{r}(t)}{dt^3}(\Delta t)^3 + \dots \quad (2.50)$$

$$\vec{r}(t - \Delta t) = \vec{r}(t) - \vec{v}(t)\Delta t + \frac{\vec{a}(t)}{2}(\Delta t)^2 - \frac{1}{6} \frac{d^3\vec{r}(t)}{dt^3}(\Delta t)^3 + \dots \quad (2.51)$$

The addition Equations 2.50 and 2.51 leads to Equation 2.52.

$$\vec{r}(t + \Delta t) = 2\vec{r}(t) - \vec{r}(t - \Delta t) + \vec{v}(t)\Delta t + \vec{a}(t)(\Delta t)^2 + \dots \quad (2.52)$$

$$\vec{v}(t) = \frac{\vec{r}(t + \Delta t) - \vec{r}(t - \Delta t)}{2\Delta t} \quad (2.53)$$

At this point, velocities can be computed from the definition of time derivative. Equation 2.53 shows that the position of a particle can be computed from the position at the two previous time steps. The time-reversibility of the Verlet algorithm can also be observed from Equation 2.53. The volume at the phase space filled by the points compatible with a given energy remains constant under a Verlet time evolution. The main consequence of this fact is one of the major advantages of the Verlet algorithm: the energy drift for long time simulations will be small. Nevertheless, to compute the position and the velocity at a given time, the position at three different moments must be

stored, increasing considerably the memory requirements. In order to avoid this memory demands, the leapfrog algorithm<sup>130, 163a</sup> is introduced to compute velocities. The starting point in this case consists on considering velocities at a half time step before and after the actual instant (Equations 2.54 and 2.55).

$$\vec{v}(t + \Delta t/2) = \frac{\vec{r}(t) - \vec{r}(t - \Delta t)}{\Delta t} \quad (2.54)$$

$$\vec{v}(t - \Delta t/2) = \frac{\vec{r}(t + \Delta t) - \vec{r}(t)}{\Delta t} \quad (2.55)$$

The subtraction of Equation 2.55 to Equation 2.54 leads to Equation 2.56.

$$\vec{v}(t + \Delta t/2) = \vec{v}(t - \Delta t/2) + \vec{a}(t)\Delta t \quad (2.56)$$

In the leapfrog algorithm velocities are computed half time step before and after the positions are evaluated. In order to calculate the kinetic energy at each time step, it is useful to have the velocities at the same time  $t$  at which the positions are computed. This can be done by means of Equation 2.57.

$$\vec{v}(t) = \frac{\vec{v}(t + \Delta t/2) - \vec{v}(t - \Delta t/2)}{2\Delta t} \quad (2.57)$$

Besides decreasing the storage requirements of the Verlet algorithm, the leapfrog algorithm is also time-reversible and it conserves the volume in the phase space as well.

When applying the rigid body approximation, it is possible to study the translational motion of the molecules by means of the trajectory of their centre of mass (CM). The position and velocity of the CM of a rigid unit ( $\vec{R}_{CM}$  and  $\vec{V}_{CM}$ ) depend on the coordinates ( $\vec{r}_i$ ), velocity ( $\vec{v}_i$ ) and mass ( $m_i$ ) of the  $N$  particles in the unit (Equations 2.58 and 2.59). Furthermore, the resulting force applied to the centre of mass ( $\vec{F}_{CM}$ ) is the sum of the forces acting on every particle belonging to the molecule ( $\vec{F}_i$ ). Equations 2.58-60 define a new set of Newton's equations for the translational motion of the rigid body that can be integrated by means the leapfrog algorithm.

$$\vec{R}_{CM} = \frac{\sum_{i=1}^N \vec{r}_i m_i}{\sum_{i=1}^N m_i} \quad (2.58)$$

$$\vec{V}_{CM} = \frac{\sum_{i=1}^N \vec{v}_i m_i}{\sum_{i=1}^N m_i} \quad (2.59)$$

$$\vec{F}_{CM} = \sum_{i=1}^N \vec{F}_i \quad (2.60)$$

Even if the atoms in a rigid molecule are not allowed to change its relative position to the CM, their orientation evolves with time as the molecule rotates. Due to the nature of the motion of the rigid body, it is useful to define two different frames of reference: the external (ext) and the CM coordinate systems. The CM Cartesian frame of reference is centred on the CM and its orientation evolves with time as the molecule rotates. So, the coordinates of the rigid body are constant in the CM of reference, but they change in the external coordinate system. Any Cartesian coordinate system can be transformed to another by three successive rotations related to the so-called Euler angles. Then, the coordinates on external and centre of mass frame of reference are related by the rotation matrix  $\mathbf{A}$ , as it is shown on Equation 2.61.

$$\vec{r}_e = \mathbf{A} \cdot \vec{r}_i \quad (2.61)$$

$$\begin{aligned} \vec{q} &= (q_0, q_1, q_2, q_3) \\ q_0 &= \cos\left(\frac{\theta}{2}\right) \cos\left(\frac{\phi + \psi}{2}\right) \\ q_1 &= \sin\left(\frac{\theta}{2}\right) \cos\left(\frac{\phi - \psi}{2}\right) \\ q_2 &= \sin\left(\frac{\theta}{2}\right) \sin\left(\frac{\phi - \psi}{2}\right) \\ q_3 &= \cos\left(\frac{\theta}{2}\right) \sin\left(\frac{\phi + \psi}{2}\right) \\ q_0^2 + q_1^2 + q_2^2 + q_3^2 &= 1 \end{aligned} \quad (2.62)$$

$$\mathbf{A} = \begin{pmatrix} q_0^2 + q_1^2 - q_2^2 - q_3^2 & 2(q_1q_2 - q_0q_3) & 2(q_1q_3 + q_0q_2) \\ 2(q_1q_2 + q_0q_3) & q_0^2 - q_1^2 + q_2^2 - q_3^2 & 2(q_2q_3 - q_0q_1) \\ 2(q_1q_3 - q_0q_2) & 2(q_2q_3 + q_0q_1) & q_0^2 - q_1^2 - q_2^2 - q_3^2 \end{pmatrix} \quad (2.63)$$

For the sake of simplicity,  $\mathbf{A}$  can be expressed in terms of quaternions<sup>179</sup> (Equations 2.62 and 2.63).

When analysing the rotation of the rigid body, one of the most important physical magnitudes is the angular momentum  $\vec{L}$  (Equation 2.64).

$$\vec{L} = \sum_{i=1}^N m_i \vec{d}_i \times \vec{v}_i \quad (2.64)$$

$$\vec{d}_i = \vec{r}_i - \vec{R}_{CM}$$

The angular momentum is related with the angular velocity ( $\vec{\omega}$ ) by means of the inertia matrix ( $\mathbf{I}$ ), as it is shown in Equation 2.65, where  $d_{ij}$  represents the  $j^{\text{th}}$  component of the vector  $\vec{d}_i$  and  $\delta$  is the Kronecker delta function.

$$\vec{L} = \mathbf{I} \cdot \vec{\omega}$$

$$I_{jk} = \sum_{i=1}^N m_i (d_i^2 \delta_{jk} - d_{ij} d_{ik}) \quad (2.65)$$

The coordinate system at which the matrix  $\mathbf{I}$  is diagonal is chosen as the principal frame of reference (p). The choice of this system of reference allows simplifying Equation 2.65 into Equation 2.66.

$$\vec{L}_p = (I_{xx,p} \omega_{x,p}, I_{yy,p} \omega_{y,p}, I_{zz,p} \omega_{z,p})$$

$$I_{jj,p} = \sum_{i=1}^N m_i (d_i^2 - d_{ij}^2) \quad (2.66)$$

If there are external forces acting at different atomic positions of the rigid molecule, the resulting torque ( $\vec{\tau}$ ) around its CM can be expressed as the time variation of the angular moment (Equation 2.67).

$$\vec{\tau} = \frac{d\vec{L}}{dt} = \sum_{i=1}^N \vec{d}_i \times \vec{F}_i \quad (2.67)$$

Equation 2.67 can be expressed in the principal frame of reference using Equation 2.66, achieving then the Euler equations of motion for  $\vec{\omega}_p$ . However, DL\_POLY Classic uses the quaternion approach, which leads to an equivalent expression (Equation 2.68).<sup>180</sup>

$$\begin{pmatrix} \dot{q}_0 \\ \dot{q}_1 \\ \dot{q}_2 \\ \dot{q}_3 \end{pmatrix} = \frac{1}{2} \begin{pmatrix} q_0 & -q_1 & -q_2 & -q_3 \\ q_1 & q_0 & -q_3 & q_2 \\ q_2 & q_3 & q_0 & -q_1 \\ q_3 & -q_2 & q_1 & q_0 \end{pmatrix} \begin{pmatrix} 0 \\ \omega_{p,x} \\ \omega_{p,y} \\ \omega_{p,z} \end{pmatrix} = \mathbf{Q} \cdot \vec{\omega}_p \quad (2.68)$$

To include the rotational motion in the leapfrog integration Fincham's algorithm is implemented.<sup>181</sup> In the leapfrog algorithm for the translational motion the velocities are calculated half time step before the positions. Analogously, in this case, the desired quantities are  $\vec{q}(t + \Delta t)$  and  $\vec{\omega}_p(t + \Delta t/2)$ . From  $\vec{q}$ , the orientation of the molecule is known at each time step. The evolution with time of the rotational motion is studied through the angular velocity, which is directly related with the variation of the quaternions, as it is shown in Equation 2.68. Thus, with the aim at computing  $\vec{q}(t + \Delta t)$  and  $\vec{\omega}_p(t + \Delta t/2)$ , the starting point is the quaternions vector  $\vec{q}$  at half time step after  $t$  (Equation 2.69).

$$\vec{q}\left(t + \frac{\Delta t}{2}\right) = \vec{q}(t) + \frac{\Delta t}{2} \mathbf{Q}(t) \cdot \vec{\omega}(t) \quad (2.69)$$

Once  $\vec{q}(t + \Delta t/2)$  is computed, the matrices  $\mathbf{A}$  and  $\mathbf{Q}$  at the same time step can be calculated. On one hand, having  $\mathbf{A}(t + \Delta t/2)$  allows to go from the external coordinate system to the principal frame of reference. Thus, Equation 2.70 can be applied to calculate the angular momentum in the external coordinate system and, then, Equation 2.71 is used to express it in the principal frame of reference. Finally, the components of the angular velocity at half time step are obtained by means of Equation 2.72.

$$\vec{L}_e\left(t + \frac{\Delta t}{2}\right) = \vec{L}_e\left(t - \frac{\Delta t}{2}\right) + \Delta t \vec{\tau}(t) \quad (2.70)$$

$$\vec{L}_p\left(t + \frac{\Delta t}{2}\right) = \mathbf{A}^{-1}\left(t + \frac{\Delta t}{2}\right) \cdot \vec{L}_e\left(t + \frac{\Delta t}{2}\right) \quad (2.71)$$

$$\omega_{p,i}\left(t + \frac{\Delta t}{2}\right) = \frac{1}{I_{ii}} L_{p,i}\left(t + \frac{\Delta t}{2}\right) \quad (2.72)$$

On the other hand, having  $\vec{q}(t + \Delta t/2)$  also makes possible the calculation of  $\mathbf{Q}(t + \Delta t/2)$ . Then,  $\vec{q}(t + \Delta t)$  can be straightforward computed, as indicates Equation 2.73.

$$\vec{q}(t + \Delta t) = \vec{q}(t) + \Delta t \cdot \mathbf{Q}\left(t + \frac{\Delta t}{2}\right) \vec{\omega}\left(t + \frac{\Delta t}{2}\right) \quad (2.73)$$

### ***c) Implementation of the Constant Temperature and Pressure Constraints***

#### *c.1) Constant Temperature: Nosé-Hoover Thermostat*

The previously described equations of motion with its corresponding implementation in the leapfrog algorithm include no constraints for the external properties as temperature or pressure. It is very important to take into account such constraints in order to perform MD simulations at the different statistical ensembles. For instance, to simulate a canonical or NVT ensemble, the number of particles and volume are straightforward kept constant. Nevertheless, keeping the temperature constant requires a more sophisticated treatment. The Equipartition Theorem (Equation 2.74) relates the temperature of the system with the kinetic energy (or velocity) of the particles in the system. There are quite simple methods to keep the dynamics of the particles compatible with the desired temperature, as the velocity scaling method<sup>182</sup> or the Andersen approach.<sup>183</sup> In the case of the velocity scaling method, the strategy consists in scaling the velocities of the system by a factor, chosen to achieve the desired temperature. Despite the advantages related to its simplicity, this scaling method does not describe the NVT behaviour exactly, because, even if the temperature should be constant, the NVT ensemble presents energy fluctuations inversely proportional to the number of particles.

The Andersen method is based on the substitution of a random particle by a new velocity, sampled from a Maxwell-Boltzmann distribution. Even if the velocity distribution is chosen to be compatible with the desired  $T_0$ , the velocity substitution can lead to a dramatic change in the velocity of a particle in a single time step. Such substitution causes the dynamics obtained to be



different to the real dynamics of the system and makes the Andersen method unsuitable for the study of dynamical properties.

$$\left\langle \frac{1}{2} m v_i^2 \right\rangle = \frac{1}{2} k_B T \quad (2.74)$$

Extended Lagrangian methods are one of the most interesting approaches for NVT MD simulations.<sup>163a</sup> They consist on the inclusion of extra degrees of freedom in the Lagrangian of the system and, then, the new equations of motion are derived. For instance, the Nosé-Hoover method includes descriptors of the thermal bath as extra degrees of freedom.

The Nosé method<sup>184</sup> considers the physical system coupled with a thermal bath with effective mass  $W$  and a new degree of freedom ( $s$ ), which acts as a time scaling factor. The exchange of heat due to the interaction between the physical system and the thermal bath has an associated energy, which form is chosen to respect the microcanonical description. The inclusion of new degrees of freedom can be interpreted as a change on the boundaries of our system: instead of only considering the physical system, we are considering also the heat reservoir as part of our system. Therefore, artificial additional coordinates and velocities must be taken into account, as a consequence of the new degrees of freedom included.

The main idea of the Nosé extended-Lagrangian formulation is expressed in Equation 2.75 and 2.76 where  $\mathbb{L}_{Nosé}$  stands for the modified Lagrangian and  $C$  is a parameter to be determined later. Equations 2.77 are the definition of the conjugated moments.

$$\mathbb{L}_{Nosé} = \sum_{i=1}^N \frac{1}{2} m_i s^2 \dot{\vec{r}}_i^2 - U(\vec{r}^N) + \frac{W}{2} \dot{s}^2 - C k_B T \ln s \quad (2.75)$$

$$H_{Nosé} = \sum_{i=1}^N \frac{\vec{p}_i^2}{2m_i s^2} + U(\vec{r}^N) + \frac{p_s^2}{2W} + C k_B T \ln s \quad (2.76)$$

$$\begin{aligned} \vec{p}_i &= \frac{\partial \mathbb{L}}{\partial \dot{\vec{r}}_i} = m_i s^2 \dot{\vec{r}}_i \\ p_s &= \frac{\partial \mathbb{L}}{\partial \dot{s}} = W \dot{s} \end{aligned} \quad (2.77)$$

The Hamiltonian shown in Equation 2.76 is used to calculate the partition function  $Q_{\text{Nosé}}$  in Equation 2.78, where  $\vec{p}' = \vec{p}/s$ . If  $C=3N+1$ , the canonical ensemble functions are recovered.

$$Q_{\text{Nosé}} = \frac{C'}{N!} \int d\vec{p}'^N d\vec{r}^N \exp\left(-\frac{1}{k_B T} \frac{3N+1}{C} H(\vec{p}', \vec{r})\right)$$

$$C' = \frac{1}{Ck_B T} \int dp_s \exp\left(-\frac{3N+1}{Ck_B T} \frac{p_s^2}{2W}\right) \quad (2.78)$$

$$H(\vec{p}', \vec{r}) = \sum_{i=1}^N \frac{\vec{p}'_i{}^2}{2m_i} + U(\vec{r}^N)$$

Hoover carried out a simplification of Nosé's method, by introducing on the equations of motion the friction coefficient  $\xi$ , which will be treated as a new variable (Equation 2.79).

$$\xi = \frac{s' p_s'}{W} \quad (2.79)$$

Introducing the new variable  $\xi$  and dropping the primes, we get the new set of equations of motion collected on Equations 2.80-83.

$$\dot{\vec{r}}_i = \frac{\vec{p}_i}{m_i} \quad (2.80)$$

$$\dot{\vec{p}}_i = -\frac{\partial U(\vec{r}^N)}{\partial \vec{r}_i} - \xi \vec{p}_i \quad (2.81)$$

$$\dot{\xi} = \frac{1}{W} \left( \sum_{i=1}^N \frac{\vec{p}_i^2}{m_i} - Ck_B T \right) \quad (2.82)$$

$$\frac{\dot{s}}{s} = \frac{d \ln s}{dt} = \xi \quad (2.83)$$

The conserved quantity for these equations of motion is shown in Equation 2.84. It is worth noting that this quantity is conserved along the motion but is not properly a Hamiltonian, because no equations of motion can be derived from it.

$$H'_{Nosé} = \sum_{i=1}^N \frac{\vec{p}_i^2}{2m_i} + U(\vec{r}^N) + \frac{\xi^2 W}{2} + Ck_B T \ln s \quad (2.84)$$

Equations 2.80-82 form a closed set of unique equations that describes the motion of a system in the canonical ensemble with the correct scaling of time, while Equation 2.83 is redundant. Furthermore, Equation 2.82 can be manipulated using Equation 2.74 to achieve a more suitable expression for the interpretation of the parameter  $W$  (Equation 2.85). Hence,  $W$  can be interpreted as a parameter of the coupling with the thermal bath. For instance, for high values of  $W$ , the coupling will be small and, thus, the velocities only are altered with small changes each time step and the system is closer to the microcanonical ensemble. In contrast, if  $W$  is small, the coupling is strong and, then, the desired temperature is reached quickly. Usually, instead of manipulate the coupling between the physical system and the thermal bath by means of the effective mass  $W$ , a relaxation time is defined (Equation 2.86). In the simulations presented in this Thesis, the thermostat relaxation time is set to 0.02 ps.

$$\dot{\xi} = \frac{N_d k_B}{W} (T_{inst}(t) - T_0) \quad (2.85)$$

$$\tau_{therm}^2 = \frac{W}{N_d k_B T} \quad (2.86)$$

The implementation of the Nosé-Hoover equations of motion in the leapfrog algorithm is performed as it is shown on Equations 2.87-91. Those equations should be solved on an iterative way to self-consistency.

$$\xi(t + \Delta t/2) = \xi(t - \Delta t/2) + \Delta t \frac{N_d k_B}{T} (T_{inst}(t) - T_0) \quad (2.87)$$

$$\xi(t) = \frac{1}{2} (\xi(t - \Delta t/2) + \xi(t + \Delta t/2)) \quad (2.88)$$

$$\vec{v}(t + \Delta t/2) = \vec{v}(t - \Delta t/2) + \Delta t (a(t) - \xi(t) \vec{v}(t)) \quad (2.89)$$

$$\vec{v}(t) = \frac{1}{2} (\vec{v}(t - \Delta t/2) + \vec{v}(t + \Delta t/2)) \quad (2.90)$$

$$\vec{r}(t + \Delta t/2) = \vec{r}(t) + \Delta t \cdot \mathbf{v}(t + \Delta t/2) \quad (2.91)$$

### c.2) Constant Pressure: The Andersen Barostat

The constant temperature on the NVT ensemble is achieved by the coupling of the physical system to a thermal bath that alters somehow the velocities of particles in order to reach the desired temperature. In order to reproduce the dynamics of a physical system at constant pressure, as in the NPT ensemble, the coupling of the physical system with an external piston is introduced. This piston makes the volume of the box change isotropically in such a way that the internal pressure  $p_{\text{int}}$  reaches the desired reference pressure  $p_0$ . There are some methods to consider also cell shape variations, which are recommended for non-homogeneous systems. Nevertheless, in the simulations presented throughout this Thesis the cell is cubic and the variation in the volume is the same over the three coordinated axes. Andersen implemented the coupling with the piston as an extended Lagrangian method, in which the volume has been included as a new degree of freedom.<sup>183</sup> More precisely, DL\_POLY Classic package implements the Andersen method through the Martyna approach.<sup>185</sup>

The Andersen approach considers a scaling of the  $\vec{r}^N$  coordinates as it is indicated in Equation 2.92. The inclusion of the volume as a new degree of freedom adds two extra terms to the system Lagrangian: the kinetic and potential energy associated with the piston (the last two terms in Equation 2.92).

$$\vec{\rho}_i = \frac{\vec{r}_i}{V^{1/3}} \quad (2.92)$$

$$\mathbb{L}_{\text{And}} = \sum_{i=1}^N \frac{V^{2/3} m_i \vec{p}_i^2}{2} - U(V^{1/3} \vec{\rho}^N) + \frac{M}{2} \dot{V}^2 - P_0 V \quad (2.93)$$

From Equation 2.93, the new equations of motion are derived (Equations 2.95-97), in which Equation 2.94 has been used for the sake of simplicity.

$$\chi(t) = \frac{1}{3} \frac{d \ln V(t)}{dt} \quad (2.94)$$

$$\dot{\vec{r}}_i = \vec{v}_i + \chi \vec{r}_i \quad (2.95)$$

$$\dot{\vec{v}}_i = \frac{F(\vec{r}^N)}{m_i} - \chi \vec{v}_i \quad (2.96)$$

$$M\ddot{V} = -P_0 + \frac{1}{3V} \left( \sum_{i=1}^N m_i \vec{v}_i^2 + \sum_{i>j} \vec{r}_{ij} \vec{F}_{ij} \right) \quad (2.97)$$

Equation 2.97 can be interpreted as the Newton's Third Law for V, as it stands for a balance between the external pressure caused by the piston and the internal pressure caused by the physical system.

The Andersen barostat can be coupled to the Nosé-Hoover thermostat in order to reproduce the dynamics of a NPT system. DL\_POLY Classic performs such coupling by means of the Melchionna approach,<sup>186</sup> generating a new set of equations of motion (Equations 2.98-101).

$$\dot{\vec{r}}_i = \vec{v}_i + \chi(\vec{r}_i - \vec{R}_{CM}) \quad (2.98)$$

$$\dot{\vec{v}}_i = \frac{F(\vec{r}^N)}{m_i} - (\xi + \chi)\vec{v}_i \quad (2.99)$$

$$\dot{\xi} = \frac{N_d k_B}{W} (T_{inst}(t) - T_0) + \frac{1}{W} (M \chi^2 - k_B T) \quad (2.100)$$

$$\dot{\chi} = \frac{3V}{M} (P_{int}(t) - P_0) - \xi \chi \quad (2.101)$$

Analogously to Equation 2.86, a relaxation time for the barostat can be established (Equation 2.102).

$$\tau_{baros}^2 = \frac{M}{N_d k_B T_0} \quad (2.102)$$

The Andersen-Hoover methodology can also be implemented following the leapfrog algorithm. This implementation is summarised on Equations 2.103-110 and their integration should be performed in an iterative way for self-consistency.

$$\xi(t + \Delta t/2) = \xi(t - \Delta t/2) + \frac{\Delta t N_d k_B}{W} (T_{inst}(t) - T_0) + \frac{\Delta t}{W} (M \chi(t) - k_B T) \quad (2.103)$$

$$\xi(t) = \frac{1}{2} (\xi(t + \Delta t/2) + \xi(t - \Delta t/2)) \quad (2.104)$$

$$\chi(t + \Delta t/2) = \chi(t - \Delta t/2) + \Delta t \left( \frac{3V(t)}{M} (P_{int}(t) - P_0) - \chi(t) \xi(t) \right) \quad (2.105)$$

$$\chi(t) = \frac{1}{2} (\chi(t + \Delta t/2) + \chi(t - \Delta t/2)) \quad (2.106)$$

$$\vec{v}(t + \Delta t/2) = \vec{v}(t - \Delta t/2) + \Delta t (\vec{a}(t) - (\xi(t) + \chi(t)) \vec{v}(t)) \quad (2.107)$$

$$\vec{v}(t) = \frac{1}{2} (\vec{v}(t + \Delta t/2) + \vec{v}(t - \Delta t/2)) \quad (2.108)$$

$$\vec{r}(t + \Delta t) = \vec{r}(t) + \Delta t (\vec{v}(t + \Delta t/2) + \chi(t + \Delta t/2) (\vec{r}(t + \Delta t/2) - \vec{R}_{CM})) \quad (2.109)$$

$$\vec{r}(t + \Delta t/2) = \frac{1}{2} (\vec{r}(t) + \vec{r}(t + \Delta t)) \quad (2.110)$$

Finally, from Equation 2.94 it is possible to calculate the volume for the next time step, as it is shown in Equation 2.111.

$$V(t + \Delta t) = V(t) \exp(3\chi(t + \Delta t/2)) \quad (2.111)$$

### 2.3.2 - Classical Molecular Dynamics Simulations with POMs

There are several examples in the literature about classical MD techniques applied on POM systems, as MD methods are suitable to study the interaction of POMs with solvents and different species present in solution. For instance, Classical MD simulations have been performed to analyze the behaviour of POMs forming dendrizymes<sup>187</sup> or in the presence of organic dendrimers.<sup>188</sup>

The interaction of POMs with the solvent has also gained relevance. López et al. analysed the hydrogen bond formation at different oxygen sites of a Keggin

anion in aqueous solution.<sup>16c</sup> Furthermore, the presence of cationic species in solution affects the behaviour of POMs. In 2008, ion pairs between Keggin anions and monovalent cations were characterised for the first time.<sup>147</sup> Moreover ion pairs, the presence of cations in solution can also lead to the formation of POM assemblies.<sup>177, 189</sup>

MD simulations have been also been used to study the adsorption of POMs on surfaces. For example, Aparicio-Anglès et al. proposed a reduction mechanism for the  $[\alpha\text{-SiW}_{12}\text{O}_{40}]^{4-}$  Keggin on a silver surface in the presence of potassium cations.<sup>16a</sup> By means of MD the authors studied the location of the cations and their exchange with the bulk. Then, these configurations were used to analyse the electronic structure by means of DFT.

The study of encapsulated species in POMs is an important research field in the MD domain. For instance, Miró and co-workers studied the water and counter-ion structures that surround different U systems, namely,  $[\text{U}^{\text{VI}}\text{O}_2]^{2+}$ ,  $[(\text{U}_{\text{VI}}\text{O}_2)_2(\mu^2\text{-O}_2)]^{2+}$ ,  $[(\text{U}_{\text{VI}}\text{O}_2)_5(\mu^2\text{-O}_2)_5]$ , and  $[(\text{U}^{\text{VI}}\text{O}_2)_{20}(\mu^2\text{-O}_2)_{30}]^{20-}$ .<sup>190</sup> The authors conclude that the latter system encapsulates an ice-like water cluster. Furthermore, Fernández et al. analysed the  $\text{Mo}_{57}\text{V}_6$  system, namely,  $[\text{H}_8\text{Mo}_{57}\text{V}_6(\text{NO}_6)\text{O}_{183}(\text{H}_2\text{O})_{18}]^{21-}$ , by means of DFT.<sup>16b</sup> Then, the authors used MD simulations in order to study the behaviour of the 18 water encapsulated in different conditions. Fernández and co-workers showed that these encapsulated water molecules form a high ordered structure over a wide range of temperatures, which influence the interaction with the cations. The  $\text{Mo}_{57}\text{V}_6$  system can be compared with the  $\text{Mo}_{132}$  Keplerate, because of the similar building blocks and the  $(\text{metal})_6\text{O}_6$  type pores with crown ether-like structure. Regarding the  $\text{Mo}_{132}$  capsule, which is the main topic of this Thesis, several articles analysing the properties of the encapsulated water molecules by means of MD have been published in recent years. Particularly, our group has contributed to this topic studying the behaviour of water molecules confined in  $\text{Mo}_{132}$  capsules with different inner decorations.<sup>12a</sup> The fact of having formate or sulphate ligands changes the cavity sizes, which influences the packing density of the water molecules encapsulated. In both cases these 100 water molecules encapsulated exhibit a concentric layered structure with icosahedral symmetry when cations are prevented to enter into the capsule. In the case of formate inner decoration, as the ligands are smaller, four shells are found, two of them with under-occupation. In contrast, sulphate inner ligands only allow

the formation of three shells and the cavity is completely filled. Furthermore, under encapsulation, the three-dimensional hydrogen bond network of bulk water is distorted, leading to the concentric layered structure of water.<sup>12b</sup> The water molecules of these layers form three hydrogen bonds, while the remaining one links different layers and the hydrophilic POM inner surface. Also, the dynamics of the confined water molecules show that almost no exchange between layers is observed. In addition, when cavities with formate and sulphate ligands are compared, additional degrees of freedom are found in the formate case, making the encapsulated water to behave in a more liquid-like way.<sup>12c</sup> Moreover, our group has also contributed to the study of the case of Mo<sub>132</sub> with acetate ligands, regarding the capsule as a nanoreactor where catalytic reactions can take places.<sup>11b</sup> The catalytic behaviour is achieved by means of the controlled removal of the acetate ligands, which are substituted by labile water ligands. MD techniques were used to check the lability of different ligands and the influence that such effect has on the ability of methyl tert-butyl ether to enter the capsule.



UNIVERSITAT ROVIRA I VIRGILI

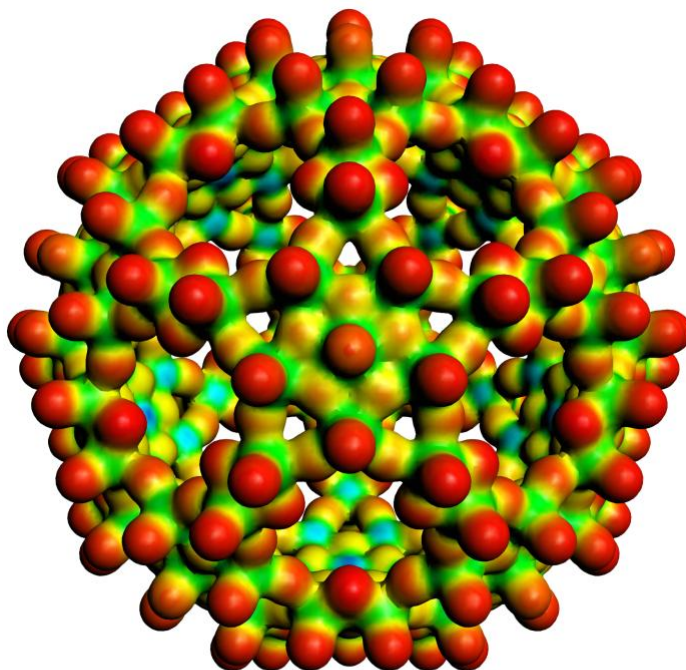
KEPLERATES: FROM ELECTRONIC STRUCTURE TO DYNAMIC PROPERTIES.

María Dolores Melgar Freire

Dipòsit Legal: T 258-2016

## Chapter 3: Electronic Structure of Keplerates

---



UNIVERSITAT ROVIRA I VIRGILI

KEPLERATES: FROM ELECTRONIC STRUCTURE TO DYNAMIC PROPERTIES.

María Dolores Melgar Freire

Dipòsit Legal: T 258-2016

## 3.1 - Introduction

Giant molecules, with hundreds of atoms, are a big challenge for electronic structure studies. However, Keplerates, considered as giant molecules due to its nanometric size, present icosahedral symmetry. Therefore, their computational requirements are considerably reduced, making possible to perform DFT calculations on this type of molecules. In former studies carried out in our group,<sup>44</sup> DFT methodology has been employed to study the electronic structure of two Keplerate capsules, namely  $\text{Mo}_{132}(\mu\text{-O})_2$ <sup>191</sup> and  $\text{W}_{72}\text{Mo}_{60}(\mu\text{-O})_2$ .<sup>192</sup> Our group used the Amsterdam Density Functional software (ADF2009)<sup>118</sup> and the VWN functional, together with TZP basis for the metal centres and DZP for the remaining atoms. Relativistic corrections were included with ZORA.<sup>193</sup> Guanidinium counter-cations were included in order to avoid the positive orbitals energy characteristic of an anion in the gas phase. After the optimisation of the structures at the gas phase, subsequent single point calculations with COSMO<sup>194</sup> as solvent model have been performed.

In the last years, new Keplerates systems were synthesised. For instance, the sulphur-bridge variants  $\text{Mo}_{132}(\mu\text{-S})_2$ <sup>42</sup> and  $\text{W}_{72}\text{Mo}_{60}(\mu\text{-S})_2$ <sup>195</sup> and the mixed oxide/sulphide  $\text{W}_{72}\text{Mo}_{60}(\mu\text{-O})(\mu\text{-S})$ .<sup>196</sup> Even if it has not been synthesised yet, theoretical analysis of the  $\text{W}_{132}$  system can be also be performed. Furthermore, Leclerc et al. found that in mixed W and Mo pentagons, the W atom is preferably found at the central position of the mixed pentagonal units  $[\text{W}(\text{Mo}_5)]$ .<sup>197</sup> This motivates the study of these pentagonal units in the Keplerate geometry  $\text{W}_{12}\text{Mo}_{120}$ . Also, Cronin suggested the possibility of the existence of a fully oxidised the  $\text{Mo}_{132}(\mu\text{-O})_2$  capsule. Thus, it makes sense to perform a systematic study at the DFT level of the electronic structure of different examples of Keplerates.

Furthermore, we wanted to use the geometry and the charge distribution from these DFT calculations to perform Molecular Dynamics simulations. Former studies have been published, with the participation of our research group, using Molecular Dynamics to analyse the layered structure that water molecules form inside the  $\text{Mo}_{132}$  capsule. In this case, a geometry extracted from X-ray experiments and a semiempirical parameterization for the point

charges distribution have been used. The study presented in this chapter allows us to use the results from DFT (geometry and charge distribution) as input parameters for subsequent Molecular Dynamics simulations.

The present ability to perform geometry optimizations of such big molecules as Keplerates with a continuum solvent model, the new Keplerate systems synthesised in the last years and the aim to use the DFT results to improve Molecular Dynamics simulations are the main motivations to perform the studies presented in this chapter.

### 3.1.1 - Goals

New Keplerates are coming. Thus, we present in this chapter a systematic study of the Keplerate family to analyse the electronic structure of these systems. Therefore, the main goals of this chapter are:

- Analysis of the effects on the electronic structure of the already known Keplerates when some variations in the capsule components take place:
  - W/Mo ratio on the metal-oxo framework
  - S or O bridging sites at the linkers
  - Presence of different bidentate ligands
  - Inclusion of coordination waters on the DFT calculations
- Prediction the theoretical stability in terms of electronic structure of some Keplerate systems that have been not reported in the literature at the moment.
  - $W_{132}$
  - $W_{12}Mo_{120}$
  - Fully oxidised  $Mo_{132}$

## 3.2 - Computational Details

The standard computational methodology used throughout this chapter consists in performing full geometry optimizations by means of the Amsterdam Density Functional program (ADF2012).<sup>118</sup> With this purpose, the GGA BP86 functional has been used together with a TZP basis. Also, relativistic corrections were introduced by scalar-relativistic zero-order regular approximation (ZORA<sup>193</sup>) and the solvent was represented by the continuum model COSMO<sup>194</sup>. The atomic radii values correspond to the Van der Waals radii from the MM3 method by Allinger<sup>198</sup> divided by 1.2. The numerical integration parameter which controls the precision of numerical integrals has been set to 4.5.

Few calculations related to this chapter were performed at a different DFT level. In those cases, it will be indicated when presented.

## 3.3 - Results

### 3.3.1 - Effects of the DFT functional and the COSMO model

In the precedent study about the electronic structure of Keplerates,<sup>44</sup> the optimization of the electron density has been not carried out including solvent effects. In order to perform a systematic study of the Keplerate family, the first step consists in making a decision about the DFT level that better fits our needs. With this purpose, full geometry optimizations of a set Keplerate systems are performed, namely:  $\text{Mo}_{132}(\mu\text{-O})_2$ ,<sup>191</sup>  $\text{Mo}_{132}(\mu\text{-S})_2$ ,<sup>42</sup>  $\text{W}_{72}\text{Mo}_{60}(\mu\text{-O})_2$ <sup>192</sup> and  $\text{W}_{72}\text{Mo}_{60}(\mu\text{-S})_2$ .<sup>195</sup> Those Keplerates were chosen because of their representative composition and their already known structure by means of X-ray experiments. Four geometry optimizations were performed for each system at different DFT levels, with LDA VWN and GGA BP86 functionals, both with and without COSMO solvent model. All these calculations were carried under constraints of the  $D_{5d}$  point symmetry group. Then, we compare our DFT optimised geometry with the experimental geometry reported. Such comparison was performed evaluating a set of interatomic distances and comparing those values with the ones extracted from the X-ray geometry, by

means of the statistical variance ( $\sigma^2$ ), whose expression corresponds to Equation 3.1. In this equation,  $n$  represents the number of interatomic distances taken into account,  $x_i$  stands for the value of such distances from the DFT calculations and  $\mu$  is the mean value extracted from X-ray results.

$$\sigma^2 = \frac{1}{n} \sum_{i=1}^n (x_i - \mu)^2 \quad (3.1)$$

Tables 3.1-4 show the interatomic distances considered to compute the statistical variance. In these tables, when more than one value is present, they represent the minimum and the maximum value obtained for the given distance. Furthermore, the  $\sigma^2$  values obtained for each optimization are included. The minimum value for  $\sigma^2$  is highlighted in italics. Figure 3.1 explains the labels used to represent the interatomic distance.  $M^{\text{central}}$  represents the central metal centre on the pentagon, while  $M_{\text{penta}}$  are the remaining metal centres on the pentagon and  $M_{\text{linker}}$  the ones on the linker.  $O_{\text{penta}}$  are the oxygen atoms that link metal centres on the pentagon, while  $O_{\text{linker}}$  are the ones which join the pentagon and the linker units.  $O_{\text{term}}$  stand for the terminal oxygens, which can belong to both the linker and the pentagon. The bridge positions of the linkers can be represented by  $O_{\text{bridge}}$  or  $S_{\text{bridge}}$ , depending on the Keplerate composition. The diameter of the capsule was interpreted as the distance between the terminal oxygens of the central atoms of two opposite pentagons.

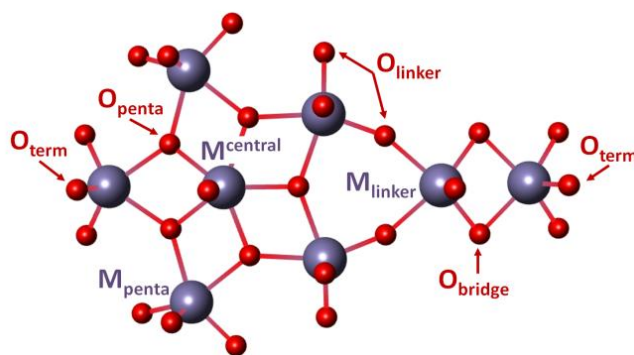


**Figure 3.1:** Schematic representation of the pentagon-linker moiety present on Keplerates, where the nomenclature used on Tables 1-4 has been highlighted. It is worth noting that the metal centre positions can be occupied by W or Mo atoms depending on the system. Also, there are some examples of Keplerates where the  $O_{\text{bridge}}$  has been substituted by  $S_{\text{bridge}}$ .

**Table 3.1:**  $\text{Mo}_{132}(\mu\text{-O})_2$  selected interatomic distance in Å and their statistical variance relative to the X-ray mean value (not shown) for different DFT levels.

$\text{Mo}_{132}(\mu\text{-O})_2$	LDA	LDA (COSMO)	GGA	GGA (COSMO)
$\text{Mo}^{\text{central}}\text{-O}_{\text{penta}}$	2.01	2.01	2.04	2.03-2.04
$\text{Mo}_{\text{penta}}\text{-O}_{\text{penta}}$	2.09	2.07	2.12	2.10-2.11
$\text{Mo}_{\text{penta}}\text{-O}_{\text{term}}$	1.71	1.71	1.72	1.72-1.73
$\text{Mo}^{\text{central}}\text{-O}_{\text{term}}$	1.70	1.69-1.70	1.71	1.709
$\text{Mo}_{\text{penta}}\text{-O}_{\text{linker}}$	1.81	1.81-1.82	1.83	1.83
$\text{Mo}_{\text{linker}}\text{-O}_{\text{linker}}$	2.03	2.01	2.06	2.05-2.06
$\text{Mo}_{\text{linker}}\text{-Mo}_{\text{linker}}$	2.61-2.62	2.61-2.62	2.65-2.66	2.64
$\text{Mo}_{\text{linker}}\text{-O}_{\text{term}}$	1.70	1.70-1.71	1.71-1.72	1.72
$\text{Mo}_{\text{linker}}\text{-O}_{\text{bridge}}$	1.94	1.94	1.96	1.96
$\text{O}_{\text{bridge}}\text{-O}_{\text{bridge}}$	2.74	2.77	2.77	2.79
<i>Diameter</i>	29.06-29.07	28.99-29.98	29.40-29.41	29.52
$\sigma^2$	<b>0.000329</b>	<b>0.0496</b>	<b>0.00594</b>	<b>0.00284</b>

**Table 3.2:**  $\text{Mo}_{132}(\mu\text{-S})_2$  selected interatomic distance in Å and their statistical variance relative to the X-ray mean value (not shown) for different DFT levels.

$\text{Mo}_{132}(\mu\text{-S})_2$	LDA	LDA (COSMO)	GGA	GGA (COSMO)
$\text{Mo}^{\text{central}}\text{-O}_{\text{penta}}$	2.01	2.00	2.03	2.03
$\text{Mo}_{\text{penta}}\text{-O}_{\text{penta}}$	2.07-2.08	2.06-2.07	2.11	2.10
$\text{Mo}_{\text{penta}}\text{-O}_{\text{term}}$	1.71	1.71	1.72	1.7
$\text{Mo}^{\text{central}}\text{-O}_{\text{term}}$	1.69	1.69-1.70	1.71	1.711
$\text{Mo}_{\text{penta}}\text{-O}_{\text{linker}}$	1.81	1.81	1.83	1.83
$\text{Mo}_{\text{linker}}\text{-O}_{\text{linker}}$	2.04	2.03	2.09	2.08
$\text{Mo}_{\text{linker}}\text{-Mo}_{\text{linker}}$	2.85-2.85	2.84-2.85	2.91	2.91
$\text{Mo}_{\text{linker}}\text{-O}_{\text{term}}$	1.70	1.70	1.71	1.72
$\text{Mo}_{\text{linker}}\text{-S}_{\text{bridge}}$	2.33	2.33	2.36	2.36
$\text{S}_{\text{bridge}}\text{-S}_{\text{bridge}}$	3.58	3.60	3.61	3.63
<i>Diameter</i>	29.82-29.87	29.82-29.59	30.30-30.34	30.40-30.42
$\sigma^2$	<b>0.00205</b>	<b>0.00581</b>	<b>0.00188</b>	<b>0.00634</b>



**Table 3.3:**  $W_{72}Mo_{60}(\mu-O)_2$  selected interatomic distance in Å and their statistical variance relative to the X-ray mean value (not shown) for different DFT levels.

$W_{72}Mo_{60}(\mu-O)_2$	LDA	LDA (COSMO)	GGA	GGA (COSMO)
$W^{central}-O_{penta}$	2.00	2.00	2.03	2.03
$W_{penta}-O_{penta}$	2.09	2.07	2.12	2.11
$W_{penta}-O_{term}$	1.72	1.72	1.73-1.74	1.74
$W^{central}-O_{term}$	1.71	1.71	1.72	1.72
$W_{penta}-O_{linker}$	1.81	1.81	1.82-1.83	1.83
$MO_{linker}-O_{linker}$	2.04	2.03	2.09	2.07-2.08
$MO_{linker}-MO_{linker}$	2.59	2.58	2.63	2.62
$MO_{linker}-O_{term}$	1.70	1.70-1.71	1.71	1.72
$MO_{linker}-O_{bridge}$	1.93-1.94	1.94	1.95-1.96	1.96
$O_{bridge}-O_{bridge}$	2.75	2.77-2.78	2.78	2.82
<b>Diameter</b>	<b>28.94-28.97</b>	<b>28.91-28.96</b>	<b>29.41-29.42</b>	<b>29.47-29.50</b>
$\sigma^2$	<b>0.00165</b>	<b>0.00321</b>	<b>0.0152</b>	<b>0.00315</b>

**Table 3.4:**  $W_{72}Mo_{60}(\mu-S)_2$  selected interatomic distance in Å and their statistical variance relative to the X-ray mean value (not shown) for different DFT levels.

$W_{72}Mo_{60}(\mu-S)_2$	LDA	LDA (COSMO)	GGA	GGA (COSMO)
$W^{central}-O_{penta}$	2.00	2.00	2.03	2.03
$W_{penta}-O_{penta}$	2.08	2.07	2.12	2.11
$W_{penta}-O_{term}$	1.72	1.73	1.74	1.74
$W^{central}-O_{term}$	1.71	1.71	1.72	1.72
$W_{penta}-O_{linker}$	1.81	1.81	1.82-1.83	1.83
$MO_{linker}-O_{linker}$	2.06	2.05	2.11	2.10
$MO_{linker}-MO_{linker}$	2.83-2.84	2.83-2.84	2.89-2.90	2.90
$MO_{linker}-O_{term}$	1.70	1.70-1.71	1.71	1.72
$MO_{linker}-O_{bridge}$	2.32-2.33	2.33	2.35	2.35-2.36
$S_{bridge}-S_{bridge}$	3.58	3.59-3.60	3.61	3.62
<b>Diameter</b>	<b>29.92-29.95</b>	<b>29.91-29.93</b>	<b>30.40-30.46</b>	<b>30.50-30.51</b>
$\sigma^2$	<b>0.000719</b>	<b>0.00376</b>	<b>0.000684</b>	<b>0.00418</b>

Considering the statistical variance values showed on Tables 3.1-4, the lower values and, thus, the best fitting with X-ray results, is for LDA or GGA functionals, depending on the system. But all the  $\sigma^2$  values are almost of the same order of magnitude and quite low for all the cases studied. Furthermore, the largest absolute change with respect X-ray results are related to the diameter of the capsule. Even if the difference is larger than for other interatomic distances, the relative error is smaller, because diameter is one order of magnitude larger than the other interatomic distance considered. Nevertheless, the presence of a continuum solvent model is needed to place the electronic levels at a proper energy value.<sup>199</sup> Otherwise, at the gas phase, the electronic levels of the anion will be positive, in total disagreement with experimental electrochemical results. This COSMO effect is shown in Table 3.5, comparing the electronic levels energy of the calculations with and without solvent model.

**Table 3.5:** HOMO, LUMO and the corresponding gap values (in eV) for the four Keplerates analysed at different DFT levels.

	LDA			LDA (COSMO)		
	HOMO	LUMO	Gap	HOMO	LUMO	Gap
$Mo_{132}(\mu-O)_2$	4.6	5.6	<b>1.0</b>	-5.6	-4.6	<b>1.1</b>
$W_{72}Mo_{60}(\mu-O)_2$	4.6	6.0	<b>1.4</b>	-5.7	-4.1	<b>1.6</b>
$Mo_{132}(\mu-S)_2$	4.3	5.7	<b>1.4</b>	-5.8	-4.3	<b>1.5</b>
$W_{72}Mo_{60}(\mu-S)_2$	4.2	6.1	<b>1.8</b>	-5.8	-3.9	<b>1.9</b>
	GGA			GGA (COSMO)		
	HOMO	LUMO	Gap	LUMO	HOMO	Gap
$Mo_{132}(\mu-O)_2$	4.6	5.7	<b>1.0</b>	-5.6	-4.5	<b>1.1</b>
$W_{72}Mo_{60}(\mu-O)_2$	4.5	6.0	<b>1.5</b>	-5.7	-4.0	<b>1.6</b>
$Mo_{132}(\mu-S)_2$	4.3	5.7	<b>1.4</b>	-5.7	-4.3	<b>1.5</b>
$W_{72}Mo_{60}(\mu-S)_2$	4.2	6.0	<b>1.9</b>	-5.8	-3.9	<b>1.9</b>

Table 3.5 shows that, with COSMO, LDA and GGA functionals give the same results in terms of HOMO-LUMO gaps. It is worth noting that GGA functionals, even if, generally, they do not give very accurate results in terms of absolute energy values, they are quite good at describing electronic structure and gap trends. Our systematic study has the main goal to compare the electronic structure among the Keplerate family. Hence, we are more concerned about the HOMO-LUMO trend than about the exact energy values. For those reasons,

the DFT level chosen to perform such study will involve a GGA functional (BP86) together with the COSMO continuum solvent model. Furthermore, this is the highest DFT level that we can reach for these systems nowadays.

### 3.3.2 - Electronic Structure of Well-Known Keplerate Systems

The electronic structure of Keplerates is a good example of the typical profile of polyoxometalates. One of the most useful tools to study the electronic structure is the Density of States (DOS). The DOS is a function that represents the number of electronic levels per energy unit. In the case of atoms or small molecules, the distribution of energy levels is discrete. In the case of solids, the contribution of the different units overlaps, resulting on a band structure. Keplerates are discrete molecules, but with a huge number of atoms and electrons. Such electron population leads to an overlap of electronic levels similar to the one observed in solids. The Total Density of States (TDOS) includes all the energy levels available for the molecule. In contrast, the Partial Density of States (PDOS) gives the contribution to the TDOS of a specific type of atom.

Figure 3.2 shows, as an example, the  $\text{Mo}_{132}$  DOS from -30 eV to 10 eV. The deepest band in Figure 3.2 corresponds to the 2s orbitals from the oxygen atoms (Figure 3.3a). Figure 3.2 also shows the characteristic oxo-band of polyoxometalates. The oxo-band includes the p orbitals of the different oxygen atoms types present on  $\text{Mo}_{132}$  (Figure 3.3b, c, d, and e). The HOMO band is composed of the 60 d orbitals of the  $\text{Mo}^{\text{V}}$  atoms of the 30 linkers. Those orbitals form the metal-metal bond between the linker metal centres (Figure 3.3f). Finally, the LUMO band includes all the d orbitals from the pentagon Mo atoms (Figure 3.3g).

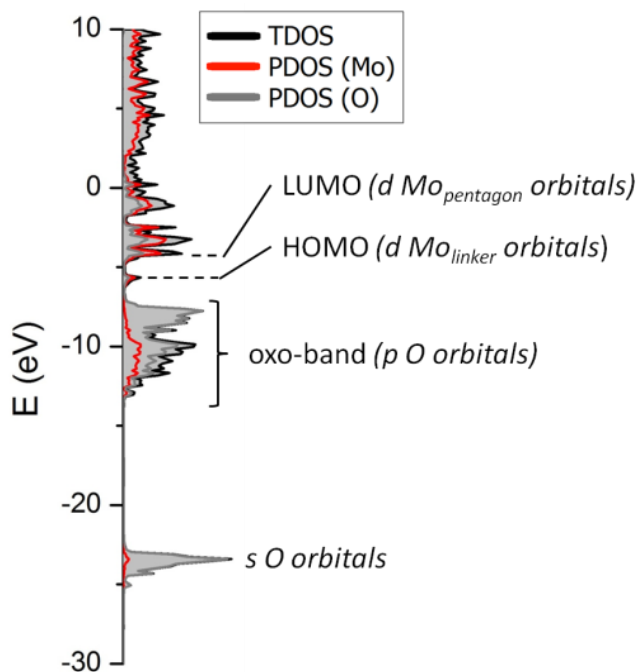


**Figure 3.2:** Representation of the  $\text{Mo}_{132}$  DOS as a function of the energy. The energy range comprises from -30eV to 10eV. Total Density of States (black) and Partial Density of States (red for Mo and grey for O) are represented together.

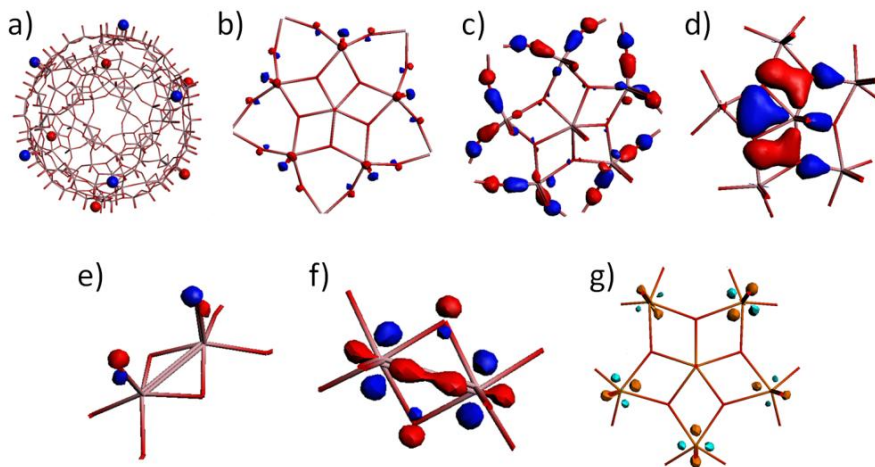


**Figure 3.3:** Examples of different types of  $\text{Mo}_{132}$  orbitals. **a)** *s* oxygen orbitals, corresponding to the deepest band on Figure 3.2. **b, c, d, e)** *p* oxygen orbitals belonging to the oxo-band. **f)** HOMO band orbital, corresponding to the metal-metal bond, which involves the *d* orbitals of the linker Mo atoms. **g)** LUMO orbital related to the *d* orbitals of the pentagon Mo atoms. Note that for the LUMO orbital different colours were used to highlight the fact that this is a non-occupied orbital.

$\text{Mo}_{132}(\mu\text{-O})_2$  is the most well-known Keplerate, but some changes in its composition can lead to other family members (Figure 3.4). For example, if the pentagonal metal centres are changed from Mo to W, the resulting structure is the  $\text{W}_{72}\text{Mo}_{60}(\mu\text{-O})_2$  system. For both  $\text{Mo}_{132}$  and  $\text{W}_{72}\text{Mo}_{60}$  capsules, bridges positions on the linkers can be substituted from O to S, reducing the pore size.

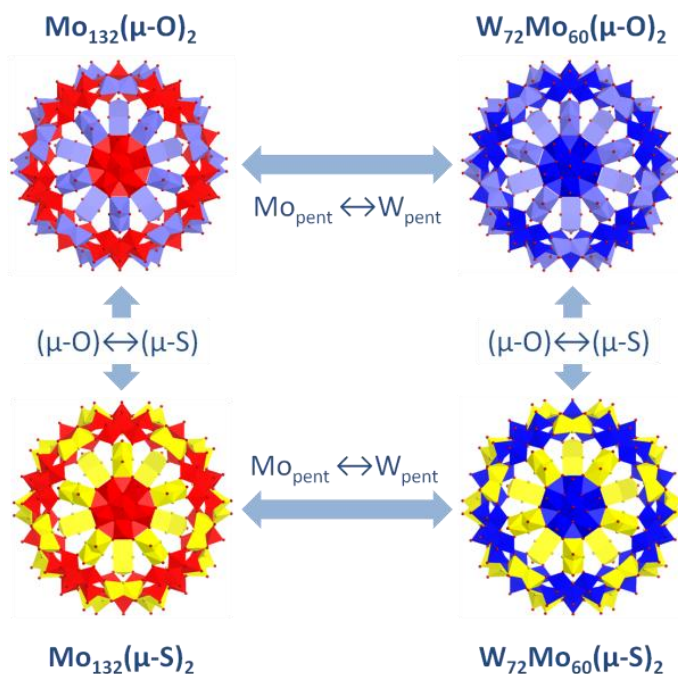


**Figure 3.4:** Schematic representations of the differences between four members of the Keplerate family. Red moieties represent Mo based pentagons; while dark blue is reserved for the W based ones. Light blue linkers are the ones with oxo-bridges, while the yellow linkers, these oxygen atoms have been substituted by sulphur.

Furthermore, in 2013 a mixed sulphur-oxo bridges Keplerate was synthesised for the first time.<sup>196</sup> In the case of this mixed-bridges Keplerate, Schäffer and co-workers were able to obtain an X-ray structure. The X-ray data presents crystallographic disorder in the bridge positions, while the metal-metal bond distance was the same for all the linkers. In other words: all the linkers are composed by one sulphur- and one oxo-bridge. The inherent disorder leads to different isomeric possibilities.

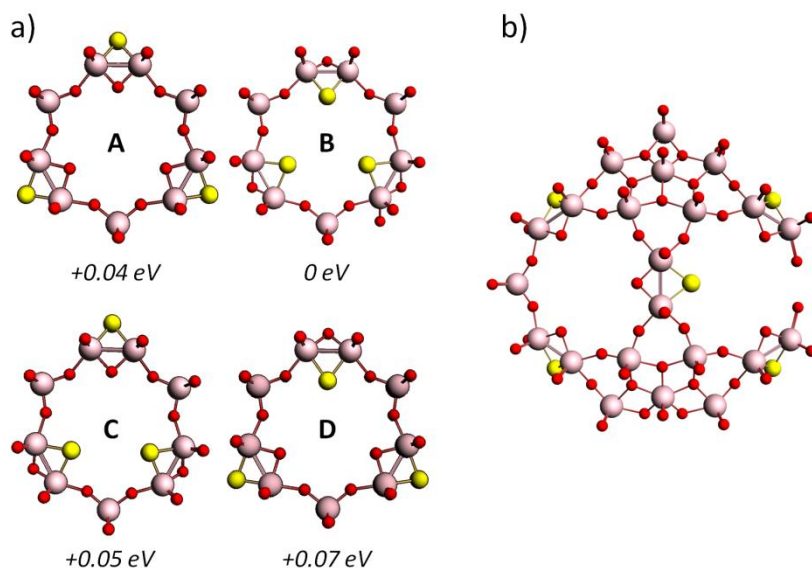


**Figure 3.5:** a) Schematic representation of the different pore possibilities with the mixed-bridges linkers. The complete structure used on the geometry optimizations comprises the three pentagons and the three linkers surrounding the pore. The energies in eV represent the difference between the most stable configuration (B) and the remaining possibilities. b) Representation of the irreducible fragment used to generate the  $S_6$  symmetric Keplerates with mixed bridges. Note that this unit can be described by means of the combination of two pores. The fragment shown in this figure is an A+D structure.

**Table 3.6:** Bonding energy and HOMO-LUMO gap (in eV) for different examples of the computed mixed-bridges Keplerates. The bonding energy values are referred to the first system, which is the one that shows the lowest value.

Irreducible Fragment	Pore Composition (#A, #B, #C, #D)	Bonding Energy (eV)	HOMO-LUMO gap (eV)
B+C	(8,6,6,0)	0	1.76
A+B	(6,2,12,0)	+0.4	1.74
A+C	(2,6,12,0)	+0.6	1.73
B+D	(2,0,12,6)	+0.1	1.75
C+C	(2,0,12,6)	+0.4	1.74
C+A	(6,2,12,0)	+0.4	1.73

**Table 3.7:** Comparison between the experimental X-ray and theoretical DFT (GGA BP86 with COSMO) results in terms of evaluating a set of interatomic distances. The labels for this distance are explained in Figure 3.1. When two distances appear, they represent the maximum and the minimum value founded for the DFT results. Also, the  $\sigma^2$  value has been highlighted in bold.

$W_{72}Mo_{60}(\mu-O)(\mu-S)$	Experimental	GGA (COSMO)
$W_{central}^{central}-O_{penta}$	2.02	2.02-2.03
$W_{penta}^{penta}-O_{penta}$	2.05	2.09-2.12
$W_{penta}^{penta}-O_{term}$	1.71	1.74
$W_{central}^{central}-O_{term}$	1.54	1.72
$W_{penta}^{penta}-O_{linker}$	1.79	1.82-1.83
$MO_{linker}^{linker}-O_{linker}$	2.07	2.01-2.12
$MO_{linker}^{linker}-MO_{linker}$	2.68	2.73-2.74
$MO_{linker}^{linker}-O_{term}$	1.66	1.72
$MO_{linker}^{linker}-O_{bridge}$	1.89	1.95-1.96
$MO_{linker}^{linker}-S_{bridge}$	2.36	2.36
$S_{bridge}^{bridge}-O_{bridge}$	3.24	3.23-3.24
Diameter	28.68	29.72-29.84
$\sigma^2$		<b>0.0122</b>

In order to evaluate if there is a preferred structure among the mixed-bridge isomers, the stability in terms of bonding energy of the different pore configurations is evaluated, taking into account all the possible combinations for the linker bridges (Figure 3.5a). The complete optimised pore systems comprises three pentagonal units  $[(Mo^{VI})Mo^V_5O_{21}]$  and three linker moieties  $[Mo^V_2O_2(\mu-O)(\mu-S)]$ , resulting in a charge of -12. The bonding energy for these four pores is pretty much the same, which means that all the possibilities should be equally likely. Therefore, any combination of the mixed-bridges linkers will lead to Keplerates with equivalent stability. To check such hypothesis, some examples of the mixed-bridges Keplerate are studied. The systems chosen have a different proportion of the pores described in Figure 3.5a. The Keplerate structures were generated from the irreducible unit that leads to the highest symmetry possible ( $S_6$ ). The irreducible fragment can be described in terms of two types of pores, whose combination lead to the structure shown in Figure 3.5b. There are 14 pore combinations possible, resulting in 10 different systems and 2 pairs of chiral structures. As the ADF software does not allow performing optimizations under the constraint of a  $S_6$  point symmetry group,  $C_1$  was used instead. Table 3.6 collects the information

about bonding energy and HOMO-LUMO gap for some examples of these mixed structures studied. Results from Table 3.6 show that the stability of mixed-bridges systems is pretty much the same. Thus, in order to study the electronic structure, the system of the first row in Table 3.6 will be taken as a representative example. The geometry of such system was compared with the X-ray results from Schäffer et al. with the same procedure followed for Tables 3.1-4 (Table 3.7).

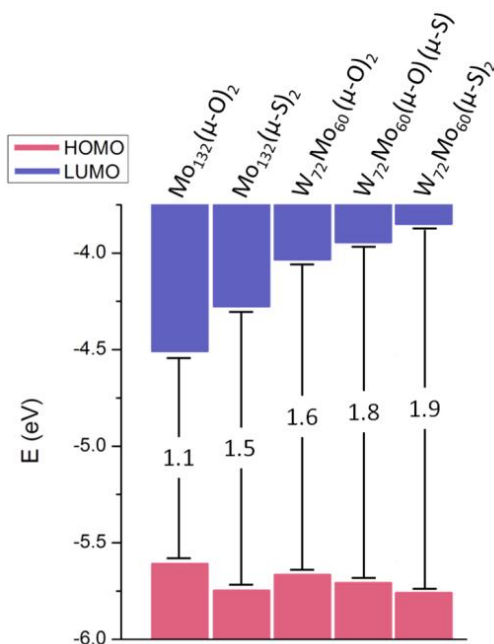
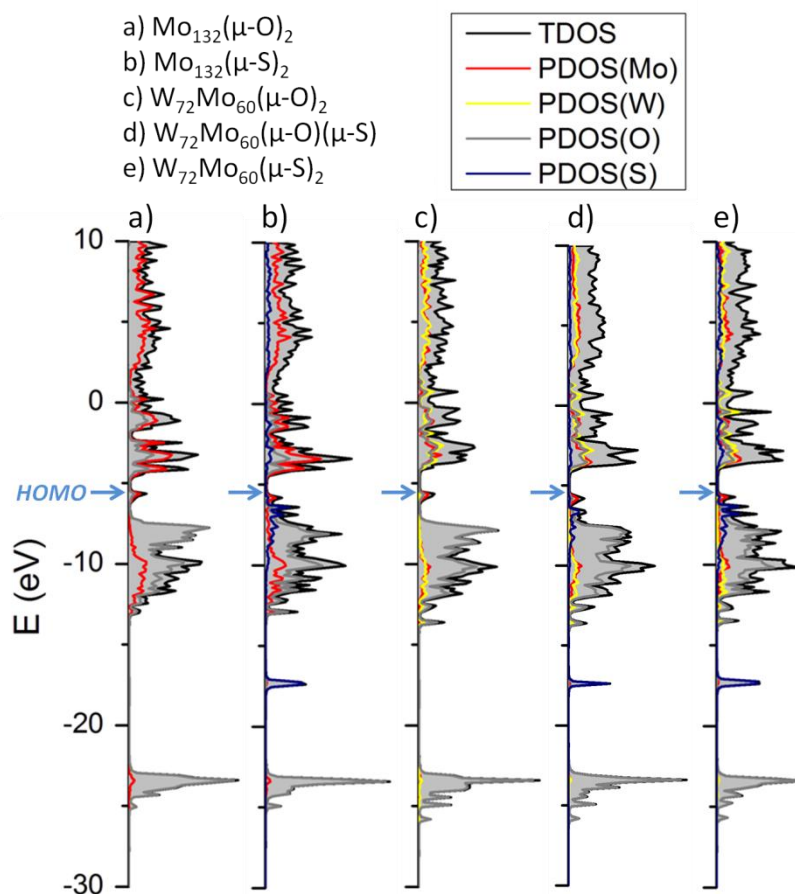


**Figure 3.6:** HOMO (pink) and LUMO (violet) energies (in eV) and its corresponding gap value for the Mo<sub>132</sub> and W<sub>72</sub>Mo<sub>60</sub> systems with bridge positions occupied by O or S atoms.

Figure 3.6 shows how the ratio of W/Mo in the pentagonal units and S and/or O bridges in the linkers affect the HOMO-LUMO gap and, then, the stability of the system: the gap increases with the presence of W and S. The presence of W makes the LUMO level higher, because this level is related to the d orbitals of the metal centres on the pentagon (Figure 3.3g). As the LUMO energy is less negative than in the case of Mo-Mo linker bonds, the W-W bond would be easier to oxidise. The fact of having sulphur-bridges in the linkers makes the HOMO level decrease, as the HOMO level is related to the metal-metal bond on the linkers. When there are sulphur-bridges, the distances between these two metal centres changes from 2.64 Å to 2.91 Å, making the metal-metal bond



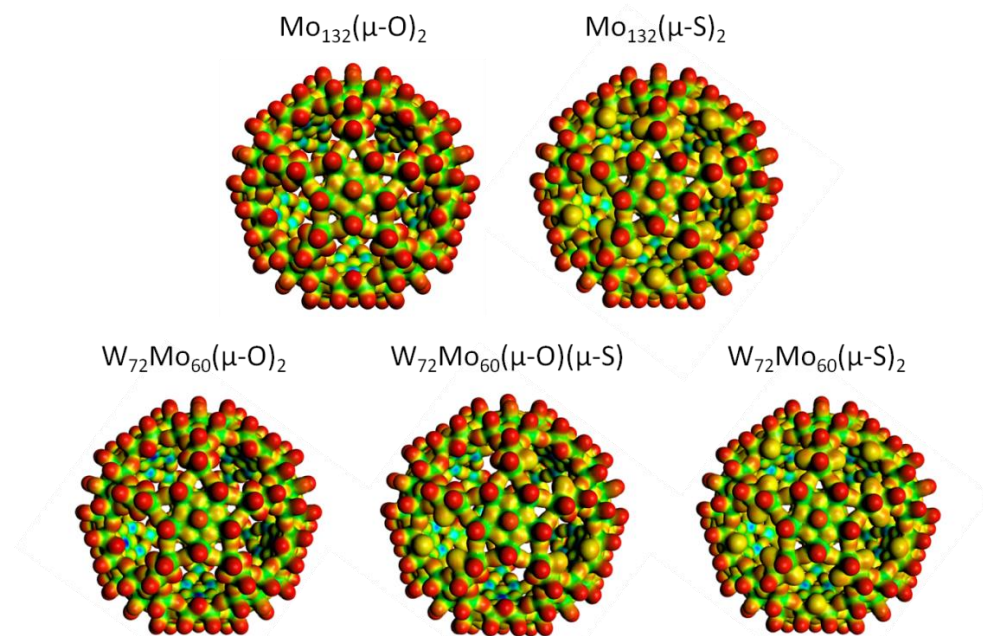
weaker. Nevertheless, the fact that the HOMO level in such case is lower is a consequence of the influence of the bridging sites to the metal-metal bond. Summing up, regarding the HOMO-LUMO gap,  $W_{72}Mo_{60}(\mu-S)_2$  is the most stable system of the studied set.



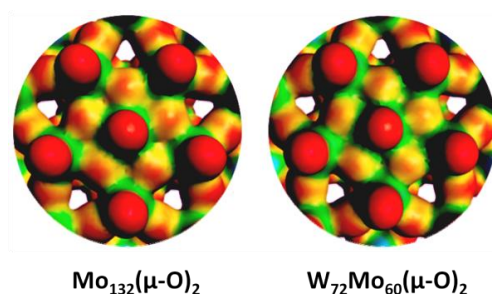
**Figure 3.7:** DOS for different Keplerates, including TDOS (black) and PDOS (red for Mo, yellow for W, grey for O and dark blue for S). The constant HOMO level has been highlighted.

Figure 3.7 compares the DOS for the set of Keplerates whose HOMO-LUMO gap was represented in Figure 3.6. Starting from the left, the first system  $Mo_{132}(\mu-O)_2$  has already been analysed as an example of POM and Keplerate DOS (Figure 3.2). Figure 3.7 shows that the DOS of the Keplerates with W pentagons and sulphur bridges are quite similar, in terms of the HOMO and LUMO levels and the presence of the oxo-band. Nevertheless, there are some differences. The most remarkable feature is the appearance of new bands related to S

orbitals (Figure 3.7b, d, and e). The 3s sulphur orbitals are located between the 2s O orbitals band and the oxo-band. Also, p orbitals related to these sulphur-bridges are found between the oxo-band and the HOMO band.



**Figure 3.8:** MEP plotted as a projection onto the electronic density for the Keplerates with Mo or W pentagons and S and/or O linker bridges.



**Figure 3.9:** Highlight on the MEP of the Mo (right) and W (left) based pentagonal units.

Besides DOS, Molecular Electrostatic Potential (MEP) is also a good tool to evaluate the effects of the different composition of Keplerates would have on the external properties of the systems. With this purpose, the electrostatic potential is projected onto the electronic density (Figure 3.8). In Figure 3.8, red colour indicates negatively charged regions, while blue represents positively

charged areas. All the five systems studied showed a very similar MEP potential pattern, which means that they should have very resembling similar external properties and, therefore, quite similar self-assembly behaviour in order to form supramolecular structures, such as blackberries.<sup>200</sup> In spite of the very similar MEP patterns, there are some differences on the systems studied. When pentagons are formed of W atoms, the oxygen atoms that link those metal centres are less negatively charged than when Mo is present. This effect, highlighted in Figure 3.9, is due to the different properties of Mo-O and W-O bond, resulting on less basic oxygens. But the most remarkable difference between the MEP showed in Figure 3.8 is the change of the electrostatic potential when sulphur-bridges are formed. Also, the change on the pore size can be appreciated. Such changes in the pore imply differences in the pore-cation interactions.

### 3.3.3 - Not Empty Capsules: Presence of Ligands and Coordination Water Molecules

All the systems described in the previous section have been considered as empty capsules, which means that the POM has been treated as a polyanion with a charge of -12 and only the metal-oxo framework has been taken into account. Such approach is just an approximation used to evaluate the capsule stability. To improve this model and check if a more realistic description could influence our stability results, a different bidentate ligands have been considered decorating the inner surface of the  $\text{Mo}_{132}(\mu\text{-O})_2$  capsule. Those ligands are experimentally known to be weakly attached to the linkers and they make these capsules even more negatively charged. The geometry optimizations performed for the system composed of  $\text{Mo}_{132}(\mu\text{-O})_2$  and 30 ligands were carried out at the standard DFT level. To reduce the computational cost, these optimizations were carried under constraints of a  $C_i$  point symmetry group, with the exception of formate, carbonate and sulphate ligands without coordination waters. The fact that these ligands present a plane of symmetry, allows keeping the  $D_{5d}$  point symmetry group of the Keplerate system.

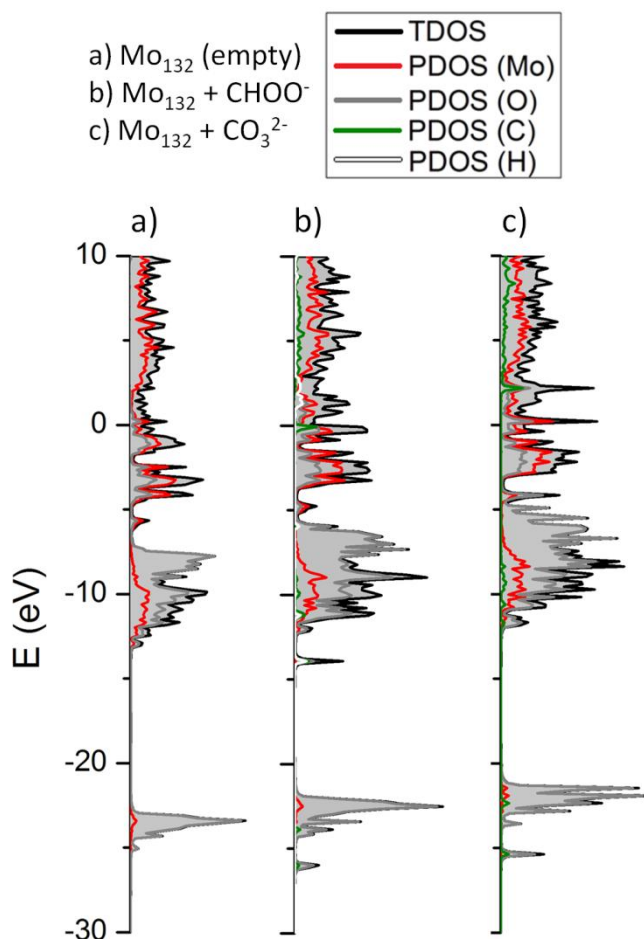


**Figure 3.10:** DOS examples of three different types of  $\text{Mo}_{132}(\mu\text{-O})_2$ : the empty capsule (a), with a charge of -12; the decorated with 30 formate ligands system (b), resulting on a charge of -42, and, finally, with 30 carbonate ligands (c), with a charge of -72. Total density of states (TDOS, black) has been represented together with the partial density of states (PDOS) for all the type of atoms present on those systems (Mo (red), O (grey), C (green) and H (white)).

In the presence of ligands, the electronic levels of the  $\text{Mo}_{132}$  Keplerate are shifted up, because of the change on the molecular charge (from -12 to -42 or -72, depending on the ligand charge). The larger the ligand charge, the larger the shifting: for the -42 systems the DOS displacement is around 1 eV, while for -72 systems it is about 1.5 eV. The different shifts depending on the charge can be observed on the DOS plotted on Figure 3.10. Furthermore, the inclusion of ligands alters the DOS of the  $\text{Mo}_{132}$  capsule as well, as new electronic levels must be taken into account. For instance, comparing Figure 3.10a and b shows

how the inclusion of formate ligands gives rise to a new set of levels between the deep 2s O orbitals and the oxo band.

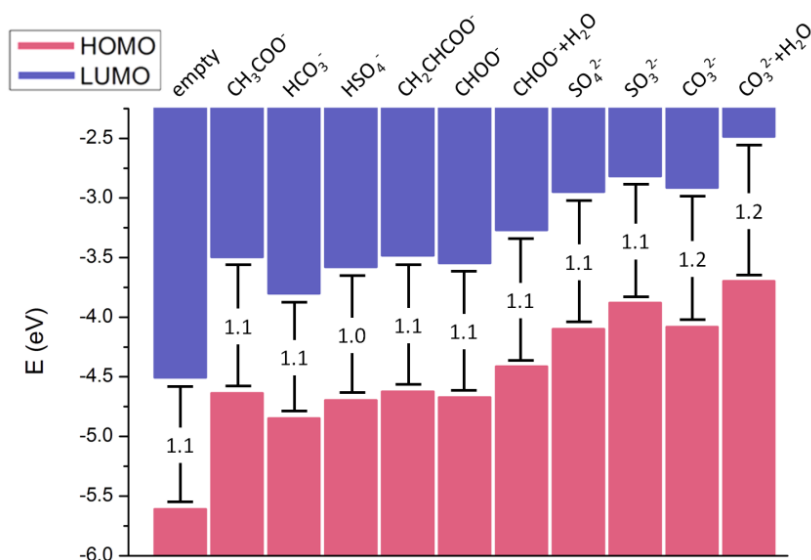


**Figure 3.11:** HOMO (pink), LUMO (violet) and the corresponding gap for the  $\text{Mo}_{132}(\mu\text{-O})_2$  systems empty and coordinated with different bidentate ligands. The label "+H<sub>2</sub>O" indicates that, in addition of the mentioned ligands, 72 water molecules have been considered coordinated to the pentagon metal centres.

Regarding the HOMO and LUMO levels, Figure 3.11 shows that there is almost no change in the gap when different inner ligands are considered. For instance, the empty  $\text{Mo}_{132}$  capsule has a gap of 1.1 eV. When acetate, bicarbonate, bisulphate, acrylate, and formate groups are acting as internal ligands the system presents almost the same gap (1.1 eV for all the mentioned systems except for the bisulphate case, for which the computed gap is 1.0 eV). A very similar behaviour is found when divalent ligands are considered.  $\text{SO}_4^{2-}$ ,  $\text{SO}_3^{2-}$  systems have a gap about 1.1 eV. A slight increase of the HOMO-LUMO gap is found for the case of carbonate ligands (1.2 eV). The fact that the  $\text{Mo}_{132}$  capsule keeps almost constant its HOMO-LUMO gap when changing the inner surface decoration means that the system's stability is given by the inherent POM's stability and it is almost independent on the particular features of the specific ligands considered. In addition, in the case of formate and carbonate ligands the presence of coordination water molecules has been considered. The inclusion of such water molecules does not affect the HOMO-LUMO gap, but the DOS is shifted up less than 1 eV.

### 3.3.4 - Predictions

All the structures presented on the previous section were already characterised by means of X-ray experiments and reported in the literature. Nevertheless, there are more composition variants that can be performed and studied from a theoretical point of view. In some cases, there are experimental leads that support our results. This section aims at evaluating the theoretical stability of these new systems in terms of their electronic structure, i.e. the HOMO-LUMO gap.

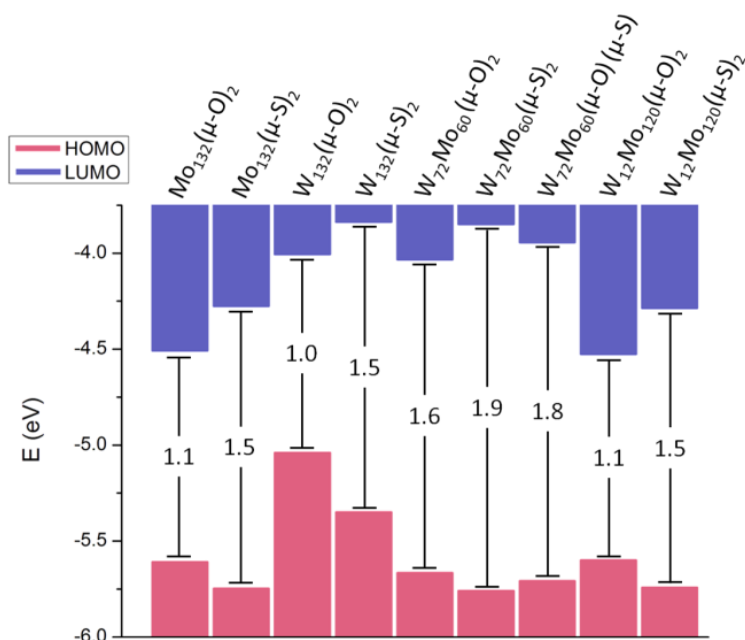


**Figure 3.12:** HOMO (pink), LUMO (violet) and the corresponding gap for the empty Keplerate systems presented in previous section compared with the new ones proposed in this section.

Keplerates with W atoms hitherto introduced present W atoms only at the pentagonal motifs. So, the question that naturally arises is what would happen when the 132 metal centres were occupied by W instead of Mo (W<sub>132</sub>). Furthermore, in 2009, Leclerc et al. demonstrated that adding molybdate on the [HBW<sub>11</sub>O<sub>39</sub>]<sup>8-</sup> ion leads to the formation of mixed pentagonal units [W(Mo<sub>5</sub>)], in which the W atom is preferably located at the central position of the pentagon.<sup>197</sup> Hence, the possibility of having this type of mixed pentagons in Keplerates (W<sub>12</sub>Mo<sub>120</sub>) has been checked as well. Both systems, W<sub>132</sub> and

$W_{12}Mo_{120}$ , have been computed at the standard DFT level with sulphur and oxo-bridges.

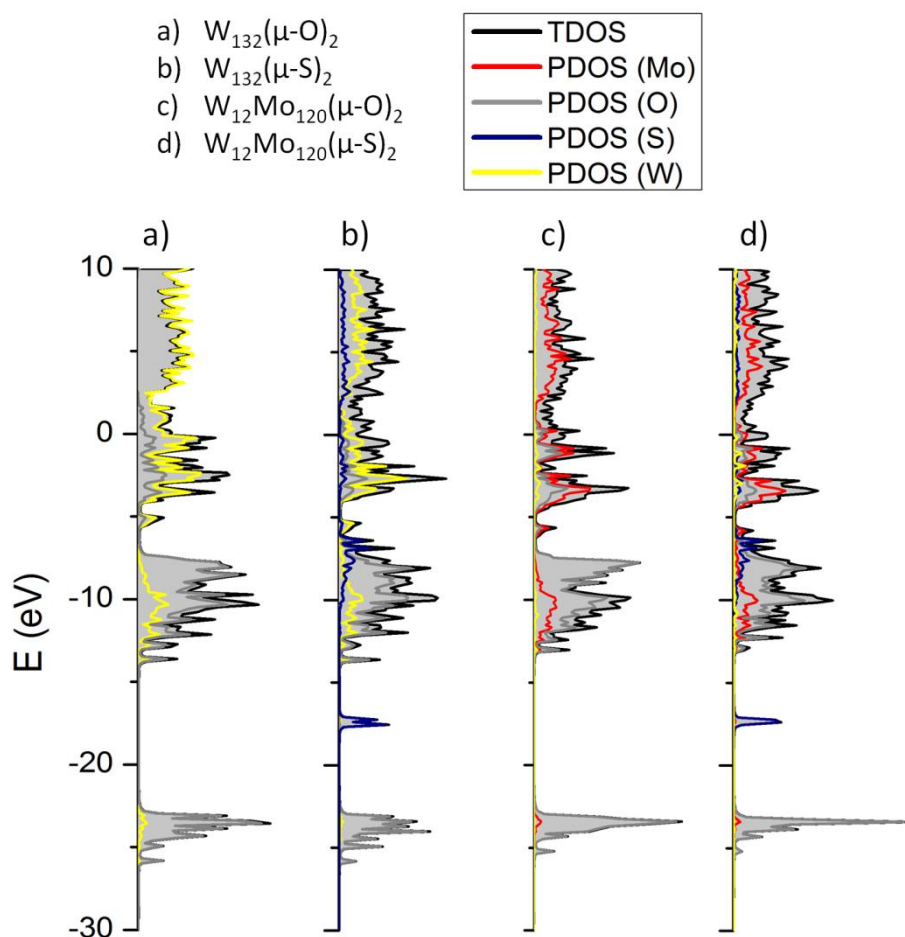


**Figure 3.13:** DOS comparison between the  $W_{132}$  and  $W_{12}Mo_{120}$  systems with sulphur and oxo-bridges. TDOS (black) and PDOS (red for Mo, grey for O, blue for S and yellow for W) are represented together.

Figure 3.12 compares the HOMO and LUMO results of these new systems with the Keplerate systems presented in the previous section. Furthermore, Figure 3.13 collects the DOS representation for these new systems. The most remarkable result is that the HOMO level is not constant anymore for the  $W_{132}$  systems. This is because of the fact that the HOMO level is related to the metal-metal bond that involves the metal centres on the linker (Figure 3.3f). Hence, changing from Mo linkers to W linkers strongly affects bond properties, making



the HOMO level higher in energy. Nevertheless, the LUMO level, related to the pentagon metal centres (Figure 3.3g), is also higher in the case of W pentagons. Consequently, the HOMO-LUMO gap for the  $W_{132}$  systems is the same that for  $Mo_{132}$  systems. In the case of mixed pentagonal motifs, both the HOMO and LUMO levels are very similar to the  $Mo_{132}$  systems. The LUMO orbitals involve the metal centres from the pentagon, except the central position (Figure 3.3g). Thus, changing this central position from Mo to W does not affect the LUMO energy. So, the mixed pentagon systems  $W_{12}Mo_{120}$  will have a very similar stability to the  $Mo_{132}$  capsule. Furthermore, it is worth noting that the trend observed on the previous systems of increasing the HOMO-LUMO gap by introducing sulphur-bridges is still present.

**Table 3.8:** Comparison between the experimental X-ray results and the geometry optimised by means of DFT (GGA BP86 with COSMO) for  $W_{12}Mo_{120}(\mu-S)_2$ . The labels used to describe the interatomic distance are explained in Figure 3.1. When two values appear for a same distance, they represent the maximum and minimum values found for the optimised geometry. Furthermore, the statistical variance has been highlighted in bold.

$W_{12}Mo_{120}(\mu-S)_2$	Experimental	GGA (COSMO)
$W^{\text{central}}-O_{\text{penta}}$	2.03	2.02-2.03
$Mo_{\text{penta}}-O_{\text{penta}}$	2.04	2.11
$Mo_{\text{penta}}-O_{\text{term}}$	1.76	1.73
$W^{\text{central}}-O_{\text{term}}$	1.72	1.73
$Mo_{\text{penta}}-O_{\text{linker}}$	1.81	1.83
$Mo_{\text{linker}}-O_{\text{linker}}$	2.06	2.08
$Mo_{\text{linker}}-Mo_{\text{linker}}$	2.84	2.91
$Mo_{\text{linker}}-O_{\text{term}}$	1.68	1.72
$Mo_{\text{linker}}-S_{\text{bridge}}$	2.32	2.36
$S_{\text{bridge}}-S_{\text{bridge}}$	3.66	3.62
Diameter	29.75	30.45-30.48
$\sigma^2$		<b>0.00563</b>

Moussawi, from the group of Molecular Solids in the Institute Lavoisier (University of Versailles-Saint Quentin), was able to synthesise and isolate crystals of  $W_{12}Mo_{120}(\mu-S)_2$  with W at the pentagonal central position.<sup>201</sup> Preliminary X-ray results allow us to perform the geometry comparison with our DFT calculations following the same procedure of Tables 3.1-4 and 3.6. Such comparison by means of the evaluation of certain interatomic distances is shown in Table 3.8.



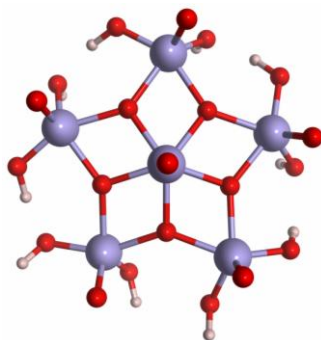


**Figure 3.14:** Ball and sticks representation of a model structure used in the study of the pentagonal motifs. The six metal centres (in violet) can be occupied by both W and Mo atoms. Red balls represent oxygen atoms while white is reserved for the capping hydrogen atoms.

As the results of our experimental collaborators show a trend for the W atom to be located at the central site of the pentagonal units, different pentagonal motifs have been checked at the standard DFT level. The pentagonal structures analysed have an increasing number of W atoms, starting with a Mo based pentagon and changing one by one the remaining metal centres by W atoms. Furthermore, the oxygen atoms that should be linked to other fragments of the POM have been capped with hydrogen atoms (Figure 3.14). It is worth noting that for each W/Mo ratio the different isomeric possibilities are checked as well. Figure 3.15 shows the schemes for the different W/Mo ratios and their corresponding isomers.

The 16 possible structures for the mixed pentagonal building block shown in Figure 3.15 have been optimised at the standard DFT level to obtain their bonding energy and the HOMO and LUMO energies, in order to explain the experimental observed trend for the W to be located at the central position of the pentagonal motifs. Numerical values for the bonding energy ( $\Delta E$ ), HOMO and LUMO energies, and the corresponding gap are collected in Table 3.9. It is worth noting that the HOMO energy keeps constant as increasing the number of W atoms of the pentagonal unit.

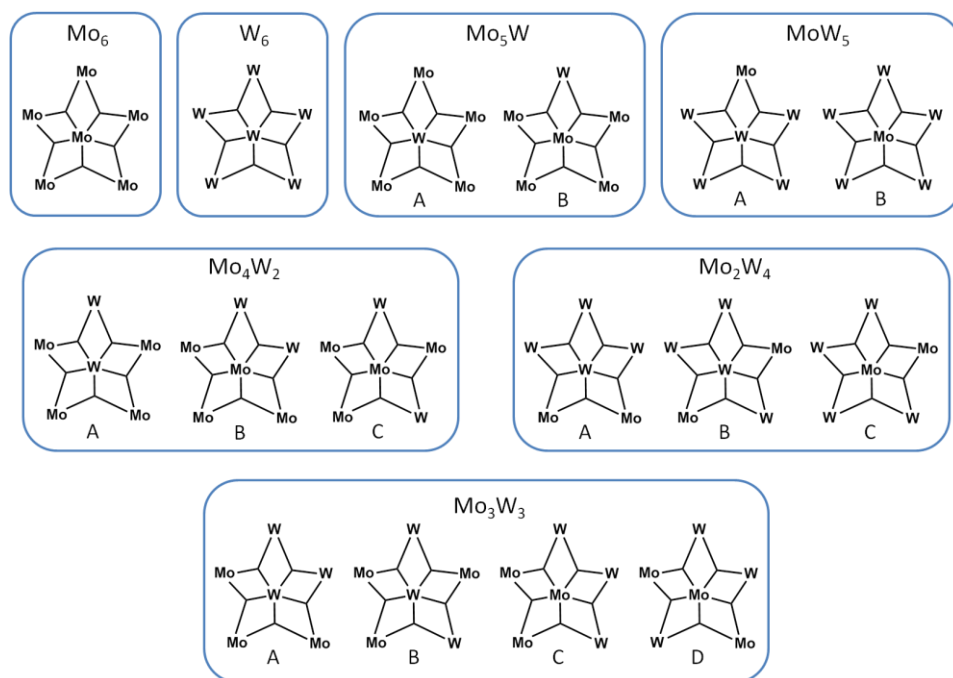


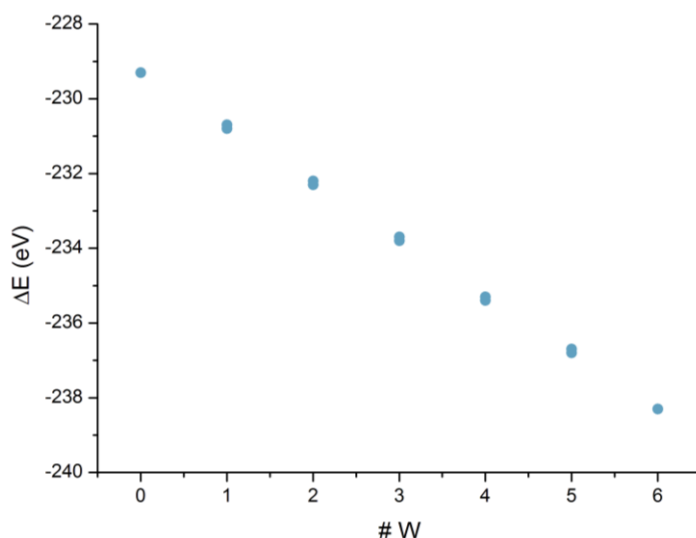
**Figure 3.15:** Schematic representations of the isomers of the pentagonal units (see Figure 3.14 for the general detailed structure) arising from the possibility of locating W and Mo atoms at metal sites in the pentagonal motifs for different ratios of W/Mo.

**Table 3.9:** Numerical values in eV for the bonding, HOMO and LUMO energies, and the related gap for the 6 possible pentagon configurations and their corresponding isomers.

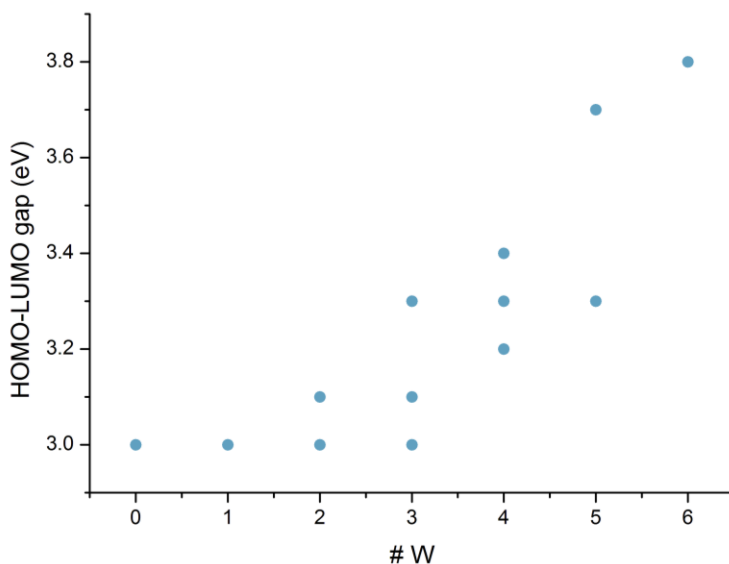
Pentagonal unit	Isomer	$\Delta E$ (eV)	HOMO (eV)	LUMO (eV)	Gap (eV)
<b>Mo<sub>6</sub></b>	-	-229.3	-9.4	-6.4	3.0
<b>Mo<sub>5</sub>W</b>	A	-230.8	-9.4	-6.4	3.0
	B	-230.7	-9.4	-6.4	3.0
<b>Mo<sub>4</sub>W<sub>2</sub></b>	A	-232.3	-9.4	-6.4	3.0
	B	-232.2	-9.4	-6.3	3.1
	C	-232.2	-9.4	-6.3	3.1
<b>Mo<sub>3</sub>W<sub>3</sub></b>	A	-233.8	-9.4	-6.4	3.0
	B	-233.8	-9.4	-6.3	3.1
	C	-233.7	-9.4	-6.3	3.0
	D	-233.7	-9.4	-6.1	3.3
<b>Mo<sub>2</sub>W<sub>4</sub></b>	A	-235.3	-9.4	-6.1	3.2
	B	-235.4	-9.4	-6.1	3.3
	C	-235.4	-9.4	-6.0	3.4
<b>MoW<sub>5</sub></b>	A	-236.7	-9.4	-6.1	3.3
	B	-236.8	-9.4	-5.7	3.7
<b>W<sub>6</sub></b>	-	-238.3	-9.4	-5.6	3.8

Figure 3.16 and 3.17 represent the bonding energy and the HOMO-LUMO gap, respectively, as a function of the number of W atoms in the pentagonal motif. Figure 3.16 shows that the substitution of a Mo atom by a W atom decreases the bonding energy on 1.5 eV, independently on the number of W atoms already present in the pentagonal moiety and on the position of new W atom. The HOMO-LUMO gap trend (Figure 3.17) also shows an increase of the stability of the pentagon as the number of W atoms increases. Both trends in the bonding energy and in the HOMO-LUMO gap are justified in terms of the strength of the W-O bond compared with the Mo-O bond.

Moreover, no special preference for the W atoms to be located at the central position of the pentagonal unit is observed. For a given number of W atoms, we find that the bonding energy has the same value for all the isomers. In terms of the HOMO-LUMO gap, even if in some cases different values are associated to each isomer, the highest gap does not match with the W at the central site. Further studies, both theoretical and experimental, must be performed in this context in order to shed some light on these new pentagonal structures.



**Figure 3.16:** Bonding energy in eV for the pentagonal systems on Figure 3.15 as a function of the number of W atoms.



**Figure 3.17** Representation of the HOMO-LUMO gap for the pentagonal motifs on Figure 3.15 as a function of the number of W atoms.

Finally, following a suggestion from Cronin (University of Glasgow, UK), we have studied the electronic stability of the fully oxidised  $\text{Mo}_{132}$ . The partially oxidised Keplerate  $[\text{Mo}_{132}(\mu\text{-O})_2]^{12-}$  present  $\text{Mo}^{\text{V}}$  in the linkers and  $\text{Mo}^{\text{VI}}$  in the pentagonal units, while the fully oxidised Keplerate  $[\text{Mo}_{132}(\mu\text{-O})_2]^{48+}$  has only  $\text{Mo}^{\text{VI}}$  at all the metal positions, including the linkers. Such change on the oxidation state of the Mo in the linkers makes the system charge change from -12 to +48.

Cronin group are experts on Electrospray Ionization (ESI) Mass Spectrometry (MS). ESI consists on applying a high potential to the liquid solution of the sample, in order to obtain very charged droplets (aerosol). Then, these droplets are analysed in a mass spectrometer. The MS principle consists on the fact that particles with different charge/mass ratio will have different trajectories in the presence of a magnetic field (Lorentz law), which makes possible to be separately detected. ESI-MS experiments of a partially oxidised solution of  $\text{Mo}_{132}(\mu\text{-O})_2$  suggested the existence of the fully oxidised variant.<sup>202</sup>

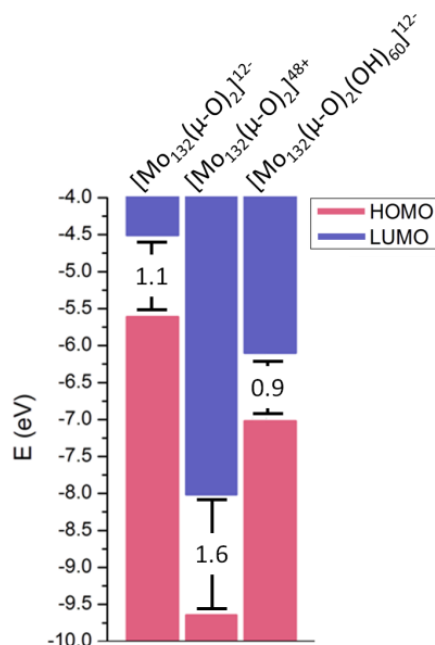


**Figure 3.18:** HOMO (pink), LUMO (violet), and the corresponding gap for the partially oxidised  $\text{Mo}_{132}$  oxo-Keplerate and the fully oxidised version (empty and with  $\text{OH}^-$  groups acting as ligands).

Firstly, we have analysed the electronic structure of the  $[\text{Mo}_{132}(\mu\text{-O})_2]^{48+}$  as an empty capsule at the standard DFT level, resulting on a HOMO-LUMO gap of 1.6 eV (Figure 3.18). Such gap value represents an increase of 0.5 eV with respect to the partially oxidised Keplerate, which means a larger stability from an electronic point of view. The change from  $\text{Mo}^{\text{V}}$  to  $\text{Mo}^{\text{VI}}$  linkers means removing the electrons involved in the metal-metal bond in the linkers. In the case of  $[\text{Mo}_{132}(\mu\text{-O})_2]^{12-}$ , these electrons were occupying the HOMO level. Once they are removed, the space between the LUMO level and the new HOMO level increases, resulting on a larger gap. Such gap increase can be observed in Figure 3.18, as well as in Figure 3.19a and b, in which the DOS of these two systems are plotted. If the oxidation process takes place on the thio-Keplerate instead of the oxo capsule, this gap increase will not be as large, because of the presence of the S orbitals just below the HOMO level (Figure 3.7b). It is worth noting that, because of the different electrostatic charge, the DOS of the fully oxidised  $\text{Mo}_{132}(\mu\text{-O})_2$  is shifted down 4 eV with respect to the partially oxidised one. Moreover, there are some geometric differences between the partially and fully oxidised Keplerates related to the lack of metal-metal bond on the linkers: the distance between the metal centres will change from 2.6 Å to 3 Å as

a consequence of the removal of the electrons related to the metal-metal bond in the linkers.

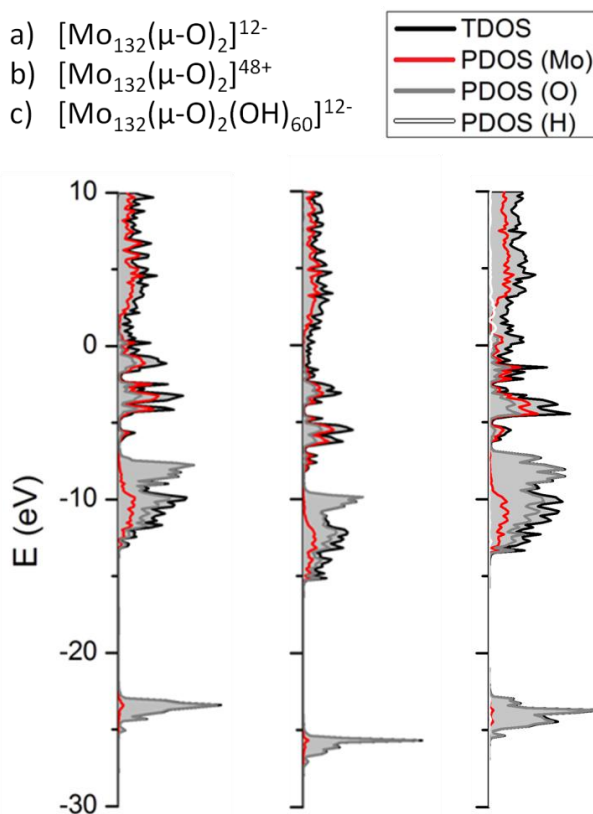


**Figure 3.19:** DOS for  $\text{Mo}_{132}$  oxo-Keplerate partially and fully oxidised (empty and with  $\text{OH}^-$  groups acting as ligands). TDOS (black) and PDOS (red for Mo, grey for O and white for H) are represented together.

Comparing the HOMO and LUMO levels of the empty partially and fully oxidised  $\text{Mo}_{132}(\mu\text{-O})_2$  (Figure 3.19a and b respectively) we observe that for the fully oxidised Keplerate, even if the gap is larger, the so negative HOMO and LUMO energies cause the system to be strongly oxidant. Furthermore, the  $m/z$  ratio of the fully oxidised  $\text{Mo}_{132}$  presented at the moment does not match with the ESI-MS experiments performed by the University of Glasgow group.<sup>202</sup> Therefore, we propose a new configuration for this system with 2  $\text{OH}^-$  groups acting as internal ligands for each linker. If, in addition to these 60  $\text{OH}^-$  groups, we consider also 20 water molecules (for instance, one at each pore) the  $m/z$  ratio is 1666.3836, which is in very close agreement with the ESI-MS experiments.

A partial geometry optimization followed by a single point calculation of the Keplerate and 60 OH<sup>-</sup> groups has been performed. These results are shown in Figure 3.18 and Figure 3.19. The DOS of this system is not shifted down with respect the original capsule as much as the empty fully oxidised Keplerate, because the charge with OH<sup>-</sup> groups is -12 instead of +48. Furthermore, the HOMO-LUMO gap is slightly smaller than the partially oxidised Keplerate, because the presence of the OH groups leads to the emergence of new orbitals at a very similar place that the HOMO level in the original system (Figure 3.19c).

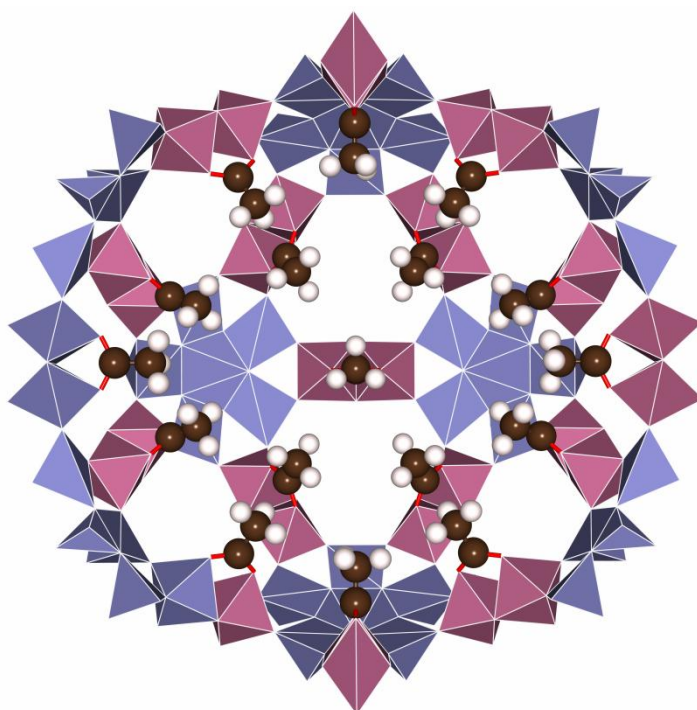
It is worth noting that the fully oxidised Mo<sub>132</sub> results presented in this chapter are preliminary results, as experimental structure is needed in order to make better theoretical approximations.

## 3.3 - Conclusions

- The highest DFT approach that we have access to nowadays for performing the systematic study of the Keplerate family comprises a GGA functional (BP86) together with a continuum solvent model (COSMO).
- All the Keplerate family members present similar electronic structure profiles (DOS and HOMO-LUMO gap).
- The presence of W pentagons and sulphur-bridges increases the HOMO-LUMO gap, and, thus, the system's stability.
- The inclusion of bidentate ligands and coordination water molecules in our model does not affect the HOMO-LUMO trend: the capsule's stability is what determines the system's stability.
- Other Keplerate systems, not reported on the literature yet, as W<sub>132</sub> and W<sub>12</sub>Mo<sub>120</sub> are stable from an electronic and theoretical point of view.
- The fully oxidised version of Mo<sub>132</sub>(μ-O)<sub>2</sub> shows a larger gap than the partially oxidised one. This means that the fully oxidised variant is also stable from an electronic and theoretical point of view. Nevertheless, more experiments are needed in order to achieve an experimental structure that could help us to improve our model.

# Chapter 4: Interaction between the Mo<sub>132</sub> Capsule and its Internal Ligands

---





UNIVERSITAT ROVIRA I VIRGILI

KEPLERATES: FROM ELECTRONIC STRUCTURE TO DYNAMIC PROPERTIES.

María Dolores Melgar Freire

Dipòsit Legal: T 258-2016

## 4.1 - Introduction

As it was mentioned in the *General Introduction*, in Mo<sub>132</sub> and W<sub>72</sub>Mo<sub>60</sub> species the ligands L in the linker units (Mo<sup>V</sup><sub>2</sub>(μ-X)<sub>2</sub>O<sub>2</sub>(L<sup>n-</sup>), X=O, S) are bidentate oxygen donor anions such as formate,<sup>21a, 203</sup> acetate,<sup>50b, 204</sup> sulfate,<sup>205</sup> sulfite,<sup>64</sup> hipophosphite,<sup>50b, 206</sup> carbonate,<sup>10a</sup> etc. From a pure electrostatic point of view, it seems non rational that a large number (30 units) of anionic ligands (charge -1, -2) coordinate to the anionic capsule [(Mo<sup>VI</sup>(Mo<sup>VI</sup>)<sub>5</sub>O<sub>21</sub>(H<sub>2</sub>O)<sub>6</sub>)<sub>12</sub>(Mo<sup>V</sup><sub>2</sub>(μ-O)<sub>2</sub>O<sub>2</sub>(L<sup>n-</sup>))<sub>30</sub>]<sup>(12+n)-</sup>, which formally holds a charge of -12. The whole system raises then its charge to -42 or -72 upon ligands coordination. Actually, the inner surface of the capsule offers many coordination sites. The coordinatively unsaturated Mo<sup>V</sup> atoms in the linkers are the anchoring points for the bidentate ligands, provided that the Mo<sup>VI</sup> ions in the pentagonal motifs coordinate water molecules. This is likely the situation ever observed in X-ray crystal structures, so our models will rely on this observation.

In Chapter 3, we studied the electronic structure of the whole Keplerates family, and for Mo<sub>132</sub>, with and without inner ligands (Figure 3.11, Chapter 3). It was found that the presence of ligands in the linker units has little effect on the electronic structure in terms of its HOMO-LUMO gap, which remained almost constant along the ligand series. A global shift up of all orbital energies was observed, which is dependent on the ligand charge, but that does not affect the nature of the molecular orbitals in a significant extent. This indicated that, although ligands coordinate to the capsule, their interaction should not be very strong.

In this chapter we aimed at studying the interaction between the Mo<sub>132</sub> capsule and different types of ligands, in terms of a bonding energy decomposition analysis. This procedure enables decomposing the energy changes upon bonding of two atomic or molecular fragments in several energy terms: steric interaction (Pauli repulsion and electrostatic interaction), orbital interaction and difference in solvation energy. This sort of analysis is largely dependent on the model used. Given the ionic nature of the capsule components, the most important variable for defining fragments as models is the total charge of the

distinct parts. Therefore, we choose to define simple models to check their validity instead of taking into account the whole capsule, both for the sake of simplicity and computational costs. Firstly, we built a model comprised of a linker unit and two pentagonal units, namely  $[(H_8Mo^VI_6O_{21})_2(Mo^V_2O_4)]^{6+}$ , which were protonated in the terminal oxygens to saturate the dangling bonds. Although this model retains the main characteristics of the linker's chemical environment, the presence of protons in the pentagons make the whole model highly positively charged. Going to the other extreme, protons were not added, so we defined the anionic fragment  $[(Mo^VI_6O_{21})_2(Mo^V_2O_4)]^{10-}$ , just as it is highlighted in Figure 4.1. This model holds an unrealistic high negative charge. Finally, we considered the whole capsule  $[(Mo^VI_6O_{21})_{12}(Mo^V_2O_4)_{30}]^{12-}$  and studied the simultaneous coordination of the 30 ligands.

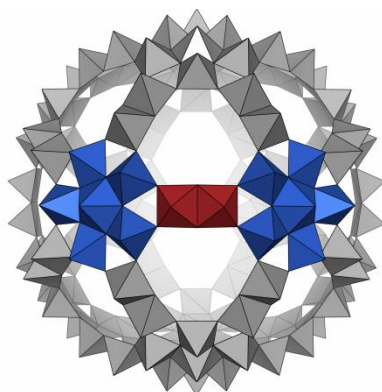


**Figure 4.1:** Polyhedral representation of the  $Mo_{132}$  capsule, as viewed along the  $C_2$  axis of the  $I_h$  point symmetry group. The  $[(Mo^VI_6O_{21})_2(Mo^V_2O_4)]^{10-}$  fragment has been highlighted (blue for pentagons and red for the linker).

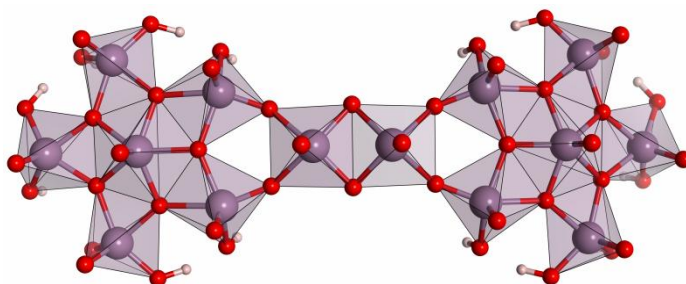


**Figure 4.2:** Polyhedral representation of the  $[(H_8Mo^VI_6O_{21})_2(Mo^V_2O_4)]^{6+}$  model. Violet polyhedra and balls stands for Mo atoms, while red and white spheres represent oxygen and hydrogen atoms, respectively.

## 4.2 - Computational Details

All the calculations presented in this Chapter were carried out with the ADF2012 program system.<sup>118</sup> Our standard method comprises including scalar relativistic ZORA effects with the BP86 DFT functional. Basis sets were of triple  $\zeta$  plus polarization quality in all atoms, TZP, which included frozen cores up to 4p for Mo and 1s for O and C atoms. Solvent effects were introduced non-explicitly by means of the COSMO model.

The energy decomposition analysis<sup>119, 207</sup> (EDA) in ADF makes sense when it is applied to well-defined fragments. So in our case, the capsule (or a model of) and the ligand are logically the fragments of choice. Since ADF requires the fragments to be in the gas-phase when running a “fragments calculation” for performing the corresponding EDA treatment afterwards, the energy that ADF provides in such kind of calculations is  $\Delta E_{\text{sol}}^{\text{frag}}$ .

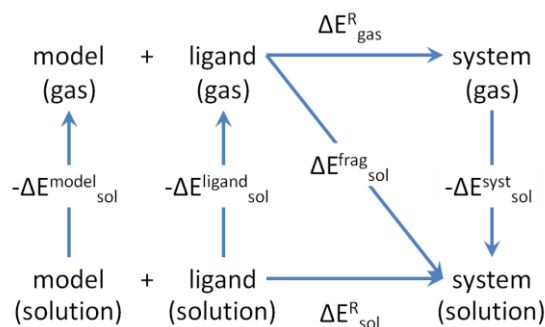


**Figure 4.3:** Scheme and notation for the different energies used in this study. All the energies are expressed in eV.

To compute the Total Bonding Energy, which we label as  $\Delta E_{\text{sol}}^{\text{R}}$  in Figure 4.3, we use Equation 4.1.

$$\Delta E_{\text{sol}}^{\text{R}} = E_{\text{sol}}^{\text{syst}} - E_{\text{sol}}^{\text{capsule}} - E_{\text{sol}}^{\text{lig}} \quad (4.1)$$

When we carry out a “fragments calculation” with ADF, the program give us  $\Delta E_{\text{sol}}^{\text{frag}}$  (Equation 4.2).

$$\begin{aligned} \Delta E_{sol}^{frag} &= E_{sol}^{syst} - E_{gas}^{model} - E_{gas}^{lig} = \\ (E_{sol}^{syst} - E_{gas}^{syst}) + (E_{gas}^{syst} - E_{gas}^{model} - E_{gas}^{lig}) &= \Delta E_{sol}^{syst} + \Delta E_{gas}^R \end{aligned} \quad (4.2)$$

The combination of Equation 4.1 and 4.2 results on Equation 4.3. Note that  $E_{sol}^i$ - $E_{gas}^i$  is the solvation energy of species  $i$ .

$$\Delta E_{sol}^R = \Delta E_{sol}^{frag} + (E_{gas}^{model} - E_{sol}^{model}) + (E_{gas}^{lig} - E_{sol}^{lig}) \quad (4.3)$$

Of course, we can also compute  $\Delta E_{sol}^R$  directly, just evaluating the energy in solution of the whole system and of the fragments to know  $E_{sol}^{syst}$ ,  $E_{sol}^{model}$  and  $E_{sol}^{lig}$  as in Equation 4.1, or alternatively, following back the thermodynamic cycle as it is shown in Equation 4.4.

$$\Delta E_{sol}^R = \Delta E_{gas}^R + \Delta E_{sol}^{syst} - \Delta E_{sol}^{model} - \Delta E_{sol}^{lig} \quad (4.4)$$

However, since we aim at decomposing the interaction energy between fragments, we need to use the fragments approach. We selected the case of the positively charged Mo<sub>132</sub> model with acetate ligands as an example to show the application of the different procedures. The results in Figure 4.3 and Equation 4.5 show that the different procedures are fully equivalent.

$$\begin{aligned} \Delta E_{sol}^{frag} &= (E_{sol}^{syst} - E_{gas}^{syst}) + (E_{gas}^{syst} - E_{gas}^{lig} - E_{gas}^{model}) \Rightarrow \\ &\Rightarrow \Delta E_{sol}^{frag} = -31.5672 - 17.0069 = -48.5741 \\ \Delta E_{sol}^R &= (E_{sol}^{syst} - E_{gas}^{syst}) - (E_{sol}^{model} - E_{gas}^{model}) - (E_{sol}^{lig} - E_{gas}^{lig}) + \\ &+ (E_{gas}^{syst} - E_{gas}^{lig} - E_{gas}^{model}) \Rightarrow \Delta E_{sol}^R = -31.5672 + 43.2952 + \\ &+ 3.2717 - 17.0069 = -2.0072 \end{aligned} \quad (4.5)$$

To compute and decompose the Total Bonding Energy,  $\Delta E_{sol}^R$ , we started optimising the capsule's geometry (or model of) with the ligand (or ligands). Then we performed single point calculations of the different fragments at their geometry optimised for the whole system. Finally, we used the previously obtained files for carrying out a fragments calculation.

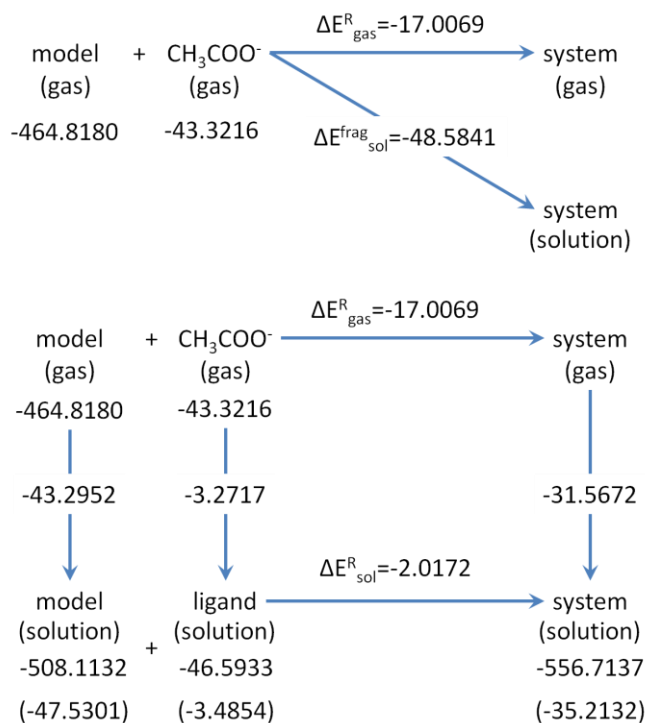


**Figure 4.4:** Comparison between the different procedures for obtaining the Bonding Energy, namely with or without the fragment approach (top and bottom, respectively). All the energies are expressed in eV. Numbers in brackets are the solvation energy contribution to the total bonding energy.

## 4.3 - Results

### 4.3.1 - $[(H_8Mo^VI_6O_{21})_2(Mo^V_2O_4)]^{6+}$ Model

Table 4.1 collects the bonding energies for different ligands computed through fragments calculations as described above, and their decomposition in the different energy terms. Note that there are clear but different trends for monovalent anions and for divalent anions. When we look at the results for two-charged ligands ( $SO_4^{2-}$ ,  $SO_3^{2-}$ , and  $CO_3^{2-}$ ), we see that the electrostatic interaction is attractive in all cases, and that the values almost double those computed for monovalent anions. Note also that the same trend can be observed in the difference in solvation energy term, which actually plays

against bonding and almost cancels with the electrostatic term. Regarding the sign of the difference in solvation energy term, it means that the solvation energy of the separated fragments is larger than the whole system, and this would be equivalent to say there is desolvation cost for making the fragments interact. Actually, we think that is an artefact of the model that derives from the fact that the whole system is less charged (+5) than its former counterparts (-1 and +6). The Pauli repulsion and the orbital interaction terms show also similar trends. In all the cases, the total bonding energy is negative, being the most stable the ligand-complex with CO<sub>3</sub><sup>2-</sup>. This is consistent with the fact that CO<sub>3</sub><sup>2-</sup> is the most basic ligand with the lowest pK<sub>b</sub>. Therefore, for this model, the total bonding energy sign is dominated by the attractive electrostatic interaction and the favourable orbital interaction terms.

**Table 4.1:** Bonding energy decomposition in eV for the interaction between the [(Mo<sup>VI</sup><sub>6</sub>O<sub>21</sub>H<sub>8</sub>)<sub>2</sub>(Mo<sup>V</sup><sub>2</sub>O<sub>4</sub>)]<sup>6+</sup> model and various ligands. The energy terms considered are Pauli repulsion, electrostatic interaction, orbital interaction and the difference on solvation energy. The total bonding energy is indicated, as well.

	SO <sub>4</sub> <sup>2-</sup>	SO <sub>3</sub> <sup>2-</sup>	HSO <sub>4</sub> <sup>-</sup>	CO <sub>3</sub> <sup>2-</sup>	HCO <sub>3</sub> <sup>-</sup>	HCOO <sup>-</sup>	CH <sub>3</sub> COO <sup>-</sup>
<i>Pauli Rep.</i>	7.25	9.10	4.20	10.89	5.61	5.75	6.15
<i>Electr. Int.</i>	-31.19	-33.69	-15.84	-37.22	-18.08	-18.26	-18.57
<i>Orbital Int.</i>	-8.33	-10.39	-4.07	-11.88	-4.90	-4.86	-5.39
<i>Diff. Solv. Energy</i>	30.02	31.46	14.82	33.80	15.66	15.53	15.80
<b><i>T. Bonding Energy</i></b>	<b>-2.25</b>	<b>-3.52</b>	<b>-0.89</b>	<b>-4.40</b>	<b>-1.70</b>	<b>-1.84</b>	<b>-2.02</b>

**Table 4.2:** Bonding energy decomposition in eV for the interaction between the [(Mo<sup>VI</sup><sub>6</sub>O<sub>21</sub>H<sub>8</sub>)<sub>2</sub>(Mo<sup>V</sup><sub>2</sub>O<sub>4</sub>)]<sup>6+</sup> model and various ligands with different carbon chains. Labels meaning are explained in Figure 4.6.

	A	B	C	D	E	F
<i>Pauli Rep.</i>	6.21	6.42	6.11	6.26	6.46	6.22
<i>Electr. Int.</i>	-18.46	-18.54	-18.40	-18.44	-18.48	-18.31
<i>Orbital Int.</i>	-5.56	-5.78	-5.52	-5.66	-5.88	-5.70
<i>Diff. Solv. Energy</i>	15.83	15.91	15.85	15.77	15.94	15.71
<b><i>Total Bonding Energy</i></b>	<b>-1.98</b>	<b>-1.99</b>	<b>-1.97</b>	<b>-2.06</b>	<b>-1.95</b>	<b>-2.08</b>

If we focus our attention on the single-charged ligands, we see that they have similar bonding energies but  $HSO_4^-$ , which is the least stable ligand. This is fully consistent with its largest  $pK_b$ , since it is feeble basic ligand. Hydrogencarbonate and carboxylates behave similarly, being  $CH_3CHOO^-$  the most stable ligand/complex system, basically because the larger contribution of the orbital interaction term.

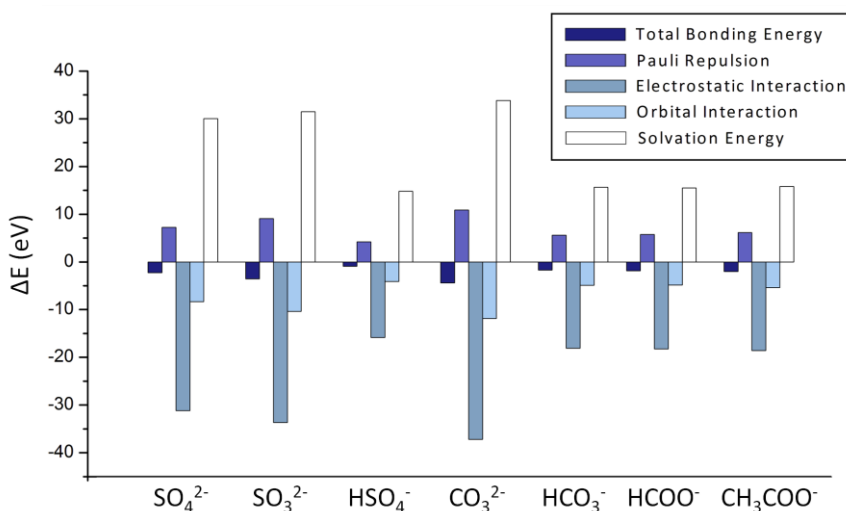


**Figure 4.5:** Representation of the bonding energy with its decomposition into the different energy terms regarding the interaction of the  $[(Mo^VI_6O_{21}H_8)_2(Mo^V_2O_4)]^{6+}$  model with a set of bidentate ligands.

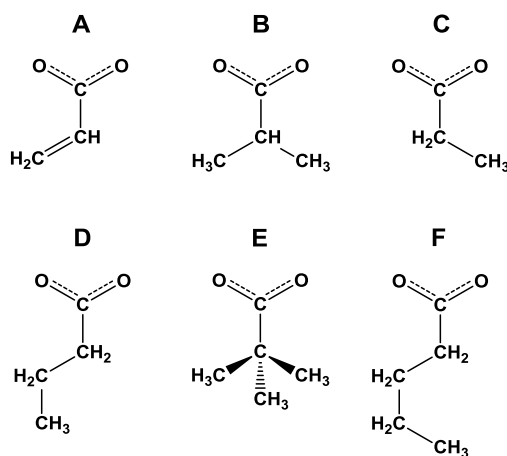


**Figure 4.6:** Correspondence of the Table 4.2 and Table 4.4 labels with ligands.



Table 4.2 shows the bonding energy and its decomposition for various carboxylate ligands, which differ only in the carbon chain. All of them have almost the same results, because they have all the same charge, and the changes in the carbon chain are at each step further binding site, so the bonding properties remain almost equivalent for all the examples. Another remarkable feature is that these energies are located at an intermediated point between the HCOO<sup>-</sup> and the CH<sub>3</sub>COO<sup>-</sup> ones, which could also be included in the examples of modified carbon chains.

### 4.3.2 - [(Mo<sup>VI</sup><sub>6</sub>O<sub>21</sub>)<sub>2</sub>(Mo<sup>V</sup><sub>2</sub>O<sub>4</sub>)]<sup>10-</sup> Model

We followed the same procedure described in the previous section by considering an alternative model of the capsule, i.e. a negatively charged fragment. In this case, also two pentagons joined together with a linker build up the model, but with any protons. Since the model unit is negatively charged, we expected to observe differences in the energy decomposition terms with respect the cationic model. Table 4.3 collects the bonding decomposition terms for the new negatively charged model.

The main difference between the results in Table 4.3 and those in Table 4.1 is that now the electrostatic contribution shows positive values instead of negative ones, and that the difference in solvation energy also reversed the sign. This is due to the change in the model total charge. With this model, the whole system is more charged (-11) than its fragments (-1 and -10), so solvation contributes to bonding. The total bonding energy values are less negative, because we are considering the interaction between two negatively charged fragments, which must be less favourable than the case with the positively charged model. It is worth noting that the values are still negative in all the cases. Ligands/capsule stability follows the same order than pK<sub>b</sub> values. Note that the values of the Pauli repulsion term almost match those computed with the positively charged model, and that the orbital interaction contributions are now smaller in absolute value.

Table 4.4 shows the bonding energy decomposition for the interaction between the negatively charged model and the same carboxylate ligands that were analysed in Table 4.2. As expected, no surprises arise from these results, just confirming the similarity between the bonding properties of these ligands.

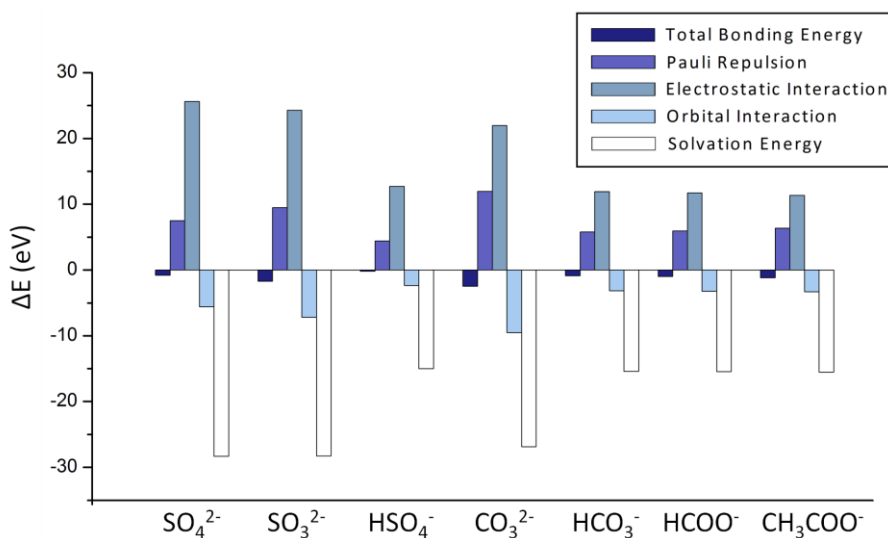


**Figure 4.7:** Representation of the bonding energy with its decomposition into the different energy terms for the  $[(Mo^{VI}_6O_{21})_2(Mo^V_2O_4)]^{10-}$  model with a set of bidentate ligands.

**Table 4.3:** Bonding energy decomposition in eV of the interaction between the  $[(Mo^{VI}_6O_{21})_2(Mo^V_2O_4)]^{10-}$  model and various ligands.

	$SO_4^{2-}$	$SO_3^{2-}$	$HSO_4^-$	$CO_3^{2-}$	$HCO_3^-$	$HCOO^-$	$CH_3COO^-$
<i>Pauli Rep.</i>	7.49	9.47	4.43	11.96	5.79	5.96	6.36
<i>Electr. Int.</i>	25.63	24.29	12.73	21.97	11.91	11.74	11.33
<i>Orbital Int.</i>	-5.59	-7.18	-2.33	-9.52	-3.15	-3.22	-3.30
<i>Diff. Solv. Energy</i>	-28.33	-28.29	-15.00	-26.88	-15.40	-15.47	-15.53
<b><i>T. Bonding Energy</i></b>	<b>-0.79</b>	<b>-1.71</b>	<b>-0.18</b>	<b>-2.47</b>	<b>-0.85</b>	<b>-0.99</b>	<b>-1.16</b>

**Table 4.4:** Bonding energy decomposition in eV of the interaction between the  $[(Mo^{VI}_6O_{21})_2(Mo^V_2O_4)]^{10-}$  model and various ligands with different carbon chains. Labels meaning are indicated on Figure 4.6.

	A	B	C	D	E	F
<i>Pauli Rep.</i>	6.43	6.69	6.36	6.53	6.73	6.50
<i>Electr. Int.</i>	11.27	10.92	11.24	11.03	10.84	10.97
<i>Orbital Int.</i>	-3.16	-3.28	-3.24	-3.23	-3.26	-3.14
<i>Diff. Solv. Energy</i>	-15.64	-15.43	-15.52	-15.49	-15.36	-15.50
<b>Total Bonding Energy</b>	<b>-1.11</b>	<b>-1.10</b>	<b>-1.17</b>	<b>-1.16</b>	<b>-1.04</b>	<b>-1.17</b>

What it is clearly revealed by the results presented until now is that i) the decomposition energy analysis is strongly dependent on the model, and ii) the trends amongst the ligands are reproduced independently of the model.

### 4.3.3 - $[(Mo^{VI}_6O_{21})_{12}(Mo^V_2O_4)_{30}]^{12-}$ Capsule

Finally, and to eliminate ambiguities, we followed the same fragment procedure by considering a full capsule in order to compare with the results provided by the two aforementioned models. Instead of taking into account just a part of  $Mo_{132}$ , we used the whole  $Mo_{132}$  capsule and computed the bonding interaction between the empty Keplerate and the 30 ligands decorating the inner surface of the capsule.

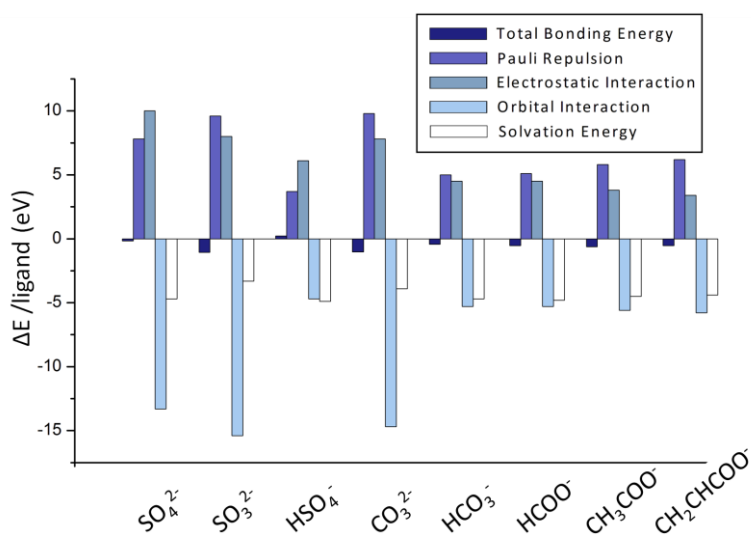


**Figure 4.8:** Bonding energies per ligand in eV with its decomposition into the different energy terms for the interaction of the  $Mo_{132}$  capsule with a set of bidentate ligands.

The most remarkable feature about these results is that, regarding stability, we see exactly the same trends as in the previous models. Even if all energy values are, in this case, smaller in absolute value, the changes in energy among the different ligands are quite similar. The signs for the different contributions to the total bonding energy are the same as in the negatively charged model, namely, negative contribution of the difference in solvation energy and positive contribution of the electrostatic interaction term. Note that the Pauli repulsion term matches again the values obtained with the other two models, being the differences due to small changes in the geometrical parameters upon bonding. Another remarkable result from Table 4.5 is that the difference in solvation energy does not depend on the charge as clearly as in the previous models. We believe that this is because the smaller charge density in the capsule. Although the charge is -12, the much larger molecular surface of the capsule with respect the small models attenuates the differences in volume upon bonding, which were responsible of the large effects observed in the models. Being electrostatic interactions much smaller and solvation/desolvation effects almost constant along the ligand series, the orbital interaction term plays the main role in the bonding. In all, carbonate is the most strongly bound ligand, and, according to the results in Table 4.5, HSO<sub>4</sub><sup>2-</sup> would not coordinate to the capsule.

**Table 4.5:** Bonding energy decomposition in eV of the interaction between the Mo<sub>132</sub> capsule and the inner 30 ligands, including the following terms: Pauli repulsion, electrostatic interaction, orbital interaction, difference in solvation energies, both for the whole system and per ligand. The total bonding energy (for the whole system and per ligand) is also included.

	SO <sub>4</sub> <sup>2-</sup>	SO <sub>3</sub> <sup>2-</sup>	HSO <sub>4</sub> <sup>-</sup>	CO <sub>3</sub> <sup>2-</sup>
<i>Pauli Rep.</i>	235.2	289.1	110.1	295.1
<i>Pauli Rep. / ligand</i>	7.8	9.6	3.7	9.8
<i>Electrost. Int.</i>	298.5	239.1	182.3	232.8
<i>Electrost. Int. / ligand</i>	10.0	8.0	6.1	7.8
<i>Orbital Int.</i>	-397.9	-461.2	-139.9	-442.1
<i>Orbital Int. / ligand</i>	-13.3	-15.4	-4.7	-14.7
<i>Diff. Solv. E</i>	-141.0	-98.7	-145.7	-116.5
<i>Diff. Solv. E / ligand</i>	-4.7	-3.3	-4.9	-3.9
<i>Total Bonding E.</i>	-5.2	-31.7	6.8	-30.7
<b><i>Total Bonding E. / ligand</i></b>	<b>-0.2</b>	<b>-1.1</b>	<b>0.2</b>	<b>-1.0</b>

	HCO <sub>3</sub> <sup>-</sup>	HCOO <sup>-</sup>	CH <sub>3</sub> COO <sup>-</sup>	CH <sub>2</sub> CHCOO <sup>-</sup>
<i>Pauli Rep.</i>	148.8	152.1	172.7	186.0
<i>Pauli Rep. / ligand</i>	5.0	5.1	5.8	6.2
<i>Electrost. Int.</i>	136.1	134.6	113.8	102.3
<i>Electrost. Int. / ligand</i>	4.5	4.5	3.8	3.4
<i>Orbital Int.</i>	-157.9	-158.3	-168.9	-172.9
<i>Orbital Int. / ligand</i>	-5.3	-5.3	-5.6	-5.8
<i>Diff. Solv. E</i>	-139.5	-144.5	-136.3	-131.7
<i>Diff. Solv. E / ligand</i>	-4.7	-4.8	-4.5	-4.4
<i>Total Bonding E.</i>	-12.5	-16.1	-18.7	-16.2
<b><i>Total Bonding E. / ligand</i></b>	<b>-0.4</b>	<b>-0.5</b>	<b>-0.6</b>	<b>-0.5</b>

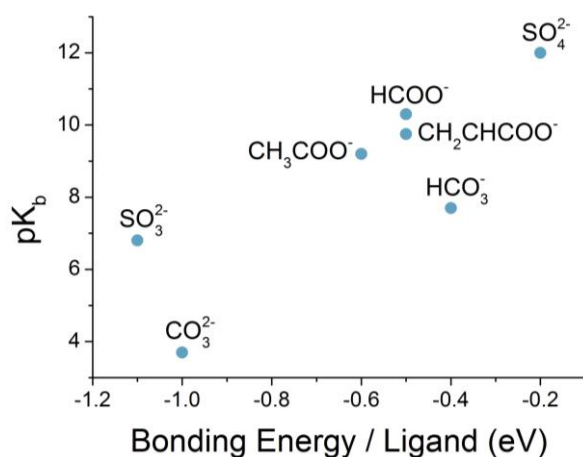


**Figure 4.9:** Comparison between the  $pK_b$  values (Table 4.6) and the bonding energies per ligand for the set of ligands collected in Table 4.5.

As a summary, we performed calculations with three different models for studying the interaction between the Mo<sub>132</sub> capsule and the inner ligands. In the first two models, we have replaced the capsule by a fragment composed of two pentagons joined together with a linker. In the first case, this fragment was totally protonated, being positively charged. The second one, without protons, is negatively charged. Finally, we performed calculations taking into account the whole capsule with 30 inner ligands. The three models show the same behaviour, although the second model results are more consistent with the full system model than the first one, due to the fragment charges. The trends in ligands stability are the same for these models, being carbonate the most stable ligand, followed by CH<sub>3</sub>COO<sup>-</sup>, CH<sub>2</sub>CHCOO<sup>-</sup>, HCOO<sup>-</sup>, HCO<sub>3</sub><sup>-</sup> and finally SO<sub>4</sub><sup>2-</sup>. This order in stability is in good agreement with the order suggested taking into

account the ligands  $pK_b$  values. Table 4.6 collects the  $pK_b$  numerical values for all the ligands studied throughout this chapter. Finally, Figure 4.9 represents those  $pK_b$  values in comparison of the total bonding energies per ligand for the whole-capsule model.

**Table 4.6:**  $pK_b$  values for the different ligands considered throughout this chapter. Note that A-E labels are indicated in Figure 4.6. Numerical values have been extracted from the Handbook of Chemistry and Physics.<sup>208</sup>

Ligand	$pK_b$
CO <sub>3</sub> <sup>2-</sup>	3.7
SO <sub>3</sub> <sup>2-</sup>	6.8
HCO <sub>3</sub> <sup>-</sup>	7.7
E	9.0
C	9.1
B	9.2
D	9.2
F	9.2
CH <sub>3</sub> COO <sup>-</sup>	9.2
A	9.75
HCOO <sup>-</sup>	10.3
SO <sub>4</sub> <sup>2-</sup>	12.0
HSO <sub>4</sub> <sup>-</sup>	14

## 4.4 - Conclusions

Bonding energy decompositions have been analysed for the three models proposed ( $[(H_8Mo^VI_6O_{21})_2(Mo^V_2O_4)]^{6+}$ ,  $[(Mo^VI_6O_{21})_2(Mo^V_2O_4)]^{10-}$  and the complete Mo<sub>132</sub> capsule). In this section, we summarise the main conclusions that can be extracted from the numerical values of the different terms considered during such energy decompositions.

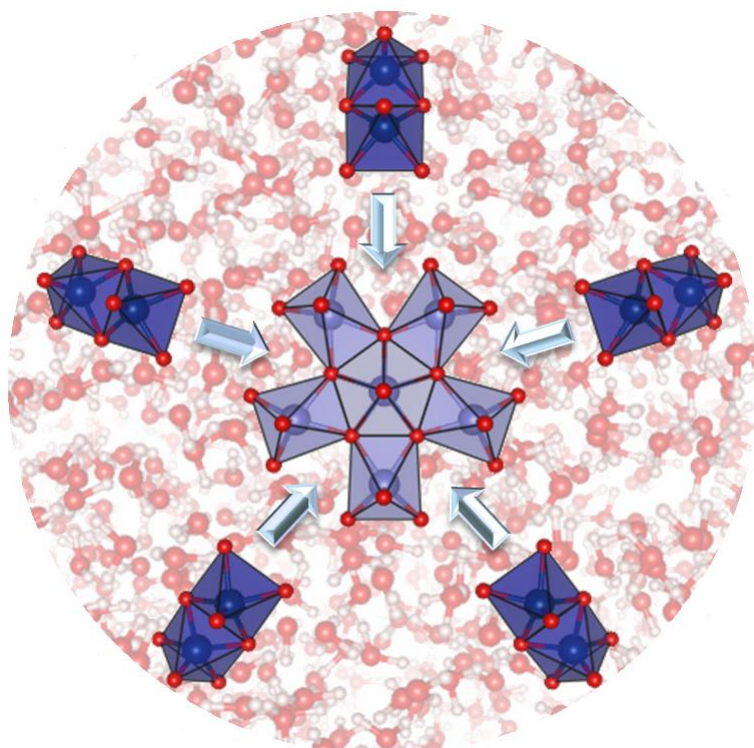
- In the case of the  $[(H_8Mo^VI_6O_{21})_2(Mo^V_2O_4)]^{6+}$  model, the bonding energy trends observed were dominated by the electrostatic interaction and the favorable orbital interaction term, because the whole system (model + ligand) is less charged than its fragments.
- For the  $[(Mo^VI_6O_{21})_2(Mo^V_2O_4)]^{10-}$  model, the electrostatic interaction and the difference on solvation energies has different sign compared with

the positively charged model, because in this case, the whole system (model + ligand) is more charged than its fragments.

- In the case of the negatively charged model, it has been shown that even of such negative charge, bonding energies for the set of ligands studied are negative as well.
- Comparing the negative and positive models, we saw that the decomposition energy analysis is dependent on the model applied.
- In the case of carboxylate ligands with different carbon chains, independently of the model used, we observe the same bonding energy results, because those ligands have the same charge and the changes in the carbon chain are one bond far away from the binding site. The bonding energy for this set of ligands is located at an intermediate point between formate and acetate ligands.
- Numerical values of the energy decomposition when the whole Keplerate is considered show that the solvation energy contribution does not depend on the charge as much as the other models because of the lower charge density of the Mo<sub>132</sub> macro-ion. Furthermore, the most important contribution to the bonding energy is the orbital interaction term.
- All the three models have shown the same trends in stability for the set of ligands, which is (from the most stable to the less): CO<sub>3</sub><sup>2-</sup>, CH<sub>3</sub>COO<sup>-</sup>, CH<sub>2</sub>CHCOO<sup>-</sup>, HCOO<sup>-</sup>, HCO<sub>3</sub><sup>-</sup>, SO<sub>4</sub><sup>2-</sup> (HSO<sub>4</sub><sup>-</sup> has not been included in this list because the full-system model shows a positive bonding energy for this ligand). Such stability trend is similar to the pK<sub>b</sub> values of the ligands.

# Chapter 5: Formation Pathway of $\text{Mo}_{132}$

---





UNIVERSITAT ROVIRA I VIRGILI

KEPLERATES: FROM ELECTRONIC STRUCTURE TO DYNAMIC PROPERTIES.

María Dolores Melgar Freire

Dipòsit Legal: T 258-2016

## 5.1 - Introduction

POMs can be interpreted as molecular clusters composed of repeating units that, sometimes, appear in multiple POM systems. These building blocks consist on assemblies of polyhedra units that arise from the metal centres coordination. There are several units that are present in different POM systems (Figure 5.1). The  $MO_6$  unit appears on almost all the POM structures. There are other units whose presence is less common. For example, the  $Mo_8$  moiety, formed by a pentagonal dipyramid surrounded by 7  $MoO_6$  is found in several POM systems, as the  $Mo_{154}$  wheel,  $Mo_{57}V_6$  and  $Mo_{57}Fe_6$ . These structural common features lead to the idea, proposed by Müller's group<sup>209</sup>, that POMs arise from the combination of the different building blocks present on a dynamic library. This condensation of building blocks is pH dependent and can be controlled in some way by the variation of the experimental reducing conditions. Nevertheless, the exact assembly pathway of building blocks, which drives to the huge variety of POM structures, is still unknown and it is one of the biggest challenges in POM science nowadays.

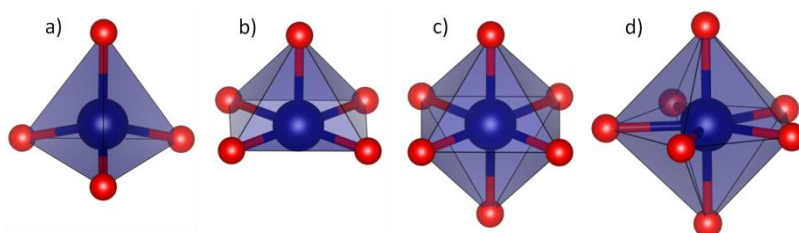


**Figure 5.1:** Examples of  $MO_n$  units, represented with ball and sticks and polyhedra models a)  $MO_4$  b)  $MO_5$  c)  $MO_6$  d)  $MO_7$

In the case of  $Mo_{132}$ , there are two main types of building blocks. On one hand, there is the pentagonal unit (blue polyhedra in Figure 5.2a), which is composed by six  $Mo^{VI}$  centres and 21 oxygen atoms. This composition leads to a pentagonal motif with five  $Mo^{VI}$  in its vertices and one  $Mo^{VI}$  in its centre. This moiety has anionic character and, in order to complete the coordination sphere of the metal atoms, coordination water molecules are found on the inner surface of the capsule, below the metal positions. On the other hand, there is the linker unit, which is a dimer of  $Mo^V$  (red polyhedra in Figure 5.2a).  $Mo^V$

atoms are linked together by means of two bridge sites, usually occupied by oxygen atoms. Furthermore, each metal centre has its corresponding terminal oxygen. Experimentally, it has been proved that several bidentate ligands can be linked in a labile way to the dimer unit, due to its cationic character.

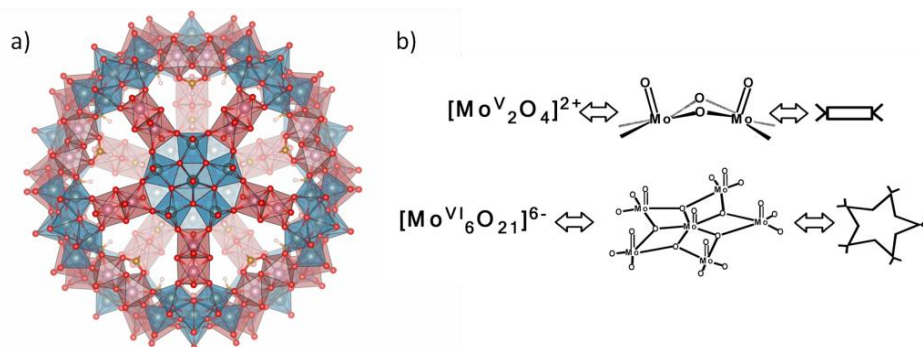


**Figure 5.2:** a) Polyhedra representation of  $Mo_{132}$ , highlighting its two types of building blocks: pentagons (blue) and linkers (red). b) Formula and schematic representation of  $Mo_{132}$  building blocks linkers and pentagons. This linker and pentagon symbols are used in Figure 5.17.

The combination of theoretical and experimental techniques is a powerful approach to analyse the POM formation issue. With this perspective, our group has collaborated with Poblet's group (Universitat Rovira i Virgili (URV)) and Roy's group (Indian Institute of Science, Education and Research). This chapter collects our contribution to this project, in which theoretical methods and experimental techniques have been combined in order to shed light into the condensation process of building blocks that drives to the  $Mo_{132}$  formation. The experimental approach includes Electrospray Ionization Mass Spectroscopy (ESI-MS) and Raman Spectroscopy analysis performed at different moments of the  $Mo_{132}$  formation process. This part has been performed by Roy's group. The theoretical approach consists in two main techniques. On one hand, Car-Parrinello Molecular Dynamics (CP-MD) have been performed by Poblet's group to analyse the stability and degree of protonation of the main building blocks of  $Mo_{132}$ . Finally, our contribution consists on the application of DFT methods to compute the Raman spectrum for a set of structures suggested as intermediate steps on the  $Mo_{132}$  formation. Furthermore, we also estimate condensation energies between pentagonal and dimeric building blocks.

ESI-MS is the application of electrospray ionization (ESI) before the mass spectroscopy procedure. The first step of ESI consists in applying a high potential to the liquid solution of the sample. Then, an aerosol is obtained, formed of very charged droplets. This charge allows the droplets to be analysed in a mass spectrometer. MS is an application of the Lorentz law, which establishes that particles with different mass/charge ratio ( $m/z$ ) will have different trajectories in the presence of a magnetic field. These different trajectories makes possible to separate particles with different  $m/z$  values. MS techniques have been widely applied to POMs since the early 80's.<sup>210</sup> POMs are very suitable molecules for this kind of studies due to their characteristic charge and composition. ESI-MS has been used to study cluster species in solution because it gives information not only about the number of heteroatoms and the degree of protonation, but also about the relative proportions of the cluster species present in the sample.<sup>211</sup> ESI-MS allows extracting the complete formula of the POM compound, including all the protons. This is one of the most important advantages of this technique with respect to crystallographic approaches.

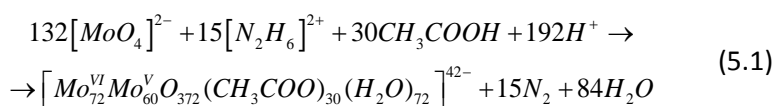
Raman spectroscopy is also a very useful tool to identify molecules. The Raman spectrum of a compound has a characteristic fingerprint because the Raman effect is influenced not only by the atoms' mass but also by their bond structure. The fundamental idea of the Raman spectroscopy is the inelastic scattering of the radiated photon. Initially, each molecule in the sample is in a rovibrational state. When the sample is irradiated with light of a given frequency, the electric field of the light interacts with the electron density of the molecule depending on its polarizability, resulting on an induced dipole moment. This interaction leads to excitation of the molecule, which changes to a higher rovibrational state. Then, the molecule can come back to the original state (elastic or Rayleigh scattering) or to a different one (Raman scattering). If this level is higher in energy than the initial one, the effect is known as *Stokes shift*. In contrast, if the molecule was initially on a rovibrational state which is not the ground state, the final state upon excitation can be lower in energy than the original state (*Anti-Stokes shift*). The Raman spectrum is, thus, composed of the different components in frequency of the inelastically scattered photons. The scattering phenomenon depends not only on the type of atoms present in the molecule, but also on the bond structure, which is related to the electron density and, thus, to the polarizability. So, a Raman

spectrum acts as a fingerprint of the molecule, allowing the identification of molecules and the study of the changes in the molecular bond structure. Raman spectroscopy gives complementary information to infrared spectroscopy (IR) studies. There are normal modes that would be silent for IR but not for Raman and vice-versa, because of the molecule's symmetry and the particular features of both techniques.

CP-MD is a computational method born in 1985, which combines DFT and Molecular Dynamics (MD).<sup>212</sup> On one hand, DFT gives quite accurate results for chemical bonding studies, but has a high computational cost. On the other hand, MD uses empirical interatomic potentials, which cause problems to describe covalent or metallic bonds systems. Moreover, electron properties are not taken into account in MD. CP-MD considers the Born-Oppenheimer approximation, so the motion of nuclei and electrons can be considered separately. DFT is used to compute the ground state of the system: core electrons are represented by pseudopotentials and valence electrons, by a plane wave basis set. Once the electron density is computed, the forces on the nuclei can be calculated. In order to solve the dynamics of coupled electron-ion system, CP-MD method proposes a set of pseudo-Newtonian equations of motion. The most remarkable feature of this method compared with classical MD, is that in CP-MD interatomic bonds can be broken and new bonds can be formed, which makes CP-MD a very interesting tool to study chemical reactions and structural phase transitions.

### 5.1.1 - Summary of Roy's group experimental results

The synthesis of  $Mo_{132}$  (and many other polymolybdates) has three main steps:<sup>213</sup> dissolution of molybdate in water, reduction of the solution and, finally, an acidification process. Firstly,  $(NH_4)_6Mo_7O_{24} \cdot 4H_2O$  is dissolved in water, together with  $CH_3COONH_4$ . Then, the reduction is achieved by the addition of  $N_2H_6 \cdot SO_4$ . Finally, the acidification process is carried out by the addition of 50% (v/v)  $CH_3COOH$ . Equation 5.1 stands for the formation reaction of  $Mo_{132}$ .



Raman (Figure 5.3) and mass spectroscopy studies (Figure 5.4, 5.5 and 5.6) have been performed at different steps of the formation process of  $\text{Mo}_{132}$ . MS-ESI results give information about which building blocks are present at each step of the synthesis. After the dissolution of heptamolybdate in water, the mass spectrum (Figure 5.4) shows a high abundance on isopolymolybdates, namely  $[\text{Mo}_7\text{O}_{24}]^{6-}$  fragments. Those fragments integrate the dynamic library of building blocks for further combination. They can be divided in two main groups:  $[\text{HMo}_m\text{O}_{3m+1}]^{1-}$  and  $[\text{Mo}_m\text{O}_{3m+1}]^{2-}$  ( $m=1-6$ ). It is worth mentioning that the pentagon building block is already present at this stage. After reduction, the mass spectra profile becomes more complicated (Figure 5.5). Mixed valence fragments appear, combining  $\text{Mo}^{\text{V}}$  and  $\text{Mo}^{\text{VI}}$  metal centres. Upon reduction, the linker moieties start to show up. After acidification, the number of pentagonal units decreases and larger species are formed, indicating the condensation of primary building blocks (Figure 5.6).

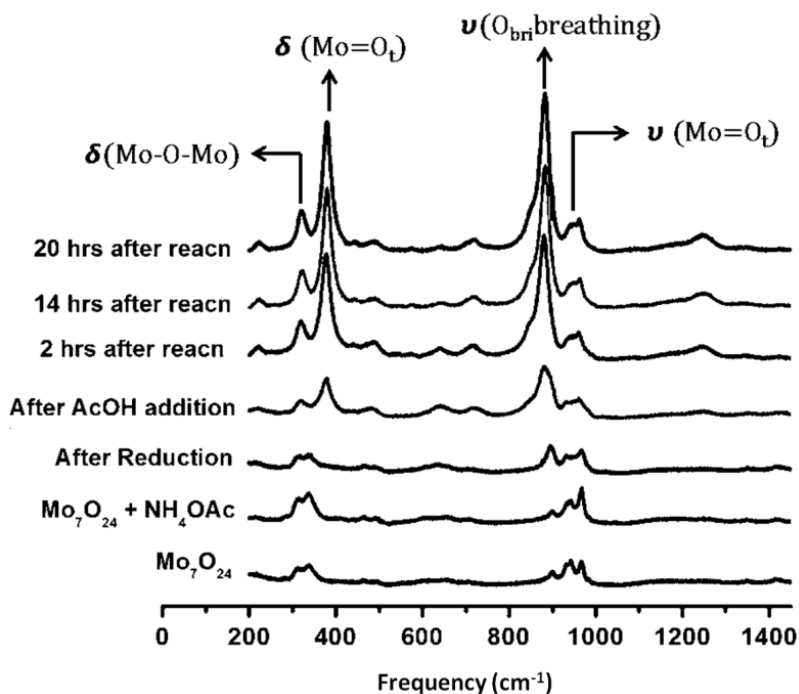


**Figure 5.3:** Raman spectra collected at different stages of the  $\text{Mo}_{132}$  synthesis.  $\nu$  represents bending vibrations, while  $\delta$  refers to stretching modes.

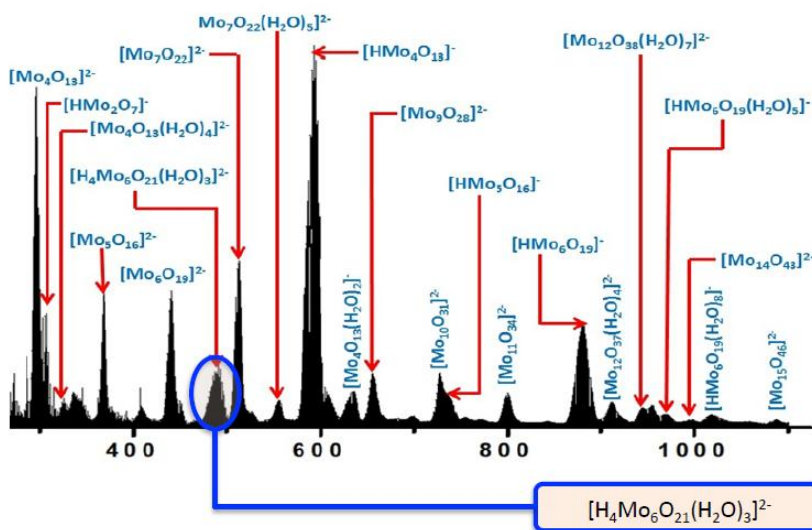


**Figure 5.4:** Mass spectrum after the dissolution of  $[Mo_7O_{24}]^{6-}$  in water. Pentagonal motif has been highlighted on the dynamic library of building blocks.

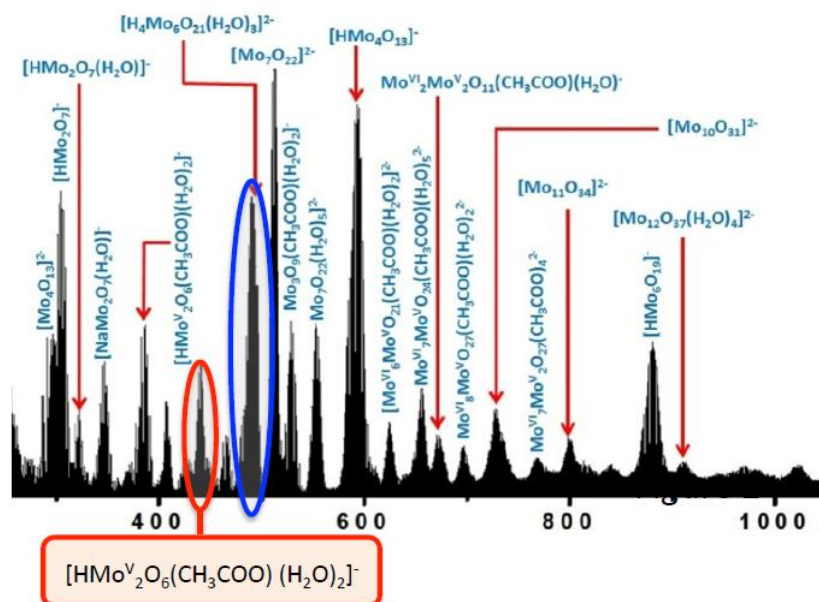


**Figure 5.5:** Mass spectrum after reduction. Blue circle highlights the pentagonal motif already mentioned in Figure 5.4. The linker unit is emphasised in red.

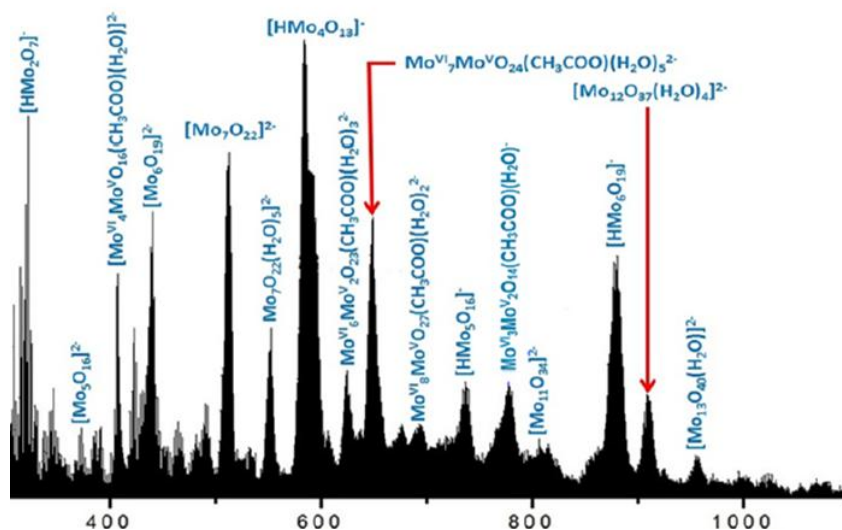


Figure 5.6: Mass spectrum upon acidification.

The Raman spectra collected at different moments of the Mo<sub>132</sub> synthesis (Figure 5.3), shows that the Raman Mo<sub>132</sub> fingerprint is almost already formed upon the acidification process, which means that the condensation between building blocks have already started at this step, in agreement with the ESI-MS experiments. After acidification, the main peaks of the Raman spectrum intensify. Finally, 20 h after the reaction started, the complete formation of the Mo<sub>132</sub> cluster can be assumed. The Mo<sub>132</sub> Raman spectrum has four main peaks, which form the Mo<sub>132</sub> Raman fingerprint. The first peak, at 314 cm<sup>-1</sup>, is related to the bending vibration of non-terminal oxygen atoms (oxygen atoms linked with more than one Mo atom). The second peak, at 374 cm<sup>-1</sup>, corresponds to the bending mode of terminal oxygens (oxygen atoms only bonded to one Mo atom). Also, there are two main contributions to the stretching modes: non-terminal oxygen atoms at 880 cm<sup>-1</sup> and terminal oxygen atoms at 950 cm<sup>-1</sup>.



## 5.1.2 - Summary of Poblet's group CP-MD results

CP-MD studies have been performed on the pentagonal and the linker motifs to check how these species behave in solution. A simulation of 17 ps has been carried out for the pentagonal unit and 146 surrounding water molecules. The starting  $[Mo^VI_6O_{15}(OH)_6]$  system evolves after 5 ps into a  $[Mo_6O_{18}(OH)_3]^{3-}$  structure (Figure 5.7a) and 3 hydronium cations. This indicates that the three-protonated pentagon should be the pentagonal configuration in acidic conditions. During the production run, two water molecules are incorporated to the pentagonal moiety, completing the coordination sphere of the metal centres. Particularly, the central position exhibits permanent coordination with a water molecule. Furthermore, it has been observed that the three hydroxo ligands change their position as the intramolecular proton transfers occur.

In the case of the linker, a  $[Mo^V_2O_8H_6(CH_3COO)]^-$  structure with 58 water molecules was simulated. After 3 ps, one oxo bridge is broken and the coordination of the two metal centres becomes different. Figure 5.7b shows how one Mo atom is 6-coordinated (two oxo, two hydroxo, one aqua and one carboxylate ligands), while the other Mo atom is 5-coordinated (two oxo, two hydroxo and one carboxylate ligands). During the subsequent 26 ps, the metal centres keep the same coordination, even if the ligands change during the simulations due to several proton transfers. The acetate group is always bonded with the linker by the coordination with at least one metal centre. Different initial linker configurations have been checked. The same pattern has been found in those simulations: one 5-coordinated Mo atom and one 6-coordinated Mo atom. Figure 5.7c shows an example of these alternative structures.



**Figure 5.7:** CP-MD structures after equilibration run: the three-protonated pentagonal motif (a) and the linker unit (b and c).

### 5.1.3 - Goals

This chapter collects our contribution to the study of the formation pathway of  $\text{Mo}_{132}$ . Regarding the experimental and CP-MD results mentioned above, DFT method has been applied pursuing the following goals:

- Modelling  $\text{Mo}_{132}$  Raman spectra evolution:
  - Computation by means of DFT of the Raman spectrum for the starting  $[\text{Mo}_7\text{O}_{24}]^{6-}$  molybdate (non-reduced and reduced species) and for the subsequent  $\text{Mo}_{132}$  main building blocks and some of their combinations.
  - Comparison between the experimental and the computed Raman spectra.
- Evaluation of condensation energies at the DFT level involving pentagonal and dimeric units with different degrees of protonation.

## 5.2 - Computational Details

The main part of the computational work regarding this chapter has been carried out by means of the Amsterdam Density Functional program (ADF2012).<sup>118</sup> With this software, Raman spectra and studies on the combination of building blocks have been performed. With this purpose, a GGA BP86<sup>93</sup> functional and a TZP basis set have been used. Relativistic corrections were introduced by the ZORA approximation.<sup>193</sup> Also, solvent effects have been taken into account by means of a continuum solvent model (COSMO).<sup>194</sup> The atomic radii values correspond to the Van der Waals radii from the MM3 method developed by Allinger<sup>198</sup> divided by 1.2. The numerical integration parameter which controls the precision of numerical integrals has been set at 5 for energy optimizations and at 6 for numerical frequencies studies.

Unfortunately, ADF2012 does not allow Raman intensities calculation for unrestricted determinants. Thus, alternative software should be used for reduced species as  $[\text{Mo}_7\text{O}_{24}]^{7-}$ . Among the several choices available for DFT programs, we have chosen the Gaussian09 (G09) software.<sup>214</sup> This option is one of the most widely used in the context of Computational Chemistry. To achieve

an equivalent DFT level to the ADF2012 studies with G09, a BPV86 functional<sup>88, 93c, 107</sup> together with a 6-311G\*<sup>215</sup> basis set for O atoms and a LANL2TZ<sup>216</sup> basis set for Mo atoms have been used.<sup>217</sup> In this case, the solvent effects have been introduced by means of the PCM solvent model.<sup>218</sup> With this DFT specifications, ADF and G09 have been used to compute the Raman spectrum of  $[Mo_7O_{24}]^{6-}$ , leading to fully equivalent results.

## 5.3 - Results

### 5.3.1 - Theoretical Raman Spectra

Raman spectroscopy has been used to track the formation pathway of  $Mo_{132}$  experimentally. With this purpose, Raman experiments have been carried out at different steps of  $Mo_{132}$  synthesis. Figure 5.3 shows this spectrum evolution. In order to better understand the meaning of the peaks shown in Figure 5.3, the theoretical Raman spectrum of different building blocks and their combination have been generated. Figures 5.8-15 collect those theoretical Raman spectra. A more detailed description of each particular spectrum is carried out on the following paragraphs.

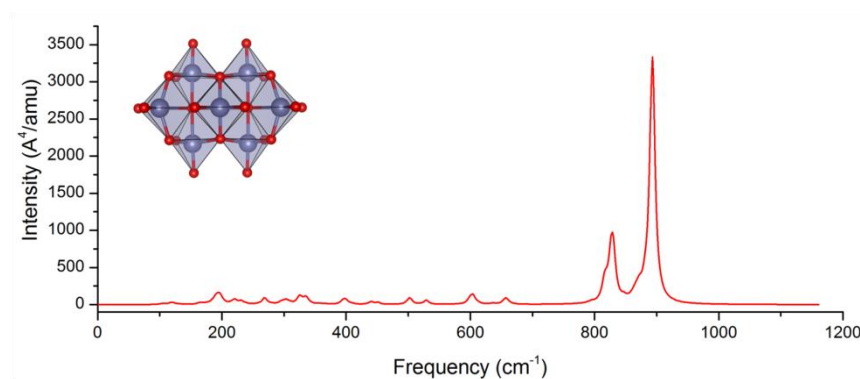


**Figure 5.8:** Raman spectrum of  $[Mo_7O_{24}]^{6-}$ .

Figure 5.8 shows the Raman spectra of  $[Mo_7O_{24}]^{6-}$ , which is the polyoxometalate dissolved on the first step of  $Mo_{132}$  synthesis. In this case, the most intense main peaks lie around 900  $cm^{-1}$ . Those peaks arise from the Mo-O stretching vibrations of the terminal oxygen atoms. The anti-symmetric

vibration at  $830\text{ cm}^{-1}$  has a Raman scattering activity of  $547\text{ \AA}^4\cdot\text{amu}^{-1}$ , while the symmetric vibration is more intense ( $3300\text{ \AA}^4\cdot\text{amu}^{-1}$ ). Around  $300\text{ cm}^{-1}$ , there is a set of very low peaks, which correspond to the bending modes of terminal oxygen atoms.

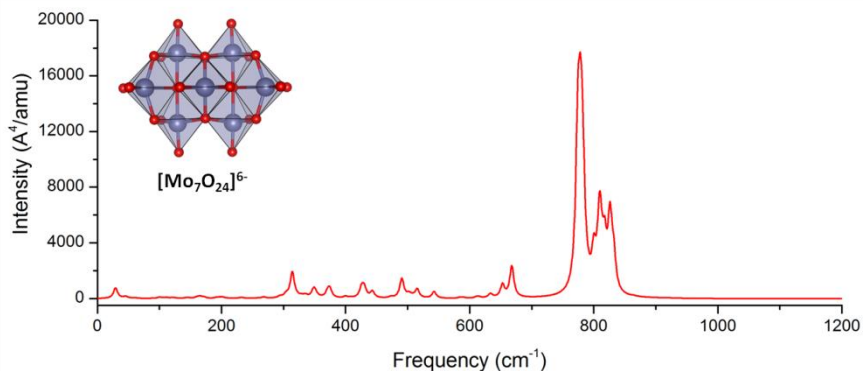


Figure 5.9: Raman spectrum of  $[\text{Mo}_7\text{O}_{24}]^{7-}$ .

During the synthesis of  $\text{Mo}_{132}$ , the dissolution of  $[\text{Mo}_7\text{O}_{24}]^{6-}$  in water is followed by a reduction step. In order to check if this reduction affects the  $\text{Mo}_7\text{O}_{24}$  spectrum, Raman intensities for the reduced heptamolybdate have been calculated (Figure 5.9). In this case, Raman intensities show higher values than for the previous system. Around  $630\text{ cm}^{-1}$ , we found bending and stretching vibrations of non-terminal oxygen atoms, which total an intensity of  $3500\text{ \AA}^4\cdot\text{amu}^{-1}$ . A more intense set of signals ( $180000\text{ \AA}^4\cdot\text{amu}^{-1}$ ) arises from  $770$  to  $830\text{ cm}^{-1}$  and it is assigned to the stretching of terminal oxygens.

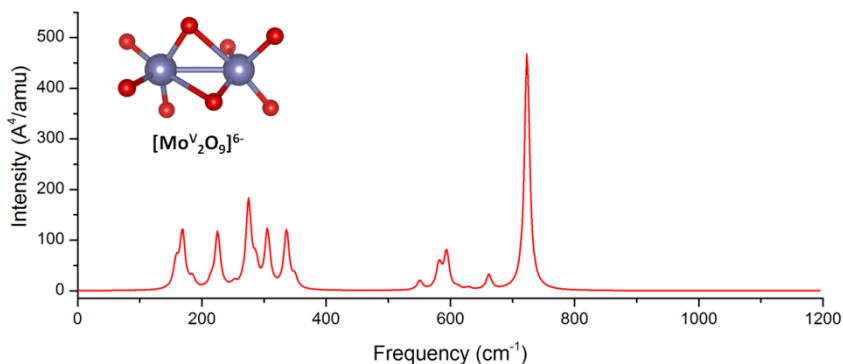
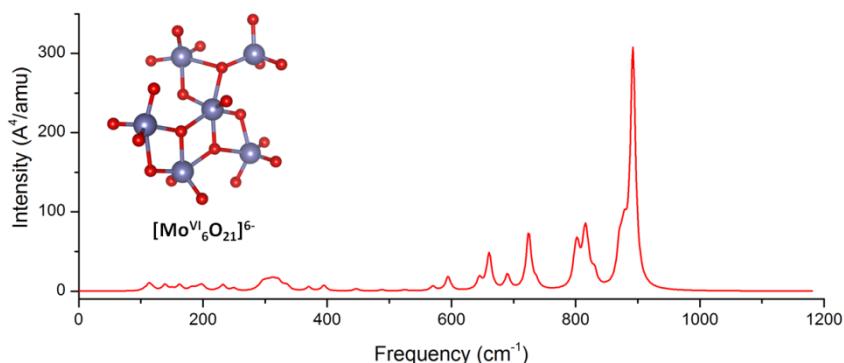
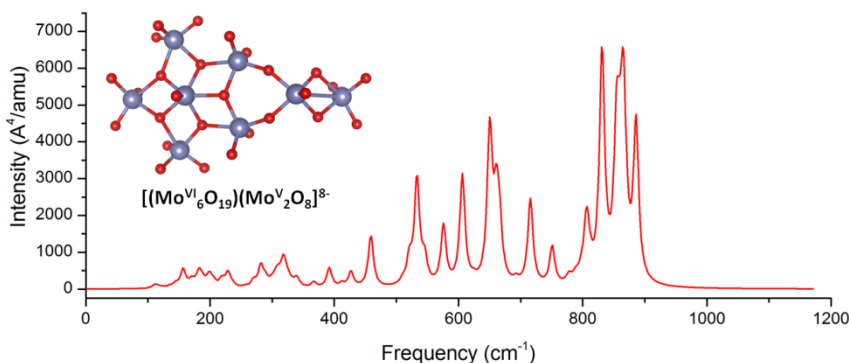


Figure 5.10: Raman spectrum of the linker unit.



**Figure 5.11:** Raman spectrum of the pentagonal motif.

Figures 5.10 and 5.11 correspond to the spectra of the two main building blocks of  $Mo_{132}$ : linkers and pentagonal units, respectively. It is worth mentioning that the pentagonal unit arises after the dissolution of  $[Mo_7O_{24}]^{6-}$  in water, while the linker unit appears upon reduction. Both systems present much less intense Raman signals than the other structures studied in this chapter. The linker spectrum (Figure 5.10) has a main peak at  $723 \text{ cm}^{-1}$  ( $500 \text{ \AA}^4 \cdot \text{amu}^{-1}$ ) corresponding to the terminal oxygens symmetric stretching. In the case of the pentagonal moiety (Figure 5.10), we found again the symmetric stretching of terminal oxygen atoms around  $900 \text{ cm}^{-1}$  with an intensity of  $300 \text{ \AA}^4 \cdot \text{amu}^{-1}$ .



**Figure 5.12:** Raman spectrum of the unit composed of on a linker and a pentagon.

Linkers and pentagonal motifs can condensate, leading to a variety structures. Inspired in the ESI-MS results from Roy's group, assemblies of linkers and pentagons are proposed and their theoretical Raman spectra are computed. Figure 5.12 is the Raman spectrum of the combination of a pentagonal unit and a linker. In this case, a set of new peaks around  $650 \text{ cm}^{-1}$  arises. One of the

most important contributions to this band ( $5000 \text{ \AA}^4 \text{ amu}^{-1}$ ) is associated with the bridging oxygen scissoring and the pentagon non-terminal oxygens bending. Furthermore, the terminal oxygen stretching is located around  $850 \text{ cm}^{-1}$  ( $6000 \text{ \AA}^4 \text{ amu}^{-1}$ ), as it was for the previous systems.

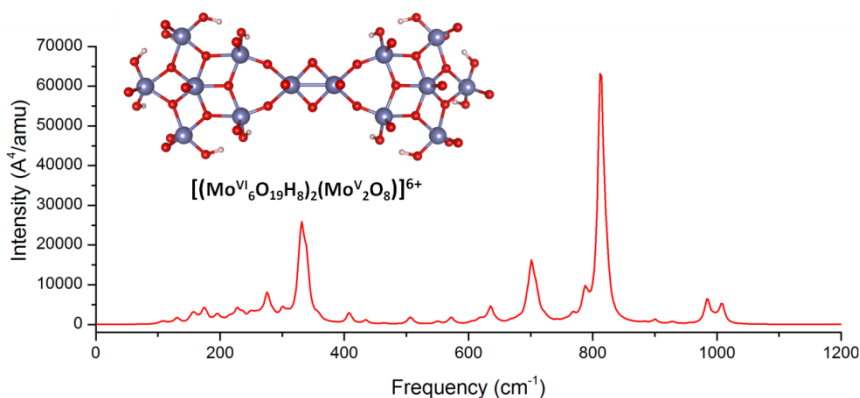


**Figure 5.13:** Raman spectrum of the moiety formed of two protonated pentagons joined together by a linker.

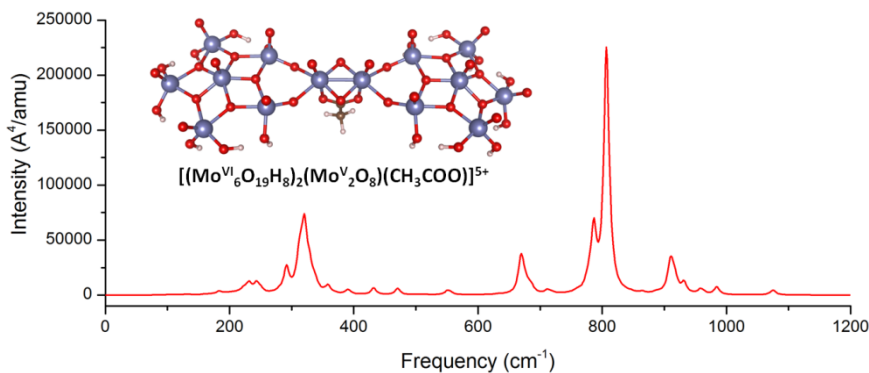


**Figure 5.14:** Raman spectrum of the moiety formed of two protonated pentagons joined together by a linker, to which an acetate ligand is bonded.

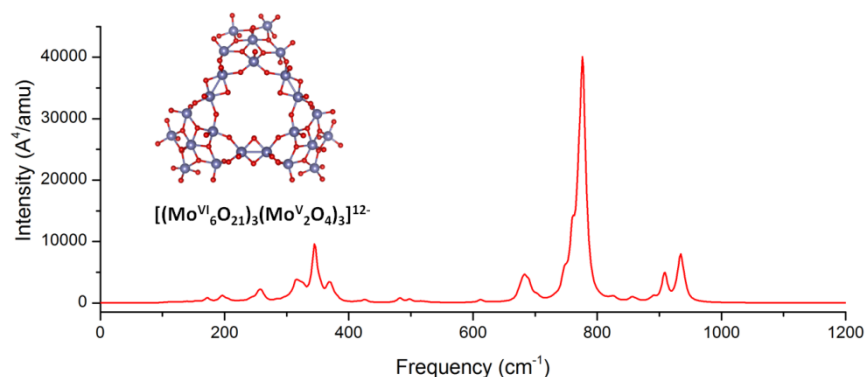


**Figure 5.15:** Raman spectrum of the pore model, made up of three pentagons assembled by three linkers.

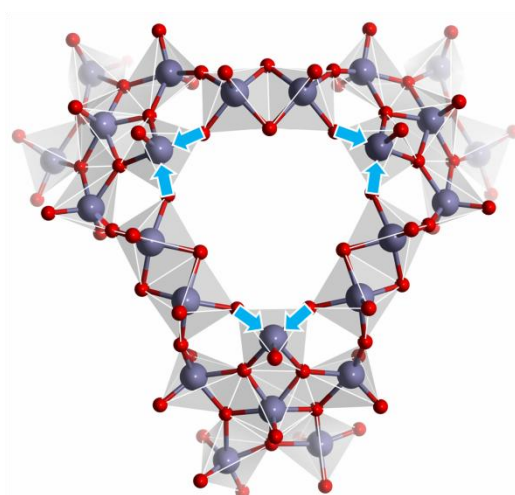


**Figure 5.16:** Polyhedra and ball and sticks representation of the pore model (violet for Mo atoms and red for O atoms) with the displacement vectors (blue arrows) for the normal mode at  $777 \text{ cm}^{-1}$ .

Figure 5.13 shows the Raman spectra of the combination between a linker and two pentagonal motifs. In this case, terminal oxygen atoms that should be linked to other moieties in the POM were capped with hydrogen atoms. The spectrum for this system shows two peaks related to the bridging oxygen wagging modes at  $275 \text{ cm}^{-1}$  ( $8000 \text{ \AA}^4 \cdot \text{amu}^{-1}$ ) and  $330 \text{ cm}^{-1}$  ( $25000 \text{ \AA}^4 \cdot \text{amu}^{-1}$ ). At  $700 \text{ cm}^{-1}$  there is the bridging oxygen symmetric stretching mode ( $15000 \text{ \AA}^4 \cdot \text{amu}^{-1}$ ). The main peak of the spectrum ( $60000 \text{ \AA}^4 \cdot \text{amu}^{-1}$ ) is located at  $813 \text{ cm}^{-1}$  and it corresponds to the symmetric stretching of the oxygen atoms that join together pentagons and linkers (pentagon-linker bridging oxygens). As

in previous cases, the set of peaks regarding the terminal oxygen stretching appear around  $1000\text{ cm}^{-1}$  ( $6000\text{ \AA}^4\text{amu}^{-1}$ ). The presence of bridging ligands at the linker ( $\text{HCOO}^-$ ,  $\text{CH}_3\text{COO}^-$ ,  $\text{HCO}_3^-$ ,  $\text{CO}_3^{2-}$  and  $\text{SO}_4^{2-}$ ) does not affect the spectrum in significant manner (Figure 5.14). This feature is extended to other pentagon-linker structure. In some cases small changes appear due to the bridging oxygens and to the ligand atoms themselves.

The pore framework model is the largest unit whose Raman spectrum is computed and reported in this Chapter (Figure 5.15). This moiety is composed of three pentagons joined together by three linkers (Figure 5.16). Near  $345\text{ cm}^{-1}$ , there is the peak ( $1000\text{ \AA}^4\text{amu}^{-1}$ ) corresponding to the pentagon non terminal oxygens bending. Around  $690\text{ cm}^{-1}$ , a band of vibrations appears, which is also related to different types of non terminal oxygens bending modes, totalling an intensity of  $10000\text{ \AA}^4\text{amu}^{-1}$ . The spectrum main peak ( $33400\text{ \AA}^4\text{amu}^{-1}$ ) is located at  $777\text{ cm}^{-1}$  and it is caused by the pentagon-linker bridging oxygens (Figure 5.16). Finally, around  $920\text{ cm}^{-1}$ , two peaks arise due to the terminal oxygen atoms stretching.

Pentagon-linker system can be understood as different steps of a condensation process between the linker and the pentagon building blocks, which finally lead to a pore-type structure. Experimentally, pentagonal moieties are found by ESI-MS after the dissolution of  $[\text{Mo}_7\text{O}_{24}]^{6-}$  in water. Upon reduction, ESI-MS peaks related to the linker formation arise. After acidification, the signal corresponding to the pentagonal motifs decrease, with an increase in intensity of around  $900\text{ cm}^{-1}$  band in Raman spectrum. This fact can be interpreted as a condensation phenomenon: primary building blocks as pentagons start to condense and form new structures, making the pentagon ESI-MS peak less intense. This idea is supported by the computed Raman spectra for different building blocks combination. Figure 5.17 collects the experimental spectra recorded at different stages of the synthesis process (Figure 5.17a) and the theoretical spectra computed for different species explained before (Figure 5.17b). Figure 5.17 makes easier the comparison between the experimental and the theoretical results. For instance, the Raman spectrum of the combination of two pentagons and one linker is in good agreement with the experimental spectrum measured after acidification. These similarities are stronger for larger systems, such as the pore framework model. The differences between the experimental and theoretical relative intensities can be explained



in terms of the other building blocks and their combinations present in solution, which were not included on the theoretical analysis, in which only one molecule is simulated at a time. Both theoretical and experimental spectra show two main regions of Raman vibrations ( $300\text{-}400\text{ cm}^{-1}$  and  $800\text{-}900\text{ cm}^{-1}$ ). The recorded spectra after two hours of standing show intensification of signals, keeping the same spectrum profile. The experimental Raman band around  $900\text{ cm}^{-1}$  can be associated to the  $813\text{ cm}^{-1}$  band of system vi and the  $777\text{ cm}^{-1}$  band of the pore model. These modes correspond to the vibration of the pentagon-linker bridging oxygens as the condensation between linkers and pentagons occurs (Figure 5.16). This vibration has been highlighted in Figure 17a as  $O_{\text{bri}}$ (breathing). When pentagons start to condense, new structures pentagon-linker like are formed, and the bridging oxygen atoms between the two building blocks contribute to the Raman spectra, making up the characteristic Raman fingerprint of the Mo<sub>132</sub> cluster.

Müller group proposed the idea of a virtual library of building blocks in solution, whose combinations lead to a huge variety of POM systems. In the case of Mo<sub>132</sub> synthesis, the pentagonal motif arises after dissolution of heptamolybdate in water and the dimeric linkers are formed upon reduction. The acidification step produces the optimal conditions for the assembly of the already formed building blocks. This condensation occurs between fragments with complementary charge, as linkers and pentagons (cationic and anionic character, respectively). The computed Raman spectra for systems resulting from the combination of linkers and pentagons show the same pattern as the experimental spectra. This means that these structures are a very important point during the Mo<sub>132</sub> formation. Particularly, the pore framework model studied in this section shows the same strong peak at  $800\text{-}900\text{ cm}^{-1}$  than the experimental spectra at the end of the synthesis reaction. We interpret this structure, composed of three pentagons joined together by three linkers, as the starting point of the 3D Mo<sub>132</sub> structure emergence. Once the pore framework is formed, in order to reduce the surface energy, the spherical cluster structure should show up.

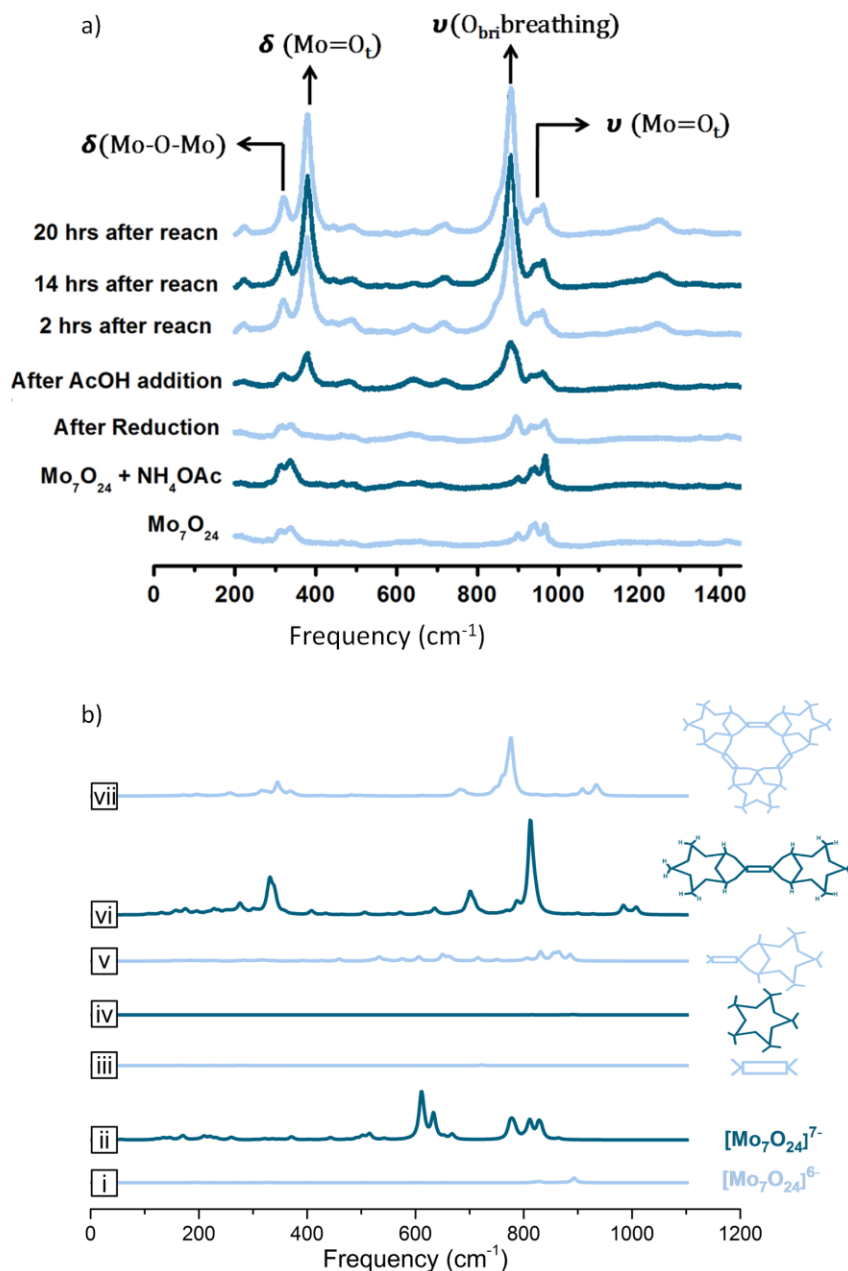


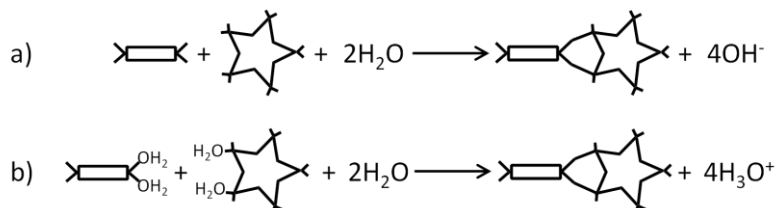
**Figure 5.17:** a) Experimental Raman spectra recorded at different stages of the Mo<sub>132</sub> synthesis. b) Collection of the theoretical Raman spectra corresponding to systems present at the beginning of the Mo<sub>132</sub> synthesis (Mo<sub>7</sub>O<sub>24</sub> species) or suggested as condensation structures during the synthesis process. It is worth noting that some systems seem to be Raman silent because of the different order of magnitude of the different system's signals. Symbols in the right are explained in Figure 5.2.

### 5.3.2 - Condensation Process

From ESI-MS and Raman results, it can be concluded that after the acidification process, condensations between the building blocks occur, leading to larger fragments and, finally, to the cluster formation. This condensation is known to be dependent on the solution pH and, so, on the degree of protonation of the building blocks. Building blocks combined should have complementary charge. For instance, negatively charged pentagons and positively charged linkers can condense to form larger structures, such as the fragments found on the after acidification ESI-MS (Figure 5.4). Furthermore, our DFT Raman studies show that the theoretical spectra profile of pentagon-linker structures is in quite good agreement with the experimental spectra recorded once the synthesis reaction is finished.

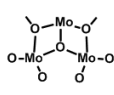
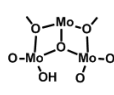
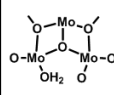
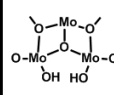
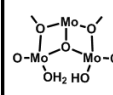
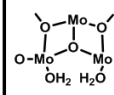
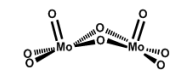
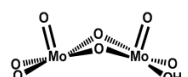
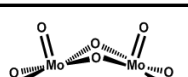
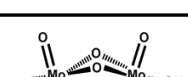
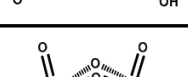
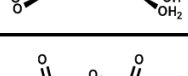
Due to its relevance, we took the pentagon and linker condensation as an example to evaluate by means of DFT its reaction energy as a function of the protonation degree. With this purpose, we have computed the bonding energies for the two building blocks with an increasing number of protons (i. e. from no protons to four protons in all at the condensation sites) and checked the reaction energy for all the possible combinations that would lead to the same final system, namely, system v on Figure 5.17b. Different degrees of protonation are related to different pH conditions: no protons simulate basic conditions, while a high presence of protons would be related to acidic conditions. Condensation reaction energies of the system proposed are summarised in Table 5.1. The first row shows the different pentagonal structures taken into account. The first column represents the different linker configurations considered. In both cases increasing degrees of protonation are contemplated. Each cell in Table 5.1 represents the reaction energy values when the condensation occurs between the different possibilities of linker and pentagons. The inner labels on each cell indicate the products obtained upon condensation. For example, in the case of the condensation between the first row and first column elements, namely, a non-protonated linker and a non-protonated pentagon, need two water molecules to condense, forming the final linker-pentagon structure and 4OH<sup>-</sup> groups. This reaction results on a condensation energy of  $-21.1\text{kcal}\cdot\text{mol}^{-1}$  (Figure 5.18a). In contrast, the last element of Table 5.1 (last row and last column combination) is an example of fully protonated building blocks: all the condensation sites have two protons.

Thus, the four-protonated linker and pentagon need two water molecules to condense and generate the final linker-pentagon structure and 4 hydronium ions. This condensation has a reaction energy of  $48\text{kcal}\cdot\text{mol}^{-1}$  (Figure 5.18b).

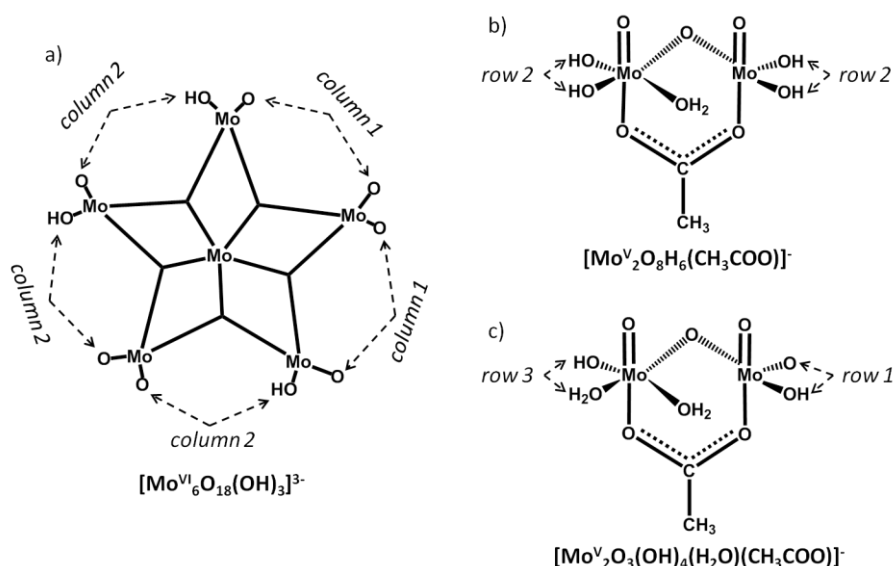


**Figure 5.18:** Schematic representation of linker and pentagon condensation reactions for the first row and first column (a) and the last row and last column elements in Table 5.1 (b). Linker and pentagon symbols (rectangle and star, respectively) are detailed in Figure 5.2.

**Table 5.1:** Condensation reaction energies (in  $\text{kcal}\cdot\text{mol}^{-1}$ ) between linkers (rows) and pentagonal fragments (columns) as a function of their protonation degree. The inner labels indicate the products obtained upon condensation. White labels highlight the formation of water molecules as products.

						
	-21.1 4OH <sup>-</sup>	-44.1 3OH <sup>-</sup>	-74.6 2OH <sup>-</sup>	-72.5 2OH <sup>-</sup>	-155.1 OH <sup>-</sup>	-172.8 2H <sub>2</sub> O
	-2.6 3OH <sup>-</sup>	-25.6 2OH <sup>-</sup>	-56.1 OH <sup>-</sup>	-54.0 OH <sup>-</sup>	-102.8 2H <sub>2</sub> O	-97.1 H <sub>3</sub> O <sup>+</sup>
	25.7 2OH <sup>-</sup>	2.8 OH <sup>-</sup>	-27.8 2H <sub>2</sub> O	-25.7 2H <sub>2</sub> O	-17.4 H <sub>3</sub> O <sup>+</sup>	-11.7 2H <sub>3</sub> O <sup>+</sup>
	16.2 2OH <sup>-</sup>	-6.8 OH <sup>-</sup>	-37.3 2H <sub>2</sub> O	-35.2 2H <sub>2</sub> O	-27.0 H <sub>3</sub> O <sup>+</sup>	-21.2 2H <sub>3</sub> O <sup>+</sup>
	24.5 OH <sup>-</sup>	1.5 2H <sub>2</sub> O	28.1 H <sub>3</sub> O <sup>+</sup>	30.2 H <sub>3</sub> O <sup>+</sup>	38.5 2H <sub>3</sub> O <sup>+</sup>	44.2 3H <sub>3</sub> O <sup>+</sup>
	-28.9 2H <sub>2</sub> O	5.3 H <sub>3</sub> O <sup>+</sup>	31.9 2H <sub>3</sub> O <sup>+</sup>	34.0 2H <sub>3</sub> O <sup>+</sup>	42.3 3H <sub>3</sub> O <sup>+</sup>	48.0 4H <sub>3</sub> O <sup>+</sup>

Low pH situations (bottom-right part of Table 5.1) generate positive reaction energies, indicating unstable products. In contrast, high pH conditions (top-left part of Table 5.1) cause favourable reactions, as the values on Table 5.1 are more negative. Nevertheless, the most energetically favourable condensation occurs when the number of protons in the linker and in the pentagon adds up 4 protons in total. These reactions usually have water molecules as products (white inner labels in Table 5.1) and correspond to the elements in Table 5.1 around the diagonal. Data from Table 5.1 indicates that the two building blocks will condense only under certain pH conditions.

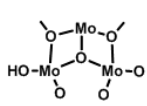
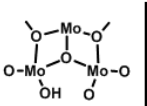
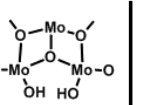
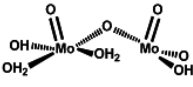
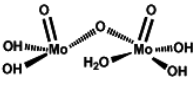
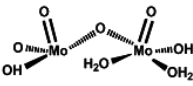


**Figure 5.19:** Schematic representation of the structures obtained from CP-MD simulations. The labels in italics indicate the condensation sites possibilities studied in Table 5.2.

In order to make a more realistic model for the pentagon-linker condensation reactions, we followed the same procedure applied for the results in Table 5.1, but in this case different linker and pentagons configurations were studied. The structures analysed in Table 5.2 were obtained by Poblet's group from CP-MD simulations performed on the pentagonal unit  $[Mo^{VI}_6O_{21}]^{6-}$  and on dimers with stoichiometry  $[Mo^V_2O_8H_6(CH_3COO)]^-$ . The structures suggested by these simulations were a three-protonated pentagon  $[Mo^{VI}_6O_{18}(OH)_3]^{3-}$  and two different kinds of dimers:  $[Mo^V_2O_3(OH)_4(H_2O)(CH_3COO)]^-$  and  $[Mo^V_2O_3(OH)_2(H_2O)_2(CH_3COO)]^-$ . Details of these geometries are shown in Figure 5.7. Furthermore, schematic representations of these structures are collected

in Figure 5.19. Moreover, in Figure 5.19 the different condensation possibilities are indicated in italics. In the case of the pentagon (Figure 5.19a), there are two possibilities for the binding sites. The first column in Table 5.2 considers the absence of protons at the pentagon binding sites. The second column represents the possibility of having one site occupied by a hydroxyl group and the remaining site without protons. Besides the possibility of having two consecutive hydroxyl groups in the pentagon condensation sites, changing the order of the terminal groups of one of the Mo atoms, has also been considered. The inclusion of this change is justified by the CP-MD results, as many intramolecular proton transfers on the pentagonal motifs are observed. Also, DFT studies of the three-protonated pentagon shows that the bonding energy difference between the original CP-MD structure and the structure with two consecutive hydroxyl groups is  $5.3 \text{ kcal}\cdot\text{mol}^{-1}$ . This difference is small enough to justify the inclusion of this new possibility in our studies.

**Table 5.2:** Condensation reaction energies (in  $\text{kcal}\cdot\text{mol}^{-1}$ ) between linkers (rows) and pentagonal fragments (columns) as a function of their protonation degree. The linker and pentagonal structures were extracted from CP-MD simulations and optimised at the standard DFT level. The inner labels indicate the products obtained upon condensation. White labels highlight the formation of water molecules as products. Further details on the meaning of rows and columns are indicated in Figure 5.19.

			
	110.3 <small>3OH<sup>+</sup></small>	72.8 <small>2OH<sup>+</sup></small>	5.2 <small>OH<sup>+</sup></small>
	61.6 <small>2OH<sup>+</sup></small>	26.4 <small>OH<sup>+</sup></small>	-11.8 <small>2H<sub>2</sub>O</small>
	15.8 <small>2OH<sup>+</sup></small>	-12.0 <small>2H<sub>2</sub>O</small>	-32.8 <small>H<sub>3</sub>O<sup>+</sup></small>

As far as the linker is concerned, there are two possible structures. The first one (Figure 5.19b) has the same degree of protonation in both sides: the condensation from the right is equivalent to the one from the left. These results correspond to the second row in Table 5.2. The second structure suggested by

CP-MD simulations (Figure 5.19c) is less symmetric than the first one. In this case, if the condensation takes place from the left, both binding sites are occupied by hydroxyl groups. In contrast, if the condensation occurs from the right, only one of the binding sites is protonated. This absence of symmetry leads to two different possibilities, corresponding to row 1 and 3 of Table 5.2.

The trend observed in Table 5.2 describes the same pattern observed in Table 5.1: the most favourable cases (bottom-right part of Table 5.2) correspond to condensations having four protons in all at the condensation sites and give water as product (white inner labels in Table 5.2). The different energy ranges presented in both tables can be explained in terms of the differences in the structures studied. Even if in both tables condensation occurs between a pentagon and a dimer, the structures studied have different geometry configurations and charge.

From Table 5.1 and Table 5.2 results, we conclude that the protonation degree of the units involved is a critical for condensation. Therefore, this condensation is very pH dependent and it should be more favourable at intermediate pH values.

## 5.4 - Conclusions

- Computed Raman spectra of structures resulting from the combination of pentagons and linkers have common features with the spectra measured experimentally. For instance, all the systems studied from a theoretical point of view present bending modes of the oxygen atoms at low frequencies and stretching vibrations of the terminal oxygens at 800-900 cm<sup>-1</sup>.
- Systems formed by two or more pentagons and their corresponding linkers present the same Raman pattern observed experimentally upon acidification.
- Particularly, the spectrum of the pore framework (three pentagons and three linkers) has a strong peak around 800 cm<sup>-1</sup>, related to the stretching of the bridging pentagon-linker oxygens. This peak is in good agreement with the Mo<sub>132</sub> Raman fingerprint.

- Condensation between linkers and pentagons is more favourable when both structures have an intermediate degree of protonation, totalling 4 protons in all. With less or more protons, the condensation energies indicate less favourable reactions.
- The dependence of the condensation energy with the degree of protonation means that these reactions are very pH-dependent and they should be more favourable at intermediate pH values.



UNIVERSITAT ROVIRA I VIRGILI

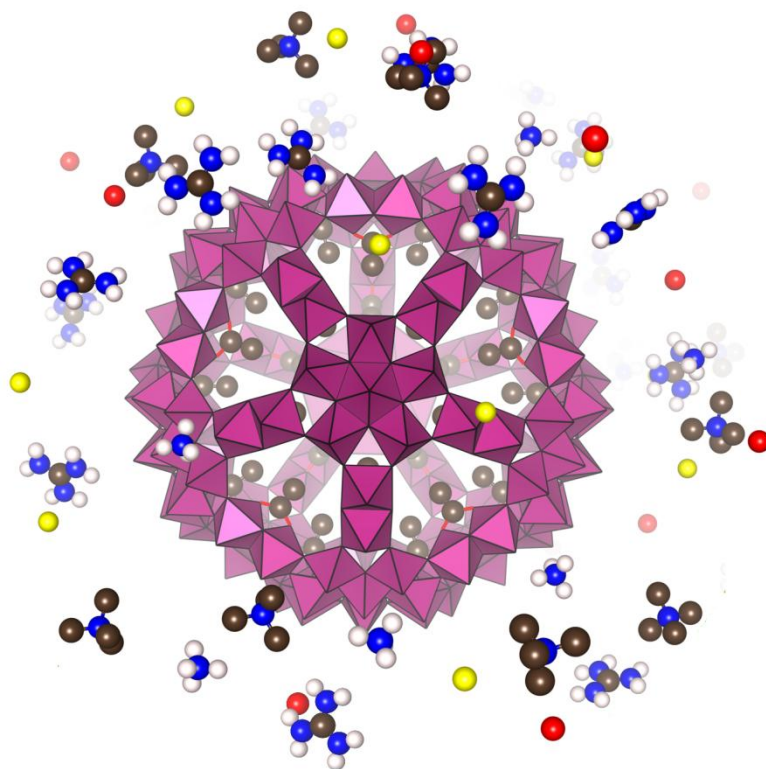
KEPLERATES: FROM ELECTRONIC STRUCTURE TO DYNAMIC PROPERTIES.

María Dolores Melgar Freire

Dipòsit Legal: T 258-2016

# Chapter 6: Ionic Behaviour of $\text{Mo}_{132}$ in Aqueous Solution

---



UNIVERSITAT ROVIRA I VIRGILI

KEPLERATES: FROM ELECTRONIC STRUCTURE TO DYNAMIC PROPERTIES.

María Dolores Melgar Freire

Dipòsit Legal: T 258-2016

## 6.1 - Introduction

Keplerates present several features that make them an interesting object of study, particularly in aqueous solution, in which they are stable under controlled conditions. The icosahedral symmetry of Keplerates results in a hollow cluster with 20 hexagonal pores, through which molecules can be exchanged from the inside of the cavity to the outer medium and vice-versa. Moreover, the characteristic large negative charge of Keplerates causes strong interactions between the POM capsule and the cationic species present in solution. The structure of the hexagonal pores, together with the large charge of the capsule, make these pores capable of being plugged by cations with the appropriate size and shape. It is well-known that Keplerate pores can be closed in a stepwise way,<sup>54-55</sup> enabling the possibility to use such POM clusters as capsules for different molecular species. Particularly, Mo<sub>132</sub> has been used as a paradigm for the study of different phenomena. For instance, the tuneability of the cavity properties allows the study of the behaviour of encapsulated matter.<sup>12a</sup> Furthermore, Mo<sub>132</sub> pores can be applied to the study of molecular transport phenomena at the nanoscale by analogy with the channels of a biological cell.<sup>205</sup>

Most of the mentioned properties, as the charge or the size of the cavity, as well as the hydrophobic/hydrophilic character, can be easily modified. For instance, focusing on the Mo<sub>132</sub> capsule, changes on the bidentate ligands that decorate the inner surface have a significant influence on the characteristics of the system. As an example, if the cavity is decorated with acetate ligands, the charge of the cluster is -42. Furthermore, the inner surface of the capsule acquires a hydrophobic character due to the methyl groups of the acetate ligands. The available space left by the ligands is a spherical hollow with a radius of about 8.75 Å while the radius of the empty capsule is estimated to be 13.5 Å, as follows from the DFT calculations (see Chapter 3). In contrast, if we consider sulphate ligands instead, the charge of the cluster changes to -72, and the available space in the cavity a radius of 10.10 Å (cf. Chapter 3). Furthermore, the decoration with sulphate instead of acetate ligands changes the character of the inner surface of Mo<sub>132</sub> from hydrophobic to hydrophilic. Changes in the size of the cavity, the hydrophobic/hydrophilic character of the

inner surface, or in the charge of the cluster, thus can significantly alter the interaction with other species present in solution. In this way, the environment of the encapsulated species can be under drastically different conditions.

In this chapter we present new results regarding the properties of Mo<sub>132</sub> capsules in aqueous solution, with different cations, obtained by means of Molecular Dynamics simulations. In particular, we address different relevant questions. These are: a) how the molecular details of the capsule influence the properties of the contained matter. Here, we use the force field obtained from our previous DFT calculations (cf. Chapter 2) and compare our results with the properties calculated directly using a force field taken from the experimentally obtained structure of the capsule.<sup>12</sup> b) How the process of plugging the pores with large cations takes place in the system and how it is influenced by the temperature and the structure of the cation. c) How different cations distribute around and inside the POM and how it does change with temperature.

### 6.1.1 - Summary of the State of the Art

Much work has been devoted in recent years to the study of the properties and behaviour of liquids,<sup>219</sup> particularly of water,<sup>220</sup> in confined environments. Encapsulated water has special importance in the field of molecular biology, as its relevance in protein folding and activity has been established.<sup>221</sup> In an environment such as a biological cell, the effects of confinement become not negligible: water properties in such conditions are different from the bulk. The cause of these differences lies in the interactions between the confining surface and water, together with the interplay between the geometry of the container and the 3D lattice of the hydrogen bonds. The geometry of the confining surface causes short- and long-range modifications on the structure and dynamic properties of water. Generally, the layers of water in contact with the confining surface show different structural features as compared to these of the innermost molecules. For instance, in the case of hydrophilic surfaces, strong hydrogen bonds between water molecules and the confining structure are found. The dynamics of the water molecules in direct contact with the surface is slower than for bulk water. Moreover, it has been argued that the layered structure encountered in water into a Mo<sub>132</sub> capsule is strongly related

to the formation of a consistent hydrogen bond network under confinement.<sup>12b,c</sup>

On one hand, computational studies on supercooled water suggest the existence of two polymorphic phases: Low Density Water (LDW) and High Density Water (HDW). Such polymorphism is thought having its origin at a liquid-liquid critical point buried in the region where physically a solid phase occurs. The characteristic parameters of such critical point are still controversial. Computational studies suggest that it could be located at  $T_c=193$  K and  $p_c=1332$  atm,<sup>222</sup> while some experimental approaches considers that it could be around  $T_c=220$  K and  $p_c=1000$  atm.<sup>223</sup> Fuentevilla and co-workers developed a parametric equation that predicts the critical point to be at  $T_c=232$  K and  $p_c=270$  atm.<sup>224</sup> Some authors even propose that the critical point should be located at negative pressures.<sup>225</sup> On the other hand, liquid water forms rapidly exchanging LDW and HDW micro-domains, which differ on the strength of the hydrogen bond network (HDW has weaker hydrogen bonds than LDW, so the former is also more reactive than the latter).<sup>226</sup> Such bimodal distribution can be understood as reminiscences of the mentioned LDW/HDW phases at supercooled conditions.<sup>227</sup> Some authors consider that the LDW/HDW micro-domains are responsible for the anomalous behaviour of water.<sup>226</sup>

The application of classical MD simulations to the study of HDW/LDW micro-domains has already been performed and compared with experimental results in a variety of containers and environments. Examples of such studies can be found, regarding hydrophobic surfaces, such as graphite channels,<sup>228</sup> and carbon nanotubes,<sup>229</sup> as well as hydrophilic walls, such as silica pores,<sup>227b, 230</sup> mica surfaces,<sup>231</sup> or reverse micelles<sup>232</sup>. Systems whose cavity size is of the order of magnitude of the correlation length responsible for the three-dimensional hydrogen bond network (which is estimated about 1 nm for bulk water at ambient conditions<sup>233</sup>) are of special interest, because they will significantly alter the phase diagram of water.<sup>12c</sup> This is the case of the Mo<sub>132</sub> capsule, whose cavity diameter is around 1.35 nm. The application of Classical MD techniques to analyse the behaviour of encapsulated species, fundamentally water, inside Mo<sub>132</sub>, shows a very good agreement when compared with experiments.<sup>12</sup>

Altering the decoration of the inner surface of a Mo<sub>132</sub> capsule permits us to modify the volume of the hollow of the capsule as well as the direct interaction of the ligands with water. One of the most typical examples of bidentate ligands in the case of Mo<sub>132</sub> are acetate groups (Mo<sub>132</sub>(CH<sub>3</sub>COO<sup>-</sup>)).<sup>50b, 204</sup> The size and hydrophobic character of such acetate ligands reduce the cavity of the capsule. Encapsulated water molecules are experimentally observed to form a small {H<sub>2</sub>O}<sub>40</sub> cluster. This cluster is composed of 2 dodecahedral {H<sub>2</sub>O}<sub>20</sub> shells.

If acetate ligands are replaced by formate groups (Mo<sub>132</sub>(HCOO<sup>-</sup>)),<sup>21a, 213</sup> the cavity will be larger and template effects arise. A larger cavity is able to host a larger water cluster. In both acetate and formate systems the outer layers of water show a strong interaction with the metal atoms, particularly with those of the 12 pentagonal moieties due to their particular coordination. The position of these 72 metal centres forces a particular geometric organization for the water layer closer to the capsule wall. The constraint imposed on this outer layer propagates to the centre of the capsule through steric repulsion, as well as hydrogen bonding structure. As a consequence, in the case of formate ligands, the inner layers retain part of the imposed geometry from the outermost layer. Such structure is progressively lost as the geometrical centre of the capsule is approached. This kind of water clusters has also been reported in other confining molecules as fullerenes.<sup>234</sup> Furthermore, the dynamics and structure of water molecules encapsulated on Mo<sub>132</sub>(HCOO<sup>-</sup>) is similar to the findings for silica pores with the same radius and reverse micelles.<sup>230j</sup>

In the case of Mo<sub>132</sub> decorated with formate ligands, if NH<sub>4</sub><sup>+</sup> acts as counter-cation to keep the solution neutral, some of these cations are able to penetrate into the capsule. The counter-cations thus interact with the encapsulated water molecules, adding a new factor to the competition between the capsule constraint and the hydrogen bond formation. In such conditions, the {H<sub>2</sub>O}<sub>80</sub> cluster that forms in a capsule with no cations inside, arranges in two layers close to the POM inner surface: a {H<sub>2</sub>O}<sub>60</sub> shell and a more external {H<sub>2</sub>O}<sub>20</sub> with dodecahedral symmetry. If, instead of NH<sub>4</sub><sup>+</sup>, formamidinium or guanidinium groups are acting as counter-cations, the uptake of cations will be avoided due to size exclusion at the pores, because of the larger size of the new counter-cation species.<sup>7a, 206a, 235</sup>

In this section we aim at focusing on two particular cases of inner decoration of the  $\text{Mo}_{132}$  capsule (formate and sulphate ligands) because they correspond to cavities with different radius, due to the ligands' size, and they have been characterised both experimentally and theoretically. Particularly, our group has contributed to the theoretical study of both capsules by means of classical MD simulations.<sup>12</sup> The radial distribution function for the water molecules encapsulated in both systems ( $\text{Mo}_{132}(\text{HCOO}^-)$  and  $\text{Mo}_{132}(\text{SO}_4^{2-})$ ) is shown in Figure 6.1. Such  $g(r)$  functions have been calculated by means of MD simulations considering a closed capsule with guanidinium cations fixed at the  $\text{Mo}_{132}$  pores and, moreover, no external solvent has been included.

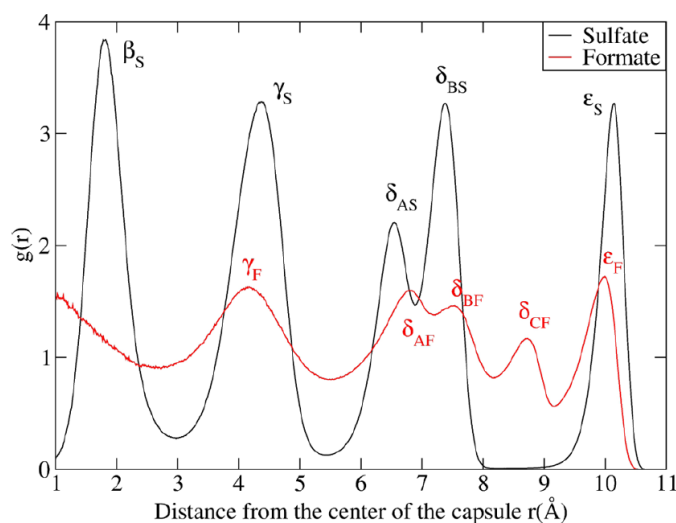


**Figure 6.1:** Radial distribution function of water molecules from the centre of the  $\text{Mo}_{132}$  Keplerate, with formates (red line) and sulphates (black line), as it was published in ref. [12c]. The notation used for the water layers is explained on Tables 6.1 and 6.2.

When the uptake of cations is avoided because of the size of guanidinium groups, the cavity of the  $\text{Mo}_{132}(\text{HCOO}^-)$  will be only occupied by a  $\{\text{H}_2\text{O}\}_{100}$  cluster and the corresponding 72 coordination waters ( $\epsilon_F$  on Figure 6.1). Moreover, the template effects of the POM scaffold will be stronger, as no counter-cations will alter the water structure, which, in this case, is composed of four concentric shells instead of the two dodecahedra observed in the case of acetate ligands. The description of the water layers observed inside the  $\text{Mo}_{132}(\text{HCOO}^-)$  is available in Table 6.1 and the corresponding radial distribution function is shown in Figure 6.1. In addition to the structures analysed in Table 6.1, MD simulations show<sup>12c</sup> that there are also a few molecules visiting the



centre of the capsule. It is worth noticing that in Table 6.1 no description of the coordination layer ( $\epsilon_F$  in Figure 6.1) is included.

**Table 6.1:** Description of the four layers arrangement of the water cluster encapsulated in  $\text{Mo}_{132}(\text{HCOO}^-)$ . It includes, not only the number of water molecules in each layer, but also their location, extracted both from experimental and theoretical procedures. Moreover, the geometrical structure of each layer it is also mentioned. The subindex 20/2 indicates that those layers are only partially occupied (see text for further details). It is worth noting that the coordination water shell (the one in closest contact with the inner surface of the POM) is not included.

Notation	Composition	Location (experimental)	Location (theoretical)	Geometry
$\gamma_F$	$\{\text{H}_2\text{O}\}_{20}$	3.92-4.13	4.4	Dodecahedral
$\delta_{AF}$	$\{\text{H}_2\text{O}\}_{20/2}$	6.72-6.78	6.9	Dodecahedral
$\delta_{BF}$	$\{\text{H}_2\text{O}\}_{60}$	7.59-7.78	7.9	Distorted rhombicosidodecahedral
$\delta_{CF}$	$\{\text{H}_2\text{O}\}_{20/2}$	8.31-8.70	8.8	Dodecahedral

**Table 6.2:** Description of the four layers arrangement of the water cluster encapsulated in  $\text{Mo}_{132}(\text{SO}_4^{2-})$ . It is worth noting that the experimental studies have been performed for a Keplerate decorated with 20  $\text{H}_2\text{PO}_2^-$  and 10  $\text{SO}_4^{2-}$ , while the theoretical approach considers a full sulphate decoration. This table includes, the number of water molecules in each layer, and their location, extracted both from experimental and theoretical procedures. Moreover, the geometrical structure of each layer it is also mentioned. It is worth noting that the coordination water shell (the one in closest contact with the inner surface of the POM) is not included.

Notation	Composition	Location (experimental)	Location (theoretical)	Geometry
$\gamma_S$	$\{\text{H}_2\text{O}\}_{20}$	3.84-4.04	4.4	Dodecahedral
$\delta_{AS}$	$\{\text{H}_2\text{O}\}_{20}$	6.51-6.83	6.7	Dodecahedral
$\delta_{BS}$	$\{\text{H}_2\text{O}\}_{60}$	7.56-7.88	7.4	Distorted rhombicosidodecahedral

An alternative inner decoration of the  $\text{Mo}_{132}$  capsule is a mixture of 20  $\text{H}_2\text{PO}_2^-$  and 10  $\text{SO}_4^{2-}$ .<sup>50b, 235</sup> The main differences with respect to the formate case is that only three layers of water are formed and that these layers are fully occupied, because 20  $\text{H}_2\text{PO}_2^-$  and 10  $\text{SO}_4^{2-}$  ligands are larger than formates. Description of these water cluster substructures is collected in Table 6.2. The MD simulations to which Table 6.2 refers have been performed considering a fully  $\text{SO}_4^{2-}$  internal decoration instead of a mixture  $\text{H}_2\text{PO}_2^-/\text{SO}_4^{2-}$ , so the comparison between theoretical and experimental results must be done taking into account such

difference. Experimentally, the sulphate capsule has not been considered due to its large charge (-72). Instead, a less charged system Mo<sub>132</sub>(H<sub>2</sub>PO<sub>2</sub><sup>-</sup>; SO<sub>4</sub><sup>2-</sup>) is used, resulting on a molecular charge of -52. Such lower charge allows the removal of the NH<sub>4</sub><sup>+</sup> ions and its replacement by guanidinium counter-ions, while the capsule decorated with only SO<sub>4</sub><sup>2-</sup> does not. Moreover, the properties of water clusters in Mo<sub>132</sub>(SO<sub>4</sub><sup>2-</sup>) have been compared with reverse micelles of similar sizes.<sup>12b, 236</sup> One of the conclusions of the authors in ref. [12b] was that in reverse micelles no layered structure was observed, because the micelle wall is not rigid enough (as it is in the POM capsule) to impose a constraint sufficiently strong as to alter the organization of the encapsulated water molecules.

Table 6.2 does not include the description for the coordination water molecules ( $\epsilon_s$ ) and the so-called  $\beta_s$  shell, which is composed by four molecules moving around the centre of the capsule. The  $\beta_s$  layer can be considered analogous to the set of molecules found to visit the centre of the Mo<sub>132</sub>(HCOO<sup>-</sup>) capsule. As the cavity of the formate capsule is larger than in the case of sulphate ligands, the centre of the cavity in the former situation is less structured than in the latter.

In spite of the different distributions, the total number of water molecules encapsulated is in both cases, Mo<sub>132</sub>(HCOO<sup>-</sup>) and Mo<sub>132</sub>(SO<sub>4</sub><sup>2-</sup>), the same: 72 coordination water molecules and a {H<sub>2</sub>O}<sub>100</sub> cluster. As the cavity with sulphates is smaller than in the case of formates, Mo<sub>132</sub>(HCOO<sup>-</sup>) and Mo<sub>132</sub>(SO<sub>4</sub><sup>2-</sup>) can easily be regarded as containers of forms of LDW and HDW water nanodrops, respectively. Therefore, the comparison between the structures of encapsulated water inside a Mo<sub>132</sub>(HCOO<sup>-</sup>) or Mo<sub>132</sub>(SO<sub>4</sub><sup>2-</sup>) cavity shows that, due to the commensurability between the size of the Mo<sub>132</sub> cavity and the correlation length of water, confinement selects one of the two forms of water. Hence, small changes of the system can lead to the splitting of the water encapsulated into HDW/LDW configurations.<sup>12c</sup>

Figure 6.1 compares the radial distribution function profiles obtained from MD simulations on the formate and sulphate closed capsules.<sup>12c</sup> As far as dynamic regimes are concerned, both formate and sulphate ligands inside the POM have common characteristics: both present few molecules around the centre of the

capsule ( $\beta$ ), internal dodecahedral shells ( $\gamma$ ), a set of two-dimensional arrays of hydrogen bonds ( $\delta$ ) and finally the coordination water layer ( $\epsilon$ ).

Comparing Tables 6.1 and 6.2, the location of the concentric water layers is almost the same for  $\gamma$  and two innermost  $\delta$  shells in both, formates and sulphates cases. So, the  $\delta_{\text{CF}}$  layer can be interpreted as a new shell that arises as a consequence of the larger size of the cavity decorated with formates. Consequently, the appearance of the  $\delta_{\text{CF}}$  layer allows the system to flicker between  $\delta_{\text{AF}}$  and  $\delta_{\text{CF}}$ . In other words, when one position in the dodecahedral  $\delta_{\text{AF}}$  is occupied, the corresponding site on  $\delta_{\text{CF}}$  will be empty and vice-versa. This under-occupation is indicated in Table 6.1 with the subindex 20/2 and it is related to the overlapping of the radial distribution function  $\delta$  peaks in Figure 6.1.

All these simulations have been performed considering that the capsules are plugged with large cations. The model of the capsule is rigid with the positions of the atoms taken from the X-ray analysis.

### 6.1.2 - New Model for the $\text{Mo}_{132}$ Keplerate in Aqueous Solution

In the previously mentioned MD simulations, the SPC/E force field model for water was used. All the new simulations presented on this Chapter, however, were performed using the TIP4P/2005 because, although the computational cost will be higher (the latter is a four-site model while SPC/E is a three-site model only), TIP4P/2005 model is able to better reproduce the behaviour of water molecules at a wide range of conditions.<sup>162</sup>

Regarding the  $\text{Mo}_{132}$  capsule, the MD simulations mentioned in the previous section used the molecular force field based on the positions of atoms extracted from X-ray experiments and a parametric approach for the point charges distribution (Charge Equilibration Method).<sup>167</sup> This model will be referred to as primitive capsule model. The new model proposed in Chapter 2 (see section on *Point Charges Distribution*) aims at achieving a better description of the charge distribution in the Keplerate by solving the quantum-mechanical problem by means of DFT. The result is that the primitive and new capsules are slightly different. The radius of the capsule (distance between two

centres of opposite pentagons) is of 12.82 Å for the X-ray geometry and 13.34 Å for the DFT obtained configuration. The effects of these differences between the models are studied in this chapter.

To summarise, we are using a different water model (which should not affect our results), a more realistic configuration, namely, a Mo<sub>132</sub> open capsule in solution instead of a closed capsule without external solvent, and a different POM characterization (geometry and charges extracted from quantum calculations, as well as the presence of cations of different nature in the solution). Therefore, the comparison between closed and open capsules must be performed thoroughly and taking into account the mentioned differences between models.

### 6.1.1 - Goals

In the context of the previous studies related to the water molecules structures formed inside of Mo<sub>132</sub> cavities, with different inner decorations that modify the cavity properties, this Chapter aims at collecting a series of MD simulations in order to describe the behaviour of Mo<sub>132</sub> in solution with open pores and different kinds of counter-cations. The main goals of this Chapter are, thus:

- Comparison between the primitive and current model results.
- Description of the distribution of cations around or inside the capsule for a set of cationic species.
- Effects of the temperature on the distribution of water molecules and counter-cations.

## 6.2 - Computational Details

The MD simulations collected in this chapter have been carried out using the DL\_POLY Classic 1.9 program package<sup>176</sup>. A simulation box with initial dimensions of 7x7x7 nm<sup>3</sup> was considered, containing one Mo<sub>132</sub> anion with 30 fixed ligands, the corresponding 42 counter-cations and 11000 TIP4P/2005 water molecules. This results on a system with a density of 1.09 g·cm<sup>-3</sup> and a concentration of Mo<sub>132</sub> anions  $C^0=0.0048 \text{ mol}\cdot\text{L}^{-1}$ . Acetate and formate ligands have been considered as inner surface decoration of the Mo<sub>132</sub> cavity.

All the molecular species present in the simulation box were treated as rigid bodies, in order to reduce computational cost. Even if with this approach flexibility of the pores cannot be reproduced, our results are in good agreement with experimental observations. In spite of the limitations of this simplifying approach, rigid body motion is a good approximation that allows us to properly reproduce the behaviour of the Mo<sub>132</sub> capsule in aqueous solution.

Intermolecular interactions are modelled using Lennard-Jones (LJ) potentials and electrostatic forces. In the case of the Keplerate, LJ parameters from previous studies have been used.<sup>46a, b, 16c, 146b, 174</sup> Regarding the electrostatic parameters for the Mo<sub>132</sub> cluster, partial charges were derived from the Voronoi Density Deformation population analysis<sup>174a</sup> of the optimised electron density at the standard DFT level (ADF2012 / COSMO / ZORA / BP86 / TZP).

Moreover, ligands and counter-cations parameters were extracted from the OPLS-AA force field.<sup>145b, 146a</sup> Water molecules were represented by means of the TIP4P/2005 model<sup>162</sup>. Crossed interactions between unlike atoms have been calculated from Lorentz-Berthelot combining rules.<sup>144</sup>

Long-range Coulombic interactions were evaluated through the Ewald summation technique, with a convergence parameter of 0.210 and considering a maximum of six wave vectors in each direction. Translational equations of motion were integrated using the Verlet leapfrog algorithm with a time step of 1 fs and a cut-off radius of 16 Å.

The simulations were carried out in the NPT ensemble, controlled by a Nosé-Hoover thermostat and a Andersen barostat with relaxation times of 0.02 ps and 0.1 ps, respectively. Periodic boundary conditions were used in all cases. The initial configurations were generated with the Packmol<sup>137</sup> software. The standard procedure for almost all the simulations presented in this chapter consists of an equilibration run of 1 ns followed by a production run of 4 ns. Trajectory snapshots were stored each 1000 time steps. Those snapshots were used to compute the radial distribution function  $g(r)$ . In order to calculate the  $g(r)$  for the species with respect to the centre of the cavity, the simulation box was divided into concentric shells of width of 0.035 Å with their origin at the centre of the Mo<sub>132</sub> capsule.

## 6.3 - Results

### 6.3.1 - Comparison Between the Primitive and the New model

Let us consider in the first place simulations using the primitive model of the capsule with closed gates and SPC/E water molecules<sup>12</sup> (system 1) and compare them with the results of an open system with the same primitive model for the capsule, but with TIP4P/2005 and guanidinium cations initially distributed randomly inside the simulation box and out of the capsule (system 2). In both cases, temperature was set to 298 K. In Figure 6.1 the red line represents the radial distribution function for the water molecules in system 1. In turn, Figure 6.2 shows the profiles of water and guanidinium cations for the POM up to a radius of 20 Å from the centre of the capsule for system 2. Several aspects are to be considered here. In the first place, we observe in Figure 6.2 that the guanidinium cations are not able to plug the pores but they only linger around the gates at somehow two characteristic distances of 15 Å and 18 Å from the centre of the Keplerate. No clear pairing of these cations with the capsule is then observed. Hence, the results of the primitive model for the capsule indicate that no plugging occurs with guanidinium at this high temperature and water exchange between the inner and outer media then is allowed.

Secondly, as far as the structure of water is concerned, in Figure 6.2 we still observe the  $\beta$ ,  $\gamma$ ,  $\delta$ , and  $\epsilon$  layers, but these show slightly different features when compared to Figure 6.1. On the one hand, the  $\delta_{\text{AF}}$  sublayer observed in the system 1, it has become a shoulder for system 2, while the  $\delta_{\text{CF}}$  sublayer is still visible. Moreover, in the open system, we find presence of water molecules inside the pores, which correspond to the small peak at the right hand side of the  $\epsilon$  shell in Figure 6.2, referred to as  $\zeta$  layer from now on. Even including these latter molecules, the occupation of the system 2 is only of 168 instead of the 172 used in the simulations with closed gates.<sup>12</sup> Hence, in general, the number of molecules in each peak is inferior for the open system than for the closed. The original choice of 172 water molecules encapsulated in the original simulations was due to the experimental value observed through the X-ray analysis at 188 K. Hence, the simulations of the system with closed gates (system 1) may reveal effects of strong confinement due to this forced density.

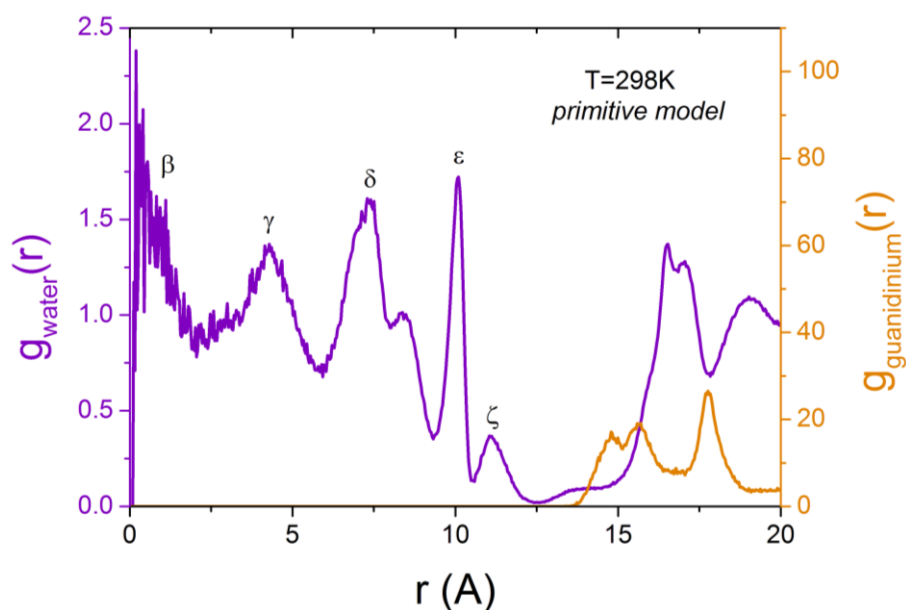


**Figure 6.2:** Radial distribution functions from the centre of the  $\text{Mo}_{132}(\text{HCOO}^-)$  capsule for the water molecules (violet) and the guanidinium counter-cations (orange). These radial distribution functions were extracted from MD simulations at  $T=298$  K performed using the primitive model for the Keplerate description but considering the capsule as an open system (system 2).

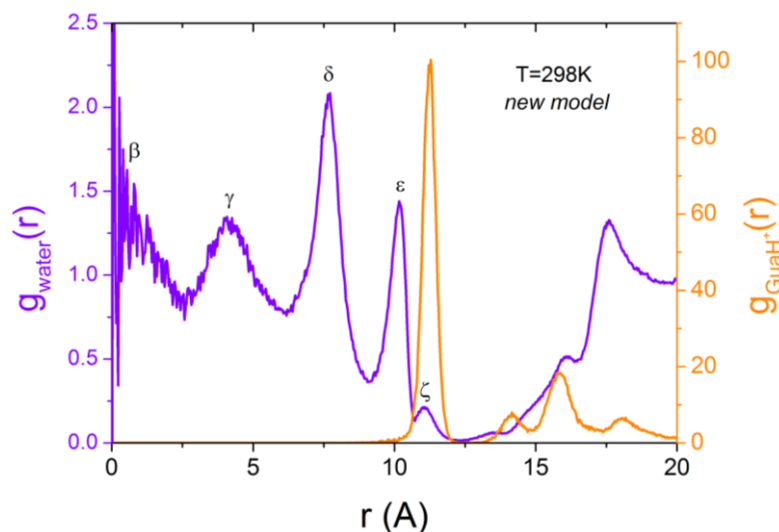


**Figure 6.3:** Radial distribution functions from the centre of the  $\text{Mo}_{132}(\text{HCOO}^-)$  capsule for the water molecules (violet) and the guanidinium counter-cations (orange). These radial distribution functions were extracted from MD simulations at  $T=298$  K performed using the new model for the Keplerate description and considering thus the capsule as an open system (system 3).

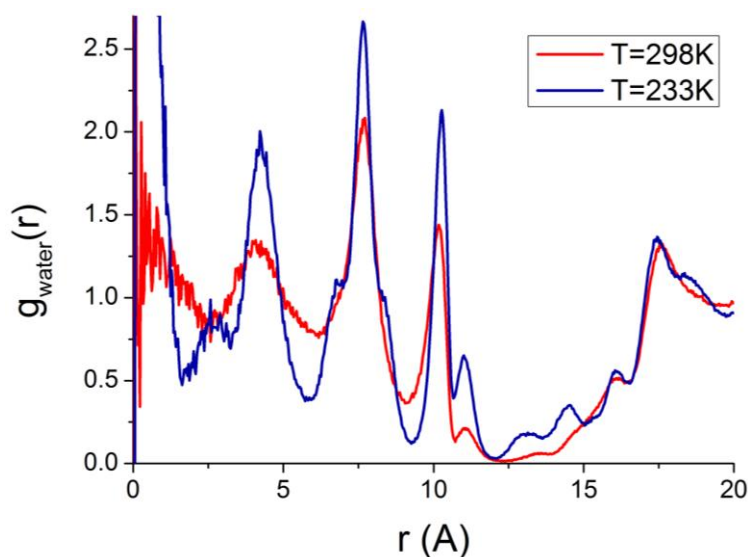


**Figure 6.4:** Radial distribution for the oxygen atoms of water molecules from the centre of the  $\text{Mo}_{132}(\text{HCOO}^-)$  capsule at  $T=298$  K (red line) and  $T=233$  K (blue line). Notice the increase of the number of molecules inside the pore ( $\zeta$  layer) when lowering the temperature. There is a correlation between the increase of the  $\zeta$  shell and the appearance of the substructure in the  $\delta$  layer. We will see the same correlation when changing the type of counter-cation. Furthermore, the structure near the centre of the capsule is different, although it involves only few molecules, and can be strongly influenced by details of the force field.



Thirdly, the same simulations with open gates have been performed with the new model for the capsule (system 3). Figure 6.3 shows the radial distribution function for the water molecules in the case of the open capsule in aqueous solution with the new model, TIP4P/2005 water, and the same model for the guanidinium counter-ions,<sup>145b, 146a</sup> under the same conditions as in the simulations of Figure 6.2 (T=298 K; p=1 atm). Table 6.3 compares the location and population of the encapsulated water shells, extracted from the radial distribution function of the primitive and the new model simulations, both for the open capsule (systems 2 and 3). For the new model with the open capsule (system 3), we observe the total disappearance of the substructure of the  $\delta$  layer. Additionally, this layer is located slightly farther away from the centre than for the primitive model, and its high is significantly larger than in system 2, although the total number of molecules for the latter is larger than for the former due to its larger width.

Hence, in comparison with system 1, namely with closed gates, the pores open, together with the slightly larger volume of the capsule represented by the new model (system 3), make the system less structured at high temperature. However, the substructure of the  $\delta$  shell is latent in the system. For instance, when decreasing the temperature to T=233 K\* two shoulders appear at both sides of the original  $\delta$  layer (Figure 6.4). Such shoulders can be considered as the precursors of the  $\delta_{AF}$  and  $\delta_{CF}$  shells observed in the experiments done at 188 K, which would be enhanced as the temperature is significantly decreased, and the overall density of water inside the capsule, increased. In the same direction go the observations made with different cations, which we discuss in the next subsection. When  $NH_4^+$  are acting as counter-cations, for instance, the  $\zeta$  layer is larger than in guanidinium, and the  $\delta_{AF}$  and  $\delta_{CF}$  substructures appear under the same conditions.

The other water layers ( $\beta$ ,  $\gamma$ , and  $\epsilon$ ) are similarly described by both the primitive and the new models at T=298 K, considering the capsule open in both cases (systems 2 and 3), while the structures for system 1 (closed gates) is significantly different. As we have already mentioned, these differences may lie

---

\* Notice that for the TIP4P/2005 at p=1 atm the transition between liquid and solid phases is located around 251 K, instead of the 273.15 K experimentally observed for water at these conditions. Hence, 233 K corresponds to metastable supercooled water, whose long life-time is due to the smallness of the system.<sup>168</sup>

on the different overall density inside the capsule when open or closed pores are considered.

As far as guanidinium counter-ions are concerned, the most salient feature of system 3 is the high peak indicating that the guanidinium cations are inside the pore, plugging indeed the gate, unlike the observations of system 2 (see Figures 6.2 and 6.3). The number of plugged pores is around 11 out of 20 in average at 298 K. The other guanidinium molecules remain close to the surface, near the pores. Therefore, at this temperature the plugging effect is incomplete and transport through the pores is allowed. The properties of the primitive capsule (system 2) do not permit the formation of plugged pores mostly due to the geometrical constraints.

**Table 6.3:** Location and population of the water layers formed in the inside of the  $\text{Mo}_{132}(\text{HCOO}^-)$ , considering the capsule's pores initially open and the plugging counter-cations randomly distributed outside the Keplerate at  $T=298$  K. Both, primitive and new, models have been considered (systems 2 and 3, respectively).

<i>Primitive Model (system 2)</i>			<i>New Model (system 3)</i>		
Notation	Location	Population	Notation	Location	Population
$\gamma$	4.3	27	$\gamma$	4.1	28
$\delta$	7.4	81	$\delta$	7.7	73
$\epsilon$	10.1	41	$\epsilon$	10.2	49

To end this comparison between models, we review the more relevant conclusions. We have observed that there is a quite significant impact of the explicit consideration of the external medium and the transport of matter through the pores. It is reflected in, for example, the lower number of water molecules trapped inside the hollow of the cavity in systems 2 and 3 at 298 K. It seems then that forcing 172 molecules into the cavity (system 1) is a strong constraint that influences the way water molecules arrange inside. One has to keep in mind that the experiments revealing the structure of the water layers are done at 188 K suggesting that at such low temperature the system allows larger number of water molecules to accommodate inside. Hence, with open pores and external medium it is not to be expected that the same structure remains unchanged at 298 K. The structure observed during previous work of our group<sup>12</sup> (system 1) would correspond to higher water density, which, for these models, would require much larger pressure.

Moreover, the new model for the capsule has a slightly larger volume, which further affects how the layers stack inside the cavity, due to a commensurability constraint. However, it is remarkable the fact that guanidinium cations can fit well into the pores with this model. Therefore, we will use the new model in the rest of our analysis, since we will centre our attention to the effects related to the counter-cations for a POM in contact with an external medium.

Finally, we come to the conclusion that some of the studied features are strongly dependent on the details of the force field used for both the capsule, water molecules as well as counter-cations. As we have seen, small changes show strong differences. Moreover, it is known that the models used for the water cannot quantitatively yield simultaneously density and pressure. Therefore, since our simulations were done at constant atmospheric pressure, we estimate that some of the properties studied depend more strongly on the working density than the nominal pressure. Hence, simulation results have to be interpreted with care.

### 6.3.2 - Analysis of the behaviour of different counter-cations

In this section we thus proceed to study the interactions of the Keplerate macro-anion and the counter-cations in aqueous solution. For this purpose, a set of MD studies in the NPT ensemble are performed for a simulation box that includes the Mo<sub>132</sub> capsule, represented by the new model, with its corresponding 30 fixed formate ligands, 42 counter-cations randomly distributed, and 11000 TIP4P/2005 water molecules. As far as the cations are concerned, different species have been tested: Li<sup>+</sup>, Na<sup>+</sup>, NH<sub>4</sub><sup>+</sup>, guanidinium (C(NH<sub>2</sub>)<sub>3</sub> or Guam<sup>+</sup>) and tetra-methyl ammonium (NMe<sub>4</sub><sup>+</sup>). Among these, the size of Li<sup>+</sup>, Na<sup>+</sup>, and NH<sub>4</sub><sup>+</sup> allows them to cross the pores and exchange between the inner and outer media. Notice, however, that the charge of the walls of the anion will affect its preferred location, depending on the equilibrium between the electrostatic interaction, the solvation layer, as well as the entropic effects. Guanidinium and tetra-methyl ammonium, in turn, are excluded from the inside of the cavity due to its large size. The shape of these counter-cations roughly corresponds to that of the gates. Therefore, both are candidates to be used as plugs for the capsule.

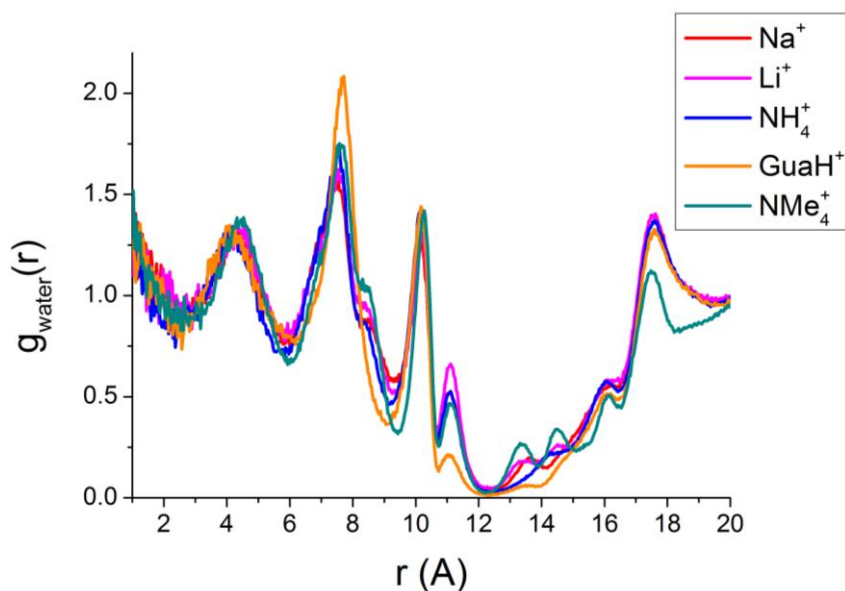


**Figure 6.5:** Radial distribution function of the oxygen atom of water molecules from the centre of the capsule. These results have been extracted from MD simulations in the NPT ensemble at  $T=298$  K and  $p=1$  atm. Each colour represents the results obtained when a different counter-cation: red for sodium ( $Na^+$ ), pink for lithium ( $Li^+$ ), blue for ammonium ( $NH_4^+$ ), orange for guanidinium ( $GuaH^+$ ) and dark cyan for tetra-methyl ammonium ( $NMe_4^+$ ) cations.

Figure 6.5 shows that the layered structure of water molecules encapsulated is roughly the same despite the presence of some counter-cations in the cavity or at the gates. Table 6.4 collects the location of the radial distribution peaks and the population of each layer. Figure 6.5 and Table 6.4 show that the location and population of each layer does not show dramatic changes when different cationic species are present. Furthermore, the number of water molecules encapsulated inside the  $Mo_{132}$  macro-ion is very similar for all the simulations with different counter-cations: 156 for the sodium simulations, 159 for the lithium counter-cations, 155 in the case of ammonium cations, 152 for guanidinium and tetra-methyl ammonium cations. These values are calculated by means of the integration of the radial distribution function from the centre of the capsule to the end of the  $\epsilon$  shell. The molecules in the  $\zeta$  shell are thus excluded. The number of water molecules in the pore ( $\zeta$  layer) is 23 in the case of sodium simulations, 26 when lithium cations are present, 21 when ammonium groups are acting as counter-cations and 18 when the cationic species is tetra-methyl ammonium. In the case of guanidinium simulations the number of water molecules that are preferably found at the pores is

considerably less (8 water molecules only). The low number of molecules in the pore for this latter case is due to the plugging of guanidinium counter-cations, which fit into the pore, displacing the water molecules that would naturally occupy this space (see Figure 6.5). As we have mentioned, the occupation of the  $\zeta$  layer is correlated to the formation of the substructure of the  $\delta$  layer. Notice in Figure 6.5 that the shoulders of the  $\delta$  shell appear always that there are around 20 water molecules in the pore. Instead, if these molecules are removed by a large cation, the  $\delta$  peak is structureless. Despite the fact that the  $\epsilon$  layer in  $g(r)$  is located between the  $\zeta$  and  $\delta$  layers, the former is in fact confined under the  $\text{Mo(V)}$  pentagons, so that the  $\zeta$  and  $\delta$  shells are in direct contact precisely at the pores. Therefore, the correlation between these two layers should not be surprising. Finally, radial distribution functions from Figure 6.5 also show some differences on the behaviour of the external solvation shells of the  $\text{Mo}_{132}$  capsule. We will see later that the peaks observed correspond to the solvation shells of cations preferably located at these particular positions.

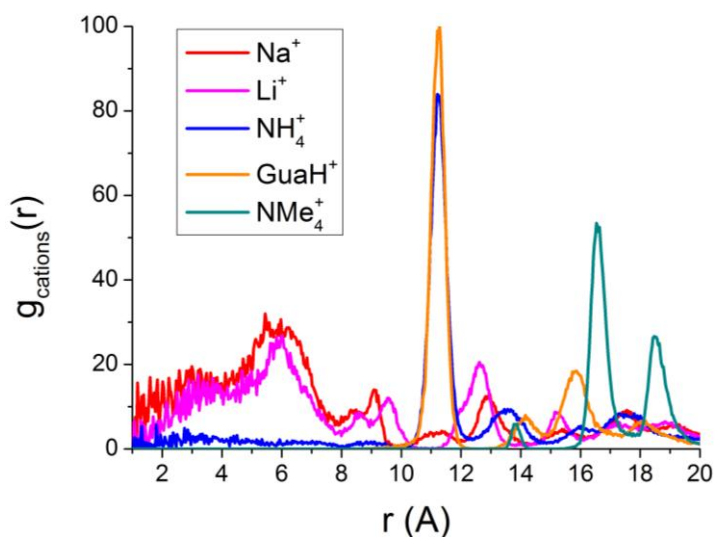


**Figure 6.6:** Radial distribution function of counter-cations from the centre of the  $\text{Mo}_{132}(\text{HCOO}^-)$  capsule. These results have been extracted from MD simulations in the NPT ensemble at  $T=298$  K and  $p=1$  atm. Each colour represents an independent simulation in which a different cationic species acts as counter-cation: red for sodium ( $\text{Na}^+$ ), pink for lithium ( $\text{Li}^+$ ), blue for ammonium ( $\text{NH}_4^+$ ), orange for guanidinium ( $\text{GuaH}^+$ ) and dark cyan for tetra-methyl ammonium ( $\text{NMe}_4^+$ ) cations.

**Table 6.4:** Location and population of the water layers encapsulated  $Mo_{132}(HCOO^-)$  in the presence of different species acting as counter-cations. These results have been extracted from MD simulations in the NPT ensemble at  $T=298$  K and  $p=1$  atm.

Counter-cation	Layer	Peak (Å)	Population
$Na^+$	$\beta$	0	2
	$\gamma$	4.29	26
	$\delta$	7.53	82
	$\epsilon$	10.18	46
	$\zeta$	11.08	23
$Li^+$	$\beta$	0	3
	$\gamma$	4.40	26
	$\delta$	7.54	84
	$\epsilon$	10.19	46
	$\zeta$	11.12	26
$NH_4^+$	$\beta$	0	2
	$\gamma$	4.17	24
	$\delta$	7.54	78
	$\epsilon$	10.16	51
	$\zeta$	11.08	21
$GuaH^+$	$\beta$	0	2
	$\gamma$	4.14	28
	$\delta$	7.73	73
	$\epsilon$	10.19	49
	$\zeta$	11.05	8
$NMe_4^+$	$\beta$	0	2
	$\gamma$	4.49	27
	$\delta$	7.63	82
	$\epsilon$	10.29	41
	$\zeta$	11.12	18

Regarding the cation distribution, two different patterns are found. Figure 6.6 shows that small cations as sodium or lithium are able to penetrate into the capsule, while larger cations, such as guanidinium or tetra-methyl ammonium, are located near and at the pores. Ammonium cations are surprisingly more likely located at the pores that in the cavity, despite the fact that its size is

smaller than the size of the pores. Nevertheless, one cation is able to penetrate into the capsule and it placed around the centre of the capsule. These results are compatible with the experimental findings.<sup>50b</sup>

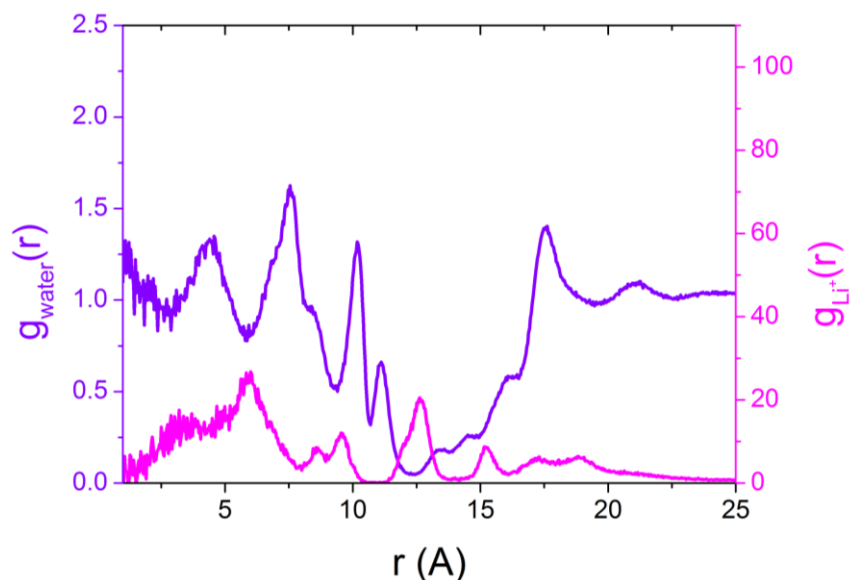


**Figure 6.7:** Comparison between the radial distribution functions from the centre of the capsule  $\text{Mo}_{132}(\text{HCOO}^-)$  for the water molecules (violet) and the lithium counter-cations (pink). Due to the different order of magnitude of both  $g(r)$ , two different scales were used.

Figure 6.7 shows the comparison between the radial distribution functions for the lithium counter-cation and the water molecules. The cations inside the cavity are preferably placed in the valleys between the native  $\beta$ - $\epsilon$  layers of water, without significantly modify their size and shape. Moreover, we find some of these cations (4) occupying a region in the centre of the pore, just after the  $\zeta$  shell. The cations in the external medium lay also at the valleys of the radial distribution function of water molecules, indicating that the peaks in the water profile are related to solvation shells of these cations. The genuine radial distribution function of bulk water is visible only after 17 Å from the centre of the capsule. The analysis of the behaviour of  $\text{Na}^+$  is completely analogous to lithium.

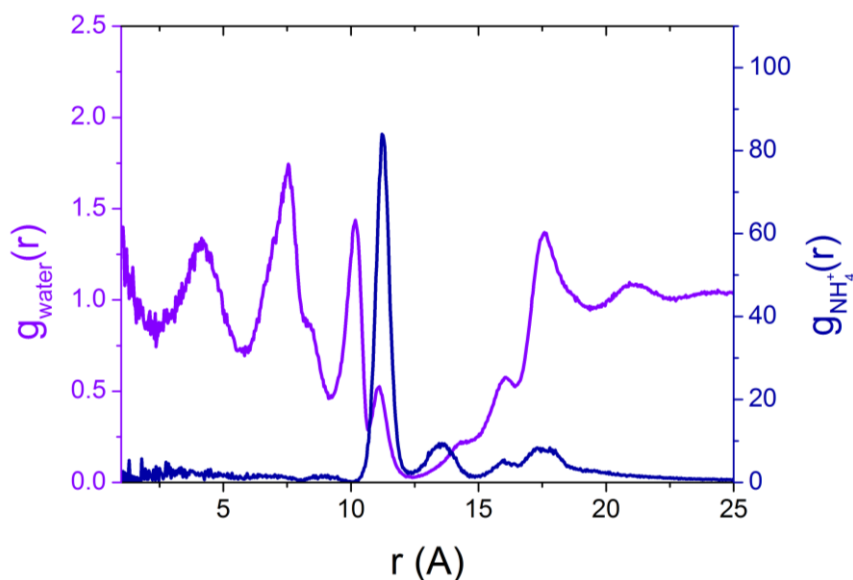


**Figure 6.8:** Comparison between the radial distribution functions from the centre of the capsule  $\text{Mo}_{132}(\text{HCOO}^-)$  for the water molecules (violet) and the ammonium counter-cations (blue). Due to the different order of magnitude of both  $g(r)$ , two different scales were used.

In the case of ammonium cations (Figure 6.8), we observe a large peak (11 molecules) right at the location of the  $\zeta$  layer. This peak corresponds to counter-cations inside the pore but around  $1.5 \text{ \AA}$  closer to the centre than the lithium cations. This location is equivalent to the peak of  $g(r)$  observed for complexed guanidinium counter-cations. Moreover, only one molecule is found inside the cavity. This is a remarkable effect since the pores do not exclude ammonium due to its smaller size. Hence, the coordination with the water molecules at the pore is responsible for the stability of this particular location. In addition, notice that the size of the  $\zeta$  layer is the same as for the lithium simulations, unaffected by the presence of  $\text{NH}_4^+$  at the entrance of the pores. As a consequence, we observe again that the substructure of the  $\delta$  peak is visible at the studied temperature for this cation.

Table 6.5 gives the number of cations found inside the capsule or at the pores, calculated from the integration of the radial distribution functions of the cations.



**Table 6.5:** Number of cations encapsulated and at the pores for the set of  $\text{Mo}_{132}(\text{HCOO}^-)$  simulations with different species acting as counter-cations.

counter-cation	# cations inside	# cations at the pores
$\text{Na}^+$	6	4
$\text{Li}^+$	6	5
$\text{NH}_4^+$	1	11
$\text{GuaH}^+$	0	11
$\text{NMe}_4^+$	0	1

Larger cations, as guanidinium and tetra-methyl ammonium, are preferably found near the pores and outside the capsule, due to their exclusion by size. For both cases, the simulation starts with all the counter-cations randomly distributed in the outer medium. After a short time of the order of 250 ps,  $\text{C}(\text{NH}_2)_3^+$  and  $\text{NMe}_4^+$  groups are spontaneously driven to the vicinity of the pores, eventually closing some of them. When a  $\text{C}(\text{NH}_2)_3^+$  or  $\text{NMe}_4^+$  plugs a pore, it forms a pair which lasts the whole simulation, mostly without changing the relative orientation of the counter-cation with respect to the capsule.

Comparing  $\text{C}(\text{NH}_2)_3^+$  and  $\text{NH}_4^+$  radial distribution pattern (Figures 6.3 and 6.8, respectively), guanidinium cations are preferably located at the pores, right at the position where the  $\zeta$  layer should be and at the same location of the ammonium groups in the aforementioned simulation. However, with respect to the latter, the  $\zeta$  layer is removed by the larger size of the guanidinium cation. Obviously, the defective water molecules in the  $\zeta$  shell perturb the nearest environment up to the point that the substructure of the  $\delta$  layer is not visible. This correlation is one of the more interesting findings of this Chapter.

At this point it is interesting to look at the plugging of the gates due to the presence of guanidinium counter-cations. we observe that guanidinium cations are indeed plugging 11 out of  $\text{Mo}_{132}$  pores, according to the area under the peak of the  $g(r)$  at 11.5 Å (Figure 6.9a). Some cations remain close to the POM surface at rather well defined positions out of the capsule, at 14, 16 and 18 Å from the centre of the capsule. These peaks are labelled as *outside* 1, 2 and 3 and their average population is 2, 9, and 5, respectively. These layers are solvated guanidinium counter-ions. The peak *outside* 1 corresponds to counter-cations placed at the external surface of the pores that are not plugged by the

11 complexed guanidinium groups (Figure 6.9b). Water molecules bridge the guanidinium cations with the negative centres in the structure of the pore. The peak *outside 2* corresponds to the solvated guanidinium molecules that are located on top of unoccupied pores solvated by a water layer (Figure 6.9c). Finally, the peak *outside 3* gathers solvated counter-ions wandering on the solvated surface of the POM. The remaining 15 cations are completely solvated in the bulk.

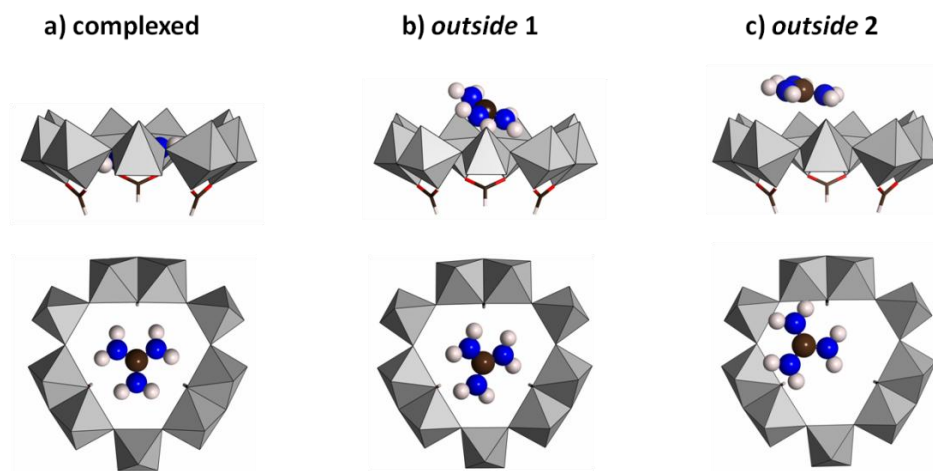


**Figure 6.9:** Schematic representation of the location of the guanidinium cations with respect to the  $Mo_{132}(HCOO^-)$  pores. Grey polyhedra stand for the  $MoO_6$  units of the Keplerate. Red, brown and white sticks represent the oxygen, carbon and hydrogen atoms of the formate ligands, respectively. Finally, blue, brown and white balls are the nitrogen, carbon and white atoms of the counter-cation, respectively. Complexed guanidinium cations (a) are found at the central position of the pores. A similar location is observed for the counter-ions of region *outside 1*, but at a larger distance from the centre of the capsule. Finally, guanidinium molecules in the region *outside 2* are likely placed further away from the POM surface, and its position with respect to the centre of the gate is less symmetric in comparison with a) and b) situations. Although the configurations shown in this figure are snapshots of 4 ns MD simulations, the characteristics aforementioned for the complexed counter-cations, as well as those from regions *outside 1* and *2*, are general tendencies observed during the whole simulation.

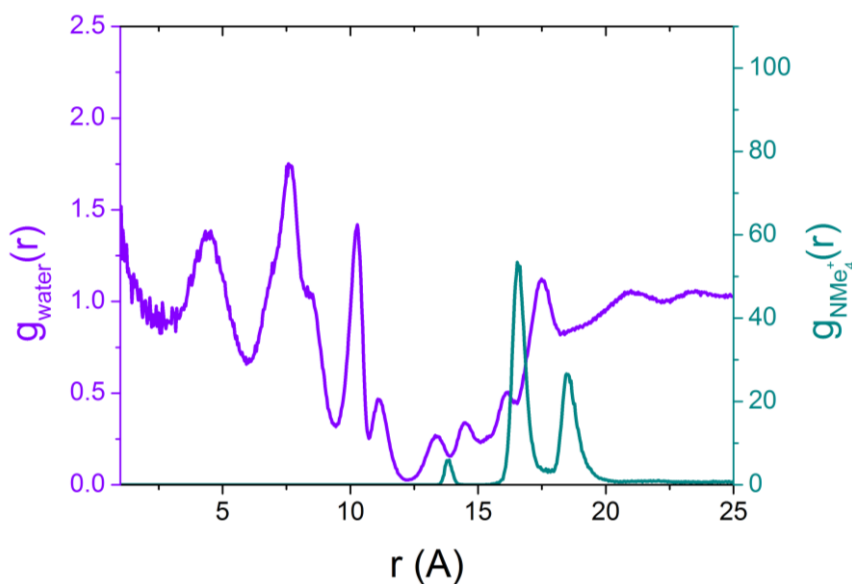


**Figure 6.9:** Comparison between the radial distribution functions from the centre of the capsule  $Mo_{132}(HCOO^-)$  for the water molecules (violet) and the tetra-methyl ammonium counter-cations (dark cyan). Due to the different order of magnitude of both  $g(r)$ , two different scales were used.

As far as the tetra-methyl ammonium is concerned (Figure 6.9), we find at 298 K one single counter-cation complexed with the pore, thus effectively plugging the gate. Figure 6.9 represents the radial distribution functions for water molecules, together with tetra-methyl ammonium counter-cations. The plugging  $NMe_4^+$  is located at the outer part of the pore, instead of inside, as was the case of guanidinium and ammonium cations. Moreover, 16 additional cations dwell on the pores with the same orientation than the plugging counter-cation at a distance of 16 Å from the centre of the capsule. These 16 counter-cations are strongly bound to the capsule, but could be arguable whether they plug the gate or not, forbidding species from exchanging between the inner and outer media. Although these cations belonging to the 16 Å peak are further away from the macro-ion than the plugging cations, we have observed that they are moving together with the capsule, as a complex. In Chapter 7 we discuss in depth the role played by the hydrophobic character of tetra-methyl ammonium cations in their affinity for the Keplerate anion.

Our model considers the Keplerate as a rigid molecule. Experimentally, however, it is observed that the Mo<sub>132</sub> pores are flexible, allowing the entrance of larger guests than the pore dimensions would suggest, without causing irreversible damage of the pore.<sup>8b, 237</sup> Experimental studies on the interaction of tetra-methyl ammonium cations and the Mo<sub>132</sub> macro-ion show that almost no encapsulation occurs for this cation. Moreover, experimental analyses regarding small cations show that, indeed, these cations are able to enter the capsule and interact distorting in some way the concentric water shells formed under confinement. Both facts allows us to conclude that, even with the rigid body approach, our model reproduces the experimental results.<sup>57</sup>

### 6.3.3 - Temperature Effects

The last set of MD simulations presented in this chapter has as objective the analysis of the effects of the temperature has on the distribution of cations in a with respect to the POM macro-anion. On the one hand, the dependence of the plugging, for species such as guanidinium or tetra-methyl ammonium, with temperature, is by itself of relevance. The conditions under which the capsule is completely isolated from the outer medium can have direct implications in both scientific and technological applications of Keplerates. On the other hand, besides the inherent interest in the effects due to temperature in confined environments, it is experimentally observed that some NMR anomalies arise when decreasing the temperature for the system Keplerate + NH<sub>4</sub><sup>+</sup> in aqueous solution,<sup>238</sup> which deserve the separate analysis.

Let us first consider the set of MD simulations, within the NPT ensembles at different temperatures, for the Mo<sub>132</sub>(HCOO)<sub>3</sub>capsule and guanidinium as counter-cations, to keep the system electrically neutral. The analysis of the system's behaviour has been performed at different temperatures. Firstly, at T=298 K and T=273 K we have performed a 1 ns equilibration run from random distributions of C(NH)<sub>3</sub><sup>+</sup> outside the capsule, followed by a 4 ns production run. Then, from the final state at 273 K, we have performed a progressive cooling of the system in which we have lowered the temperature by 2.5 K each 250 ps, until T=235.5 K. The simulations corresponding to some cooling steps (T=270.5 K, T=263 K, T=253 K and T=248 K) have been extended to 4 ns, in order to avoid transient effects and loosing ergodicity.

One has to keep in mind that the TIP4P/2005 phase diagram of bulk water is shifted 20 K to lower temperatures with respect to the experimental observed solid-liquid coexistence line at 1 atm. Hence, the solid-liquid transition occurs around  $T=251\text{K}$ .<sup>162</sup> Therefore, the temperature of 273 K corresponds to a liquid phase for the water model under consideration, while the temperature of 235.5 K would correspond to a metastable state of supercooled water. For such small system, as well as in the presence of the capsule and the counter-ions, the metastable state is expected to last very long time, much larger than the overall time used in the simulations. Therefore, the process of annealing has been used to lead the system to the thermal equilibrium when the relaxation processes in the system are being significantly made slower by the decrease of the temperature and the increase of the viscosity of water.

We have analysed in the previous section the radial distribution function from the centre of the  $\text{Mo}_{132}(\text{HCOO}^-)$  capsule for guanidinium counter-cations at 298 K and  $p=1$  atm (Figure 6.3). Summing up, the  $g(r)$  has 4 peaks. The highest peak corresponds to 11 complexed cations inside the pores. In the outer medium but close to the POM surface, there are three additional peaks, namely regions *outside* 1, 2, and 3, corresponding to an average population of 2, 9. Taking the counter-cations in these three external layers, together with the aforementioned complexed ones, the number of bound counter-ions is of 27, while the remaining 15 cations are wandering in the bulk. It is therefore expected that the decrease of the temperature would allow the progressive closing of the twenty pores since, at this latter configuration, the anion would still keep a charge of -31. The additional peaks at outer locations turned to be a competing effect due to the effective lowering of the overall charge of the macro-anion.

The simulation at 273 K has been carried out starting from the same initial configuration as the one at 298 K. Figure 6.10 shows the corresponding radial distribution functions for water molecules and counter-cations. In this case, after 4ns, we observe that there are only 7 plugging complexed cations, while the external peaks sum up to 24 counter-ions, which particularly accumulate in *outside* 2. Therefore, when the temperature decreases from 298 K to 273 K, although the number of complexed plugging cations decreases from 11 to 7, we observe an increase on the number of counter-cations in the vicinity of the capsule, from 27 to 31. We can infer that, if we admit that the final

configuration is in thermal equilibrium and that the simulations performed are indeed ergodic, the solvation shell of the pore competes with the counter-ion that would be likely found deep inside the pore. For the same reason, the external peaks are enhanced by the stability of the solvation shells of the guanidinium counter-cations, together with the decrease of the Debye length with the temperature.

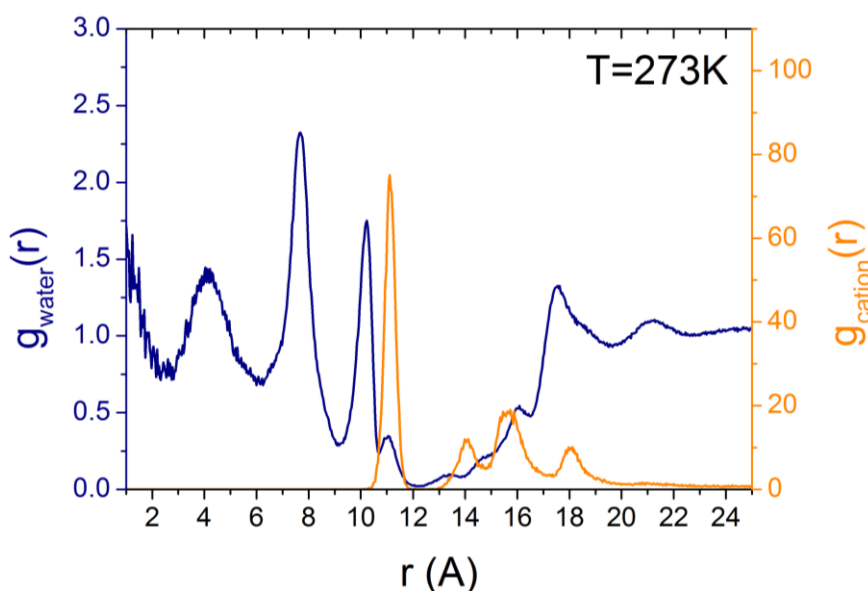


**Figure 6.10:** Radial distribution function from the centre of the  $\text{Mo}_{132}(\text{HCOO})$  Keplerate for water molecules and guanidinium counter-cations. These results were calculated from the trajectories of a 4 ns MD simulations in the NPT ensemble, with  $T=273$  K and  $p=1$  atm.

The analysis of the structures, obtained through an annealing process, as mentioned, reinforces the previous statements. In this case, however, the number of counter-cations complexed with the pores increases up to 10, while the total number of bound cations rises up to 29. This fact suggests that the anomalous value of 7 complexed counter-cations at 273 K may be due to a violation of the ergodicity in a system of slow relaxation.

Therefore, we can conclude that the plugging process is complex, and that the interaction between the counter-cations and the POM is mediated by the structure of water in a non trivial way. We may consider that complexed counter-ions, together with those in the peaks *outside* 1 and 2 are effectively

impairing the transport of substances across the gates. Using this criterion, we can estimate that already at 298 K the system would be practically closed.

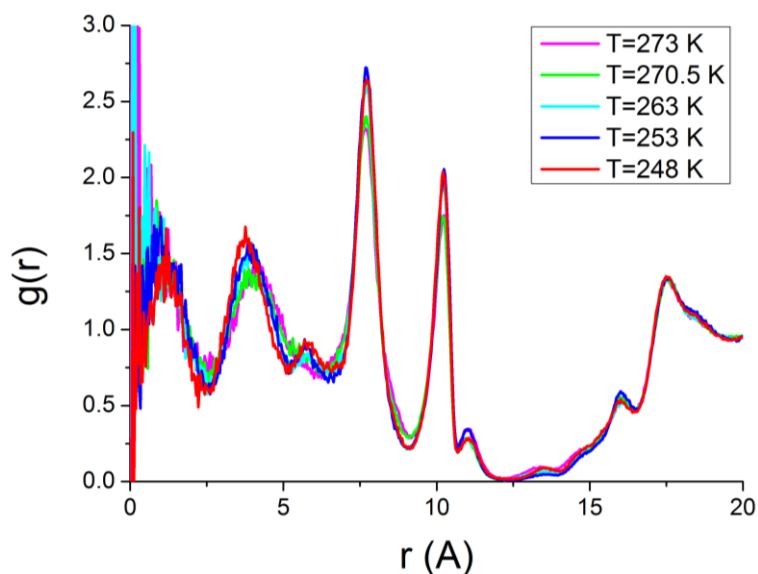


**Figure 6.11:** Radial distribution function of water molecules from the centre of the  $\text{Mo}_{132}(\text{HCOO}^-)$  capsule, extracted from NPT simulations of 4 ns length at  $p=1$  atm and at different temperatures.

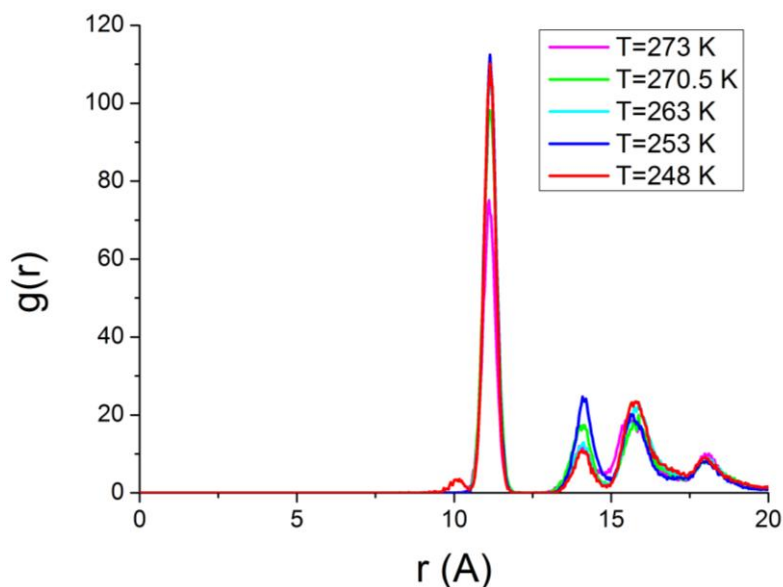


**Figure 6.12:** Radial distribution function of guanidinium counter-cations from the centre of the  $\text{Mo}_{132}(\text{HCOO}^-)$  capsule, extracted from NPT simulations of 4 ns length at  $p=1$  atm and at different temperatures.

In Figure 6.11 we show the radial distribution function from the centre of the capsule for the water molecules. When decreasing the temperature, we observe that the  $g(r)$  profiles are analogous to the ones at 298 K and 273 K. We observe that the peaks become sharper as the temperature is decreased, as it should be expected. We only detect a new kink between  $\gamma$  and  $\delta$  layers from 263 K and below. Although it has no clear explanation, it could be due to changes in the structure at the vicinity of the liquid-solid transition of our model for water (estimated at 251 K).

As far as guanidinium counter-cations are concerned, we observe in Figure 6.12 that the peak associated with the guanidinium counter-cations complexed with the pore increases as the temperature decreases. The high of the remaining outer layers (*outside* 1, 2, and 3) has a non monotonic behaviour, due to the mediation of the water molecules, but also due to the collective nature of the interaction: the increase of the number of counter-cations closer to the centre of the cavity weakens the overall electrostatic attraction felt at the outer layers, changing their structure. Let us finally remark that at 248 K we find one of the complexed ones, right at the inner entrance of the pore.

To introduce a different view in the complexation and the plugging of the pores by the guanidinium counter-cations, we analysed the diffusion coefficient of different species at different locations.

The self-diffusion coefficient ( $D$ ) of a particle is related to its mean squared displacement ( $\langle \text{MSD} \rangle$ ) at long times, according to Equation 6.1, where  $t$  stands for time. It is expected that the POM behaves diffusively, as indicated in Equation 6.1 at long times, which we estimate of the order of  $\tau \sim R^2/6D$ , where  $R$  is the hydrodynamic radius of the POM. Using the known radius of the Keplerate and the observed diffusion coefficient, we estimate that  $\tau \sim 5 \text{ ns}$ . For  $t \gg \tau$ , we thus expect that the MSD of the centre of the POM, as well as the one of any atom at its surface, is comparable, since the translational motion of the whole ensemble is the major contribution to the MSD. However, for short times, the translation of the centre of mass and the rotational diffusion can be separately observed. For such a short time simulation, we can split the MSD of any atom in the PM into two contributions, according to Equation 6.2, where  $r$  represents the distance of the given atom to the centre of mass the Keplerate,  $D_{\text{trans}}$  stands for the translational diffusion coefficient, related to the motion of



the centre of mass, and  $D_{\text{rot}}$  is the rotational diffusion coefficient around the centre of the capsule of the tagged particle solidly attached to the POM.

$$\langle MSD \rangle = 6Dt \quad (6.1)$$

$$\langle MSD(r) \rangle = 6(D_{\text{trans}} + D_{\text{rot}} r^2)t \quad (6.2)$$

When two particles are moving together, they may have different self-diffusion coefficients, but their rotational diffusion coefficient value will be the same, since the difference in MSD scales with the difference in  $r^2$ . Therefore, if we consider different atoms belonging to the Mo<sub>132</sub> macro-ion and we compute their self-diffusion coefficient, those values will lay in a straight line when represented as a function of the distance to the centre of mass of the Keplerate, because of the rigid body approximation. Therefore, we can identify whether a counter-ion or water molecule is complexed with the Keplerate for times up to the order of 5 ns, by representing its diffusion coefficient as a function of the square of the distance to the centre, and verifying that it lays in the same straight line as the molybdenum or oxygen atoms of the capsule. Thus, the analysis of the self-diffusion coefficient averaged over the particles belonging to a given peak of the  $g(r)$  gives us information about the relative motion between such particle and a the Keplerate anion.

In order to calculate the self-diffusion coefficient of water molecules, we have developed a purpose-made code to compute the MSD of each molecule. Firstly, such MSD values were averaged over time. Such time average is performed dividing the total length of the simulation in time windows of 100 ps with time origins shifted 10 ps each, to increase the statistics. Furthermore, this code is able to distinguish which particles belong to a given peak of radial distribution in order to perform an average over such molecules, and assign a self-diffusion coefficient to each peak of  $g(r)$ . Our code considers that a molecule belongs to a given region when it spends at least the 99% of the time window in the same region. To assign a single  $r$  value to whole peak, the  $r$  values of the molecules that spend at least the 99% of the time window in that region have also been averaged. This procedure is applied for water molecules and counter-cations.

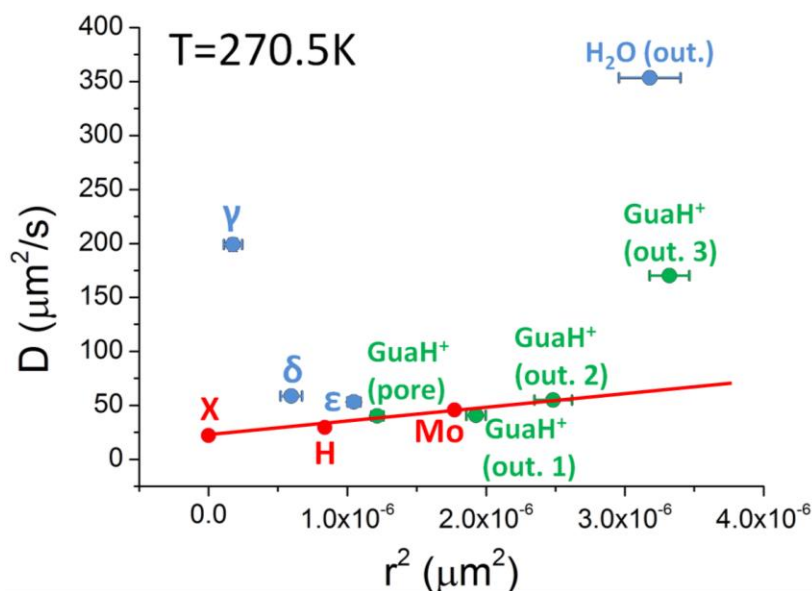


**Figure 6.13:** Self-diffusion coefficients ( $D$ ) of POM atoms (red), water layers (blue) and guanidinium counter-cations (green) as a function of the squared distance to the centre of the capsule. The red line indicates the values of  $D$  that would correspond to the moieties moving with the Keplerate ion. Such line has been calculated from the values of  $D$  for the POM atoms. These results have been extracted from NPT MD simulations at  $p=1$  atm. In this case,  $T$  was set to 270.5 K.

We thus evaluate the self-diffusion coefficient of water molecules located at different layers, as well as and counter-cations, upon cooling. For reference, we calculate this property for two types of atoms belonging to the POM unit, thus rigidly linked to the capsule, as well as the centre of mass, represented by X in Figure 6.13). The two types of atoms are the hydrogen atoms from the formates groups and the molybdenum atoms from the POM's scaffold. Self-diffusion coefficients of X, H and Mo define a straight line, from which the translational and rotational diffusion coefficients can be extracted. For the rest of species, the closer the diffusion coefficients are to this line, the more complexed these particles are to the Keplerate.

Figure 6.13 is a representative example of the series of simulations at different temperatures performed. For the selected temperature of 270.5 K values of  $D$  of the  $\gamma$  water layer suggest that its dynamics is closer to bulk water than other encapsulated water shells, as its  $D$  is considerably higher than the straight line defined by the POM atoms, as it is for the water molecules in the outside of the capsule. In contrast,  $\delta$  and  $\epsilon$  water shells have values of  $D$  closer to the line

defined by X, H and Mo atoms, which means that these layers act as solvation shells of the inner surface of the cavity, strongly bound to it. Such behaviour is in agreement with experimental observation of bound and free water and previous MD studies performed in our group.<sup>12</sup> These results suggest that the innermost layers of water have almost bulky properties, while the outermost layers have a stronger interaction with the confining surface. Let us define a new parameter  $d$ , which is the difference between the value of  $D$  for a given water shell and the value of  $D$  given by the straight line at the same distance. Figure 6.14 shows the variation of  $d$  for the  $\delta$  and  $\epsilon$  water shells as a function of the temperature. It is clear that as the temperature decreases,  $d$  decreases as well, which means that when cooling, the motion of the  $\delta$  and  $\epsilon$  water shells is more solidly following the motion of the Keplerate. Such feature of the bound water layers was not observed neither for the innermost  $\gamma$  dodecahedron nor the external water molecules.

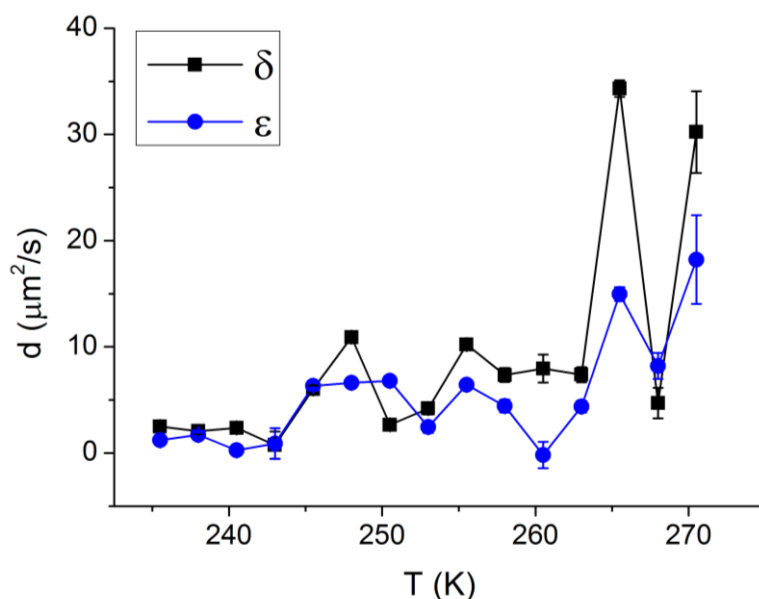


**Figure 6.14:** Evolution with temperature of the parameter  $d$  for the  $\delta$  (black squares) and  $\epsilon$  (blue circles) water layers encapsulated inside a  $Mo_{132}(HCOO^-)$  cavity and in the presence of guanidinium counter-cations.

As the temperature decreases, the dynamics of the guanidinium cations belonging to the regions *outside* 1 and 2 tend to be solidly follow the dynamics of the Keplerate. This effect is not observed for counter-cations belonging to region *outside* 3. In Figure 6.13 we observe that the cations inside the pore as well as in layers *outside* 1 and 2 are indeed complexed with the anion, confirming our previous statement about the fact that cations in the pore and in the proximal outer layers act as plugs of the gates.

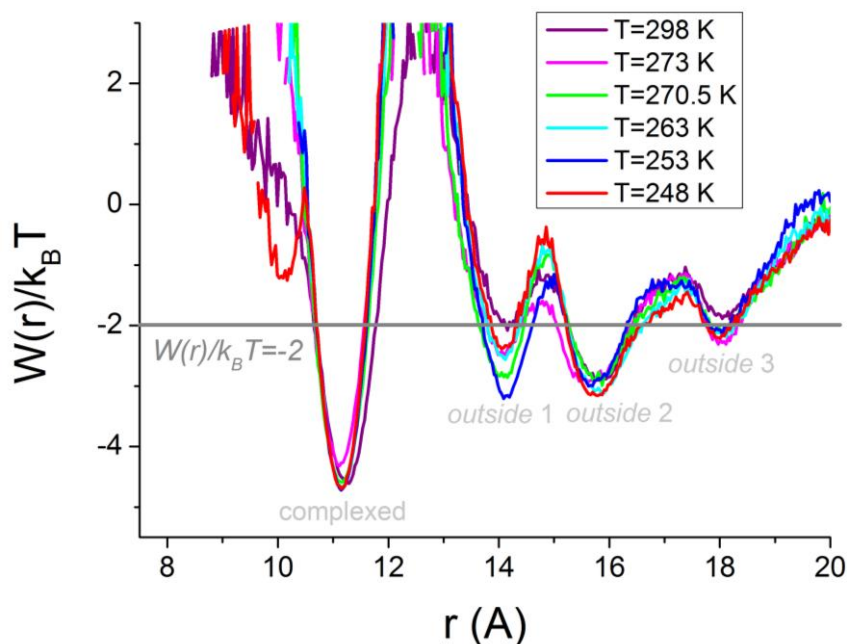


**Figure 6.15:** Representation of the potential of mean force for the guanidinium counter-cations as a function of the distance of the cations to the centre of the  $\text{Mo}_{132}(\text{HCOO}^-)$  capsule. These results have been extracted from 4 ns MD simulations in the NPT ensemble at  $p=1$  atm. Different temperatures have been included:  $T=298$  K and the extended simulations of the cooling process. The dark grey line stands for the Bjerrum criterion.

The mean force potential is defined as Equation 6.3.<sup>147</sup> Following the Bjerrum criterion (Equation 6.4) indicates that the effective energy of attraction by the anion to a given position at  $r$  is twice the thermal energy and the cation can be considered as effectively paired. Figure 6.15 shows the profile of  $W(r)/k_B T$  for  $T=298$  K and the corresponding temperatures of the cooling process. For all the temperatures analysed, the position inside the pores is largely favoured by several  $k_B T$ , while *outside* 1 is only weakly favoured at 298 K and could be considered as paired, according to the Bjerrum, criterion for lower

temperatures. The position *outside 2* is stable even at high temperature, while *outside 3* is not too strongly bound for this range of temperatures. Therefore, the dynamic, as well as the thermodynamic considerations, support our statements about the plugging of the guanidinium counter-cations in the Keplerate.

$$g(r) \equiv \exp\left(\frac{-W(r)}{k_B T}\right) \quad (6.3)$$

$$\frac{W(r)}{k_B T} = -\ln g(r) \leq -2 \quad (6.4)$$

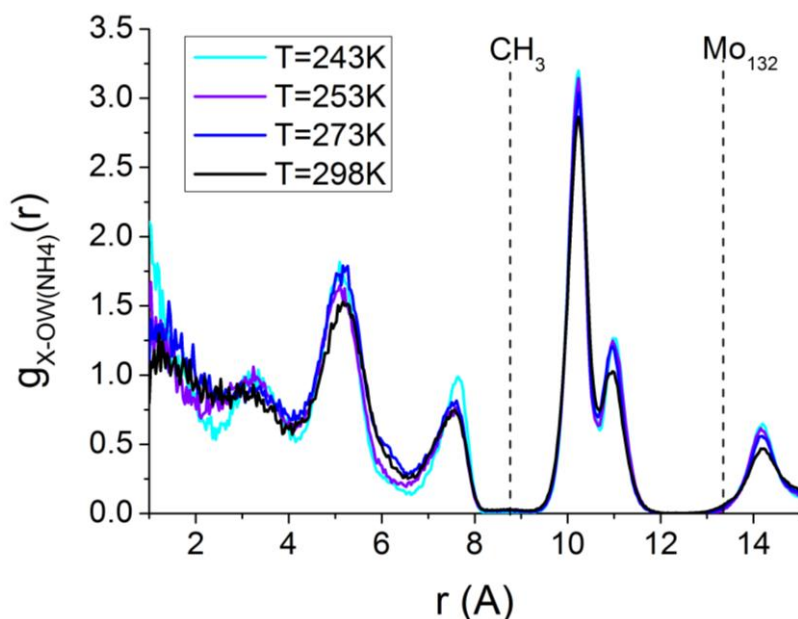


**Figure 6.16:** Radial distribution function from the centre of the capsule of the  $\text{Mo}_{132}(\text{CH}_3\text{COO}^-)$  capsule for water molecules for the 4 ns simulations performed at different temperatures and at  $p=1$  atm. Lighter colours represent lower temperatures.

Finally, we analyse the set of simulations at different temperatures  $T=298$ ,  $273$ ,  $253$ , and  $243$  K, a  $\text{Mo}_{132}$  capsule with acetate ligands as inner surface decoration and ammonium as counter-cation. With respect to the previous cases analysed, acetates are larger in size than the formate ligands, but also they confer a hydrophobic character to the environment of the pore at the inner surface of the cavity. In turn, ammonium cations are not impaired for crossing the pores by size exclusion. Therefore, the phenomenology of this system is

expected a priori to be significantly different from the one previously studied. Moreover, the anomalies observed in NMR spectrum for this system justify a thorough analysis through simulations.

Figure 6.16 shows the radial distribution function of the water molecules at the different temperatures considered for the  $\text{Mo}_{132}(\text{CH}_3\text{COO}^-)$ . As compared to the Keplerate with formate ligands (Figure 6.10), the radial distribution profile is significantly different from the pattern in Figure 6.16. In the latter, there is a gap caused by the hydrophobic methyl groups of the acetate ligands (dashed line in Figure 6.16), which alters the neighbouring  $\delta$  and  $\epsilon$  layers. The reduction of space for the  $\delta$  layer has significantly decreased its high and no substructure in form of shoulders is observed. In turn, the  $\epsilon$  layer is enhanced, together with the  $\zeta$  layer inside the pore, which has multiply its high by a factor near 5. Lowering the temperature sharpen the peaks lying in the hollow of the capsule, as one could expect.

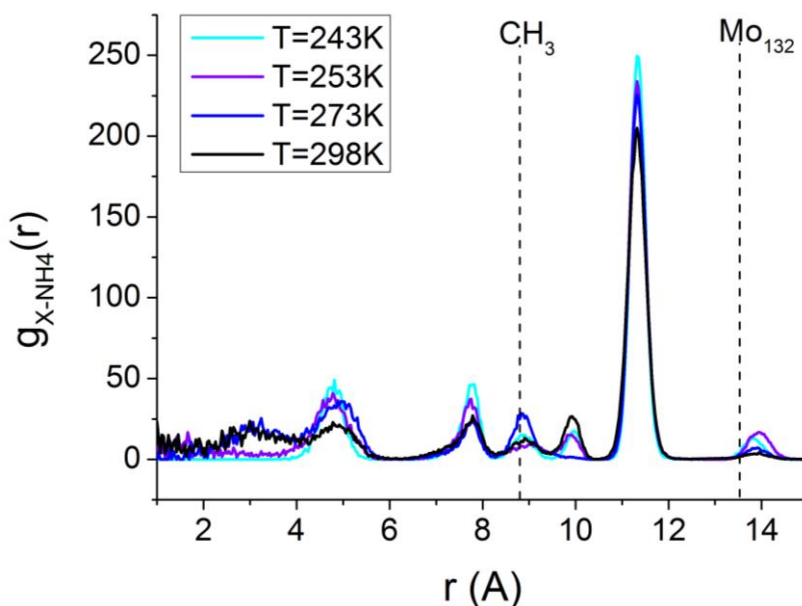


**Figure 6.17:** Radial distribution function from the centre of the capsule of the  $\text{Mo}_{132}(\text{CH}_3\text{COO}^-)$  capsule for water molecules for the 4 ns simulations performed at different temperatures and at  $p=1$  atm. Lighter colours represent lower temperatures.

With regard to the ammonium radial distribution function, Figure 6.17 shows a different structure from the one for the guanidinium cations previously studied. Here, few counter-ions are found in the hollow of the cavity, occupying positions corresponding to the valleys between water layers. The most remarkable feature of Figure 6.17 is the high peak for ammonium cations inside the pores, right at the position occupied by guanidinium molecules in the previously studied case. This coincidence also occurs when formate ligands are considered (see Figure 6.6 for comparison). Notice that the enhancement of the  $\zeta$  layer corresponds to the solvation of the ammonium cations inside the pores. Guanidinium cations excluded the presence of a large amount of water molecules at this location. Moreover, ammonium counter-ions are present in three small peaks close to the methyl groups of the acetate ligands, namely, *inside 1*, *inside 2*, and *inside 3*, at 10, 9, and 7.5 Å from the centre of the capsule, respectively. Lowering the temperature alters the relative population of these peaks in a non monotonous way. While *inside 3* increases when decreasing the temperature, as it is expected, the *inside 1* peak found at 298 K disappears at 273 K, to reappear again at lower temperatures. The peak *inside 2* follows the opposite tendency. Therefore, it seems that the ammonium counter-cations of peak *inside 1* move to flanking positions of the methyl groups of the acetate ligands at 273 K, to return to their original location at lower temperatures. We believe that such a displacement of ammonium cations is responsible for the anomalies observed in the NMR spectrum.

NMR experiments are based on the interaction between an external and the nuclear magnetic field. Such interaction is very dependent on the close environment of the nucleus studied. Changes on the electron density influence the degree of shielding/deshielding of a nucleus from an external magnetic field, which modify the Larmor frequency, which is eventually detected in an NMR experiment.<sup>239</sup> There are several factors that can cause changes on the electronic density of the hydrogen atoms in the methyl groups of the acetate ligands. For instance, one factor is the variation of the local electric field at the position of such hydrogen atoms, whose spin is sensitive to the NMR experiment. Unfortunately, the model used for the acetate ligands considers methyl groups represented as a united atom, in which the H atoms parameters are not explicitly described except through redefined Lennard-Jones parameters of the ensemble.

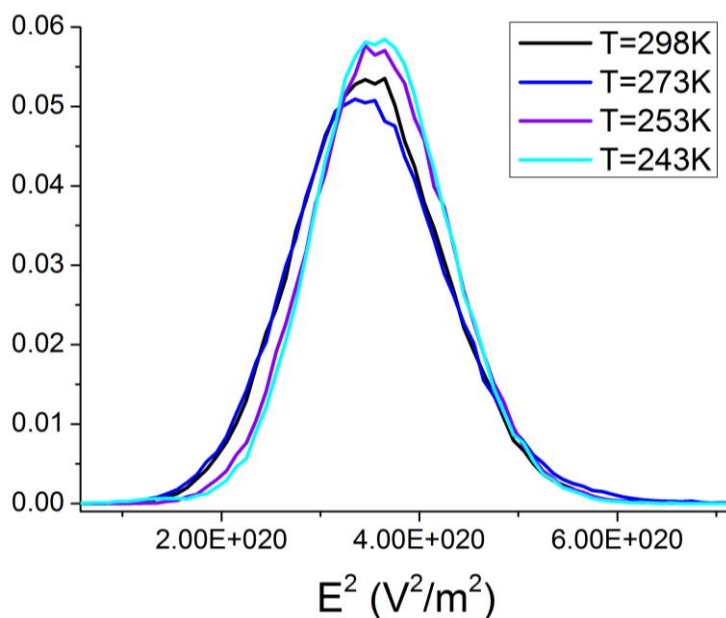


**Figure 6.18:** Histogram profile of the square of the modulus of the electric field felt by the methyl groups of the  $\text{Mo}_{132}(\text{CH}_3\text{COO}^-)$  capsule computed at each snapshot of a 4 ns simulation performed at different temperatures. Lighter colours represent lower temperatures.

In this context, we calculate the square of the modulus of the electric field ( $E^2$ ) at the centre of the methyl group of the acetate ligands decorating the inner surface of the  $\text{Mo}_{132}$  cavity, as an estimate of the effect that the local environment would have on the electronic density of the hydrogen atoms located in its vicinity. We sample the values of  $E^2$  at a frequency larger than the Larmor precession frequency, estimate of the order of 100 MHz, understanding that the NMR chemical shifts correspond to long-standing properties of the system.

Hence,  $E^2$  is computed for each methyl group every 1 ps and normalised histograms are calculated for each temperature overall 4 ns. These histograms are bell-like distributions and they are collected in Figure 6.18. From this figure it is shown that, as the temperature decreases,  $E^2$  histograms are thinner, higher and shifted to the right, namely, to higher values of  $E^2$ . This trend is broken by the results at  $T=273$  K, which gives a peak lower and shifted to the left with respect to the curve at  $T=298$  K. This anomaly is related to the local environment of the methyl groups, and coincides with the aforementioned



disappearance of the peak *inside* 1 and rising of the peak *inside* 2, precisely at this temperature.

We have checked that, when lithium cations replace ammonium counter-ions in the same system, this anomaly is not present. This fact is also experimentally observed.<sup>238</sup> Therefore, although our calculations are not conclusive, the anomalous behaviour of ammonium molecules at 273 K, together with the lithium results, strongly suggest that the observed anomaly in the NMR spectrum could be directly related to the features described in this Chapter.

## 6.4 -Conclusions

The preceding analysis on the behaviour of Mo<sub>132</sub> capsules with different ligands and counter-cations permits us to draw the following conclusions.

- We have shown that the choice of a VDD tessellation for the assignment of point charges to atomic positions, using the molecular geometry obtained from DFT calculations, and considering the Mo<sub>132</sub> capsule as a rigid open system in aqueous solution, yields a similar structural picture as previous analyses using the primitive model based on X-ray positions obtained from the experiments and a parametrical approach for the point charges assignment.<sup>12</sup>
- In agreement with experimental observations, MD simulations on the Mo<sub>132</sub>(HCOO<sup>-</sup>) macro-ion and small cations, as lithium or sodium, show how such small cations are able to enter the capsule and interact with the layered structure of encapsulated water molecules, without strongly distorting the structure of the nanodrop.<sup>12b, c</sup> In contrast, larger cations, as guanidinium and tetra-methyl ammonium, are not found in the hollow of the capsule due to size exclusion at the pores.
- Guanidinium cations can be strongly complexed with the pores, but they are also encountered in two stable positions right at the outer entrance of the pores. Counting all the guanidinium in these positions, we find that the capsule is effectively closed up to 298 K, according to our model for the species in our system.

- Tetra-methyl ammonium cations cannot enter inside the pore and form a strong complex. Instead, they remain at stable positions at the outer gate of the pore, analogous to the external peaks of the guanidinium case, although slightly shifted outside. The potential of mean force indicates that peaks outside 2 and 3 for the tetra-methyl ammonium are strongly paired with the capsule and, therefore, they can be considered as acting as plugs. The analysis of the system  $\text{Mo}_{132}(\text{HCOO}^-)$  with tetra-methyl ammonium as counter-cations is addressed in Chapter 7.
- Ammonium cations in the  $\text{Mo}_{132}(\text{CH}_3\text{COO}^-)$  capsule present an anomalous behaviour with temperature variations. We have observed that, at 273 K, some cations move their positions to the vicinity of the methyl groups of the ligands. No such behaviour is observed for lithium cations in the same capsule. Since anomalies in the NMR spectrum are reported for the former system and not for the latter, we argue that the changes in the positions of the counter-cations must be responsible for the observed NMR anomalies.

UNIVERSITAT ROVIRA I VIRGILI

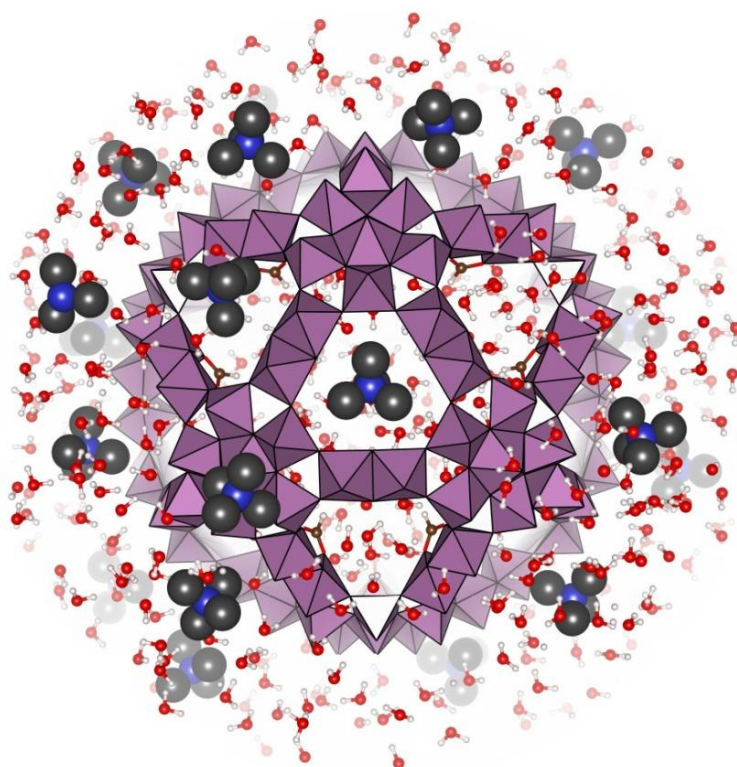
KEPLERATES: FROM ELECTRONIC STRUCTURE TO DYNAMIC PROPERTIES.

María Dolores Melgar Freire

Dipòsit Legal: T 258-2016

# Chapter 7: Hydrophobicity as Driving Force of the Plugging Process of the $\text{Mo}_{132}$ Pores

---



UNIVERSITAT ROVIRA I VIRGILI

KEPLERATES: FROM ELECTRONIC STRUCTURE TO DYNAMIC PROPERTIES.

María Dolores Melgar Freire

Dipòsit Legal: T 258-2016

## 7.1 - Introduction

The characteristic features of the Keplerate's pores allow these capsules to bind positively charged substrates. Some examples have been reported on the literature studying this host-guest interaction, but the complete understanding of the plugging process of these pores is still an important challenge. In 2002, Müller et al. published an analysis of the responsive reactivity of Keplerates depending on the pore size.<sup>206a</sup> They showed that the pore size can be modified altering the linkers that join the characteristic pentagonal units of these polytopic receptors. In 2003, the same group published another study highlighting the ability of nanoporous species to trap molecules with well-defined shape.<sup>205</sup> Müller and co-workers presented Keplerates as structures with tuneable functionalised channels (the pores) with molecular-scale filter properties. In 2006, they used Keplerates to model the gating mechanism that takes place on the transmembrane channels of the biological cells.<sup>240</sup>

The interaction between Keplerates and cations in solution can be tracked by means of NMR techniques. More precisely, <sup>1</sup>H DOSY NMR experiments allows the identification of the chemical species present in the mixture through their diffusion coefficient. This can be done by observing the attenuation of the NMR signals during a pulsed field gradient experiment. The group of Molecular Solids of the University of Versailles Saint Quentin, led by Cadot, has a wide experience not only on these techniques, but also on the synthesis and reactivity of functionalised polyoxometalates.<sup>241</sup> This chapter collects the results of a joint project with Cadot's group, in which Molecular Dynamics simulations were employed to understand the results of NMR experiments. This collaboration lead in 2015 to a publication on the Journal of American Chemistry Society.<sup>57</sup>

### 7.1.1 - Summary of Cadot's group experimental results

Experiments showed that the self-diffusion coefficient of the cations in solutions with Keplerates is strongly dependent on the balance between solvated and bind counter-cations. Cadot's group was able to characterize the plugging process of the pores in terms of its stability constants for different cationic guests. They found that the affinity of the capsule for these cationic species increases with their apolar character. Thus, the major factor that influences the selectivity in the trapping process is such "hydrophobic effect".

They studied the behaviour of a set of tetra-alkyl ammonium ions (TAA), namely,  $\text{Me}_{4-x}\text{NH}_x^+$ , with  $x=0-4$ , in the presence of the Keplerate macro-anion  $\text{Mo}_{132}$ , as  $\text{NH}_4^+$ ,  $\text{Na}^+$  or  $\text{Li}^+$  salts. The self-diffusion coefficient of the TAA cations decrease as the plugging process of the pores is taking place. Competitive effects between the TAA ions and the other cations present in solution, however, also exist.

Figure 7.1a shows the variation of the self-diffusion coefficient ( $D$ ) for tetra-methyl ammonium cations with the polyoxometalate concentration ( $C^0$ ). The values of  $D$  for the acetate ligands remain constant all over the concentration range, while  $D$  for the  $\text{NMe}_4^+$  cation is strongly affected. It is influenced, not only by the  $\text{Mo}_{132}$  concentration, but also by the other cationic species present in solution. On one hand, the dependence of the self-diffusion coefficient with  $C^0$  can be explained in terms of the pore-cation complexation: the larger the number of cations in the bulk, the higher the probability to the free cations to find a pore and form pore-cation complex. On the other hand, when  $C^0$  increases, for the three cases studied, each line tends to a different constant value. These constants are larger than the self-diffusion coefficient for the acetate ligands encapsulated, namely, for the  $\text{Mo}_{132}$  polyoxometalate. This difference on the behaviour of the  $\text{NMe}_4^+$  cations can be attributed to the competitive character of the complexation process when more than one cationic species are present in solution. This competition depends on the specific features of the counter-cation. Figure 7.1b represents the concentration dependence of  $D$  for different alkyl ammonium cations in the presence of the Keplerate ion and its corresponding ammonium counter-cations. In this case, we observe the same decrease of  $D$  as  $C^0$  increases. Also,

different asymptotic values are reached for high values of  $C^0$ , depending on the hydrophobic character of the alkyl ammonium species.

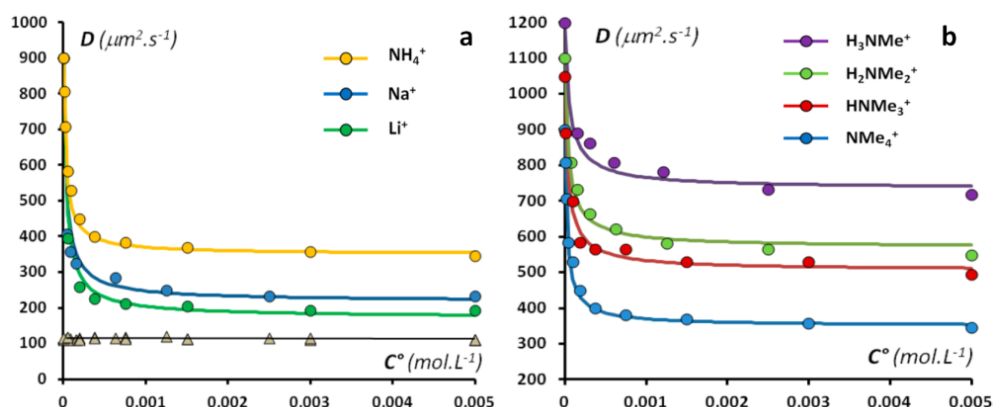


**Figure 7.1:** a) Variation of the self-diffusion coefficient ( $D$ ) of the  $\text{NMe}_4^+$  ions in the presence of different counter-cations (circle) and of the inner acetate ligands (triangle) with concentration in  $\text{Mo}_{132}$  ( $C^0$ ). b) Variation of  $D$  of the alkyl ammonium series ion with the concentration of the ammonium salt Keplerate. Solid lines represent the calculated data using stability constants. These experiments were performed at a fixed ratio of  $\text{TAA}/\text{Mo}_{132}=3$  and changing the concentration in  $\text{Mo}_{132}$  ( $C^0$ ) from 0 to  $5 \cdot 10^{-3} \text{ mol} \cdot \text{L}^{-1}$ .

To explain such behaviour, let us consider that the pores on the capsule's surface are sufficiently far apart, to assume that the behaviour of the species near one particular pore is independent from the rest. Thus, the plugging process would be depending on two equilibria in competition, as Equation 7.1 shows, where  $S^+$  represents the cationic substrate ( $\text{Me}_{4-x}\text{NH}_x^+$ , with  $x=0-4$ ),  $Y^+$  are the counter-ions ( $\text{Li}^+$ ,  $\text{Na}^+$ ,  $\text{NH}_4^+$ ,  $\text{C}(\text{NH}_2)_3^+$ ) and  $P$  the pores.  $S-P$  and  $Y-P$  represent the complexes composed by the anionic pores and the cationic species (substrate or counter-ions, respectively). Table shows the stability constant values for both equilibria proposed. From these values, the trend is clear: the more hydrophobic character of the cation (represented by the number of methyl groups in the case of alkyl-ammonium ions), the larger the stability constant. This trend suggests that the  $\text{NMe}_4^+$  cations interact in a specific way with the anionic pores. This fact has been demonstrated by means of a pores titration experiment.





**Table 7.1:** Stability constants ( $K_X$ ) of alkali, alkyl-ammonium, guanidinium and imidazolium complexes of the multi-receptor Keplerate ions at 25°C in D<sub>2</sub>O<sup>a</sup>.

<b>Ions Y<sup>+</sup></b>	<b>Li<sup>+</sup></b>	<b>Na<sup>+</sup></b>	<b>NH<sub>4</sub><sup>+</sup></b>	<b>C(NH<sub>2</sub>)<sub>3</sub><sup>+</sup></b>
<b>K<sub>Y</sub></b>	65	130	370	400
<b>Ions S<sup>+</sup></b>	<b>NMe<sub>4</sub><sup>+</sup></b>	<b>HNMe<sub>3</sub><sup>+</sup></b>	<b>H<sub>2</sub>NMe<sub>2</sub><sup>+</sup></b>	<b>H<sub>3</sub>NMe<sup>+</sup></b>
<b>K<sub>S</sub></b>	1550	900	750	475
<b>Ions S<sup>+</sup></b>	<b>Me<sub>3</sub>NEt<sup>+</sup></b>	<b>Me<sub>3</sub>NPr<sup>+</sup></b>		<b>NEt<sub>4</sub><sup>+</sup></b>
<b>K<sub>S</sub></b>	1800	1600		6500
<b>Ions S<sup>+</sup></b>	<b>N,N'-methyl-ethyl-imidazolium</b>			
<b>K<sub>S</sub></b>	5800			

<sup>a</sup>The standard error in stability constant is ca. 10%, as estimated from the accuracy and the reproducibility of the measurements.

If these results are compared with the ones from another guanidinium receptor, as the [27]-crown-O<sub>9</sub> macrocycle,<sup>34</sup> it appears that the trend is completely opposed to the results shown in Table . Lehn et al.<sup>242</sup> showed how the stability constant for the hexacarboxylate [27]-crown-O<sub>9</sub> macrocycle has a maximum for the NH<sub>4</sub><sup>+</sup> complex and decreases as the number of methyl groups in the alkyl-ammonium ion increases. The fact that the stability constant decreases with the number of methyl groups can be explained in terms of the steric hindrance between the bulky substituents attached to the macrocycle and the methyl group of the cationic species. From Figure 7.2 it is clearly shown that the steric effect will be dominant. Therefore, the hydrophobic effect is not observed on the case of the hexacarboxylate macrocycle. In contrast, in the case of Mo<sub>132</sub> capsule, as there are no bulky substituents in the vicinity of the pores which could cause such a steric effect, the hydrophobic effect becomes dominant. Thus, as the hydrophobic character of the cation increases, the stability constant slightly increases too, suggesting a “push factor” of the polar solvent.

Variable temperature <sup>1</sup>H DOSY NMR experiments have been performed to get the information of the thermodynamic parameters ( $\Delta_r H^0$  and  $\Delta_r S^0$ ) that govern this plugging process. Then, the Gibbs free energy of the complexation process ( $\Delta_r G^0$ ) can be estimated (Equation 7.2). Results are shown in Table 7.2.  $\Delta_r H^0$  values are always negative, because the interaction takes place between an anionic host (the pore) and a cationic guest.  $\Delta_r S^0$  values are also negative because of the loss of degrees of freedom when the guest is assembling the pore. Even if the values for the  $\Delta_r H^0$  are very close for the three species

proposed,  $\Delta_r S^0$  increases with the hydrophobicity of the guest.  $\Delta_r G^0$  values clearly indicate that  $NMe_4^+$  has the lower free energy and, therefore, its complexation with the Keplerate has the larger stability, while the other two species analysed have approximately the same free energy complexation. This fact is in agreement with the sequence of the complexation constants given in Table 7.1 for these three cations.

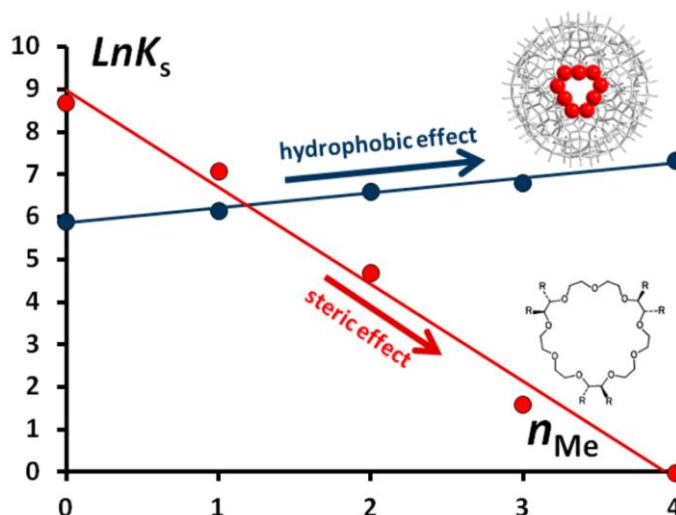


**Figure 7.2:** Correlation between  $\ln K_s$  and the number of methyl substituents ( $n_{Me}$ ) within the alkyl-ammonium series obtained with the  $Mo_{132}$  ion (blue) and the hexacarboxylate [27]-crown-09 macrocycle (red).

**Table 7.2:** Thermodynamic parameters for the plugging process of selected guests.

	$NH_4^+$	$H_2NMe_2^+$	$NMe_4^+$
$\Delta_r H^0$ (eV) <sup>a</sup>	-0.3524	-0.2487	-0.2436
$\Delta_r S^0$ (meV·K <sup>-1</sup> ) <sup>a</sup>	-0.6633	-0.3213	-0.1814
$\Delta_r G^0$ (eV)	-0.1547	-0.1530	-0.1895

<sup>a</sup>The standard error in thermodynamic parameters is ca. 20%, as estimated from the accuracy and the reproducibility of the measurements.

$$\Delta_r G^0 = \Delta_r H^0 - T\Delta_r S^0 \quad (7.2)$$

In terms of the solvation shells, apolar cations have weak hydration enthalpies, so they are easily trapped within the pores. The plugging process is spontaneous, due to the negative Gibbs free energies of the process. Together with the favourable interaction between the cation and the pore, the entropy

gain coming from the release of the water molecules which were initially structured around the hydrophobic cation, additionally favours the latter. Taking into account the values from Table 7.2, it can be concluded that a small hydrophilic guest will maintain its solvation sphere intact during the trapping process, while a large hydrophobic guest will desolvate water molecules, causing an entropy gain. Hence, if enthalpic interactions are similar, this entropy gain is the leading effect that drives the plugging process.

## 7.1.2 - Goals

Regarding the experimental results summarised above, this chapter collects results we obtained pursuing the following goals:

- Understanding the nature of interactions between the Keplerate ion and a set of cationic species (ammonium, guanidinium and tetra-methyl ammonium cations) by means of Molecular Dynamics Simulations.
- Estimation of the binding energy of the capsule and the cationic guests through DFT calculations.
- Analysis of the self-diffusion coefficient of the cationic species using their mean square displacement (MSD), extracted from Molecular Dynamics trajectories.
- Developing of a post-treatment code to distinguish between the different dynamic regimes of the cationic species, inspired by their radial distribution function.

## 7.2 - Computational Details

### 7.2.1 - Density Functional Theory (DFT)

With regard to the interaction energy between the counter-cations and the Mo<sub>132</sub> pores, a constrained optimization at the DFT level (GGA BP86/ZORA/TZP) has been performed including solvent effects (COSMO<sup>194</sup>) as implemented in the ADF2012 program<sup>118</sup>). For the COSMO implementation, the atomic radii values correspond to the Van der Waals radii from the MM3 method by

Allinger<sup>198</sup> divided by 1.2. Regarding the numerical integration, the parameter that controls the precision of numerical integrals has been set at 4.5.

First, a geometry that optimizes the energy functional at the described DFT level of the  $[(\text{Mo}^{\text{VI}}(\text{Mo}^{\text{V}})_5\text{O}_{21})_{12}(\text{Mo}^{\text{V}}_2\text{O}_4(\text{HCOO}))_{30}]^{42-}$  system has been calculated. Then, the capsule's coordinates are frozen, while two diametrically opposed counter-cations are free to choose the configuration that minimizes the system's DFT energy functional. This strategy was followed because the largest changes take place more due to the cation position rather than due to small variations of the capsule structure, due to its inherent stability, this approach reduces the computational cost significantly. The diametrically opposed positions of the counter-cations were chosen in order to have a C<sub>i</sub> symmetry, thus saving additional computational resources. Then, the bonding energy between the cation and the capsule was calculated taking into account the energies of the system without cations, the cation without the capsule and, finally, the energy corresponding to the whole system composed of the capsule and two cations.

## 7.2.2 - Classical Molecular Dynamics (MD)

MD simulations have been performed using the DL\_POLY Classic 1.9 program package<sup>176</sup> in order to study the properties of Mo<sub>132</sub> Keplerate in the presence of different cationic species in solution. For this purpose a simulation box with initial dimensions of 7x7x7 nm<sup>3</sup> was defined. This box contains one Mo<sub>132</sub> anion with 30 fixed formate ligands, the corresponding 42 counter-cations and 11000 water molecules. This results in a system with a density of 1.09g·cm<sup>-3</sup> and a concentration of Mo<sub>132</sub> anions  $C^0=0.0048 \text{ mol}\cdot\text{L}^{-1}$ .

All the molecules in this system were treated as rigid objects to reduce the computational cost. The properties calculated in this study will not depend on the details of the potential (vibrational motion, flexibility, polarizability, etc.). Hence, considering molecules as rigid bodies should not affect strongly these results. Intermolecular interactions were modelled using dispersion (Lennard-Jones (LJ) potentials) and electrostatic forces. The water molecules were represented by the TIP4P/2005 model<sup>162</sup> due to its excellent capability to reproduce bulk water properties at a wide range of conditions. Regarding the dispersions forces, for the polyoxometalate, LJ parameters from previous

studies have been employed.<sup>16c</sup> In these studies, different polyoxometalates systems were modelled.<sup>12a, 12c, 147, 177</sup> For the formate ligands and the counter-cations, the OPLS-AA force field parameters have been used.<sup>145b, 146a</sup> Crossed interactions between unlike atoms have been calculated from Lorentz-Berthelot combining rules.<sup>144</sup> Regarding the electrostatic interactions, in the case of the Keplerate, partial charges derived from the Voronoi Density Deformation population<sup>174a</sup> analysis of the electron density were used. This partial charges were obtained from a fully optimised geometry of the  $[(\text{Mo}^{\text{VI}}(\text{Mo}^{\text{V}})_5\text{O}_{21})_{12}(\text{Mo}^{\text{V}}_2\text{O}_4(\text{HCOO}))_{30}]^{42-}$  system computed by means of a DFT based method. Long-range Coulombic interactions were evaluated through the Ewald summation technique, with a convergence parameter of 0.210 and considering a maximum of six wave vectors in each direction. Translational equations of motion were integrated using the Verlet leapfrog algorithm with a time step of 1 fs and a cut-off of 16 Å.

The simulations were carried out in the NPT ensemble at standard ambient conditions (T=298 K; P=1 atm), controlled by a Nosé-Hoover thermostat and a Andersen barostat with relaxation times of 0.02 ps and 0.1 ps, respectively. Periodic boundary conditions were used in all the simulations. The initial configurations, generated with the Packmol<sup>137</sup> software, were equilibrated during 1ns while the production runs were extended until 4 ns. Both equilibration and production runs were performed with a time step of 1 fs. System snapshots were stored each 1000 time steps. These trajectories were analysed with a purpose-made post-treatment code that computes the mean squared displacement for different parts of the Mo<sub>132</sub> and the cations. For this purpose, sequential temporal windows of 100 ps long with time origins shifted 10 ps each were averaged. Furthermore, cations were treated differently depending on their relative location with respect the polyoxometalate in order to distinguish those cations associated and those not associated to the capsule. For that purpose, the simulation box was divided into a set of regions. These regions are concentric shells around the centre of mass of the polyoxometalate, and their boundaries are located to contain the peaks of the radial distribution function of the given counter-cation ( $g(r)$ ). In this context, a counter-cation belongs to a region when it spends at least the 90% of the time window in that region. For calculating  $g(r)$ , the simulation box was divided into concentric shells of width of 0.035 Å with their origin at the centre of the Mo<sub>132</sub> capsule.

## 7.3 - Results

Constrained optimizations at the DFT level have been performed for estimating the bonding energy between the polyoxometalate and the cations. We followed the same procedure for three different cations, namely: ammonium ( $\text{NH}_4^+$ ), guanidinium ( $\text{C}(\text{NH}_2)_3^+$ ) and tetra-methyl ammonium ( $\text{NMe}_4^+$ ) cations.

**Table 7.3:** Bonding energies between different cations and the Mo<sub>132</sub> capsule.

	$\Delta E$ (eV)
$\text{NH}_4^+$	-0.66
$\text{C}(\text{NH}_2)_3^+$	-1.00
$\text{NMe}_4^+$	-0.51

Results from Table 7.3 suggest, based on a purely electrostatic DFT analysis, that guanidinium pore-cation complex is the most stable pair, followed by the ammonium cation and, finally, the tetra-methyl ammonium cation. Experimental results, however, show that the formation of  $\text{NMe}_4^+$ -pore complex is instead preferred, emphasizing the importance of the hydrophobic character of the cation, as it was already mentioned. To understand this discrepancy, one should take into account that, on the one hand, DFT results reflect the electrostatic interaction between fragments partially screened by the solvent, via a continuous solvent model. This interaction is evaluated in a static context, as no time evolution was considered on the DFT analysis. We think that, in this way, hydrophobic effects cannot be properly taken into account, as the entropy cannot be evaluated by means of DFT. On the other hand, Table 7.3 represents differences between bonding energies, which cannot be directly compared with thermodynamic properties as given in Table 7.2. Nevertheless, results from Table 7.2 can be understood as the enthalpic contribution to  $\Delta E$ . Both values,  $\Delta E$  and  $\Delta H^{\text{exp}}$ , can be compared in the case of  $\text{NH}_4^+$  and  $\text{NMe}_4^+$  species. Both  $\Delta E$  and  $\Delta H^{\text{exp}}$  indicate that energetically, ammonium cations bind more strongly than  $\text{NMe}_4^+$ . Also, it is worth noting that  $\Delta E$  and  $\Delta H^{\text{exp}}$  present the same order of magnitude.

As hydrophobic effects cannot be reproduced on the basis of DFT calculations, classical Molecular Dynamics simulations of the Mo<sub>132</sub> Keplerate, water

molecules and cations have been carried out to better understand the behaviour of the system in solution.

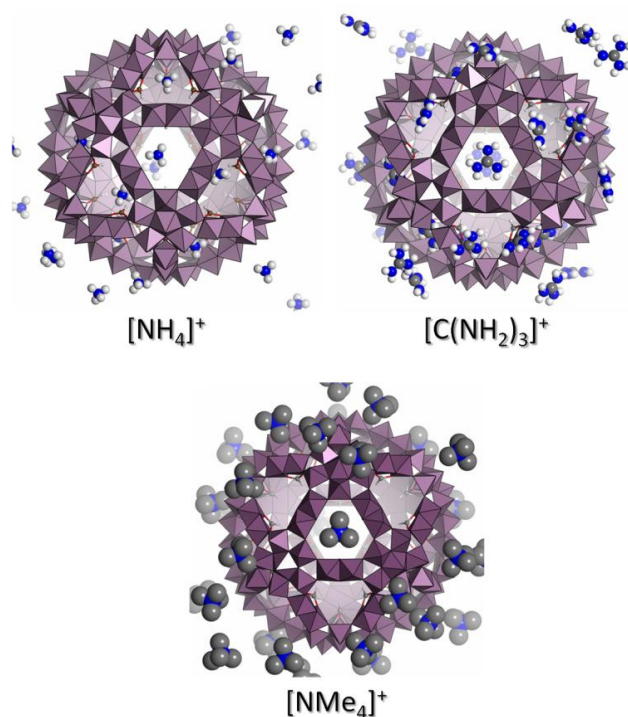


**Figure 7.3:** Snapshots from MD simulations of Mo<sub>132</sub> with different counter-cations.

According to the radial distribution function (Figure 7.4), we identified two clearly different patterns. The radial distribution functions for both the  $\text{NH}_4^+$  and the  $\text{C}(\text{NH}_2)_3^+$  systems show a similar profile, while for the  $\text{NMe}_4^+$  system, the distribution outside the capsule is more structured. In the case of  $\text{NH}_4^+$  and  $\text{C}(\text{NH}_2)_3^+$ , starting from left to right, there is a first peak (around  $r=11.2$  Å for both cases) corresponding to 12 and 11 cations respectively that are placed within the pores, just behind the metal-oxo frame-work (represented by the dashed line in Figure 7.4). None of these cations are found in positions closer to the centre of the capsule. Although the similarities in the  $g(r)$  profiles of the  $\text{NH}_4^+$  and the  $\text{C}(\text{NH}_2)_3^+$  cations, there are also some differences, due to their different nature: while the ammonium cations are small enough to move within the pores, guanidinium counter-cations have the size and the symmetry to act as plugs in the pores. Furthermore, when one guanidinium cation plugs a pore, we observe that this situation remains stable for the rest of the simulation.

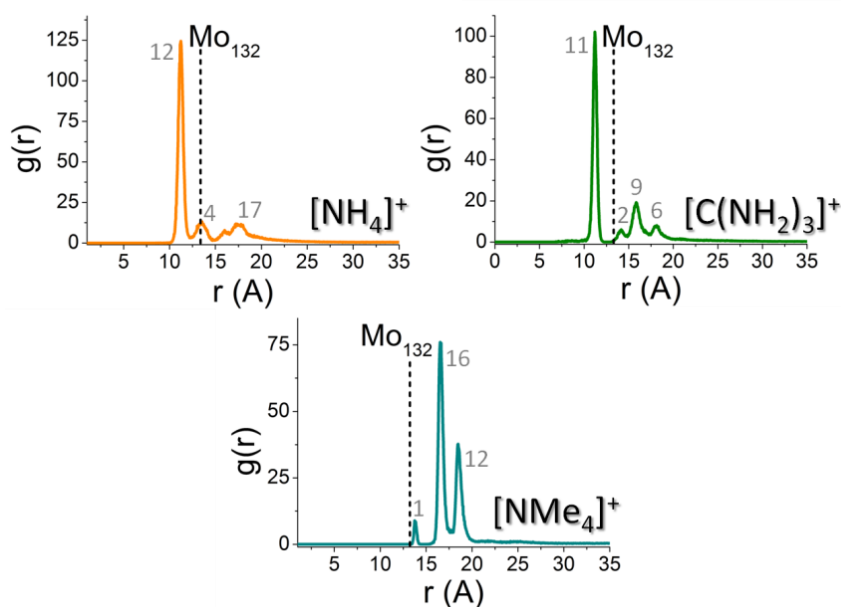


**Figure 7.4:** Radial distribution functions for the ammonium (orange), guanidinium (green) and tetra-methyl ammonium (blue) cations. The numbers in grey represent the number of cations associated to each peak. Dashed line represents the capsule metal-oxo framework.

After the main peak at around 11.2 Å, for both cases, the cations are located near the pore's entrance (second peak, at 13.56 Å for the  $NH_4^+$  system and at 14.14 Å for then  $C(NH_2)_3^+$  system) or even further away from the centre of the capsule. Therefore, for these two cations we observe that about on half of them are bind to the capsule in and around the pores, while the other half (approximately) lay at the capsule surface, in other locations, according to Figure 7.3.

In the case of  $NMe_4^+$ , the  $g(r)$  profile shows remarkable differences from the previous ones. About 17 cations among the 42 are located at the surface of the capsule. Few of them correspond to the first peak ( $r=13.81$  Å), which perfectly plug the pore, as is shown in Figure 7.3. This plugging cations show the same host-guest arrangement that observed in X-ray experiments of the single-pore model, namely  $[(\alpha-AsW_9O_{33})_3(WO(OH_2))_3(Mo_2O_2S_2(H_2O)_4)]^{13-}$  anion.<sup>243</sup> The second and third peak in the radial distribution function ( $r=16.55$  Å and  $r=18.52$  Å respectively) represent cations that remain close to the capsule surface for rather long time. Cations belonging to the second peak are located just over the pores and preferentially oriented as the plugging ones described for the first



peak, but further away from the capsule. Indeed, the average angle value between the N atoms of the  $\text{NMe}_4^+$  cations of this region, the centre of the capsule, and the corresponding pore centroid is less than  $10^\circ$ , indicating that all the cations in this region are almost perfectly facing the pores. Cations belonging to the third peak did not show any specific attraction to the pore structure and simply remain close to the capsule due to their electrostatic interaction with the latter. Furthermore, none of the tetra-methyl ammonium cations entered into the capsule. Even if experimentally few  $\text{NMe}_4^+$  can be found encapsulated, our theoretical model treats the POM and its ligands as a rigid unit and, therefore, it does not have the necessary flexibility of the pores and the lability of the ligands, that would permit  $\text{NMe}_4^+$  cations to enter the capsule.

In order to have a deeper understanding of the behaviour of these counter-cations and their interactions with the Keplerate capsule, a self-diffusion coefficient analysis has been performed. The fact that the radial distribution function presents clear and well-separated peaks in all the cases allows us to distinguish between different dynamic regimes. The self-diffusion coefficient analysis has been carried out dividing the simulation box on spherical shells according to radial distribution function profiles. Once these regions have been defined, the DL\_POLY trajectories of the central atoms of the cations (N in the case of ammonium and tetra-methyl ammonium cations and C in the case of guanidinium ions) are chosen to compute representative MSD values for the cations. To compute this MSD values, a post-treatment code specifically made for this purpose has been used. This code divides the total length of the simulation (4ns) in time windows, with a time origin shifted 10ps for consecutive windows, thus resulting in 391 time windows of 100ps. Also, the program is able to distinguish which cations belong to each region. For this purpose, trajectories of the cations that spend less than the 90% of the time window in the same region are rejected. Once the suitable trajectories are chosen, the MSD calculation reduces to the evaluation of the displacement of the ion from its position at the initial time during the time window. By construction, diffusion across the layers is discarded. This MSD value should be averaged over all the atoms in the same situation (belonging to the same region) and all the time windows.

Once the MSD has been computed, the self-diffusion coefficient can be calculated by means of Equation 7.3.

$$\langle MSD \rangle = 6D \cdot t \quad (7.3)$$

Thus, plotting the averaged MSD versus the time should result on a straight line, which slope is directly related to the self-diffusion coefficient.

**Table 7.4:** Regions considered for the MSD treatment, inspired on the peaks showed in the  $g(r)$  plots (Figure 7.4)

	NH <sub>4</sub> <sup>+</sup>	C(NH <sub>2</sub> ) <sub>3</sub> <sup>+</sup>	NMe <sub>4</sub> <sup>+</sup>
Region 1	$r < 12.55 \text{ \AA}$	$r < 12.15 \text{ \AA}$	$r < 15 \text{ \AA}$
Region 2	$12.55 \text{ \AA} < r < 15 \text{ \AA}$	$13.34 \text{ \AA} < r < 14.85 \text{ \AA}$	$15 \text{ \AA} < r < 17.7 \text{ \AA}$
Region 3	$15 \text{ \AA} < r < 22.5 \text{ \AA}$	$14.85 \text{ \AA} < r < 17.21 \text{ \AA}$	$17.7 \text{ \AA} < r < 20 \text{ \AA}$
Region 4	$r > 22.5 \text{ \AA}$	$17.21 \text{ \AA} < r < 19.09 \text{ \AA}$	$r > 20 \text{ \AA}$
Region 5	-	$r > 19.09 \text{ \AA}$	-

To distinguish which counter-cations have formed a pore-cation complex, we can take advantage of the fact that bounded cations are expected to diffuse and rotate with the Keplerate capsule. So, its measured diffusion coefficient ( $D_{ion}$ ) should scale as  $r^2$  Equation 7.4, where  $D_{trans}$  is the cation's translational diffusion coefficient,  $D_{rot}$  its rotational diffusion coefficient and  $r$  the distance between the tagged atom and the centre of the capsule. This equation is limited to short simulation times because complexed ions will diffuse like the capsule asymptotically at long times. Hence, to properly separate rotational from translational diffusion we are bound by the condition  $D_{trans} \ll R^2$ , where  $R$  is the radius of the Keplerate. This characteristic time range is about 5ns for our system, and, thus, our time windows length is short enough for Equation 7.4 to apply.

$$D_{ion}(r) = D_{trans} + D_{rot} r^2 \quad (7.4)$$

If we take as a reference the self-diffusion coefficient of different parts of the Mo<sub>132</sub> capsule (namely, the centre of the capsule, the Mo atoms and the H atoms belonging to formate ligands), these values of  $D$  should lay in a linear correlation when plotted as a function of their distance to the centre of the capsule, according to Equation 7.4. Hence, the diffusion coefficient of bound cations would satisfy the same correlation, because they move together with

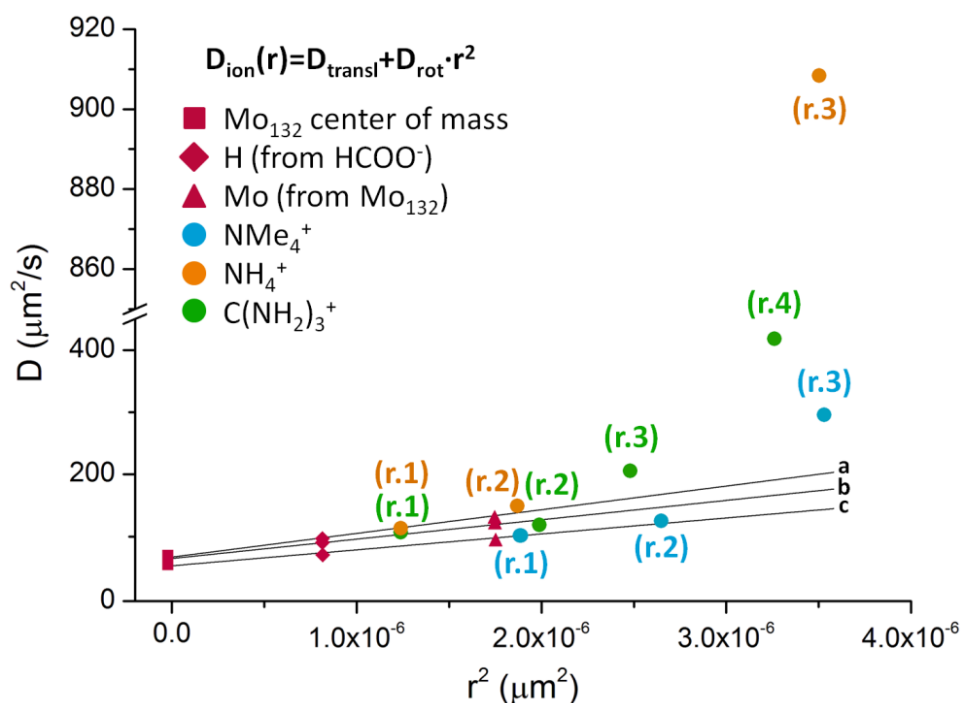
the capsule. In contrast, those cations that move free or are loosely bound to the Keplerate should exhibit diffusion coefficients expected to fall well above this linear correlation.

Table 7.5 shows the numerical values for the self-diffusion coefficient for the whole set of cations and its previously defined regions. Those numerical values differ enough from a region to another to support our approach distinguishing the different dynamic regimes for the cations.

**Table 7.5:** Self-diffusion coefficient values for the three simulations of the different parts of the polyoxometalate and the different regions defined for the counter-cations.

<b>NH<sub>4</sub><sup>+</sup></b>	<b>r<sup>2</sup> (10<sup>-6</sup>μm<sup>2</sup>)</b>	<b>D (μm<sup>2</sup>/s)</b>
<i>Centre of mass of Mo<sub>132</sub></i>	0	66.63±0.18
<i>H from HCOO<sup>-</sup> groups</i>	0.84	94.42±0.20
<i>Mo from Mo<sub>132</sub></i>	1.77	125.77±0.24
<i>NH<sub>4</sub><sup>+</sup> from region 1</i>	1.26	112.37±0.26
<i>NH<sub>4</sub><sup>+</sup> from region 2</i>	1.89	149.7±1.3
<i>NH<sub>4</sub><sup>+</sup> from region 3</i>	3.52	908.3±3.9
<i>NH<sub>4</sub><sup>+</sup> from region 4</i>	>5.06	1509.4±1.0
<b>C(NH<sub>2</sub>)<sub>3</sub><sup>+</sup></b>	<b>r<sup>2</sup> (10<sup>-6</sup>μm<sup>2</sup>)</b>	<b>D (μm<sup>2</sup>/s)</b>
<i>Centre of mass of Mo<sub>132</sub></i>	0	63.85±0.13
<i>H from HCOO<sup>-</sup> groups</i>	0.84	91.27±0.13
<i>Mo from Mo<sub>132</sub></i>	1.77	122.20±0.17
<i>C(NH<sub>2</sub>)<sub>3</sub><sup>+</sup> from region 1</i>	1.26	108.37±15
<i>C(NH<sub>2</sub>)<sub>3</sub><sup>+</sup> from region 2</i>	2.01	119.97±0.48
<i>C(NH<sub>2</sub>)<sub>3</sub><sup>+</sup> from region 3</i>	2.50	206.00±0.91
<i>C(NH<sub>2</sub>)<sub>3</sub><sup>+</sup> from region 4</i>	3.28	417.68±2.1
<i>C(NH<sub>2</sub>)<sub>3</sub><sup>+</sup> from region 5</i>	>3.64	862.50±0.74
<b>NMe<sub>4</sub><sup>+</sup></b>	<b>r<sup>2</sup> (10<sup>-6</sup>μm<sup>2</sup>)</b>	<b>D (μm<sup>2</sup>/s)</b>
<i>Centre of mass of Mo<sub>132</sub></i>	0	52.90±0.25
<i>H from HCOO<sup>-</sup> groups</i>	0.84	70.67±0.22
<i>Mo from Mo<sub>132</sub></i>	1.77	90.73±0.19
<i>NMe<sub>4</sub><sup>+</sup> from region 1</i>	1.91	103.40±0.41
<i>NMe<sub>4</sub><sup>+</sup> from region 2</i>	2.67	126.37±0.28
<i>NMe<sub>4</sub><sup>+</sup> from region 3</i>	3.55	296.35±0.81
<i>NMe<sub>4</sub><sup>+</sup> from region 4</i>	>4.00	851.60±1.6

Figure 7.5 shows the linear correlation for the three systems, defined by the entities that are on the same dynamic regime. For the three systems, the regression includes the values of  $D$  for the centre of the capsule, the Mo atoms and the H atoms from the formate groups, all of them moving as a rigid solid by construction of the model. Furthermore, Figure 7.5 also includes also the two first regions defined for the cations (see Table 7.4). But these regions have different meanings depending on the system simulated. For the guanidinium and ammonium systems, the two first regions represent the cations that are within the pores, while for the tetra-methyl ammonium system, only the first region represents such situation. Region 2, in this case, corresponds to those cations located just over the pores and oriented as the plugging ones.



**Figure 7.5:** Regression of the self-diffusion coefficient data for different entities of the Mo<sub>132</sub> capsule (centre of mass, H and Mo atoms) (red) for the three systems in the presence of different cations: NH<sub>4</sub><sup>+</sup> (orange), C(NH<sub>2</sub>)<sub>3</sub><sup>+</sup> (green) and NMe<sub>4</sub><sup>+</sup> (blue). The entities that move together lay in straight line for each simulation (a for the NH<sub>4</sub><sup>+</sup> system, b for the C(NH<sub>2</sub>)<sub>3</sub><sup>+</sup> system and c for the NMe<sub>4</sub><sup>+</sup> system). The (r.x) labels indicates both the type of cation (label colour) and the region which it belongs to (x).

**Table 7.6:** Numerical values of the regression coefficients from Figure 7.5.

	$D_{\text{trans}}$ ( $\mu\text{m}^2/\text{s}$ )	$D_{\text{rot}}$ ( $10^6 \cdot \text{s}^{-1}$ )
$\text{NH}_4^+$	66.63±0.18	38.1±2.4
$\text{C}(\text{NH}_2)_3^+$	66.85±0.13	31.2±1.5
$\text{NMe}_4^+$	52.90±0.25	25.6±1.3

Table 7.6 includes the coefficients of the linear regression shown in Figure 7.5. Both translational and rotational self-diffusion coefficient present similar values in the case of  $\text{NH}_4^+$  and  $\text{C}(\text{NH}_2)_3^+$  simulations, comparing with the  $\text{NMe}_4^+$  system. This fact could be explained in terms of the size of the dynamic unit, which will be proportional to the hydrodynamic drag. For both cases,  $\text{NH}_4^+$  and  $\text{C}(\text{NH}_2)_3^+$ , the dynamic unit comprises the polyoxometalate and the two first counter-cations regions, resulting on a radius (without taking into account the water solvation shell of these cations) of 13.74Å and 14.18Å respectively. For the  $\text{NMe}_4^+$  system, the dynamic unit also comprises the Keplerate and the two first cations regions, but in this case these two regions are located further from the centre of the capsule (region 1 cations plugs the pores, but region 2 cations do not), resulting on a radius of 16.34Å. This value is slightly larger than the previous cases; therefore, it explains the lower values for both translational and rotational diffusion coefficient observed in the case of  $\text{NMe}_4^+$ .

## 7.4 - Conclusions

- Bonding energies for the pore-cation complex were computed at the DFT level. These energies suggest that the most favourable complex would be with guanidinium as counter-cation, followed by ammonium and tetra-methyl ammonium cations, in contrast to the experimental results.
- MD simulations of the Mo<sub>132</sub> Keplerate in aqueous solution and a set of cations were performed, suggesting a stronger interaction Keplerate- $\text{NMe}_4^+$ .
- $g(r)$  profiles extracted from MD simulations show two different patterns. Guanidinium and ammonium cations present similar  $g(r)$ . In these cases, the main  $g(r)$  peak represents the cations that are placed

at the capsule's pores. In contrast,  $\text{NMe}_4^+$  cations are more structured in the outside vicinity of the capsule.

- The translational and rotational contributions to the self-diffusion coefficient allow us to distinguish the cations with the same dynamic behaviour of the capsule. Units moving together should have the same rotational self-diffusion coefficient. For the three cases studied, the cations belonging to the two first regions defined by the  $g(r)$  profiles are moving with the POM anion. Nevertheless, these regions have different meanings depending on the cationic specie. For  $\text{C}(\text{NH}_2)_3^+$  and  $\text{NH}_4^+$  cations, the main contribution to these regions comes from the cations that are placed at the pores. In contrast, the second region for  $\text{NMe}_4^+$  includes the cations that are surrounding the POM, but further away from the capsule centre.
- The increase of the stability constants with the hydrophobic character of the cationic species suggests that the complexation process can be explained in terms of the “push factor” produced by a polar solvent such as water.

UNIVERSITAT ROVIRA I VIRGILI

KEPLERATES: FROM ELECTRONIC STRUCTURE TO DYNAMIC PROPERTIES.

María Dolores Melgar Freire

Dipòsit Legal: T 258-2016

# Chapter 8: Conclusions

---



UNIVERSITAT ROVIRA I VIRGILI

KEPLERATES: FROM ELECTRONIC STRUCTURE TO DYNAMIC PROPERTIES.

María Dolores Melgar Freire

Dipòsit Legal: T 258-2016

The following lines are aimed at summarising the most relevant conclusions extracted from the previous chapters:

- Our systematic DFT study on the electronic structure of the Keplerate family (Chapter 3) shows that the composition of the capsule influences the HOMO-LUMO energy gap and, therefore, its stability. For instance, W pentagonal units and sulphur-bridges systems present a larger gap.
- In contrast, the presence of different internal ligands and coordination water molecules does not affect significantly the electronic structure of the Mo<sub>132</sub> Keplerate, which means that the inherent stability of the capsule determines the stability of the whole system.
- Keplerates not reported on the literature yet, such as W<sub>132</sub>, W<sub>12</sub>Mo<sub>120</sub> and the fully oxidised Mo<sub>132</sub>, seem to be stable from a theoretical and electronic point of view. Nevertheless, further theoretical and experimental studies must be performed.
- We have shown that even if the capsule is a macro-anion, negatively charged ligands can be labily bonded to the linker units due to the relevance of the Orbital Interaction contribution to the bonding energy.
- Comparing bonding energies between the capsule and a set of carboxylate ligands with different carbon chains, almost the same results are obtained. In contrast, when different species of bidentate ligands are considered, the trend obtained is as follows (from the most stable complex to the less): CO<sub>3</sub><sup>2-</sup>, CH<sub>3</sub>COO<sup>-</sup>, CH<sub>2</sub>CHCOO<sup>-</sup>, HCOO<sup>-</sup>, HCO<sub>3</sub><sup>-</sup>, SO<sub>4</sub><sup>2-</sup> (HSO<sub>4</sub><sup>-</sup> has not been included in this list because the full-system model shows a positive bonding energy for this ligand). Such trend in stability is pretty similar to the pK<sub>b</sub> of the ligands.
- We are able to reproduce the Raman spectra time evolution of the Mo<sub>132</sub> formation at the DFT level by considering different combinations of pentagonal and dimeric building blocks: for instance, systems formed by two pentagons and their corresponding linker present the same Raman pattern observed experimentally upon acidification. Furthermore, the characteristic Mo<sub>132</sub> Raman fingerprint corresponds to the spectrum of a pore framework composed of three pentagons and three linkers.

- From the analysis of the condensation energies computed at the DFT level between pentagons and linkers involving and increasing number of protons, we conclude that such condensation is more favourable when both structures have an intermediate degree of protonation. This feature has as consequence that condensation reactions are very pH-dependent, which is in agreement with experimental observations.
- The definition of new parameters regarding the force field of MD simulations yields a similar structural picture as previous analyses using the primitive model based on empirical parameters.<sup>12</sup> This new force field is partially extracted from the aforementioned DFT calculations.
- Our MD simulations on the  $\text{Mo}_{132}(\text{HCOO}^-)$  system show that small cations, such as lithium and sodium, are able to enter the capsule, in agreement with experimental observations. Other cationic species, such as guanidinium or ammonium, are rather located inside or near the pores. In the case of tetra-methyl ammonium counter-ions, they are stable at positions at the outer gate of the pore.
- Regarding the  $\text{Mo}_{132}(\text{CH}_3\text{COO}^-)$  system with ammonium as counter-cation, the distribution of the cations is altered upon cooling. More precisely, at 273 K, some counter-ions approach the methyl groups of the acetate ligands. This effect is not observed when the ammonium molecules are substituted by lithium. The consequence that the approximation of ammonium cations can cause on the closest environment of the hydrogen atoms of the methyl groups of the ligands could be related with the experimentally observed NMR anomalies for this system. Further studies, both theoretical and experimental, must be carried out to deepen the effects of temperature on the  $\text{Mo}_{132}$  and counter-cations behaviour at low temperatures.

# References

---

1. Turing, A. M., On computable numbers, with an application to the Entscheidungsproblem. *J. of Math.* **1936**, *58* (345-363), 5.
2. Lopez, X.; Carbo, J. J.; Bo, C.; Poblet, J. M., Structure, properties and reactivity of polyoxometalates: a theoretical perspective. *Chem. Soc. Rev.* **2012**, *41* (22), 7537-7571.
3. Müller, A.; Krickemeyer, E.; Bögge, H.; Schmidtman, M.; Beugholt, C.; Kögerler, P.; Lu, C., Formation of a Ring-Shaped Reduced "Metal Oxide" with the Simple Composition [(MoO<sub>3</sub>)<sub>176</sub>(H<sub>2</sub>O)<sub>80</sub>H<sub>32</sub>]. *Angew. Chem. Int. Ed.* **1998**, *37* (9), 1220-1223.
4. Muller, A.; Shah, S. Q. N.; Bogge, H.; Schmidtman, M., Molecular growth from a Mo<sub>176</sub> to a Mo<sub>248</sub> cluster. *Nature* **1999**, *397* (6714), 48-50.
5. Müller, A.; Beckmann, E.; Bögge, H.; Schmidtman, M.; Dress, A., Inorganic Chemistry Goes Protein Size: A Mo<sub>368</sub> Nano-Hedgehog Initiating Nanochemistry by Symmetry Breaking. *Angew. Chem.* **2002**, *114* (7), 1210-1215.
6. Müller, A.; Krickemeyer, E.; Bögge, H.; Schmidtman, M.; Peters, F., Organizational forms of matter: An inorganic super fullerene and Keplerate based on molybdenum oxide. *Angew. Chem. Int. Ed.* **1998**, *37* (24), 3360-3363.
7. (a) Merca, A.; Haupt, E. T.; Mitra, T.; Bögge, H.; Rehder, D.; Müller, A., Mimicking Biological Cation-Transport Based on Sphere-Surface Supramolecular Chemistry: Simultaneous Interaction of Porous Capsules with Molecular Plugs and Passing Cations. *Chem. Eur. J.* **2007**, *13* (27), 7650-7658; (b) Rehder, D.; Haupt, E. T. K.; Bögge, H.; Müller, A., Countercation Transport Modeled by Porous Spherical Molybdenum Oxide Based Nanocapsules. *Chem. Asian J.* **2006**, *1* (1-2), 76-81; (c) Gilles, A.; Mihai, S.; Nasr, G.; Mahon, E.; Garai, S.; Müller, A.; Barboiu, M., Highly Selective Li<sup>+</sup> Ion Transport by Porous Molybdenum-Oxide Keplerate-Type Nanocapsules Integrated in a Supported Liquid Membrane. *Isr. J. Chem.* **2013**, *53* (1-2), 102-107.
8. (a) Grego, A.; Müller, A.; Weinstock, I. A., Stepwise-Resolved Thermodynamics of Hydrophobic Self-Assembly. *Angew. Chem. Int. Ed.* **2013**, *52* (32), 8358-8362; (b) Ziv, A.; Grego, A.; Kopilevich, S.; Zeiri, L.; Miro, P.; Bo, C.; Müller, A.; Weinstock, I. A., Flexible Pores of a Metal Oxide-Based Capsule Permit Entry of Comparatively Larger Organic Guests. *J. Am. Chem. Soc.* **2009**, *131* (18), 6380-6382.
9. Müller, A.; Rehder, D.; Haupt, E. T. K.; Merca, A.; Bögge, H.; Schmidtman, M.; Heinze-Brückner, G., Artificial Cells: Temperature-

Dependent, Reversible Li<sup>+</sup>-Ion Uptake/Release Equilibrium at Metal Oxide Nanocontainer Pores. *Angew. Chem. Int. Ed.* **2004**, *43* (34), 4466-4470.

10. (a) Garai, S.; Haupt, E. T. K.; Bögge, H.; Merca, A.; Müller, A., Picking up 30 CO<sub>2</sub> Molecules by a Porous Metal Oxide Capsule Based on the Same Number of Receptors. *Angew. Chem. Int. Ed.* **2012**, *51* (42), 10528-10531; (b) Besson, C.; Schmitz, S.; Capella, K. M.; Kopilevich, S.; Weinstock, I. A.; Kögerler, P., A regioselective Huisgen reaction inside a Keplerate polyoxomolybdate nanoreactor. In *Dalton Trans.*, 2012; Vol. 41, p 9852.

11. (a) Bandeira, N. A. G.; Garai, S.; Muller, A.; Bo, C., The mechanism of CO<sub>2</sub> hydration: a porous metal oxide nanocapsule catalyst can mimic the biological carbonic anhydrase role. *Chem. Commun.* **2015**, *51* (85), 15596-15599; (b) Kopilevich, S.; Gil, A.; Garcia-Ratés, M.; Bonet-Ávalos, J.; Bo, C.; Müller, A.; Weinstock, I. A., Catalysis in a Porous Molecular Capsule: Activation by Regulated Access to Sixty Metal Centers Spanning a Truncated Icosahedron. *J. Am. Chem. Soc.* **2012**, *134* (31), 13082-13088.

12. (a) Mitra, T.; Miró, P.; Tomsa, A.-R.; Merca, A.; Bögge, H.; Ávalos, J. B.; Poblet, J. M.; Bo, C.; Müller, A., Gated and Differently Functionalized (New) Porous Capsules Direct Encapsulates' Structures: Higher and Lower Density Water. *Chem. Eur. J.* **2009**, *15* (8), 1844-1852; (b) Garcia-Ratés, M.; Miró, P.; Poblet, J. M.; Bo, C.; Avalos, J. B., Dynamics of Encapsulated Water inside Mo<sub>132</sub> Cavities. *J. Phys. Chem. B* **2011**, *115* (19), 5980-5992; (c) Garcia-Ratés, M.; Miro, P.; Müller, A.; Bo, C.; Avalos, J. B., Encapsulated Water Inside Mo<sub>132</sub> Capsules: The Role of Long-Range Correlations of about 1 nm. *J. Phys. Chem. C* **2014**, *118* (10), 5545-5555.

13. Chen, Q.; Yang, L.; Zheng, C.; Zheng, W.; Zhang, J.; Zhou, Y.; Liu, J., Mo polyoxometalate nanoclusters capable of inhibiting the aggregation of A $\beta$ -peptide associated with Alzheimer's disease. *Nanoscale* **2014**, *6* (12), 6886-6897.

14. Müller, A.; Kögerler, P.; Dress, A., Giant metal-oxide-based spheres and their topology: from pentagonal building blocks to keplerates and unusual spin systems. *Coord. Chem. Rev.* **2001**.

15. Poblet, J. M.; López, X.; Bo, C., Ab initio and DFT modelling of complex materials: towards the understanding of electronic and magnetic properties of polyoxometalates. *Chem. Soc. Rev.* **2003**, *32* (5), 297-308.

16. (a) Aparicio-Angles, X.; Miro, P.; Clotet, A.; Bo, C.; Poblet, J. M., Polyoxometalates adsorbed on metallic surfaces: immediate reduction of [SiW<sub>12</sub>O<sub>40</sub>]<sup>4-</sup> on Ag(100). *Chem. Sci.* **2012**, *3* (6), 2020-2027; (b) Fernández, J. A.; López, X.; Bo, C.; de Graaf, C.; Baerends, E. J.; Poblet, J. M., Polyoxometalates with Internal Cavities: Redox Activity, Basicity, and Cation Encapsulation in [X<sub>n</sub>+P<sub>5</sub>W<sub>30</sub>O<sub>110</sub>](15-n)- Preyssler Complexes, with X = Na<sup>+</sup>, Ca<sup>2+</sup>, Y<sup>3+</sup>, La<sup>3+</sup>, Ce<sup>3+</sup>, and Th<sup>4+</sup>. *J. Am. Chem. Soc.* **2007**, *129* (40), 12244-12253; (c) López, X.; Nieto-Draghi, C.; Bo, C.; Avalos, J. B.; Poblet, J. M.,

- Polyoxometalates in Solution: Molecular Dynamics Simulations on the  $\alpha$ -PW12O40<sup>3-</sup> Keggin Anion in Aqueous Media. *J. Phys. Chem. A* **2005**, *109* (6), 1216-1222.
17. (a) Pope, M. T., *Heteropoly and Isopoly Oxometalates*. Springer-Verlag: New York, 1983; (b) Müller, A.; Pope, M. T., *Polyoxometalates: From Platonic Solids to Anti-Retroviral Activity*. 1st ed.; Springer: 1994; (c) Miras, H. N.; Yan, J.; Long, D.-L.; Cronin, L., Engineering polyoxometalates with emergent properties. *Chem. Soc. Rev.* **2012**, *41* (22), 7403-7430.
18. (a) Nyman, M.; Burns, P. C., A comprehensive comparison of transition-metal and actinyl polyoxometalates. *Chem. Soc. Rev.* **2012**, *41* (22), 7354-7367; (b) Qiu, J.; Burns, P. C., Clusters of actinides with oxide, peroxide, or hydroxide bridges. *Chem. Rev.* **2012**, *113* (2), 1097-1120.
19. (a) Chubarova, E. V.; Dickman, M. H.; Keita, B.; Nadjo, L.; Miserque, F.; Mifsud, M.; Arends, I. W.; Kortz, U., Self-Assembly of a Heteropolyoxopalladate Nanocube: [PdII13AsV8O34 (OH) 6] 8-. *Angew. Chem. Int. Ed.* **2008**, *47* (49), 9542-9546; (b) Izarova, N. V.; Pope, M. T.; Kortz, U., Noble metals in polyoxometalates. *Angew. Chem. Int. Ed.* **2012**, *51* (38), 9492-9510.
20. Izarova, N. V.; Vankova, N.; Heine, T.; Biboum, R. N.; Keita, B.; Nadjo, L.; Kortz, U., Polyoxometalates made of gold: the polyoxoaurate [AuIII4AsV4O20] 8-. *Angew. Chem. Int. Ed.* **2010**, *49* (10), 1886-1889.
21. (a) Proust, A.; Thouvenot, R.; Gouzerh, P., Functionalization of polyoxometalates: towards advanced applications in catalysis and materials science. *Chem. Commun.* **2008**, (16), 1837-1852; (b) Yang, Y.; Zhang, B.; Wang, Y.; Yue, L.; Li, W.; Wu, L., A Photo-driven Polyoxometalate Complex Shuttle and Its Homogeneous Catalysis and Heterogeneous Separation. *J. Am. Chem. Soc.* **2013**, *135* (39), 14500-14503.
22. (a) Nohra, B.; El Moll, H.; Rodriguez Albelo, L. M.; Mialane, P.; Marrot, J.; Mellot-Draznieks, C.; O'Keefe, M.; Ngo Biboum, R.; Lemaire, J.; Keita, B., Polyoxometalate-based metal organic frameworks (POMOFs): structural trends, energetics, and high electrocatalytic efficiency for hydrogen evolution reaction. *J. Am. Chem. Soc.* **2011**, *133* (34), 13363-13374; (b) Miras, H. N.; Vilà-Nadal, L.; Cronin, L., Polyoxometalate based open-frameworks (POM-OFs). *Chem. Soc. Rev.* **2014**, *43* (16), 5679-5699.
23. Ammam, M., Polyoxometalates: formation, structures, principal properties, main deposition methods and application in sensing. *J. Mater. Chem. A* **2013**, *1* (21), 6291-6312.
24. Chai, W.; Wang, S.; Zhao, H.; Liu, G.; Fischer, K.; Li, H.; Wu, L.; Schmidt, M., Hybrid Assemblies Based on a Gadolinium-Containing Polyoxometalate and a Cationic Polymer with Spermine Side Chains for Enhanced MRI Contrast Agents. *Chem. Eur. J.* **2013**, *19* (40), 13317-13321.
25. Wang, H.; Hamanaka, S.; Nishimoto, Y.; Irle, S.; Yokoyama, T.; Yoshikawa, H.; Awaga, K., In operando X-ray absorption fine structure studies of

polyoxometalate molecular cluster batteries: polyoxometalates as electron sponges. *J. Am. Chem. Soc.* **2012**, *134* (10), 4918-4924.

26. (a) Li, J.-S.; Sang, X.-J.; Chen, W.-L.; Zhang, L.-C.; Su, Z.-M.; Qin, C.; Wang, E.-B., The research of a new polyoxometalates based photosensitizer on dye sensitized solar cell. *Inorg. Chem. Commun.* **2013**, *38*, 78-82; (b) Wei, Y.; Zhang, T.; Lang, Z.; Yan, L.; Su, Z., Theoretical design of organoimido-substituted hexamolybdates with different electron donors for dye-sensitized solar cells. *Dyes Pigm.* **2014**, *102*, 6-12.

27. (a) Clemente-Juan, J. M.; Coronado, E.; Gaita-Ariño, A., Magnetic polyoxometalates: from molecular magnetism to molecular spintronics and quantum computing. *Chem. Soc. Rev.* **2012**, *41* (22), 7464-7478; (b) Baldoví, J. J.; Cardona-Serra, S.; Clemente-Juan, J. M.; Coronado, E.; Gaita-Ariño, A.; Prima-García, H., Coherent manipulation of spin qubits based on polyoxometalates: the case of the single ion magnet [GdW<sub>30</sub>P<sub>5</sub>O<sub>110</sub>]<sup>14-</sup>. *Chem. Commun.* **2013**, *49* (79), 8922-8924.

28. (a) Yin, Q.; Tan, J. M.; Besson, C.; Geletii, Y. V.; Musaev, D. G.; Kuznetsov, A. E.; Luo, Z.; Hardcastle, K. I.; Hill, C. L., A fast soluble carbon-free molecular water oxidation catalyst based on abundant metals. *Science* **2010**, *328* (5976), 342-345; (b) Kamata, K.; Yonehara, K.; Nakagawa, Y.; Uehara, K.; Mizuno, N., Efficient stereo- and regioselective hydroxylation of alkanes catalysed by a bulky polyoxometalate. *Nature Chem.* **2010**, *2* (6), 478-483; (c) Han, Z.; Bond, A. M.; Zhao, C., Recent trends in the use of polyoxometalate-based material for efficient water oxidation. *Sci. China Chem.* **2011**, *54* (12), 1877-1887; (d) Zhu, K.; Wang, D.; Liu, J., Self-assembled materials for catalysis. *Nano Res.* **2009**, *2* (1), 1-29; (e) Heravi, M.; Sadjadi, S., Recent developments in use of heteropolyacids, their salts and polyoxometalates in organic synthesis. *J. Iran Chem. Soc.* **2009**, *6* (1), 1-54; (f) Hill, C. L.; Prosser-McCartha, C. M., Homogeneous catalysis by transition metal oxygen anion clusters. *Coord. Chem. Rev.* **1995**, *143*, 407-455; (g) Gusevskaya, E. V., Reactions of Terpenes Catalyzed by Heteropoly Compounds: Valorization of Biorenewables. *ChemCatChem* **2014**, *6* (6), 1506-1515; (h) Gaspar, A. R.; Evtuguin, D. V.; Neto, C. P., Polyoxometalate-catalyzed oxygen delignification of kraft pulp: A pilot-plant experience. *Ind. Eng. Chem. Res.* **2004**, *43* (24), 7754-7761; (i) Sun, N.; Jiang, X.; Maxim, M. L.; Metlen, A.; Rogers, R. D., Use of polyoxometalate catalysts in ionic liquids to enhance the dissolution and delignification of woody biomass. *ChemSusChem* **2011**, *4* (1), 65-73.

29. (a) Schwarz, G.; Mendel, R. R.; Ribbe, M. W., Molybdenum cofactors, enzymes and pathways. *Nature* **2009**, *460* (7257), 839-847; (b) Kowalewski, B. r.; Poppe, J.; Demmer, U.; Warkentin, E.; Dierks, T.; Ermler, U.; Schneider, K., Nature's Polyoxometalate Chemistry: X-ray Structure of the Mo Storage Protein Loaded with Discrete Polynuclear Mo-O Clusters. *J. Am. Chem. Soc.* **2012**, *134* (23), 9768-9774.

30. Rhule, J. T.; Hill, C. L.; Judd, D. A.; Schinazi, R. F., Polyoxometalates in medicine. *Chem. Rev.* **1998**, *98* (1), 327-358.
31. (a) Flütsch, A.; Schroeder, T.; Grütter, M. G.; Patzke, G. R., HIV-1 protease inhibition potential of functionalized polyoxometalates. *Bioorg. Med. Chem. Lett.* **2011**, *21* (4), 1162-1166; (b) Wang, J.; Liu, Y.; Xu, K.; Qi, Y.; Zhong, J.; Zhang, K.; Li, J.; Wang, E.; Wu, Z.; Kang, Z., Broad-Spectrum Antiviral Property of Polyoxometalate Localized on a Cell Surface. *ACS Appl. Mater. Interfaces* **2014**, *6* (12), 9785-9789.
32. Raza, R.; Matin, A.; Sarwar, S.; Barsukova-Stuckart, M.; Ibrahim, M.; Kortz, U.; Iqbal, J., Polyoxometalates as potent and selective inhibitors of alkaline phosphatases with profound anticancer and amoebicidal activities. *Dalton Trans.* **2012**, *41* (47), 14329-14336.
33. Ilyas, Z.; Shah, H. S.; Al-Oweini, R.; Kortz, U.; Iqbal, J., Antidiabetic potential of polyoxotungstates: in vitro and in vivo studies. *Metallomics* **2014**, *6* (8), 1521-1526.
34. Muller, A.; Gouzerh, P., From linking of metal-oxide building blocks in a dynamic library to giant clusters with unique properties and towards adaptive chemistry. *Chem. Soc. Rev.* **2012**, *41* (22), 7431-7463.
35. (a) Miras, H. N.; Richmond, C. J.; Long, D.-L.; Cronin, L., Solution-phase monitoring of the structural evolution of a molybdenum blue nanoring. *J. Am. Chem. Soc.* **2012**, *134* (8), 3816-3824; (b) Winter, R. S.; Cameron, J. M.; Cronin, L., Controlling the Minimal Self Assembly of "Complex" Polyoxometalate Clusters. *J. Am. Chem. Soc.* **2014**, *136* (36), 12753-12761; (c) Xuan, W.; Surman, A. J.; Miras, H. N.; Long, D.-L.; Cronin, L., Controlling the Ring Curvature, Solution Assembly, and Reactivity of Gigantic Molybdenum Blue Wheels. *J. Am. Chem. Soc.* **2014**, *136* (40), 14114-14120; (d) Nakamura, I.; Miras, H. N.; Fujiwara, A.; Fujibayashi, M.; Song, Y.-F.; Cronin, L.; Tsunashima, R., Investigating the Formation of 'Molybdenum Blues' with Gel Electrophoresis and Mass Spectrometry. *J. Am. Chem. Soc.* **2015**.
36. Vilà-Nadal, L.; Rodríguez-Fortea, A.; Yan, L. K.; Wilson, E. F.; Cronin, L.; Poblet, J. M., Nucleation Mechanisms of Molecular Oxides: A Study of the Assembly-Dissassembly of [W<sub>6</sub>O<sub>19</sub>] <sup>2-</sup> by Theory and Mass Spectrometry. *Angew. Chem. Int. Ed.* **2009**, *48* (30), 5452-5456.
37. Jiménez-Lozano, P.; Carbó, J. J.; Chaumont, A.; Poblet, J. M.; Rodríguez-Fortea, A.; Wipff, G., Nature of Zr-Monosubstituted Monomeric and Dimeric Polyoxometalates in Water Solution at Different pH Conditions: Static Density Functional Theory Calculations and Dynamic Simulations. *Inorg. Chem.* **2013**, *53* (2), 778-786.
38. Kaledin, A. L.; van Duin, A. C.; Hill, C. L.; Musaev, D. G., Parameterization of Reactive Force Field: Dynamics of the [Nb<sub>6</sub>O<sub>19</sub>H<sub>x</sub>]<sup>(8-x)-</sup> Lindqvist Polyoxoanion in Bulk Water. *J. Phys. Chem. A* **2013**, *117* (32), 6967-6974.



39. Jungwirth, P., Ion Pairing: From Water Clusters to the Aqueous Bulk. *J. Phys. Chem. B* **2014**, *118* (35), 10333-10334.
40. Müller, A.; Roy, S., En route from the mystery of molybdenum blue via related manipulatable building blocks to aspects of materials science. *Coord. Chem. Rev.* **2003**, *245* (1-2), 153-166.
41. Schäffer, C.; Todea, A. M.; Bögge, H.; Cadot, E.; Gouzerh, P.; Kopilevich, S.; Weinstock, I. A.; Müller, A., Softening of Pore and Interior Properties of a Metal-Oxide-Based Capsule: Substituting 60 Oxide by 60 Sulfide Ligands. *Angew. Chem. Int. Ed.* **2011**, *50* (51), 12326-12329.
42. Bannani, F.; Floquet, S.; Leclerc-Laronze, N.; Haouas, M.; Taulelle, F.; Marrot, J.; Kögerler, P.; Cadot, E., Cubic Box versus Spheroidal Capsule Built from Defect and Intact Pentagonal Units. *J. Am. Chem. Soc.* **2012**, *134* (47), 19342-19345.
43. Schäffer, C.; Todea, A. M.; Bögge, H.; Floquet, S.; Cadot, E.; Korenev, V. S.; Fedin, V. P.; Gouzerh, P.; Müller, A., A further step towards tuning the properties of metal-chalcogenide nanocapsules by replacing skeletal oxide by sulphide ligands. *Dalton Trans.* **2012**, *42* (2), 330.
44. Bo, C.; Miro, P., On the electronic structure of giant polyoxometalates: Mo<sub>132</sub>vs. W<sub>72</sub>Mo<sub>60</sub>. *Dalton Trans.* **2012**, *41* (33), 9984-9988.
45. Roy, S.; Planken, K. L.; Kim, R.; von d Mandele, D.; Kegel, W. K., Direct Evidence on the Existence of [Mo<sub>132</sub>] Keplerate-Type Species in Aqueous Solution *Inorg. Chem.* **2007**, *46* (21), 8469-8471.
46. Schäffer, C.; Todea, A. M.; Gouzerh, P.; Müller, A., Spontaneous self-assembly of a giant spherical metal-oxide Keplerate: addition of one building block induces "immediate" formation of the complementary one from a constitutional dynamic library. *Chem. Commun. (Camb.)* **2012**, *48* (3), 350-352.
47. Müller, A.; Das, S.; Kögerler, P.; Bögge, H.; Schmidtman, M.; Trautwein, A.; Schünemann, V.; Krickemeyer, E.; Preetz, W., A New Type of Supramolecular Compound: Molybdenum-Oxide-Based Composites Consisting of Magnetic Nanocapsules with Encapsulated Keggin-Ion Electron Reservoirs Cross-Linked to a Two-Dimensional Network *Angew. Chem. Int. Ed. Engl.* **2000**, *39* (19), 3413-3417.
48. Müller, A.; Fedin, V. P.; Kuhlmann, C.; Bögge, H.; Schmidtman, M., A hydrogen-bonded cluster with 'onion-type' structure, encapsulated and induced by a spherical cluster shell: [(H<sub>2</sub>O)<sub>n</sub> ⊂ MoVI<sub>72</sub>MoV<sub>60</sub>O<sub>372</sub>(HCO<sub>2</sub>)<sub>30</sub>(H<sub>2</sub>O)<sub>72</sub>]<sub>42</sub>-. *Chem. Commun.* **1999**, (10), 927-929.
49. Müller, A.; Bögge, H.; Diemann, E., Structure of a cavity-encapsulated nanodrop of water. *Inorg. Chem. Commun.* **2003**, *6* (1), 52-53.
50. (a) Müller, A.; Henry, M., Nanocapsule water-based chemistry. *C. R. Chimie* **2003**, *6* (8-10), 1201-1208; (b) Müller, A.; Krickemeyer, E.; Bögge, H.; Schmidtman, M.; Botar, B.; Talismanova, M. O., Drawing Small Cations into

Highly Charged Porous Nanocontainers Reveals "Water" Assembly and Related Interaction Problems. *Angew. Chem. Int. Ed.* **2003**, *42* (18), 2085-2090.

51. Müller, A.; Garai, S.; Schäffer, C.; Merca, A.; Bögge, H.; Al-Karawi, A. J. M.; Prasad, T. K., Water Repellency in Hydrophobic Nanocapsules-Molecular View on Dewetting. *Chem. Eur. J.* **2014**, *20* (22), 6659-6664.

52. (a) Faraone, A.; Fratini, E.; Todea, A. M.; Krebs, B.; Müller, A.; Baglioni, P., Dynamics of Water in Voids between Well-Defined and Densely Packed Spherical Nanocages Acting as Polyprotic Inorganic Acids. *J. Phys. Chem. C* **2009**, *113* (20), 8635-8644; (b) Faraone, A.; Fratini, E.; Garai, S.; Müller, A.; Tyagi, M.; Jenkins, T.; Mamontov, E.; Paul, R. L.; Copley, J. R. D.; Baglioni, P., Incoherent Quasielastic Neutron Scattering Study of the Relaxation Dynamics in Molybdenum-Oxide Keplerate-Type Nanocages. *J. Phys. Chem. C* **2014**, *118* (24), 13300-13312.

53. Müller, A.; Gouzerh, P., Capsules with Highly Active Pores and Interiors: Versatile Platforms at the Nanoscale. *Chem. Eur. J.* **2014**, *20* (17), 4862-4873.

54. Haupt, E. T. K.; Wontorra, C.; Rehder, D.; Merca, A.; Müller, A., Confinement and step-wise reopening of channels in an artificial cell/inorganic capsule: a <sup>7</sup>Li NMR study. *Chemistry* **2008**, *14* (29), 8808-8811.

55. Merca, A.; Bögge, H.; Schmidtman, M.; Zhou, Y.; Haupt, E. T. K.; Sarker, M. K.; Hill, C. L.; Müller, A., Cation behavior at an artificial cell interface: binding distinguished by ion hydration energetics and size. *Chem. Commun.* **2008**, (8), 948.

56. Carr, R.; Weinstock, I. A.; Sivaprasadarao, A.; Müller, A.; Aksimentiev, A., Synthetic Ion Channels via Self-Assembly: A Route for Embedding Porous Polyoxometalate Nanocapsules in Lipid Bilayer Membranes. *Nano Lett.* **2008**, *8* (11), 3916-3921.

57. Watfa, N.; Melgar, D.; Haouas, M.; Taulelle, F.; Hijazi, A.; Naoufal, D.; Avalos, J. B.; Floquet, S.; Bo, C.; Cadot, E., Hydrophobic Effect as a Driving Force for Host-Guest Chemistry of a Multi-Receptor Keplerate-Type Capsule. *J. Am. Chem. Soc.* **2015**, *137* (17), 5845-5851.

58. Petina, O.; Rehder, D.; Haupt, E. T. K.; Grego, A.; Weinstock, I. A.; Merca, A.; Bögge, H.; Szakács, J.; Müller, A., Guests on Different Internal Capsule Sites Exchange with Each Other and with the Outside. *Angew. Chem. Int. Ed.* **2010**, *50* (2), 410-414.

59. Schäffer, C.; Todea, A. M.; Bögge, H.; Petina, O. A.; Rehder, D.; Haupt, E. T. K.; Müller, A., Hydrophobic Interactions and Clustering in a Porous Capsule: Option to Remove Hydrophobic Materials from Water. *Chem. Eur. J.* **2011**, *17* (35), 9634-9639.

60. Lai, T.-L.; Awada, M.; Floquet, S.; Roch-Marchal, C.; Watfa, N.; Marrot, J.; Haouas, M.; Taulelle, F.; Cadot, E., Tunable Keplerate Type-Cluster "Mo132" Cavity with Dicarboxylate Anions. *Chem. Eur. J.* **2015**, *21* (38), 13311-13320.

61. Izarova, N. V.; Kholdeeva, O. A.; Sokolov, M. N., Catalytic properties of the macromolecular polyoxomolybdate cluster in selective oxidation of sulfides. *Russ. Chem. Bul., Int. Ed.* **2009**, *58* (1), 134-137.
62. Fan, D.; Hao, J., Fabrication and Electrocatalytic Properties of Chitosan and Keplerate-Type Polyoxometalate {Mo<sub>72</sub>Fe<sub>30</sub>} Hybrid Films. *J. Phys. Chem. B* **2009**, *113* (21), 7513-7516.
63. Kopilevich, S.; Gil, A.; Garcia-Ratés, M.; Bonet Ávalos, J.; Bo, C.; Müller, A.; Weinstock, I. A., Catalysis in a Porous Molecular Capsule: Activation by Regulated Access to Sixty Metal Centers Spanning a Truncated Icosahedron. *J. Am. Chem. Soc.* **2012**, *134* (31), 13082-13088.
64. Garai, S.; Rubčić, M.; Bögge, H.; Gouzerh, P.; Müller, A., Porous capsules with a large number of active sites: nucleation/growth under confined conditions. *Chem. Eur. J.* **2015**, *21* (11), 4321-4325.
65. Rezaeifard, A.; Haddad, R.; Jafarpour, M.; Hakimi, M., Catalytic Epoxidation Activity of Keplerate Polyoxomolybdate Nanoball toward Aqueous Suspension of Olefins under Mild Aerobic Conditions. *J. Am. Chem. Soc.* **2013**, *135* (27), 10036-10039.
66. Nakhaei, A.; Davoodnia, A., Application of a Keplerate type giant nanoporous isopolyoxomolybdate as a reusable catalyst for the synthesis of 1, 2, 4, 5-tetrasubstituted imidazoles. *Chin. J. Catal.* **2014**, *35* (10), 1761-1767.
67. Rezaeifard, A.; Haddad, R.; Jafarpour, M.; Hakimi, M., {Mo<sub>132</sub>} Nanoball as an Efficient and Cost-Effective Catalyst for Sustainable Oxidation of Sulfides and Olefins with Hydrogen Peroxide. *ACS Sustainable Chem. Eng.* **2014**, *2* (4), 942-950.
68. Yang, C.; Zhao, W.; Cheng, Z.; Luo, B.; Bi, D., Catalytic system for pyridine oxidation to N-oxides under mild conditions based on polyoxomolybdate. *RSC Adv.* **2015**, *5* (46), 36809-36812.
69. Nakhaei, A.; Davoodnia, A.; Morsali, A., Extraordinary catalytic activity of a Keplerate-type giant nanoporous isopolyoxomolybdate in the synthesis of 1,8-dioxo-octahydroxanthenes and 1,8-dioxodecahydroacridines. *Res. Chem. Int.* **2015**, *41*, 7815-7826.
70. Rezaeifard, A.; Jafarpour, M.; Haddad, R.; Tavallaei, H.; Hakimi, M., Clean and Heterogeneous Condensation of 1,2-Diamines with 1,2-Dicarbonyls Catalyzed by {Mo<sub>132</sub>} Giant Ball Nanocluster. *J. Cluster Sci.* **2015**, *26* (5), 1439-1450.
71. Nikbakht, E.; Yadollahi, B.; Farsani, M. R., Green oxidation of alcohols in water by a polyoxometalate nano capsule as catalyst. *Inorg. Chem. Comm.* **2015**, *55*, 135-138.
72. (a) Jalilian, F.; Yadollahi, B.; Farsani, M. R.; Tangestaninejad, S.; Rudbari, H. A.; Habibi, R., New perspective to Keplerate polyoxomolybdates: Green oxidation of sulfides with hydrogen peroxide in water. *Catal. Commun.* **2015**, *66*, 107-110; (b) Haddadi, H.; Korani, E.; Hafshejani, S.; Farsani, M., Highly

Selective Oxidation of Sulfides to Sulfones by H<sub>2</sub>O<sub>2</sub> Catalyzed by Porous Capsules. *J. Cluster Sci.* **2015**, *26* (6), 1913-1922.

73. Jalilian, F.; Yadollahi, B.; Riahi Farsani, M.; Tangestaninejad, S.; Amiri Rudbari, H.; Habibi, R., Catalytic performance of Keplerate polyoxomolybdates in green epoxidation of alkenes with hydrogen peroxide. *RSC Adv.* **2015**, *5* (86), 70424-70428.

74. (a) Müller, A.; Krickemeyer, E.; Das, S.; Kögerler, P.; Sarkar, S.; Bögge, H.; Schmidtman, M., Linking Icosahedral, Strong Molecular Magnets {MoFe} to Layers-A Solid-State Reaction at Room Temperature. *Angew. Chem. Int. Ed. Engl.* **2000**, *39* (9), 1612-1614; (b) Müller, A.; Luban, M.; Schröder, C.; Modler, R.; Kögerler, P.; Axenovich, M.; Schnack, J.; Canfield, P.; Bud'ko, S.; Harrison, N., Classical and quantum magnetism in giant Keplerate magnetic molecules. *Chemphyschem* **2001**, *2* (8-9), 517-521; (c) Kuepper, K.; Derks, C.; Taubitz, C.; Prinz, M.; Joly, L.; Kappler, J.-P.; Postnikov, A.; Yang, W.; Kuznetsova, T. V.; Wiedwald, U.; Ziemann, P.; Neumann, M., Electronic structure and soft-X-ray-induced photoreduction studies of iron-based magnetic polyoxometalates of type {(M)M<sub>5</sub>}<sub>12</sub>Fe<sub>III</sub>30 (M = MoVI, WVI). *Dalton Trans.* **2013**, *42* (22), 7924.

75. Kobayashi, R.; Takemura, S., Perturbation Calculation for the 16 Lowest-Energy States in Spin Doughnut Mo<sub>75</sub>V<sub>20</sub>. *Progr. Theoret. Phys.* **2009**, *122* (5), 1189-1206.

76. (a) Liu, T., Supramolecular Structures of Polyoxomolybdate-Based Giant Molecules in Aqueous Solution. *J. Am. Chem. Soc.* **2002**, *124* (37), 10942-10943; (b) Verhoeff, A.; Kistler, M.; Bhatt, A.; Pigga, J.; Groenewold, J.; Klokkenburg, M.; Veen, S.; Roy, S.; Liu, T.; Kegel, W., Charge Regulation as a Stabilization Mechanism for Shell-Like Assemblies of Polyoxometalates. *Phys. Rev. Lett.* **2007**, *99* (6), 066104; (c) Kistler, M. L.; Bhatt, A.; Liu, G.; Casa, D.; Liu, T., A Complete Macroion-“Blackberry” Assembly-Macroion Transition with Continuously Adjustable Assembly Sizes in {Mo 132} Water/Acetone Systems. *J. Am. Chem. Soc.* **2007**, *129* (20), 6453-6460.

77. Liu, T.; Langston, M. L. K.; Li, D.; Pigga, J. M.; Pichon, C.; Todea, A. M.; Müller, A., Self-recognition among different polyprotic macroions during assembly processes in dilute solution. *Science* **2011**, *331* (6024), 1590-1592.

78. Li, H.; Yang, Y.; Wang, Y.; Wang, C.; Li, W.; Wu, L., Self-assembly and ion-trapping properties of inorganic nanocapsule-surfactant hybrid spheres. *Soft Matter* **2011**.

79. Floquet, S.; Terazzi, E.; Hijazi, A.; Guénée, L.; Piguet, C.; Cadot, E., Evidence of ionic liquid crystal properties for a DODA<sup>+</sup> salt of the keplerate [Mo<sub>132</sub>O<sub>372</sub>(CH<sub>3</sub>COO)<sub>30</sub>(H<sub>2</sub>O)<sub>72</sub>]<sub>42</sub><sup>-</sup>. *New J. Chem.* **2012**, *36* (4), 865.

80. Watfa, N.; Floquet, S.; Terazzi, E.; Salomon, W.; Guénée, L.; Buchwalder, K.; Hijazi, A.; Naoufal, D.; Piguet, C.; Cadot, E., Synthesis, Characterization and Study of Liquid Crystals Based on the Ionic Association of

the Keplerate Anion  $[\text{Mo}_{132}\text{O}_{372}(\text{CH}_3\text{COO})_{30}(\text{H}_2\text{O})_{72}]_{42-}$  and Imidazolium Cations. *Inorganics* **2015**, *3* (2), 246-266.

81. Gooch, J.; Jalan, A. A.; Jones, S.; Hine, C. R.; Alam, R.; Garai, S.; Maye, M. M.; Müller, A.; Zubieta, J., Keplerate cluster (Mo-132) mediated electrostatic assembly of nanoparticles. *J. Colloid Interface Sci.* **2014**, *432* (C), 144-150.

82. Ostroushko, A. A.; Grzhegorzhevskii, K. V., Electric conductivity of nanocluster polyoxomolybdates in the solid state and solutions. *Russ. J. Phys. Chem. A* **2014**, *88* (6), 1010-1013.

83. (a) Zhou, Y.; Shi, Z.; Zhang, L.; Hassan, S. u.; Qu, N., Notable third-order optical nonlinearities of a Keplerate-type polyoxometalate in solution and in thin films of PMMA. *Appl. Phys. A* **2013**, *113*, 563-568; (b) Zhang, L.; Shi, Z.; Zhang, L.; Zhou, Y.; Hassan, S. u., Fabrication and optical nonlinearities of ultrathin composite films incorporating a Keplerate type polyoxometalate. *Mater. Lett.* **2012**, *86*, 62-64.

84. Zielinski, T. J.; Harvey, E.; Sweeney, R.; Hanson, D. M., Quantum States of Atoms and Molecules. *J. Chem. Educ.* **2005**, *82* (12), 1880.

85. Hohenberg, P.; Kohn, W., Inhomogeneous Electron Gas. *Phys. Rev.* **1964**, *136* (3B), B864-B871.

86. Kohn, W.; Sham, L. J., Self-Consistent Equations Including Exchange and Correlation Effects. *Phys. Rev.* **1965**, *140* (4A), A1133-A1138.

87. (a) Perdew, J. P.; Ruzsinszky, A.; Tao, J.; Staroverov, V. N.; Scuseria, G. E.; Csonka, G. I., Prescription for the design and selection of density functional approximations: More constraint satisfaction with fewer fits. *J. Chem. Phys.* **2005**, *123* (6), 062201; (b) Perdew, J. P.; Ruzsinszky, A.; Constantin, L. A.; Sun, J.; Csonka, G. I., Some Fundamental Issues in Ground-State Density Functional Theory: A Guide for the Perplexed. *J. Chem. Theory Comput.* **2009**, *5* (4), 902-908.

88. Vosko, S. H.; Wilk, L.; Nusair, M., Accurate spin-dependent electron liquid correlation energies for local spin density calculations: a critical analysis. *Can. J. Phys.* **1980**, *58* (8), 1200-1211.

89. Ceperley, D. M.; Alder, B. J., Ground State of the Electron Gas by a Stochastic Method. *Phys. Rev. Lett.* **1980**, *45* (7), 566-569.

90. Perdew, J. P.; Zunger, A., Self-interaction correction to density-functional approximations for many-electron systems. *Phys. Rev. B* **1981**, *23* (10), 5048-5079.

91. Cole, L. A.; Perdew, J. P., Calculated electron affinities of the elements. *Phys. Rev. A* **1982**, *25* (3), 1265-1271.

92. Perdew, J. P.; Wang, Y., Accurate and simple analytic representation of the electron-gas correlation energy. *Phys. Rev. B* **1992**, *45* (23), 13244-13249.

93. (a) Becke, A. D., Density-functional exchange-energy approximation with correct asymptotic behavior. *Phys. Rev. A* **1988**, *38* (6), 3098-3100; (b) Perdew, J. P., Erratum: Density-functional approximation for the correlation

- energy of the inhomogeneous electron gas. *Phys. Rev. B* **1986**, *34* (10), 7406-7406; (c) Perdew, J. P., Density-functional approximation for the correlation energy of the inhomogeneous electron gas. *Phys. Rev. B* **1986**, *33* (12), 8822-8824.
94. Perdew, J. P.; Chevary, J. A.; Vosko, S. H.; Jackson, K. A.; Pederson, M. R.; Singh, D. J.; Fiolhais, C., Atoms, molecules, solids, and surfaces: Applications of the generalized gradient approximation for exchange and correlation. *Phys. Rev. B* **1992**, *46* (11), 6671-6687.
95. Perdew, J. P.; Burke, K.; Ernzerhof, M., Generalized Gradient Approximation Made Simple. *Phys. Rev. Lett.* **1996**, *77* (18), 3865-3868.
96. Lee, C.; Yang, W.; Parr, R. G., Development of the Colle-Salvetti correlation-energy formula into a functional of the electron density. *Phys. Rev. B* **1988**, *37* (2), 785-789.
97. (a) Veillard, A.; Clementi, E., Correlation Energy in Atomic Systems. V. Degeneracy Effects for the Second-Row Atoms. *J. Chem. Phys.* **1968**, *49* (5), 2415-2421; (b) Savin, A.; Stoll, H.; Preuss, H., An application of correlation energy density functionals to atoms and molecules. *Theoret. Chim. Acta* **1986**, *70* (6), 407-419.
98. (a) Hu, C. D.; Langreth, D. C., Beyond the random-phase approximation in nonlocal-density-functional theory. *Phys. Rev. B* **1986**, *33* (2), 943-959; (b) Geldart, D. J. W.; Rasolt, M., Exchange and correlation energy of an inhomogeneous electron gas at metallic densities. *Phys. Rev. B* **1976**, *13* (4), 1477-1488.
99. Rasolt, M.; Geldart, D. J. W., Exchange and correlation energy in a nonuniform fermion fluid. *Phys. Rev. B* **1986**, *34* (2), 1325-1328.
100. Cohen, A. J.; Handy, N. C., Dynamic correlation. *Mol. Phys.* **2001**, *99* (7), 607-615.
101. (a) Stephens, P. J.; Devlin, F. J.; Chabalowski, C. F.; Frisch, M. J., Ab Initio Calculation of Vibrational Absorption and Circular Dichroism Spectra Using Density Functional Force Fields. *J. Phys. Chem.* **1994**, *98* (45), 11623-11627; (b) Becke, A. D., A new mixing of Hartree-Fock and local density-functional theories. *J. Chem. Phys.* **1993**, *98* (2), 1372-1377.
102. Xu, X.; Goddard, W. A., The X3LYP extended density functional for accurate descriptions of nonbond interactions, spin states, and thermochemical properties. *Proc. Natl. Acad. Sci. U.S.A* **2004**, *101* (9), 2673-2677.
103. Lynch, B. J.; Fast, P. L.; Harris, M.; Truhlar, D. G., Adiabatic Connection for Kinetics. *J. Phys. Chem. A* **2000**, *104* (21), 4811-4815.
104. Adamo, C.; Barone, V., Exchange functionals with improved long-range behavior and adiabatic connection methods without adjustable parameters: The mPW and mPW1PW models. *J. Chem. Phys.* **1998**, *108* (2), 664-675.

105. Kang, J. K.; Musgrave, C. B., Prediction of transition state barriers and enthalpies of reaction by a new hybrid density-functional approximation. *J. Chem. Phys.* **2001**, *115* (24), 11040-11051.
106. Kim, K.; Jordan, K. D., Comparison of Density Functional and MP2 Calculations on the Water Monomer and Dimer. *J. Phys. Chem.* **1994**, *98* (40), 10089-10094.
107. Becke, A. D., Density-functional thermochemistry. III. The role of exact exchange. *J. Chem. Phys.* **1993**, *98* (7), 5648-5652.
108. (a) Staroverov, V. N.; Scuseria, G. E.; Tao, J.; Perdew, J. P., Comparative assessment of a new nonempirical density functional: Molecules and hydrogen-bonded complexes. *J. Chem. Phys.* **2003**, *119* (23), 12129-12137; (b) Tao, J.; Perdew, J. P.; Staroverov, V. N.; Scuseria, G. E., Climbing the Density Functional Ladder: Nonempirical Meta-Generalized Gradient Approximation Designed for Molecules and Solids. *Phys. Rev. Lett.* **2003**, *91* (14), 146401.
109. (a) Zhao, Y.; Truhlar, D. G., A new local density functional for main-group thermochemistry, transition metal bonding, thermochemical kinetics, and noncovalent interactions. *J. Chem. Phys.* **2006**, *125* (19), 194101; (b) Zhao, Y.; Truhlar, D., The M06 suite of density functionals for main group thermochemistry, thermochemical kinetics, noncovalent interactions, excited states, and transition elements: two new functionals and systematic testing of four M06-class functionals and 12 other functionals. *Theor. Chem. Acc.* **2008**, *120* (1-3), 215-241.
110. Boese, A. D.; Handy, N. C., New exchange-correlation density functionals: The role of the kinetic-energy density. *J. Chem. Phys.* **2002**, *116* (22), 9559-9569.
111. Van Voorhis, T.; Scuseria, G. E., A novel form for the exchange-correlation energy functional. *J. Chem. Phys.* **1998**, *109* (2), 400-410.
112. Odashima, M. M.; Capelle, K., Nonempirical hyper-generalized-gradient functionals constructed from the Lieb-Oxford bound. *Phys. Rev. A* **2009**, *79* (6), 062515.
113. Kümmel, S.; Perdew, J. P., Optimized effective potential made simple: Orbital functionals, orbital shifts, and the exact Kohn-Sham exchange potential. *Phys. Rev. B* **2003**, *68* (3), 035103.
114. Attila Szabo, N. S. O., *Modern Quantum Chemistry: Introduction to Advanced Electronic Structure Theory*. Dover Publications, INC: Mineola, New York, 1982.
115. (a) Roothaan, C. C. J., New Developments in Molecular Orbital Theory. *Rev. Mod. Phys.* **1951**, *23* (2), 69-89; (b) Hall, G. G., The Molecular Orbital Theory of Chemical Valency. VIII. A Method of Calculating Ionization Potentials. *Proc. Math. Phys. Eng. Sci.* **1951**, *205* (1083), 541-552.
116. Slater, J. C., Atomic Shielding Constants. *Phys. Rev.* **1930**, *36* (1), 57-64.

117. Boys, S. F., Electronic Wave Functions. I. A General Method of Calculation for the Stationary States of Any Molecular System. *Proc. Math. Phys. Eng. Sci.* **1950**, *200* (1063), 542-554.
118. Baerends, E. J. A., J.; Bérces, A.; Bo, C.; Boerrigter, P. M.; Cavallo, L.; Chong, D. P.; Deng, L.; Dickson, R. M.; Ellis, D. E.; Faassen, M. v.; Fan, L.; Fischer, T. H.; Guerra, C. F.; Gisbergen, S. J. A. v.; Groeneveld, J. A.; Gritsenko, O. V.; Grüning, M.; Harris, F. E.; Hoek, P. v. d.; Jacobsen, H.; Jensen, L.; Kessel, G. v.; Kootstra, F.; Lenthe, E. v.; McCormack, D. A.; Michalak, A.; Osinga, V. P.; Patchkovskii, S.; Philipsen, P. H. T.; Post, D.; Pye, C. C.; Ravenek, W.; Ros, P.; Schipper, P. R. T.; Schreckenbach, G.; Snijders, J. G.; Sola, M.; Swart, M.; Swerhone, D.; Velde, G. t.; Vernooijs, P.; Versluis, L.; Visser, O.; Wang, F.; Wezenbeek, E. v.; Wiesenekker, G.; Wolff, S. K.; Woo, T. K.; Yakovlev, A. L.; Ziegler, T., Amsterdam Density Functional Program; <http://www.scm.com>.
119. te Velde, G.; Bickelhaupt, F. M.; Baerends, E. J.; Fonseca Guerra, C.; van Gisbergen, S. J. A.; Snijders, J. G.; Ziegler, T., Chemistry with ADF. *J. Comput. Chem.* **2001**, *22* (9), 931-967.
120. Kempf, J. Y.; Rohmer, M. M.; Poblet, J. M.; Bo, C.; Benard, M., Relative basicities of the oxygen sites in [V10O28]6-. An analysis of the ab initio determined distributions of the electrostatic potential and of the Laplacian of charge density. *J. Am. Chem. Soc.* **1992**, *114* (4), 1136-1146.
121. Pascual-Borras, M.; Lopez, X.; Rodriguez-Forteza, A.; Errington, R. J.; Poblet, J. M., 17O NMR chemical shifts in oxometalates: from the simplest monometallic species to mixed-metal polyoxometalates. *Chem. Sci.* **2014**, *5* (5), 2031-2042.
122. (a) Maestre, J. M.; Poblet, J. M.; Bo, C.; Casañ-Pastor, N.; Gomez-Romero, P., Electronic Structure of the Highly Reduced Polyoxoanion [PMo12O40(VO)2]5-: A DFT Study. *Inorg. Chem.* **1998**, *37* (13), 3444-3446; (b) Maestre, J. M.; Lopez, X.; Bo, C.; Poblet, J.-M.; Casañ-Pastor, N., Electronic and Magnetic Properties of  $\alpha$ -Keggin Anions: A DFT Study of [XM12O40]n-, (M = W, Mo; X = AlIII, SiIV, PV, FeIII, CoII, CoIII) and [SiM11VO40]m- (M = Mo and W). *J. Am. Chem. Soc.* **2001**, *123* (16), 3749-3758.
123. Maestre, J. M.; Sarasa, J. P.; Bo, C.; Poblet, J. M., Ab Initio Study of the Relative Basicity of the External Oxygen Sites in M2W4O194- (M = Nb and V). *Inorg. Chem.* **1998**, *37* (12), 3071-3077.
124. (a) López, X.; Bo, C.; Poblet, J.-M.; Sarasa, J. P., Relative Stability in  $\alpha$ - and  $\beta$ -Wells-Dawson Heteropolyanions: A DFT Study of [P2M18O62]n- (M = W and Mo) and [P2W15V3O62]n. *Inorg. Chem.* **2003**, *42* (8), 2634-2638; (b) López, X.; Bo, C.; Poblet, J. M., Electronic Properties of Polyoxometalates: Electron and Proton Affinity of Mixed-Addenda Keggin and Wells-Dawson Anions. *J. Am. Chem. Soc.* **2002**, *124* (42), 12574-12582; (c) López, X.; Maestre, J. M.; Bo, C.; Poblet, J.-M., Electronic Properties of Polyoxometalates: A DFT Study of  $\alpha/\beta$ -



- [XM12O40]<sub>n</sub>- Relative Stability (M = W, Mo and X a Main Group Element). *J. Am. Chem. Soc.* **2001**, *123* (39), 9571-9576.
125. Maestre, J. M.; Lopez, X.; Bo, C.; Poblet, J.-M.; Daul, C., A DFT Study of the Electronic Spectrum of the  $\alpha$ -Keggin Anion [CollW12O40]<sub>6</sub>. *Inorg. Chem.* **2002**, *41* (7), 1883-1888.
126. López, X.; Weinstock, I. A.; Bo, C.; Sarasa, J. P.; Poblet, J. M., Structural Evolution in Polyoxometalates: A DFT Study of Dimerization Processes in Lindqvist and Keggin Cluster Anions. *Inorg. Chem.* **2006**, *45* (16), 6467-6473.
127. López, X.; de Graaf, C.; Maestre, J. M.; Bénard, M.; Rohmer, M.-M.; Bo, C.; Poblet, J. M., Highly Reduced Polyoxometalates: Ab Initio and DFT Study of [PMo8V4O40(VO)4]<sub>5</sub>. *J. Chem. Theory Comput.* **2005**, *1* (5), 856-861.
128. (a) Botar, B.; Geletii, Y. V.; Kögerler, P.; Musaev, D. G.; Morokuma, K.; Weinstock, I. A.; Hill, C. L., The True Nature of the Di-iron(III)  $\gamma$ -Keggin Structure in Water: Catalytic Aerobic Oxidation and Chemistry of an Unsymmetrical Trimer. *J. Am. Chem. Soc.* **2006**, *128* (34), 11268-11277; (b) Nakagawa, Y.; Mizuno, N., Mechanism of [ $\gamma$ -H<sub>2</sub>Si<sub>2</sub>W<sub>10</sub>O<sub>40</sub>]<sub>4</sub>-Catalyzed Epoxidation of Alkenes with Hydrogen Peroxide. *Inorg. Chem.* **2007**, *46* (5), 1727-1736.
129. Laskavy, A.; Shimon, L. J. W.; Konstantinovski, L.; Iron, M. A.; Neumann, R., Activation of Molecular Oxygen by a Dioxygenase Pathway by a Ruthenium Bis-bipyridine Compound with a Proximal Selenium Site. *J. Am. Chem. Soc.* **2010**, *132* (2), 517-523.
130. M. P. Allen, D. J. T., *Computer Simulations of Liquids*. Clarendon Press: Oxford, 1987.
131. Metropolis, N.; Ulam, S., The monte carlo method. *Journal of the American statistical association* **1949**, *44* (247), 335-341.
132. Birkhoff, G. D., What is the Ergodic Theorem? *Am. Math. Monthly* **1942**, *49* (4), 222-226.
133. Metropolis, N.; Rosenbluth, A. W.; Rosenbluth, M. N.; Teller, A. H.; Teller, E., Equation of State Calculations by Fast Computing Machines. *J. Chem. Phys.* **1953**, *21* (6), 1087-1092.
134. Zwanzig, R., Proceedings of the International Symposium on Transport Processes in Statistical Mechanics, held in Brussels, August 27-31, 1956. *J. Am. Chem. Soc.* **1959**, *81* (12), 3172-3172.
135. Gibson, J. B.; Goland, A. N.; Milgram, M.; Vineyard, G. H., Dynamics of Radiation Damage. *Phys. Rev.* **1960**, *120* (4), 1229-1253.
136. Rahman, A., Correlations in the Motion of Atoms in Liquid Argon. *Phys. Rev.* **1964**, *136* (2A), A405-A411.
137. Martínez, L.; Andrade, R.; Birgin, E. G.; Martínez, J. M., PACKMOL: A package for building initial configurations for molecular dynamics simulations. *J. Comput. Chem.* **2009**, *30* (13), 2157-2164.

138. Martínez, J. M.; Martínez, L., Packing optimization for automated generation of complex system's initial configurations for molecular dynamics and docking. *J. Comput. Chem.* **2003**, *24* (7), 819-825.
139. J. P. Hansen, I. R. M., *Theory of Simple Liquids*. Academic Press: London, 1986.
140. Fender, B. E. F., Halsey Jr, G. D. , Second Virial Coefficients of Argon, Krypton, and Argon-Krypton Mixtures at Low Temperatures. *J. Chem. Phys.* **1962**, *36* (7), 1881-1888.
141. Kong, C. L., Combining rules for intermolecular potential parameters. II. Rules for the Lennard-Jones (12–6) potential and the Morse potential. *J. Chem. Phys.* **1973**, *59* (5), 2464-2467.
142. Waldman, M.; Hagler, A. T., New combining rules for rare gas van der waals parameters. *J. Comput. Chem.* **1993**, *14* (9), 1077-1084.
143. Sikora, P. T., Combining rules for spherically symmetric intermolecular potentials. *J. Phys. B* **1970**, *3* (11), 1475.
144. (a) Lorentz, H. A., Ueber die Anwendung des Satzes vom Virial in der kinetischen Theorie der Gase. *Ann. Phys.* **1881**, *248* (1), 127-136; (b) Berthelot, D., Sur le mélange des gaz. *C. R. Acad. Sci.* **1898**, *126*, 1703-1855.
145. (a) Jorgensen, W. L.; Maxwell, D. S.; Tirado-Rives, J., Development and Testing of the OPLS All-Atom Force Field on Conformational Energetics and Properties of Organic Liquids. *J. Am. Chem. Soc.* **1996**, *118* (45), 11225-11236; (b) Jorgensen, W. L.; Gao, J., Monte Carlo simulations of the hydration of ammonium and carboxylate ions. *J. Phys. Chem.* **1986**, *90* (10), 2174-2182.
146. (a) Jorgensen, W. L.; Madura, J. D.; Swenson, C. J., Optimized intermolecular potential functions for liquid hydrocarbons. *J. Am. Chem. Soc.* **1984**, *106* (22), 6638-6646; (b) Smit, B.; Karaborni, S.; Siepmann, J. I., Computer simulations of vapor-liquid phase equilibria of n-alkanes. *J. Chem. Phys.* **1995**, *102* (5), 2126-2140; (c) Smit, B.; Karaborni, S.; Siepmann, J. I., Erratum:Computer simulations of vapour-liquid phase equilibria of n-alkanes, *J. Chem. Phys.*, *102*, 2126 (1995). *J. Chem. Phys.* **1998**, *109* (EPFL-ARTICLE-200650), 352; (d) Martin, M. G.; Siepmann, J. I., Transferable Potentials for Phase Equilibria. 1. United-Atom Description of n-Alkanes. *J. Phys. Chem. B* **1998**, *102* (14), 2569-2577; (e) Cournoyer, M. E.; Jorgensen, W. L., Solvent effects on the relative energies of carbonium ions. Solvation and internal rotation for the allyl cation in liquid hydrogen fluoride. *J. Am. Chem. Soc.* **1984**, *106* (18), 5104-5112.
147. Leroy, F.; Miró, P.; Poblet, J. M.; Bo, C.; Bonet Ávalos, J., Keggin Polyoxoanions in Aqueous Solution: Ion Pairing and Its Effect on Dynamic Properties by Molecular Dynamics Simulations. *J. Phys. Chem. B* **2008**, *112* (29), 8591-8599.

148. Pauling, L., *The Nature of the Chemical Bond and the Structure of Molecules and Crystals: An Introduction to Modern Structural Chemistry*. New York, 1960.
149. Franks, F., *Water - a Comprehensive Treatise*. New York and London, 1972.
150. Kell, G. S., Precise representation of volume properties of water at one atmosphere. *J. Chem. Eng. Data* **1967**, *12* (1), 66-69.
151. (a) Burton, E. F.; Oliver, W. F., The Crystal Structure of Ice at Low Temperatures. *Proceedings of the Royal Society of London. Series A, Mathematical and Physical Sciences* **1935**, *153* (878), 166-172; (b) Poole, P. H.; Grande, T.; Sciortino, F.; Stanley, H. E.; Angell, C. A., Amorphous polymorphism. *Comput. Mater. Sci.* **1995**, *4* (4), 373-382; (c) Mishima, O.; Calvert, L. D.; Whalley, E., 'Melting ice' I at 77 K and 10 kbar: a new method of making amorphous solids. *Nature* **1984**, *310* (5976), 393-395; (d) Mishima, O.; Calvert, L. D.; Whalley, E., An apparently first-order transition between two amorphous phases of ice induced by pressure. *Nature* **1985**, *314* (6006), 76-78.
152. (a) Franzese, G.; Stanley, H. E., The Widom line of supercooled water. *J. Phys.: Condens. Matter* **2007**, *19* (20), 205126; (b) Franzese, G.; Eugene Stanley, H., A theory for discriminating the mechanism responsible for the water density anomaly. *Physica A* **2002**, *314* (1-4), 508-513; (c) Malescio, G.; Franzese, G.; Pellicane, G.; Skibinsky, A.; V. Buldyrev, S.; Stanley, H. E., Liquid-liquid phase transition in one-component fluids. *J. Phys.: Condens. Matter* **2002**, *14* (9), 2193; (d) Franzese, G.; Stanley, H. E., Liquid-liquid critical point in a Hamiltonian model for water: analytic solution. *J. Phys.: Condens. Matter* **2002**, *14* (9), 2201; (e) Franzese, G.; Marqués, M. I.; Eugene Stanley, H., Intramolecular coupling as a mechanism for a liquid-liquid phase transition. *Phys. Rev. E* **2003**, *67* (1), 011103.
153. (a) Liu, Y.; Ichiye, T., The static dielectric constant of the soft sticky dipole model of liquid water: Monte Carlo simulation. *Chem. Phys. Lett.* **1996**, *256* (3), 334-340; (b) Liu, Y.; Ichiye, T., Soft Sticky Dipole Potential for Liquid Water: A New Model. *J. Phys. Chem.* **1996**, *100* (7), 2723-2730; (c) Tan, M.-L.; Fischer, J. T.; Chandra, A.; Brooks, B. R.; Ichiye, T., A temperature of maximum density in soft sticky dipole water. *Chem. Phys. Lett.* **2003**, *376* (5-6), 646-652.
154. Berendsen, H. J. C., *Intermolecular Forces*. D. Reidel Publishing Company: 1981.
155. (a) Toukan, K.; Rahman, A., Molecular-dynamics study of atomic motions in water. *Phys. Rev. B* **1985**, *31* (5), 2643-2648; (b) Berendsen, H. J. C.; Grigera, J. R.; Straatsma, T. P., The missing term in effective pair potentials. *J. Phys. Chem.* **1987**, *91* (24), 6269-6271.
156. Svishchev, I. M.; Kusalik, P. G.; Wang, J.; Boyd, R. J., Polarizable point-charge model for water: Results under normal and extreme conditions. *J. Chem. Phys.* **1996**, *105* (11), 4742-4750.

157. Paricaud, P.; Předota, M.; Chialvo, A. A.; Cummings, P. T., From dimer to condensed phases at extreme conditions: Accurate predictions of the properties of water by a Gaussian charge polarizable model. *J. Chem. Phys.* **2005**, *122* (24), 2445-11.
158. Nada, H.; van der Eerden, J. P. J. M., An intermolecular potential model for the simulation of ice and water near the melting point: A six-site model of H<sub>2</sub>O. *J. Chem. Phys.* **2003**, *118* (16), 7401-7413.
159. Jorgensen, W. L.; Chandrasekhar, J.; Madura, J. D.; Impey, R. W.; Klein, M. L., Comparison of simple potential functions for simulating liquid water. *J. Chem. Phys.* **1983**, *79* (2), 926-935.
160. Jorgensen, W. L.; Madura, J. D., Temperature and size dependence for Monte Carlo simulations of TIP4P water. *Mol. Phys.* **1985**, *56* (6), 1381-1392.
161. Mahoney, M. W.; Jorgensen, W. L., A five-site model for liquid water and the reproduction of the density anomaly by rigid, nonpolarizable potential functions. *J. Chem. Phys.* **2000**, *112* (20), 8910-8922.
162. Abascal, J. L. F.; Vega, C., A general purpose model for the condensed phases of water: TIP4P/2005. *J. Chem. Phys.* **2005**, *123* (23), 234505.
163. (a) D. Frenkel, B. S., *Understanding Molecular Simulation: From Algorithms to Applications*. Academic Press: San Diego, San Francisco, New York, Boston, London, Sydney, Tokyo, 1996; (b) Ewald, P. P., Die Berechnung optischer und elektrostatischer Gitterpotentiale. *Ann. Phys.* **1921**, *369* (3), 253-287.
164. Andrews, L. C., *Special Functions of Mathematics for Engineers*. The International Society for Optical Engineering Oxford University Press: 1992.
165. Esselink, K., A comparison of algorithms for long-range interactions. *Comput. Phys. Commun.* **1995**, *87* (3), 375-395.
166. Wilson, S.; Dierksen, G. H., *Problem Solving in Computational Molecular Science: Molecules in Different Environments*. Springer Science & Business Media: 2012; Vol. 500.
167. Rappe, A. K.; Goddard, W. A., Charge equilibration for molecular dynamics simulations. *J. Phys. Chem.* **1991**, *95* (8), 3358-3363.
168. Breneman, C. M.; Wiberg, K. B., Determining atom-centered monopoles from molecular electrostatic potentials. The need for high sampling density in formamide conformational analysis. *J. Comput. Chem.* **1990**, *11* (3), 361-373.
169. (a) de Oliveira, A. E.; Haiduke, R. L. A.; Bruns, R. E., Atomic Mean Dipole Moment Derivatives and GAPT Charges. *J. Phys. Chem. A* **2000**, *104* (22), 5320-5327; (b) Cioslowski, J., General and unique partitioning of molecular electronic properties into atomic contributions. *Phys. Rev. Lett.* **1989**, *62* (13), 1469-1471; (c) Cioslowski, J.; Hay, P. J.; Ritchie, J. P., Charge distributions and effective atomic charges in transition-metal complexes using generalized atomic polar tensors and topological analysis. *J. Phys. Chem.* **1990**, *94* (1), 148-151; (d) Cioslowski, J.; Hamilton, T.; Scuseria, G.; Hess, B. A.; Hu, J.; Schaad, L. J.; Dupuis,

- M., Application of the GAPT (generalized atomic polar tensor) population analysis to some organic molecules and transition structures. *J. Am. Chem. Soc.* **1990**, *112* (11), 4183-4186; (e) Helgaker, T. U.; Jo, H.; Jo, P., Analytical calculation of MCSCF dipole-moment derivatives. *J. Chem. Phys.* **1986**, *84* (11), 6280-6284.
170. (a) Mulliken, R. S., Criteria for the Construction of Good Self-Consistent-Field Molecular Orbital Wave Functions, and the Significance of LCAO-MO Population Analysis. *J. Chem. Phys.* **1962**, *36* (12), 3428-3439; (b) Politzer, P.; Mulliken, R. S., Comparison of Two Atomic Charge Definitions, as Applied to the Hydrogen Fluoride Molecule. *J. Chem. Phys.* **1971**, *55* (10), 5135-5136; (c) Grier, D. L.; Streitwieser, A., Electron density analysis of substituted carbonyl groups. *J. Am. Chem. Soc.* **1982**, *104* (13), 3556-3564.
171. (a) Reed, A. E.; Weinstock, R. B.; Weinhold, F., Natural population analysis. *J. Chem. Phys.* **1985**, *83* (2), 735-746; (b) Reed, A. E.; Curtiss, L. A.; Weinhold, F., Intermolecular interactions from a natural bond orbital, donor-acceptor viewpoint. *Chem. Rev.* **1988**, *88* (6), 899-926.
172. Hirshfeld, F. L., Bonded-atom fragments for describing molecular charge densities. *Theoret. Chim. Acta* **1977**, *44* (2), 129-138.
173. (a) Bader, R. F. W., *Atoms in Molecules. A Quantum Theory*. Oxford, 1990; (b) Bader, R. F. W., Atoms in molecules. *Acc. Chem. Res.* **1985**, *18* (1), 9-15.
174. (a) Fonseca Guerra, C.; Handgraaf, J.-W.; Baerends, E. J.; Bickelhaupt, F. M., Voronoi deformation density (VDD) charges: Assessment of the Mulliken, Bader, Hirshfeld, Weinhold, and VDD methods for charge analysis. *J. Comput. Chem.* **2004**, *25* (2), 189-210; (b) Fonseca Guerra, C.; Bickelhaupt, F. M.; Snijders, J. G.; Baerends, E. J., The Nature of the Hydrogen Bond in DNA Base Pairs: The Role of Charge Transfer and Resonance Assistance. *Chem. Eur. J.* **1999**, *5* (12), 3581-3594; (c) Bickelhaupt, F. M.; van Eikema Hommes, N. J. R.; Fonseca Guerra, C.; Baerends, E. J., The Carbon-Lithium Electron Pair Bond in (CH<sub>3</sub>Li)<sub>n</sub> (n = 1, 2, 4). *Organometallics* **1996**, *15* (13), 2923-2931.
175. Aurenhammer, F., Voronoi diagrams—a survey of a fundamental geometric data structure. *ACM Computing Surveys (CSUR)* **1991**, *23* (3), 345-405.
176. Todorov, I. T.; Smith, W.; Trachenko, K.; Dove, M. T., DL\_POLY\_3: new dimensions in molecular dynamics simulations via massive parallelism. *J. Mater. Chem.* **2006**, *16* (20), 1911-1918.
177. (a) Chaumont, A.; Wipff, G., Polyoxometalate Keggin Anions at Aqueous Interfaces with Organic Solvents, Ionic Liquids, and Graphite: a Molecular Dynamics Study. *J. Phys. Chem. C* **2009**, *113* (42), 18233-18243; (b) Chaumont, A.; Wipff, G., Ion aggregation in concentrated aqueous and methanol solutions of polyoxometallates Keggin anions: the effect of counterions investigated by molecular dynamics simulations. *PCCP* **2008**, *10* (46), 6940-6953.

178. Ryckaert, J.-P.; Ciccotti, G.; Berendsen, H. J. C., Numerical integration of the cartesian equations of motion of a system with constraints: molecular dynamics of n-alkanes. *J. Comp. Phys.* **1977**, *23* (3), 327-341.
179. Hamilton, W. R., LXXVIII. On quaternions; or on a new system of imaginaries in Algebra. *Philos. Mag.* **1844**, *25* (169), 489-495.
180. Evans, D. J., On the representation of orientation space. *Mol. Phys.* **1977**, *34* (2), 317-325.
181. Fincham, D., Leapfrog Rotational Algorithms. *Mol. Sim.* **1992**, *8* (3-5), 165-178.
182. Woodcock, L. V., Isothermal molecular dynamics calculations for liquid salts. *Chem. Phys. Lett.* **1971**, *10* (3), 257-261.
183. Andersen, H. C., Molecular dynamics simulations at constant pressure and/or temperature. *J. Chem. Phys.* **1980**, *72* (4), 2384-2393.
184. (a) Nosé, S., A molecular dynamics method for simulations in the canonical ensemble. *Mol. Phys.* **1984**, *52* (2), 255-268; (b) Nosé, S., A unified formulation of the constant temperature molecular dynamics methods. *J. Chem. Phys.* **1984**, *81* (1), 511-519.
185. Martyna, G. J.; Tobias, D. J.; Klein, M. L., Constant pressure molecular dynamics algorithms. *J. Chem. Phys.* **1994**, *101* (5), 4177-4189.
186. Melchionna, S.; Ciccotti, G.; Lee Holian, B., Hoover NPT dynamics for systems varying in shape and size. *Mol. Phys.* **1993**, *78* (3), 533-544.
187. (a) Volkmer, D.; Bredenkötter, B.; Tellenbröcker, J.; Kögerler, P.; Kurth, D. G.; Lehmann, P.; Schnablegger, H.; Schwahn, D.; Piepenbrink, M.; Krebs, B., Structure and Properties of the Dendron-Encapsulated Polyoxometalate (C<sub>52</sub>H<sub>60</sub>NO<sub>12</sub>)<sub>12</sub>[(Mn(H<sub>2</sub>O))<sub>3</sub>(SbW<sub>9</sub>O<sub>33</sub>)<sub>2</sub>], a First Generation Dendrzyme. *J. Am. Chem. Soc.* **2002**, *124* (35), 10489-10496; (b) Brodbeck, R.; Tönsing, T.; Andrae, D.; Volkmer, D., Molecular Dynamics Simulations of Dendrimer-Encapsulated  $\alpha$ -Keggin Ions in Trichloromethane Solution. *J. Phys. Chem. B* **2008**, *112* (16), 5153-5162.
188. Ma, C.; Piccinin, S.; Fabris, S., Interface structure and reactivity of water-oxidation Ru-polyoxometalate catalysts on functionalized graphene electrodes. *PCCP* **2014**, *16* (11), 5333-5341.
189. (a) Bonhomme, F.; Larentzos, J. P.; Alam, T. M.; Maginn, E. J.; Nyman, M., Synthesis, Structural Characterization, and Molecular Modeling of Dodecaniobate Keggin Chain Materials. *Inorg. Chem.* **2005**, *44* (6), 1774-1785; (b) Chaumont, A.; Wipff, G., Interactions between Keggin Anions in Water: The Higher Their Charge, the Higher Their Condensation? A Simulation Study. *Eur. J. Inorg. Chem.* **2013**, *2013* (10-11), 1835-1853; (c) Chaumont, A.; Wipff, G., Do Keggin anions repulse each other in solution? The effect of solvent, counterions and ion representation investigated by free energy (PMF) simulations. *C. R. Chimie* **2012**, *15* (2-3), 107-117.

190. Miró, P.; Vlaisavljevich, B.; Dzubak, A. L.; Hu, S.; Burns, P. C.; Cramer, C. J.; Spezia, R.; Gagliardi, L., Uranyl–Peroxide Nanocapsules in Aqueous Solution: Force Field Development and First Applications. *J. Phys. Chem. C* **2014**, *118* (42), 24730-24740.
191. Müller, A.; Krickemeyer, E.; Bögge, H.; Schmidtman, M.; Peters, F., Organizational Forms of Matter: An Inorganic Super Fullerene and Keplerate Based on Molybdenum Oxide. *Angew. Chem. Int. Ed.* **1998**, *37* (24), 3359-3363.
192. Schäffer, C.; Merca, A.; Bögge, H.; Todea, A. M.; Kistler, M. L.; Liu, T.; Thouvenot, R.; Gouzerh, P.; Müller, A., Unprecedented and Differently Applicable Pentagonal Units in a Dynamic Library: A Keplerate of the Type  $\{(W)W_5\}_{12}\{Mo_2\}_{30}$ . *Angew. Chem. Int. Ed.* **2009**, *48* (1), 149-153.
193. (a) Lenthe, E. v.; Baerends, E. J.; Snijders, J. G., Relativistic regular two-component Hamiltonians. *J. Chem. Phys.* **1993**, *99* (6), 4597-4610; (b) van Lenthe, E.; Baerends, E. J.; Snijders, J. G., Relativistic total energy using regular approximations. *J. Chem. Phys.* **1994**, *101* (11), 9783-9792; (c) van Lenthe, E.; Ehlers, A.; Baerends, E.-J., Geometry optimizations in the zero order regular approximation for relativistic effects. *J. Chem. Phys.* **1999**, *110* (18), 8943-8953.
194. Klamt, A.; Schuurmann, G., COSMO: a new approach to dielectric screening in solvents with explicit expressions for the screening energy and its gradient. *J. Chem. Soc., Perkin Trans. 2* **1993**, (5), 799-805.
195. Schäffer, C.; Todea, A. M.; Bögge, H.; Cadot, E.; Gouzerh, P.; Kopilevich, S.; Weinstock, I. A.; Müller, A., Softening of Pore and Interior Properties of a Metal-Oxide-Based Capsule: Substituting 60 Oxide by 60 Sulfide Ligands. *Angew. Chem.* **2011**, *123* (51), 12534-12537.
196. Schaffer, C.; Todea, A. M.; Bogge, H.; Floquet, S.; Cadot, E.; Korenev, V. S.; Fedin, V. P.; Gouzerh, P.; Muller, A., A further step towards tuning the properties of metal-chalcogenide nanocapsules by replacing skeletal oxide by sulphide ligands. *Dalton Trans.* **2013**, *42* (2), 330-333.
197. Leclerc-Laronze, N.; Marrot, J.; Thouvenot, R.; Cadot, E., Structural Link between Giant Molybdenum Oxide Based Ions and Derived Keggin Structure: Modular Assemblies Based on the  $[BW_{11}O_{39}]_9^-$  Ion and Pentagonal  $\{M'M_5\}$  Units ( $M'=W$ ;  $M=Mo,W$ ). *Angew. Chem. Int. Ed.* **2009**, *48* (27), 4986-4989.
198. Allinger, N. L.; Zhou, X.; Bergsma, J., Molecular mechanics parameters. *J. Mol. Struct.-THEOCHEM* **1994**, *312* (1), 69-83.
199. López, X.; Fernández, J. A.; Romo, S.; Paul, J. F.; Kazansky, L.; Poblet, J. M., Are the solvent effects critical in the modeling of polyoxoanions? *J. Comput. Chem.* **2004**, *25* (12), 1542-1549.
200. (a) Haso, F.; Fang, X.; Yin, P.; Li, D.; Ross, J. L.; Liu, T., The self-assembly of a macroion with anisotropic surface charge density distribution. *Chem. Commun.* **2013**, *49* (6), 609-611; (b) Yin, P.; Li, D.; Liu, T., Solution behaviors and self-assembly of polyoxometalates as models of macroions and amphiphilic polyoxometalate-organic hybrids as novel surfactants. *Chem. Soc. Rev.* **2012**, *41*

- (22), 7368-7383; (c) Wang, Y.; Weinstock, I. A., Cation mediated self-assembly of inorganic cluster anion building blocks. *Dalton Trans.* **2010**, 39 (27), 6143-6152.
201. Moussawi, M.; Floquet, S.; Cadot, E., Private Communication. 2015.
202. Miras, H. N.; Cronin, L., Private Communication. 2013.
203. Muller, A.; Das, K.; Krickemyer, E.; Kuhlmann, C., Polyoxomolybdate clusters: Giant wheels and balls. *Inorg. Synth.* **2004**, 34, 191-200.
204. Henry, M.; Bögge, H.; Diemann, E.; Müller, A., Chameleon water: assemblies confined in nanocapsules. *J. Mol. Liq.* **2005**, 118 (1), 155-162.
205. Müller, A.; Das, S. K.; Talismanov, S.; Roy, S.; Beckmann, E.; Bögge, H.; Schmidtman, M.; Merca, A.; Berkle, A.; Allouche, L.; Zhou, Y.; Zhang, L., Trapping Cations in Specific Positions in Tuneable "Artificial Cell" Channels: New Nanochemistry Perspectives. *Angew. Chem. Int. Ed.* **2003**, 42 (41), 5039-5044.
206. (a) Müller, A.; Krickemeyer, E.; Bögge, H.; Schmidtman, M.; Roy, S.; Berkle, A., Changeable Pore Sizes Allowing Effective and Specific Recognition by a Molybdenum-Oxide Based "Nanosponge": En Route to Sphere-Surface and Nanoporous-Cluster Chemistry. *Angew. Chem. Int. Ed.* **2002**, 41 (19), 3604-3609; (b) Müller, A.; Sarkar, S.; Shah, S.; Bögge, H.; Schmidtman, M.; Kögerler, P.; Hauptfleisch, B.; Trautwein, A.; Schünemann, V., Archimedean Synthesis and Magic Numbers: "Sizing" Giant Molybdenum-Oxide-Based Molecular Spheres of the Keplerate Type. *Angew. Chem. Int. Ed. Engl.* **1999**, 38 (21), 3238-3241.
207. (a) Hoffmann, R., Building bridges between inorganic and organic chemistry (Nobel Lecture). *Angew. Chem. Int. Ed.* **1982**, 21 (10), 711-724; (b) Ziegler, T.; Rauk, A., CO, CS, N<sub>2</sub>, PF<sub>3</sub>, and CNCH<sub>3</sub> as  $\sigma$  donors and  $\pi$  acceptors. A theoretical study by the Hartree-Fock-Slater transition-state method. *Inorg. Chem.* **1979**, 18, 1755-1759; (c) Ziegler, T.; Rauk, A., A theoretical study of the ethylene-metal bond in complexes between copper (1+), silver (1+), gold (1+), platinum (0) or platinum (2+) and ethylene, based on the Hartree-Fock-Slater transition-state method. *Inorg. Chem.* **1979**, 18 (6), 1558-1565; (d) Bickelhaupt, F. M., Understanding reactivity with Kohn-Sham molecular orbital theory: E<sub>2</sub>-SN<sub>2</sub> mechanistic spectrum and other concepts. *J. Comput. Chem.* **1999**, 20 (1), 114-128; (e) Morokuma, K., Molecular Orbital Studies of Hydrogen Bonds. III. C=O...H-O Hydrogen Bond in H<sub>2</sub>CO...H<sub>2</sub>O and H<sub>2</sub>CO...2H<sub>2</sub>O. *J. Chem. Phys.* **1971**, 55 (3), 1236-1244; (f) Kitaura, K.; Morokuma, K., A new energy decomposition scheme for molecular interactions within the Hartree-Fock approximation. *Int. J. Quantum Chem.* **1976**, 10 (2), 325-340.
208. *Handbook of Chemistry and Physics*. 84th ed.; CRC Press: 2003.
209. Müller, A.; Krickemeyer, E.; Meyer, J.; Bögge, H.; Peters, F.; Plass, W.; Diemann, E.; Dillinger, S.; Nonnenbruch, F.; Randerath, M.; Menke, C., [Mo<sub>154</sub>(NO)<sub>140</sub>O<sub>420</sub>(OH)<sub>28</sub>(H<sub>2</sub>O)<sub>70</sub>](25 ± 5)<sup>-</sup>: A Water-Soluble Big Wheel with More than 700 Atoms and a Relative Molecular Mass of About 24000. *Angew. Chem. Int. Ed.* **1995**, 34 (19), 2122-2124.



210. Finke, R. G.; Droege, M. W.; Cook, J. C.; Suslick, K. S., Fast atom bombardment mass spectroscopy (FABMS) of polyoxoanions. *J. Am. Chem. Soc.* **1984**, *106* (19), 5750-5751.
211. Long, D.-L.; Streb, C.; Song, Y.-F.; Mitchell, S.; Cronin, L., Unravelling the Complexities of Polyoxometalates in Solution Using Mass Spectrometry: Protonation versus Heteroatom Inclusion. *J. Am. Chem. Soc.* **2008**, *130* (6), 1830-1832.
212. Car, R.; Parrinello, M., Unified Approach for Molecular Dynamics and Density-Functional Theory. *Phys. Rev. Lett.* **1985**, *55* (22), 2471-2474.
213. Muller, A.; Das, S. K.; Krickemeyer, E.; Kuhlmann, C.; Sadakane, M.; Dickman, M. H.; Pope, M. T., Polyoxomolybdate Clusters: Giant Wheels and Balls. *Inorganic Syntheses, Vol 34* **2004**, *34*, 191-200.
214. Frisch, M. J.; Trucks, G. W.; Schlegel, H. B.; Scuseria, G. E.; Robb, M. A.; Cheeseman, J. R.; Scalmani, G.; Barone, V.; Mennucci, B.; Petersson, G. A.; Nakatsuji, H.; Caricato, M.; Li, X.; Hratchian, H. P.; Izmaylov, A. F.; Bloino, J.; Zheng, G.; Sonnenberg, J. L.; Hada, M.; Ehara, M.; Toyota, K.; Fukuda, R.; Hasegawa, J.; Ishida, M.; Nakajima, T.; Honda, Y.; Kitao, O.; Nakai, H.; Vreven, T.; Montgomery Jr., J. A.; Peralta, J. E.; Ogliaro, F.; Bearpark, M. J.; Heyd, J.; Brothers, E. N.; Kudin, K. N.; Staroverov, V. N.; Kobayashi, R.; Normand, J.; Raghavachari, K.; Rendell, A. P.; Burant, J. C.; Iyengar, S. S.; Tomasi, J.; Cossi, M.; Rega, N.; Millam, N. J.; Klene, M.; Knox, J. E.; Cross, J. B.; Bakken, V.; Adamo, C.; Jaramillo, J.; Gomperts, R.; Stratmann, R. E.; Yazyev, O.; Austin, A. J.; Cammi, R.; Pomelli, C.; Ochterski, J. W.; Martin, R. L.; Morokuma, K.; Zakrzewski, V. G.; Voth, G. A.; Salvador, P.; Dannenberg, J. J.; Dapprich, S.; Daniels, A. D.; Farkas, Ö.; Foresman, J. B.; Ortiz, J. V.; Cioslowski, J.; Fox, D. J. *Gaussian 09*, Gaussian, Inc.: Wallingford, CT, USA, 2009.
215. (a) McLean, A. D.; Chandler, G. S., Contracted Gaussian basis sets for molecular calculations. I. Second row atoms, Z=11-18. *J. Chem. Phys.* **1980**, *72* (10), 5639-5648; (b) Krishnan, R.; Binkley, J. S.; Seeger, R.; Pople, J. A., Self-consistent molecular orbital methods. XX. A basis set for correlated wave functions. *J. Chem. Phys.* **1980**, *72* (1), 650-654.
216. Roy, L. E.; Hay, P. J.; Martin, R. L., Revised Basis Sets for the LANL Effective Core Potentials. *J. Chem. Theory Comput.* **2008**, *4* (7), 1029-1031.
217. (a) Schuchardt, K. L.; Didier, B. T.; Elsethagen, T.; Sun, L.; Gurumoorthi, V.; Chase, J.; Li, J.; Windus, T. L., Basis Set Exchange: A Community Database for Computational Sciences. *J. Chem. Inf. Model.* **2007**, *47* (3), 1045-1052; (b) Feller, D., The role of databases in support of computational chemistry calculations. *J. Comput. Chem.* **1996**, *17* (13), 1571-1586.
218. Scalmani, G.; Frisch, M. J., Continuous surface charge polarizable continuum models of solvation. I. General formalism. *J. Chem. Phys.* **2010**, *132* (11), 114110.

219. (a) Kurita, R.; Tanaka, H., Control of the liquid-liquid transition in a molecular liquid by spatial confinement. *Phys. Rev. Lett.* **2007**, *98* (23), 235701; (b) Alba-Simionesco, C.; Coasne, B.; Dosseh, G.; Dudziak, G.; Gubbins, K.; Radhakrishnan, R.; Sliwinska-Bartkowiak, M., Effects of confinement on freezing and melting. *J. Phys.: Condens. Matter* **2006**, *18* (6), R15; (c) Giovambattista, N.; Rossky, P. J.; Debenedetti, P. G., Phase transitions induced by nanoconfinement in liquid water. *Phys. Rev. Lett.* **2009**, *102* (5), 050603; (d) Hummer, G.; Szabo, A., Free energy reconstruction from nonequilibrium single-molecule pulling experiments. *Proc. Natl. Acad. Sci.* **2001**, *98* (7), 3658-3661; (e) Donadio, D.; Cicero, G.; Schwegler, E.; Sharma, M.; Galli, G., Electronic Effects in the IR Spectrum of Water under Confinement†. *J. Phys. Chem. B* **2009**, *113* (13), 4170-4175.
220. (a) Mallamace, F.; Broccio, M.; Corsaro, C.; Faraone, A.; Majolino, D.; Venuti, V.; Liu, L.; Mou, C.-Y.; Chen, S.-H., Evidence of the existence of the low-density liquid phase in supercooled, confined water. *Proc. Natl. Acad. Sci.* **2007**, *104* (2), 424-428; (b) Floquet, N.; Coulomb, J. P.; Dufau, N.; Andre, G.; Kahn, R., Confined water in mesoporous MCM-41 and nanoporous AlPO<sub>4</sub>-5: structure and dynamics. *Adsorption* **2005**, *11* (1), 139-144; (c) Wang, J.; Kalinichev, A. G.; Kirkpatrick, R. J., Structure and decompression melting of a novel, high-pressure nanoconfined 2-D ice. *J. Phys. Chem. B* **2005**, *109* (30), 14308-14313; (d) Chen, S.-H.; Liu, L.; Fratini, E.; Baglioni, P.; Faraone, A.; Mamontov, E., Observation of fragile-to-strong dynamic crossover in protein hydration water. *Proc. Natl. Acad. Sci.* **2006**, *103* (24), 9012-9016.
221. (a) Ball, P., Water: Water [mdash] an enduring mystery. *Nature* **2008**, *452* (7185), 291-292; (b) Ball, P., Water as an Active Constituent in Cell Biology. *Chem. Rev.* **2008**, *108* (1), 74-108; (c) Ball, P., Life's matrix: water in the cell. *Cell. Mol. Biol. (Noisy-le-grand)* **2001**, *47* (5), 717-720; (d) Ball, P., *H<sub>2</sub>O: A Biography of Water*. London, 1999; (e) Chaplin, M. F., A proposal for the structuring of water. *Biophys. Chem.* **2000**, *83* (3), 211-221; (f) Chaplin, M., Do we underestimate the importance of water in cell biology? *Nat. Rev. Mol. Cell Biol.* **2006**, *7* (11), 861-866.
222. Abascal, J. L.; Vega, C., Widom line and the liquid-liquid critical point for the TIP4P/2005 water model. *J. Chem. Phys.* **2010**, *133* (23), 234502.
223. Mishima, O.; Stanley, H. E., The relationship between liquid, supercooled and glassy water. *Nature* **1998**, *396* (6709), 329-335.
224. Fuentesvilla, D. A.; Anisimov, M. A., Scaled Equation of State for Supercooled Water near the Liquid-Liquid Critical Point. *Phys. Rev. Lett.* **2006**, *97* (19), 195702.
225. (a) Tanaka, H., Phase behaviors of supercooled water: Reconciling a critical point of amorphous ices with spinodal instability. *J. Chem. Phys.* **1996**, *105* (12), 5099-5111; (b) Tanaka, H., A self-consistent phase diagram for supercooled water. *Nature* **1996**, *380* (6572), 328-330.

226. (a) Wiggins, P. M., Role of water in some biological processes. *Microbiol. Rev.* **1990**, *54* (4), 432-449; (b) Wiggins, P. M., High and low density intracellular water. *Cell. Mol. Biol. (Noisy-le-grand)* **2001**, *47* (5), 735-744.
227. (a) Nilsson, A.; Pettersson, L. G., Perspective on the structure of liquid water. *Chem. Phys.* **2011**, *389* (1), 1-34; (b) Ricci, M. A.; Bruni, F.; Giuliani, A., "Similarities" between confined and supercooled water. *Faraday Discuss.* **2009**, *141*, 347-358.
228. (a) Marti, J.; Nagy, G.; Guardia, E.; Gordillo, M., Molecular dynamics simulation of liquid water confined inside graphite channels: dielectric and dynamical properties. *J. Phys. Chem. B* **2006**, *110* (47), 23987-23994; (b) Nagy, G.; Gordillo, M.; Guàrdia, E.; Martí, J., Liquid water confined in carbon nanochannels at high temperatures. *J. Phys. Chem. B* **2007**, *111* (43), 12524-12530.
229. (a) Byl, O.; Liu, J.-C.; Wang, Y.; Yim, W.-L.; Johnson, J. K.; Yates, J. T., Unusual hydrogen bonding in water-filled carbon nanotubes. *J. Am. Chem. Soc.* **2006**, *128* (37), 12090-12097; (b) Huang, L.-L.; Zhang, L.-Z.; Shao, Q.; Wang, J.; Lu, L.-H.; Lu, X.-H.; Jiang, S.-Y.; Shen, W.-F., Molecular dynamics simulation study of the structural characteristics of water molecules confined in functionalized carbon nanotubes. *J. Phys. Chem. B* **2006**, *110* (51), 25761-25768; (c) Shiomi, J.; Kimura, T.; Maruyama, S., Molecular dynamics of ice-nanotube formation inside carbon nanotubes. *J. Phys. Chem. C* **2007**, *111* (33), 12188-12193; (d) Martí, J.; Gordillo, M., Time-dependent properties of liquid water isotopes adsorbed in carbon nanotubes. *J. Chem. Phys.* **2001**, *114* (23), 10486-10492; (e) Martí, J.; Guardia, E.; Gordillo, M., Reorientational motions in sub- and supercritical water under extreme confinement. *Chem. Phys. Lett.* **2002**, *365* (5), 536-541.
230. (a) Rovere, M.; Ricci, M.; Vellati, D.; Bruni, F., A molecular dynamics simulation of water confined in a cylindrical SiO<sub>2</sub> pore. *J. Chem. Phys.* **1998**, *108* (23), 9859-9867; (b) Rovere, M.; Gallo, P., Effects of confinement on static and dynamical properties of water. *Eur. Phys. J. E Soft Matter* **2003**, *12* (1), 77-81; (c) Gallo, P.; Rovere, M.; Chen, S.-H., Dynamic crossover in supercooled confined water: Understanding bulk properties through confinement. *J. Phys. Chem. Lett.* **2010**, *1* (4), 729-733; (d) Bruni, F.; Ricci, M. A.; Soper, A. K., Water confined in Vycor glass. I. A neutron diffraction study. *J. Chem. Phys.* **1998**, *109* (4), 1478-1485; (e) Soper, A. K.; Bruni, F.; Ricci, M. A., Water confined in Vycor glass. II. Excluded volume effects on the radial distribution functions. *J. Chem. Phys.* **1998**, *109* (4), 1486-1494; (f) Gallo, P., Single particle slow dynamics of confined water. *PCCP* **2000**, *2* (8), 1607-1611; (g) Gallo, P.; Rovere, M.; Spohr, E., Glass transition and layering effects in confined water: a computer simulation study. *J. Chem. Phys.* **2000**, *113* (24), 11324-11335; (h) Hartnig, C.; Witschel, W.; Spohr, E.; Gallo, P.; Ricci, M. A.; Rovere, M., Modifications of the hydrogen bond network of liquid water in a cylindrical SiO<sub>2</sub> pore. *J. Mol. Liq.*

- 2000**, *85* (1), 127-137; (i) Malani, A.; Ayappa, K., Relaxation and jump dynamics of water at the mica interface. *J. Chem. Phys.* **2012**, *136* (19), 194701; (j) Gallo, P.; Rovere, M.; Chen, S., Anomalous dynamics of water confined in MCM-41 at different hydrations. *J. Phys.: Condens. Matter* **2010**, *22* (28), 284102; (k) Lerbret, A.; Lelong, G.; Mason, P. E.; Saboungi, M.-L.; Brady, J. W., Water confined in cylindrical pores: a molecular dynamics study. *Food Biophys.* **2011**, *6* (2), 233-240; (l) Milischuk, A. A.; Ladanyi, B. M., Structure and dynamics of water confined in silica nanopores. *J. Chem. Phys.* **2011**, *135* (17), 174709; (m) Bourg, I. C.; Steefel, C. I., Molecular dynamics simulations of water structure and diffusion in silica nanopores. *J. Phys. Chem. C* **2012**, *116* (21), 11556-11564.
231. Malani, A.; Ayappa, K.; Murad, S., Influence of Hydrophilic Surface Specificity on the Structural Properties of Confined Water†. *J. Phys. Chem. B* **2009**, *113* (42), 13825-13839.
232. (a) Rosenfeld, D. E.; Schmuttenmaer, C. A., Dynamics of water confined within reverse micelles. *J. Phys. Chem. B* **2006**, *110* (29), 14304-14312; (b) Luisi, P. L.; Straub, B. E., *Reverse Micelles: Biological and Technological Relevance of Amphiphilic Structures in Apolar Media*. Springer US: New York, 1984; (c) De, T. K.; Maitra, A., Solution behaviour of Aerosol OT in non-polar solvents. *Adv. Colloid Interface Sci.* **1995**, *59*, 95-193; (d) Levinger, N. E., Water in confinement. *Science* **2002**, *298* (5599), 1722-1723; (e) Faeder, J.; Ladanyi, B., Molecular dynamics simulations of the interior of aqueous reverse micelles. *J. Phys. Chem. B* **2000**, *104* (5), 1033-1046; (f) Pieniazek, P. A.; Lin, Y.-S.; Chowdhary, J.; Ladanyi, B. M.; Skinner, J., Vibrational spectroscopy and dynamics of water confined inside reverse micelles. *J. Phys. Chem. B* **2009**, *113* (45), 15017-15028; (g) Harpham, M. R.; Ladanyi, B. M.; Levinger, N. E.; Herwig, K. W., Water motion in reverse micelles studied by quasielastic neutron scattering and molecular dynamics simulations. *J. Chem. Phys.* **2004**, *121* (16), 7855-7868; (h) Venables, D. S.; Huang, K.; Schmuttenmaer, C. A., Effect of reverse micelle size on the librational band of confined water and methanol. *J. Phys. Chem. B* **2001**, *105* (38), 9132-9138; (i) Onori, G.; Santucci, A., IR investigations of water structure in Aerosol OT reverse micellar aggregates. *J. Phys. Chem.* **1993**, *97* (20), 5430-5434; (j) Piletic, I. R.; Moilanen, D. E.; Spry, D.; Levinger, N. E.; Fayer, M., Testing the core/shell model of nanoconfined water in reverse micelles using linear and nonlinear IR spectroscopy. *J. Phys. Chem. A* **2006**, *110* (15), 4985-4999; (k) Dokter, A. M.; Woutersen, S.; Bakker, H. J., Inhomogeneous dynamics in confined water nanodroplets. *Proc. Natl. Acad. Sci.* **2006**, *103* (42), 15355-15358; (l) Chowdhary, J.; Ladanyi, B. M., Molecular dynamics simulation of aerosol-OT reverse micelles. *J. Phys. Chem. B* **2009**, *113* (45), 15029-15039; (m) Rosenfeld, D. E.; Schmuttenmaer, C. A., Dynamics of the water hydrogen bond network at ionic, nonionic, and hydrophobic interfaces in nanopores and reverse micelles. *J. Phys. Chem. B* **2010**, *115* (5), 1021-1031; (n)

- Chowdhary, J.; Ladanyi, B. M., Molecular simulation study of water mobility in aerosol-OT reverse micelles. *J. Phys. Chem. A* **2011**, *115* (23), 6306-6316.
233. Huang, C.; Wikfeldt, K. T.; Tokushima, T.; Nordlund, D.; Harada, Y.; Bergmann, U.; Niebuhr, M.; Weiss, T.; Horikawa, Y.; Leetmaa, M., The inhomogeneous structure of water at ambient conditions. *Proc. Natl. Acad. Sci.* **2009**, *106* (36), 15214-15218.
234. (a) Ludwig, R.; Appelhagen, A., Calculation of Clathrate-Like Water Clusters Including H<sub>2</sub>O-Buckminsterfullerene. *Angew. Chem. Int. Ed.* **2005**, *44* (5), 811-815; (b) Chihaiia, V.; Adams, S.; Kuhs, W. F., Influence of water molecules arrangement on structure and stability of 5 12 and 5 12 6 2 buckyball water clusters. A theoretical study. *Chem. Phys.* **2004**, *297* (1), 271-287.
235. Müller, A.; Krickemeyer, E.; Bögge, H.; Schmidtman, M.; Roy, S.; Berkle, A., Changeable Pore Sizes Allowing Effective and Specific Recognition by a Molybdenum-Oxide Based "Nanosponge": En Route to Sphere-Surface and Nanoporous-Cluster Chemistry. *Angew. Chem.* **2002**, *114* (19), 3756-3761.
236. Zulauf, M.; Eicke, H. F., Inverted micelles and microemulsions in the ternary system water/aerosol-OT/isooctane as studied by photon correlation spectroscopy. *J. Phys. Chem.* **1979**, *83* (4), 480-486.
237. Schäffer, C.; Bögge, H.; Merca, A.; Weinstock, I. A.; Rehder, D.; Haupt, E. T. K.; Müller, A., A Spherical 24 Butyrate Aggregate with a Hydrophobic Cavity in a Capsule with Flexible Pores: Confinement Effects and Uptake-Release Equilibria at Elevated Temperatures. *Angew. Chem. Int. Ed.* **2009**, *48* (43), 8051-8056.
238. Lai, T.-L.; Floquet, S.; Roch-Marchal, C.; Marrot, J.; Haouas, M.; Taulelle, F.; Cadot, E., Private Communication. **2015**.
239. Andrew, E. R., Nuclear magnetic resonance. *Nuclear Magnetic Resonance*, by ER Andrew, Cambridge, UK: Cambridge University Press, **2009**, *1*.
240. Müller, A.; Zhou, Y.; Bögge, H.; Schmidtman, M.; Mitra, T.; Haupt, E. T. K.; Berkle, A., "Gating" the Pores of a Metal Oxide Based Capsule: After Initial Cation Uptake Subsequent Cations Are Found Hydrated and Supramolecularly Fixed above the Pores. *Angew. Chem. Int. Ed.* **2006**, *45* (3), 460-465.
241. Korenev, V. S.; Boulay, A. G.; Haouas, M.; Bannani, F.; Fedin, V. P.; Sokolov, M. N.; Terazzi, E.; Garai, S.; Müller, A.; Taulelle, F.; Marrot, J.; Leclerc, N.; Floquet, S.; Cadot, E., Tracking "Apolar" NMe<sub>4</sub><sup>+</sup> Ions within Two Polyoxothiomolybdates that Have the Same Pores: Smaller Clathrate and Larger Highly Porous Clusters in Action. *Chem. Eur. J.* **2014**, *20* (11), 3097-3105.
242. Lehn, J. M.; Vierling, P.; Hayward, R. C., Stable and selective guanidinium and imidazolium complexes of a macrocyclic receptor molecule. *J. Chem. Soc., Chem. Commun.* **1979**, (6), 296-298.
243. Pilette, M.-A.; Marrot, J.; Duval, S.; Bannani, F.; Floquet, S.; Sécheresse, F.; Cadot, E., {Mo<sub>2</sub>O<sub>2</sub>S<sub>2</sub>}<sub>2</sub><sup>+</sup>-directed synthesis of a polyoxotungstoarsenate(III).

Structure and  $^{183}\text{W}$  NMR studies of the  $[(\alpha\text{-AsW}_9\text{O}_{33})_3(\text{WO}(\text{OH})_2)_3(\text{Mo}_2\text{O}_2\text{S}_2(\text{H}_2\text{O})_4)]^{13-}$  anion. *C. R. Chimie* **2012**, *15* (2-3), 124-129.

UNIVERSITAT ROVIRA I VIRGILI

KEPLERATES: FROM ELECTRONIC STRUCTURE TO DYNAMIC PROPERTIES.

María Dolores Melgar Freire

Dipòsit Legal: T 258-2016